How large spheres spin and move in turbulent flows

Robert Zimmermann

Thèse

en vue de l'obtention du grade de **Docteur**

de l'**École Normale Supérieure de Lyon – Université de Lyon**

Laboratoire de Physique &
Ecole Doctorale de Physique et Astrophysique

How Large Spheres spin and move in Turbulent Flows

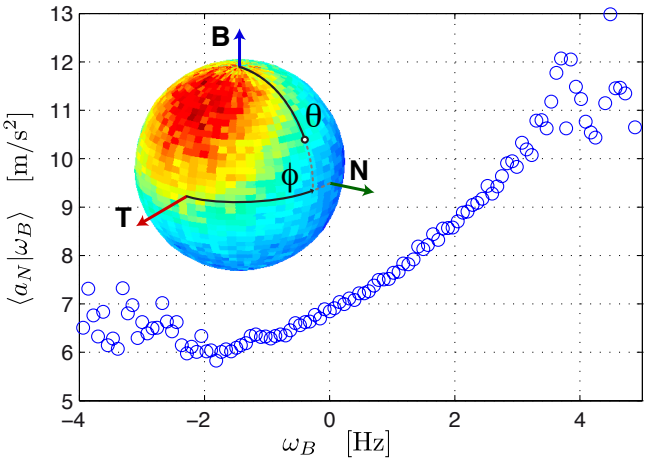

présentée et soutenue publiquement le 13 juillet 2012

par **Robert ZIMMERMANN**

sous la direction de **Romain VOLK** et **Jean-François PINTON**

après l'avis de **Haitao XU** et **Alex LIBERZON**

devant la commission d'examen formée de

Christophe	BAUDET	Examinateur
Luminita	DANAILA	Examinateur
Alex	LIBERZON	Rapporteur
Jean-François	PINTON	Directeur de thèse
Romain	VOLK	Co-directeur de thèse
Haitao	XU	Rapporteur

Fabriqué en France

Contents

1 Introduction

Nature is full of flows and many of them are turbulent and transport objects. In nature one encounters such particle-laden flows for example as rain droplets in a thundercloud, transport of pollen and seeds with the wind or of sediments in a river. They play an important role in industrial applications, too: Be it the atomizing of gasoline in a motor, sewage treatment, chemical mixers or weather balloons.

The turbulent motion of flows itself is a yet unsolved problem characterized by its high irregularity and its fluctuations in both time and space. Moreover, turbulence covers a large range of scales: Energy is injected at large scales where it drives the creation of large eddies, which continuously break up into new eddies. The whirls interact and disperse until they reach a size where viscosity plays a role and their kinetic energy is dissipated into heat. Particles immersed in such a flow are consequently subject to a complicated interaction with eddies of all sizes.

Since the time of Euler, Navier and Stokes huge progress has been made in understanding the motion of spherical particles of size D much smaller than the smallest length scale of the flow, the Kolmogorov scale η [65, 41, 22]. Because of the small size of the particle, the flow around it is locally laminar – see Fig. 1.1 – therefore the equation governing the particle velocity, $\boldsymbol{v}$, can be determined by solving the fluid equations once the fluid velocity, $\boldsymbol{u}$, is known. In the simplest case, the particles are subject to the Stokes drag and the added mass term [40, 14]; thus, the velocity $\boldsymbol{v}$ can be determined by solving a simple differential equation. For $D \to 0$, the velocity of a neutrally buoyant particle reduces to the fluid velocity, $\boldsymbol{u}$, so the particle behaves as a fluid tracer. This property is crucial for several experimental techniques [67].

With the advent of Lagrangian measurement techniques material particles are gaining attention. These particles have a size larger than η but are still small compared to the largest scales in the flow. As suggested by Fig. 1.1, their case is conceptually much more difficult.

By studying the acceleration statistics of a particle one can infer on the dynamics of the forces acting on it. Experiments have shown that upon increasing the ratio D/η from 1 to 40, the variance of the particle acceleration (*i.e.* of the forces) decreases as $(D/\eta)^{-2/3}$ [74, 55]. Nevertheless, the fluctuations of force remain non–gaussian up to $D/\eta \lesssim 40$ [54, 11, 72]. Since material particles decrease their acceleration variance with increasing size, they share common properties with heavy (inertial) particles for which the behavior is well determined by their size ratio D/η. Still, large neutrally-buoyant particles cluster differently than inertial particles [15, 16]. At present a full derivation of the equation of motion of a large particle is still not available.

Despite its importance in many technical flows the motion of particles with a size com-

parable to the large scales is surprisingly little studied. This is (partially) due to the fact the description of a solid object freely advected in a fluid requires, in addition to its translational degrees of freedom characterizing its position, three rotational degrees of freedom, specifying its orientation with respect to a reference frame. The evolution of its position and of its orientation depends, according to Newton's laws, on the forces and torque acting on the particle at each instant, which result from the interaction between the object and the turbulent flow.
In the preceding work of Yoann Gasteuil [20] it was observed that a neutrally buoyant sphere of a size $D \sim 0.6\,L_{\text{int}}$ (*i.e.* comparable to the large scales of the flow) is highly intermittent in both translation and rotation. Simulations at low turbulence levels show that particles of $D/L_{\text{int}} \sim 1$ alter the surrounding flow up to a distance of twice their diameter [48]. Recently, this has been supported by Simon Klein, Mathieu Gibert and others [32] who simultaneously followed tracer particles and rigid gel spheres in a highly turbulent environment.

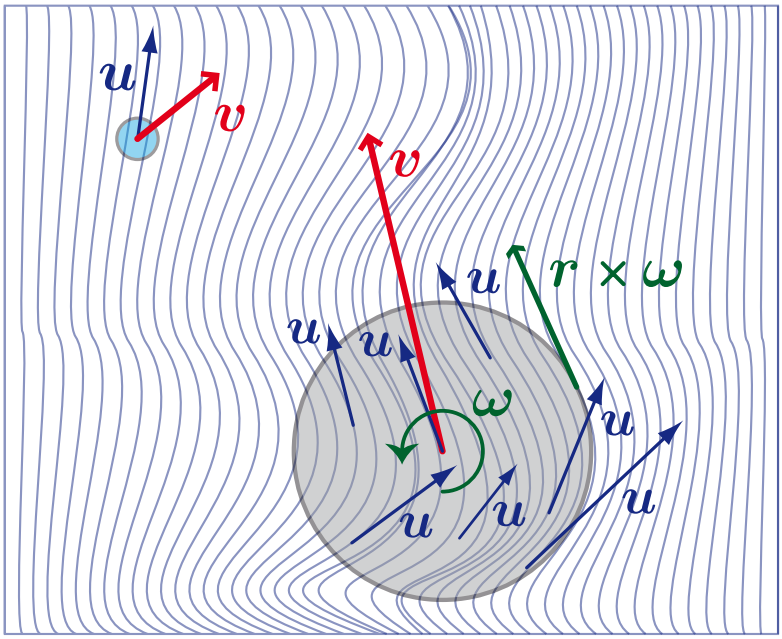

Figure 1.1: Sketch of a small and a large particle superimposed on local stream lines. Whereas the flow around the small particle is smooth, it exhibits significant spatial variations around the large particle.

The present experimental study investigates the motion of neutrally buoyant spheres whose diameter D is of the order of the integral scale L_{int}. In addition, we aim at resolving the six degrees of freedom of the particle dynamics. Therefore we developed a novel measurement technique, which enables us to obtain a simultaneous tracking in time of the particle's position and its *absolute* orientation with respect to a reference frame.

Previous studies focused on directly measuring the angular velocity without resolving the absolute orientation as a function of time. Ye and Roco [79] tracked dots painted

on a particle with high speed cameras and computed the angular velocity from their displacement between two consecutive frames. Recently, Klein *et al.* [32] adapted a particle tracking system to this approach: Fluorescent tracer particles sticked to the surface of transparent gel spheres and tracer particles suspended in the carrier flow are tracked in space, the sphere's rotation is then given by the relative displacement of the sticked particles. However, identifying which are attached to a moving sphere's surface and which are moving freely with respect to the others is a non-trivial task. A completely different ansatz was taken by Frish and Webb [18] who created an Eulerian technique measuring one component of the angular velocity using specially engineered, transparent particles which contain an embedded mirror. The reported particle diameter is less than 50 μm, which is of the order of the Kolmogorov length scale, η. Our approach is completely different: it consists in painting the particle with a suitable layout, and in retrieving its orientation. For algorithmic efficiency (and robustness) this is not done step by step but for the entire trajectory using a global path extraction. The experimental setup and the technique are presented in chapter 3.

Having access to particle's translation and rotation enables us to study the forces and torques acting on a large inertial particle, thus permitting to ask yet fundamental questions about their dynamics. More specifically three questions are addressed. First general features of the translation are presented in chapter 4. Next, we turn to the rotation of a solid large particle (chapter 5) and show that despite the highly turbulent flow rotation and translation couple according to the lift force $\boldsymbol{F}_{\text{lift}} = C_{\text{lift}}\, \boldsymbol{v}_{\text{rel}} \times \boldsymbol{\omega}$. Historically, a coupling between the rotation and translation was first reported by G. Magnus in 1852 in his article *Über die Abweichung der Geschosse, und: Über eine auffallende Erscheinung bei rotierenden Körpern*[1] [39] and a lift has been measured in laboratory experiments, when the flow is steady and laminar [79, 70, 56]. It has further been observed for stationary objects in a rotating flows but to our knowledge we report here the first observation of a lift force for a freely moving sphere in a turbulent flow. In the third part (chapter 6) we test how the particle exchanges momentum with the fluid. For that purpose we analyze the fluctuations of the particle's kinetic energy by means of the fluctuation theorem [19, 12].

Furthermore, in collaboration with SmartINST, a young startup on the ENS campus and building upon the work of Yoann Gasteuil *et al.* [20] we present a novel measurement apparatus for characterizing flows in chapter 7: An instrumented particle, which continuously transmits its three-dimensional Lagrangian acceleration. The particle embarks a small battery, a 3D accelerometer operating at 316 Hz and a wireless transmission system, its signal is then received and processed on a control computer. After a general presentation of the apparatus the developed methods for the interpretation of the acceleration signal are explained. We further test its precision by tracking the position and orientation of the particle while simultaneously recording its acceleration signal. Some parts explored during the 3½ years of this thesis do not fully fit within the storyline of the manuscript. These sidetracks are therefore presented separately in appendix A.

[1] On the deviation of projectiles, and: On a striking phenomenon of rotating bodies

2 A very intermittent introduction to turbulence

This chapter recalls some features and concepts of turbulence and the tools used. In a way it's as intermittent as our particle's motion. A slower and less intermittent introduction can be found in the following books:
Pope *Turbulent Flows* [52], Laudau and Lifschitz *Hydrodynamics* [35], Bachelor *an introduction to fluid dynamics* [7], Frisch *Turbulence: The Legacy of A. N. Kolmogorov* [17], and in Tennekes and Lumley *A First Course in Turbulence* [63]. A comprehensive source of information on the various experimental techniques, which were developed in fluid dynamics research, is found in the *Springer Handbook of Experimental Fluid Dynamics* [67].

2.1 Fluid dynamics & Scales

At some point during one's study of physics (or engineering) one learns that the motion of a fluid is govern by the Navier-Stokes equation. In most cases this is restricted to incompressible fluid of constant viscosity ν and constant (fluid) density ρ_f:

$$\left[\frac{\partial}{\partial t} + \boldsymbol{u}\cdot\nabla\right]\boldsymbol{u} = -\frac{\nabla p}{\rho_f} + \nu\nabla^2\boldsymbol{u} + \frac{1}{\rho_f}\boldsymbol{f} \tag{2.1}$$

where $\boldsymbol{u}$ is the velocity field, p the pressure and $\boldsymbol{f}$ external forces (per body volume). In addition the fluid is subject to the continuum equation $\nabla\cdot\boldsymbol{u} = 0$ and the boundary conditions. The term $(\boldsymbol{u}\cdot\nabla)\,\boldsymbol{u}$ is quadratic and only for some special cases one can find analytical solutions. Most of those fall into the regime when viscous forces dominate – *i.e.* $\nu\nabla^2\boldsymbol{u} > (\boldsymbol{u}\cdot\nabla)\,\boldsymbol{u}$ – and one therefore introduces the so-called *Reynolds number* as a dimensionless parameter relating the inertial and viscous term:

$$Re = \frac{\text{Magnitude}\left[(\boldsymbol{u}\cdot\nabla)\,\boldsymbol{u}\right]}{\text{Magnitude}\left[\nu\nabla^2\boldsymbol{u}\right]} = \frac{U\,L}{\nu} \tag{2.2}$$

where L and U represent the characteristic length and velocity scale of the flow; one can interpret the Reynolds number as an indicator of the level of turbulence. For $Re \ll 1$ the viscous term dominates and small perturbations arising from the boundaries or body forces acting on the fluid are damped out. The flow is then organized in stationary streamlines. One can picture its structure as fluid lamina which glide along each other but do not cross. Hence, this type of flow is called *laminar*.

For an increasing Reynolds number perturbations arising from the boundaries or body forces acting on the fluid are not damped out anymore and the lamina break up into

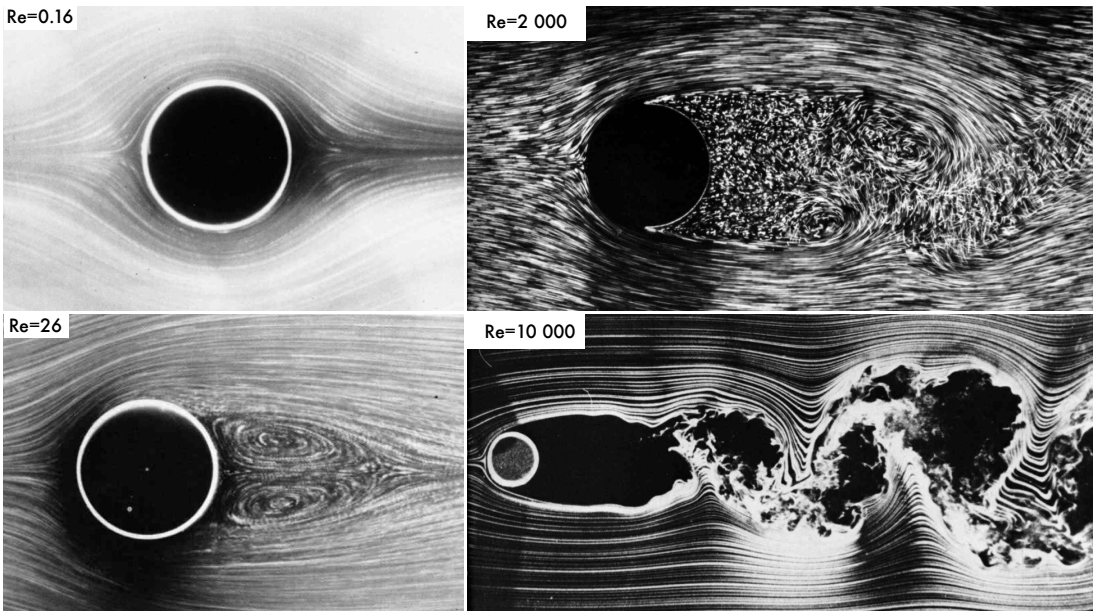

Figure 2.1: Flow behind a cylinder at different Reynolds numbers [Extract from the album of fluid motion [69]]. At very low Reynolds number ($Re = 0.16$) the flow is organized in streamlines passing smoothly around the cylinder (a so-called creeping or Stokes flow); but with increasing Reynolds number more and more eddies of different sizes appear in the flow.

many eddies, which are advected with the mean-flow. The system evolves into a spatio-temporal chaotic system which is called turbulence. In this regime mixing is enhanced, but also the drag force acting on a body moving through the flow is higher in a turbulent flow than in the laminar case. To illustrate this transition Fig. 2.1 shows extracts from the album of fluid motion[69] for the flow around a cylinder at four different Reynolds numbers. At $Re = 0.16$ the flow is organized in streamlines passing smoothly around the object, this configuration is also called a creeping or Stokes flow. But with increasing Reynolds number more structures of different sizes appear in flow. Their interaction yields the complex multi-scale nature in both time and space of fully turbulent flows. One, therefore, turns towards a statistical description of turbulent flows.

Richardson cascade Richardson formulated the multi-scale nature of turbulence in his famous poem:

> *Big whorls have little whorls that feed on their velocity,*
> *and little whorls have smaller whorls and so on to viscosity.*

In 1941 Kolmogorov published groundbreaking articles translating this idea into mathematical language: Energy is injected at a length scale L_{int} characterizing the biggest eddies. These eddies break up into smaller eddies which again break up into even smaller whirls. The cascade stops when viscosity becomes non-negligible and injected energy is

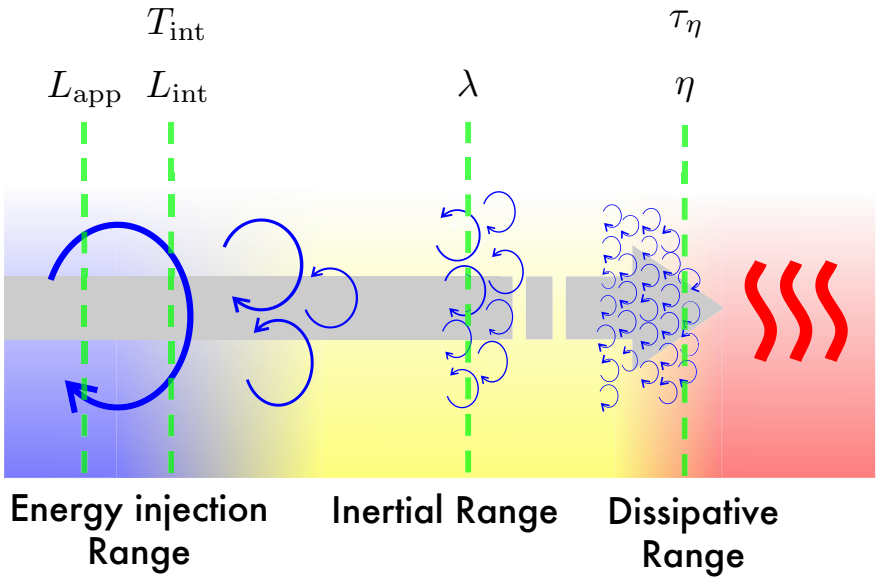

Figure 2.2: Sketch of the Richardson cascade. The system (of size L_{app}) injects energy at the size L_{int} characterizing the biggest whirls. These whirls break up into smaller whirls, which break up into even smaller eddies, and so forth. This process is stopping in the dissipative range when viscosity becomes non-negligible and the injected energy is finally converted to heat. This model does not describe the dynamics of the eddies.

converted into heat. Energy conservation dictates that the energy injected at large scales must be the energy dissipated at the small scales. One therefore defines the energy transfer rate[1] ε, as the injected power per mass unit. Dimensional arguments relate the energy transfer rate to the velocity u_l of an eddy of length l:

$$\varepsilon_l \sim \frac{u_l^3}{l} \tag{2.3}$$

Kolmogorov then assumes that far away from the energy injection scales the eddies lost their memory of their creation. If dissipation is still negligible then the statistics are fully determined by ε; this is the so-called inertial range. The end of the cascade is referred to as dissipative range which is fully characterized by viscosity, ν and energy injection rate, ε. Then the smallest characteristic length scale η and time scale τ_η of the flow are:

$$\eta = \left(\nu^3/\varepsilon\right)^{1/4} \tag{2.4a}$$

$$\tau_\eta = \left(\nu/\varepsilon\right)^{1/2} \tag{2.4b}$$

One generally speaks of η and τ_η as Kolmogorov scales. One can further derive/identify an intermediate scale situated between the largest and the smallest eddies: The Taylor micro scale, λ, and it is common to specify the turbulence level at this scale by the Reynolds

[1] The terms energy injection rate, energy transfer rate and energy dissipation rate are equal.

number based on the Taylor micro scale $R_\lambda \approx \sqrt{15\,Re}$. One can further relate the Kolmogorov scales to the biggest (or integral) scales of the flow:

$$\eta/L_{\text{int}} \propto Re^{-3/4} \tag{2.5a}$$

$$\tau_\eta/T_{\text{int}} \propto Re^{-1/2} \tag{2.5b}$$

where T_{int} is the time scale of the large eddies of the flow. A consequence of the equations (2.5) is that the Kolmogorov scales and the biggest scales of the flow become more separated with increasing Re. This conclusion is sometimes referred to as *Kolmogorov's idea of scale separation*. An illustration of the cascade is provided in Fig. 2.2. All measurements presented within this manuscript consider particles whose diameter is a fraction of the integral length scale and much larger than the Kolmogorov scale.

One should keep in mind that the Richardson cascade does not describe the dynamics within the cascade. Similarly Kolmogorov's derivations assume that the turbulent fluctuations are locally homogeneous and isotropic. Establishing such conditions in the lab is a demanding task and outside a research facility they are almost never encountered. Moreover, Blum *et al.* showed for a variety of turbulence creating apparatuses and Reynolds numbers that a signature of the large scales can still be found in the small scales [9].

2.2 Euler, Lagrange & the motion of particles

There are some things in life which are more fun doing than watching

(Jean-François Pinton)

As for many things there are (at least) two perspectives, one can either observe at fixed position without participating in the fluid's motion or one can be advected by the flow and describe the local interaction along one's trajectory through the flow. The descriptions are the so-called *Eulerian* and *Lagrangian* frame. Mathematically, the Eulerian frame works with spatio-temporal fields of either vector quantities like the fluid velocity $\boldsymbol{u}(\boldsymbol{x}, t)$ or scalars $\phi(\boldsymbol{x}, t)$ (*e.g.* the temperature). In contrast thereto the Lagrangian frame measures a vector or scalar quantity along a trajectory $\boldsymbol{Y}(t)$.

Both perspectives yield a different view on the dynamics but in the limit of infinite resolution or an infinite amount of trajectories through the flow field both expressions can be converted into the other. The Lagrangian frame is the natural choice when describing the motion of objects advected in the flow.

Normally one choses the description which is suitable for the problem asked. Complex problems necessitate informations from both sides, *e.g.* to predict the spread of volcano ash it is important to ask "how do dust particles usually behave?" as well as "how is the wind today?".

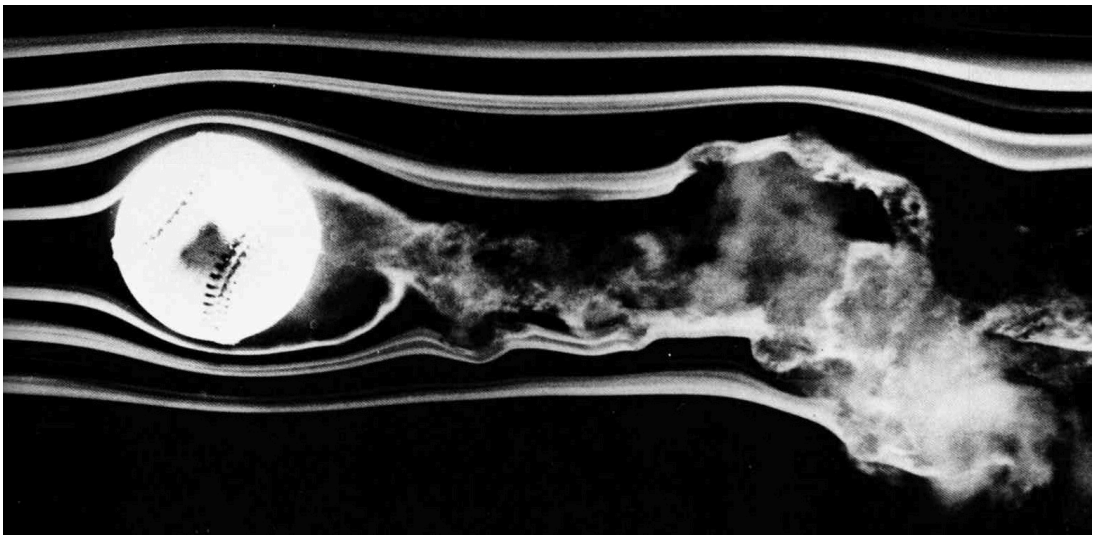

Figure 2.3: Smoke visualization of the flow around a baseball spinning at 630 rpm in a wind-tunnel at 23.5 m/s [Extract from the album of fluid motion [69]]. Note the turbulent wake which extends over several particle diameters. The stream-lines are bent downwards due to the rotation of the particle.

Particles Objects in flows come in many shapes. We focus here on homogeneous rigid spheres, which are characterized by their diameter D_{part} and their density ρ_p. The influence of their surface roughness is neglected. In order to compare different experiments one usually takes the ratio of the diameter to the biggest ($D_{\text{part}}/L_{\text{int}}$) or smallest ($D_{\text{part}}/\eta$) length scale, and of the particle's density to that of the fluid,

$$\beta \equiv \frac{3\,\rho_f}{2\,\rho_p + \rho_f} \tag{2.6}$$

All data presented in this manuscript is gained with neutrally buoyant particles – *i.e.* $\rho_p = \rho_f$ ($\beta = 1$).

After defining these parameters one can ask what happens if a particle is inserted into a flow. Fig. 2.3 shows a visualization of the flow around a spinning baseball, one sees how the stream lines are bent by the particle. The wake is clearly turbulent and extends over several particle diameters. Moreover, one observes the influence of the rotation on the streamlines. A derivation of the equation of motion for such a real-world example is an extremely complex problem.

In the case of small particles one can assume that the flow is modified only locally. Nevertheless, one has to take care of the no-slip condition: the fluid velocity matches the particle velocity at the surface. A priori the particle can (and does) rotate; hence, the no-slip condition induces the forces and torques acting on the particle. In order to characterize the flow on the scale of the particle, one defines a Reynolds number based on the particle

$$Re_p = \frac{D_{\text{part}}\,\left|\boldsymbol{v}_{\text{slip}}\right|}{\nu} \tag{2.7}$$

where the slip velocity $\boldsymbol{v}_{\text{slip}}$ is the velocity difference between particle and surrounding flow.

The equation of motion for a small particle with a small particle Reynolds number has been derived by Maxey and Riley [41] (and independently by Gatignol [22]):

$$\begin{aligned}
\rho_p \frac{\mathrm{d}}{\mathrm{d}t}\boldsymbol{v}_{\text{part}} = {} & \underbrace{\rho_f \left[\frac{\partial}{\partial t} + \boldsymbol{u}\cdot\nabla\right]\boldsymbol{u}\Big|_{\boldsymbol{Y}(t)}}_{\text{pressure gradient}} + \underbrace{(\rho_p - \rho_f)\,\boldsymbol{g}}_{\text{buoyancy force}} - \underbrace{\frac{\rho_f}{2}\frac{\mathrm{d}}{\mathrm{d}t}\left(\boldsymbol{v}_{\text{slip}} - \frac{a^2}{10}\nabla^2\boldsymbol{u}\Big|_{\boldsymbol{Y}(t)}\right)}_{\text{added mass}} \\
& - \underbrace{\frac{9\nu\rho_f}{2a^2}\left(\boldsymbol{v}_{\text{slip}} - \frac{a^2}{6}\nabla^2\boldsymbol{u}\Big|_{\boldsymbol{Y}(t)}\right)}_{\text{viscous drag}} - \underbrace{C_L\,\rho_f\,\boldsymbol{v}_{\text{slip}}\times\boldsymbol{\omega}_p}_{\text{lift force}} \\
& - \underbrace{\frac{9\rho_f}{2a}\sqrt{\frac{\nu}{\pi}}\int_0^t (t-\tau)^{-\frac{1}{2}}\frac{\mathrm{d}}{\mathrm{d}\tau}\left(\boldsymbol{v}_{\text{slip}}(\tau) - \frac{a^2}{6}\nabla^2\boldsymbol{u}\Big|_{\boldsymbol{Y}(t)}\right)\mathrm{d}\tau}_{\text{history force}}
\end{aligned} \tag{2.8}$$

It is $\boldsymbol{u}$ the flow field in absence of the particle, $a = D_{\text{part}}/2$ the particle radius, $\boldsymbol{Y}(t)$ the particle position and $\boldsymbol{v}_{\text{part}}$ its velocity. $\boldsymbol{v}_{\text{slip}} = \boldsymbol{v}_{\text{part}}(t) - \boldsymbol{u}\left[\boldsymbol{Y}(t), t\right]$ is the velocity difference between particle and unaltered flow, $\boldsymbol{u}$ (at the particle position $\boldsymbol{Y}(t)$). It should be pointed out that the particle does not act back on the flow (so-called *one-way coupling*). $\nabla^2\boldsymbol{u}\big|_{\boldsymbol{Y}(t)}$ stems from the Faxén corrections which take into account the non-uniformity (at the scale of the particle) of the flow. They vanish in a locally uniform flow field.

The different terms tell of the various forces acting on the sphere, buoyancy and pressure are the direct fluid-mechanical counter-part of Newton mechanics. As the particle moves through the flow is has to accelerate its surrounding fluid and thus loses momentum. This effect appears as an added mass. Since the flow is homogeneous at the scale of the particle the classical Stokes force is an adequate description of the viscous drag. The wake of the particle acts back on the particle and has some memory of its motion. This is accounted for with the history force term. Since its calculation is extremely demanding this term is very often omitted. In the case of a creeping (or Stokes) flow ($Re_p \ll 1$) around the particle rotation and translation decouple and there is no back-reaction from the torque on the particle velocity. In this case it is furthermore possible to reduce equation (2.8) to the Stokes drag and the added mass term [40, 14]. The inertia/density of the particle is then represented by the time scale τ_p in which it reacts to changes in the flow and the so-called *Stokes number* becomes the sole non-dimensional parameter relating the particle's inertia to the smallest time scale of the flow:

$$St \equiv \frac{\tau_p}{\tau_\eta} = \frac{D_{\text{part}}^2}{12\,\nu\,\beta}\frac{1}{\tau_\eta} = \frac{1}{12\beta}\left(\frac{D_{\text{part}}}{\eta}\right)^2 \tag{2.9}$$

It should be stressed that this simplification is limited to small particles ($D_{\text{part}} \lesssim \eta$) [15, 16].

For higher Re_p, a rotating particle experiences a lift or Magnus force. This non-linear and invsicid contribution couples rotation and translation of the particle. The term is not part of the original Maxey-Riley equation (2.8): It was added later by Auton [5, 6]. We discuss it and the rotation of larger particle in more detail at the beginning of chapter 5. Renée Gatignol further derived the torques acting on a particle [22]:

$$\begin{aligned}\frac{\mathrm{d}}{\mathrm{d}t}\left(\underline{\underline{\boldsymbol{J}}}\boldsymbol{\omega}_p\right) = \boldsymbol{T} = &\underbrace{-8\pi\rho_f\,\nu\,a^3\left(\boldsymbol{\omega}_p - \boldsymbol{\omega}_f/2\right)}_{\text{drag torque}} + \underbrace{\frac{8}{15}\pi\,a^5\,\rho_f\left[\frac{\partial}{\partial t} + \boldsymbol{u}\cdot\nabla\right]\boldsymbol{\omega}_f}_{\text{fluid vorticity}} \\ &\underbrace{-\frac{8\pi\rho_f\,\nu\,a^3}{3}\int_0^t \frac{\mathrm{d}\left(\boldsymbol{\omega}_p - \boldsymbol{\omega}_f/2\right)}{\mathrm{d}\tau}\exp\left(\frac{\nu\,(t-\tau)}{a^2}\right)\operatorname{erf}\sqrt{\frac{\nu\,(t-\tau)}{a^2}}\mathrm{d}\tau}_{\text{history torque 1}} \\ &\underbrace{-\frac{8\pi\rho_f\,a^4}{3}\sqrt{\frac{\nu}{\pi}}\int_0^t (t-\tau)^{-\frac{1}{2}}\frac{\mathrm{d}\left(\boldsymbol{\omega}_p - \boldsymbol{\omega}_f/2\right)}{\mathrm{d}\tau}\mathrm{d}\tau}_{\text{history torque 2}}\end{aligned} \tag{2.10}$$

It is $\boldsymbol{\omega}_p$ and $\boldsymbol{\omega}_f$ the angular velocity of the particle and the fluid (*i.e.* the vorticity), $\underline{\underline{\boldsymbol{J}}}$ is the inertia (tensor) of the spherical particle. The particle's angular momentum is resisted by drag torque and the two history terms and it is driven by the angular acceleration of the underlying flow. The torque does not have an equivalent of the added mass term in Eq. (2.8). In most conditions all terms except the first are neglected and one obtains:

$$\boldsymbol{T} = -8\pi\rho_f\,\nu\,a^3\,(\boldsymbol{\omega}_p - \boldsymbol{\omega}_f/2) \tag{2.11}$$

For a solid homogeneous sphere one can then compute the response time to a torque

$$\tau_p^{\mathrm{rot}} = \frac{|\underline{\underline{\boldsymbol{J}}}|}{8\pi\rho_f\,\nu\,a^3} = \frac{a^2}{15\nu} \tag{2.12}$$

Again, this is only meaningful for small particles.

Particle which are much larger than the Kolmogorov scale are not governed with these equations. Unfortunately no equation exists (yet) for the motion of large particles. Moreover, direct numerical simulations of the Navier-Stokes equation which take into account the boundary conditions of a moving object are computation-wise extremely expensive. In 2010 Aurore Naso [48] published work on a fixed particle in a turbulent flow at $R_\lambda = 20$, for comparison the turbulence in a cup of coffee has $R_\lambda \approx 100$.

2.3 Von Kármán swirling flows

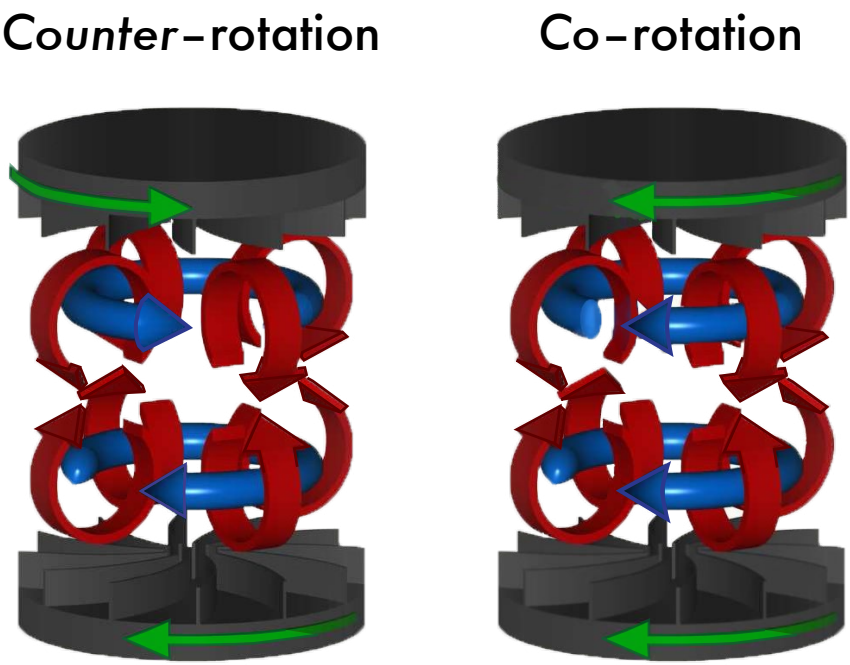

Figure 2.4: Flow structure in a von Kármán flow with co- and counter-rotating impellers [image adapted from [57]]. Note that the impellers are housed in a square vessel throughout this thesis.

The von Kármán swirling flow is a tank with two opposing propellers that create an axisymmetric flow field. The propellers[2] can be either *co-* or *counter*-rotating, leading to different flow configurations. Blades on the impellers work similar to a centrifugal pump and add a poloïdal circulation at each propeller. In the counter-rotating case the flow is highly turbulent and within a small region in the center the mean flow is little and the local characteristics approximate homogeneous turbulence. However, at a large scale it is known to have a large scale anisotropy [50, 43]. An extensive characterization can be found in the thesis of Florent Ravelet [57]. He showed [58] that with increasing propeller speed the flow undergoes a transition through several chaotic states until it reaches a fully developed turbulent state which is characterized by the fact that the fluctuations in velocity grow linearly with the propeller speed. In other words the flow is fully turbulent if RMS $\left(v(f_{\text{prop}})\right)/f_{\text{prop}} = \text{const.}$. According to [58] and as illustrated in Fig. 2.5, the transition to fully developed turbulence occurs at a Reynolds number of $Re_t = 2\pi R^2 f_{\text{prop}}/\nu \approx 3500$; in this dissertation all experiments were performed at $Re > 4000$. Hence, the flow was always fully turbulent.

The high turbulence level and confined flow in an apparatus that fits on a lab bench makes this apparatus highly appealing for Lagrangian measurements; the von Kármán flow

[2] The terms pro- and impeller are equally employed.

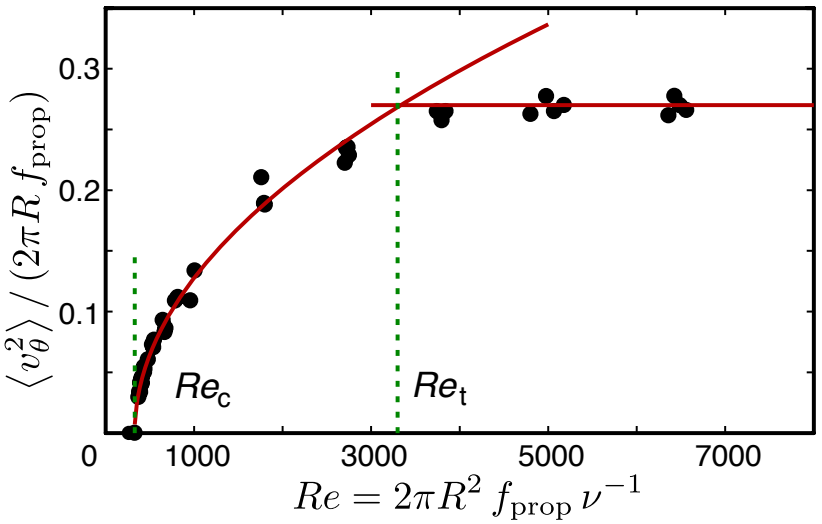

Figure 2.5: Transition to fully developed turbulence in a cylindrical von Kármán flow [figure adapted from [58]]. Note that the Reynolds number, Re, is here simply based on the propeller radius R and the propeller speed f_{prop}. Re_t marks the transition to fully developed turbulence. All measurements presented in this thesis have $Re > 4000$. Hence, the flow is fully turbulent.

became a standard tool for turbulence research [65]. Some people even refer to it as the "work-horse" of turbulence and also the "French washing machine"[3].

On the other hand co-rotating impellers create a flow similar to a hurricane: Close to the axis of rotation the flow is weak, followed by a strong toroidal component and an additional poloidal circulation induced by blades on the impellers. At the same propeller speed a co-rotating driving creates less turbulence than counter-rotating impellers, but the flow is still highly turbulent. Catherine Simand [60] has examined the properties of co-rotating von Kármán flow in detail during her thesis. Within this manuscript co-rotating driving is used as a cross-check, but the focus lies on counter-rotating impellers.

A visualization of the flow structures is provided in Fig. 2.4.

Although most experiments reported in the literature are carried out in a cylinder, the von Kármán flow of this thesis has a container built with transparent flat side walls. Thus, the cross section of the vessel is square. This rectangular design enables us to perform direct optical measurements over almost the whole flow domain. It also reduces a solid body rotation; a comparable effect can be achieved by adding baffles to a cylinder. The impellers are fitted with straight blades such that we observe the characteristic poloidal circulation due to the pumping. More details on the apparatus are found in section 3.1.

[3] This is an urban legend, the French have the same washing machines as everybody else.

2.3.1 On estimating flow parameters

When estimating the motion based on general parameters of the flow, one has the choice between Kolmogorov and large scale (apparatus) type arguments. As explained earlier the former evaluates flow parameters (*e.g.* the Kolmogorov scales $\eta \& \tau_\eta$) in the dissipative and inertial range based on energy injection rate, ε and viscosity, ν. The derivation assumes that the flow behaves locally homogeneous and isotropic in a statistical sense.

When investigating large particles with a size D_{part} comparable to the integral length scale, L_{int}, moving through the whole mixer, these assumptions are most likely no longer valid. Similar to the thesis and articles by Ravelet [57, 58], one can then focus on dimensional arguments which stem from the apparatus. These are in our case the propeller speed f_{prop}, the particle diameter D_{part} and the radius of the propeller R. Although these two choices are different in their physical background, they yield similar dimensional predictions. That is due to scaling relations of fully developed turbulence like $\varepsilon \propto f_{\text{prop}}^3$ and $\text{RMS}\,(v) \propto f_{\text{prop}}$. For a clear distinction we differentiate between the terms *Kolmogorov-type* and *dimensional* arguments.

3 Setup, Technique & Measurements

Since Newton it is known that the motion of an object is determined by the forces and torques acting on it. Its interaction with the various whirls in a flow results in a complex translation and rotation of the latter. For simplicity we limit our investigation to material spherical particles, yet we do not restrict their mass distribution.

Over the last 60 years a set of measurement techniques has become available to extract a particle's velocity and acceleration and yielded important information on the interactions with the flow [65]. For a detailed survey on these techniques the reader is referred to the *Handbook of Experimental Fluid Dynamics* [67].
Laser or Acoustic Doppler Velocimetry have direct access to the velocity. Unfortunately they cannot be extended to measure the rotation and are therefore not further discussed here. Particle Tracking Velocimetry (PTV) on the other hand follows the particle's position by means of multiple high speed cameras. Velocity and acceleration are then the derivatives of the position time-series. Furthermore this technique is able to track several particles simultaneously which enables the study of multi-particle statistics like how fast they spread.

The rotational component of the particle's motion can be obtained by tracking the displacement of dots on the sphere's surface. This was first introduced by Ye and Roco [79], unfortunately a PhD student had to identify all dots by hand. It was recently picked up by Mathieu Gibert, Simon Klein *et al.* [32] who use a PTV system to track fluorescent particles which are attached to large transparent gel spheres. Adding tracer particles to the flow allows him to directly access the flow of the fluid around the spheres. In addition, no

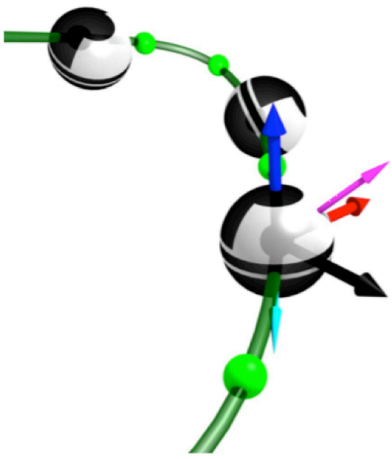

Figure 3.1: Illustration of a trajectory containing both position and orientation

student is forced anymore to identify the dots by hand. However, identifying which tracers are attached to a moving sphere's surface and which are moving freely is a non-trivial task.
Frish and Webb [18] demonstrated a completely different technique with the vorticity optical probe: They engineered transparent particles that embedded a mirror. An incident laser beam is then reflected with an angle depending on the particles orientation. The focal point of a spherical lens depends on the angle between optical axis and incident beam. Thus, an image sensor placed at the focal point can detect the angle of the incident beam. The reported particle diameter is less than 50 µm, which is of the order of the Kolmogorov length scale, η. Their technique can therefore measure two components of the fluid vorticity.

All these techniques can trace the angular velocity, however, they do not have access to the orientation of the particle. But the absolute orientation is important for problems where there is a preferential direction—such as when there is a global rotation, a temperature gradient, an imposed magnetic field or a 3D accelerometer in a rotating instrumented particles. The latter case is presented in chapter 7.

As illustrated in Fig. 3.1 we therefore developed a novel measurement technique which can follow the full six degrees of freedom – *i.e.* position and *absolute* orientation – of a sphere advected by the flow. The angular and linear velocity (and acceleration) are then the derivatives thereof.
The position is carried out with standard particle tracking techniques and two high-speed video cameras. Tracking the absolute orientation of the particle is much more challenging, both because of the specifics of angular variables, and because of the specific algorithmic requirements. In contrast to the previous techniques we simply paint the particle with a suitable layout, and then retrieve its orientation by a pattern recognition algorithm. For algorithmic efficiency (and robustness) this is not done step by step but for the entire trajectory using a global optimization scheme.

This chapter is organized as follows:

- We present the experimental setup (section 3.1).
- Next, the tracking of several particles is explained (section 3.2).
- The orientation tracking is presented in three steps: after establishing important features of the orientation algebra in 3D (section 3.3.1), the actual algorithm is explained (section 3.3.2) and tested (section 3.3.3)
- A summary of the data runs is given at the end of this chapter.

Some parts follow tightly our article published in Review of Scientific Instruments [83]. However, some parts contain more technical details now and information on the tracking of several particles is added. For readability some calculations are moved to the annexes.

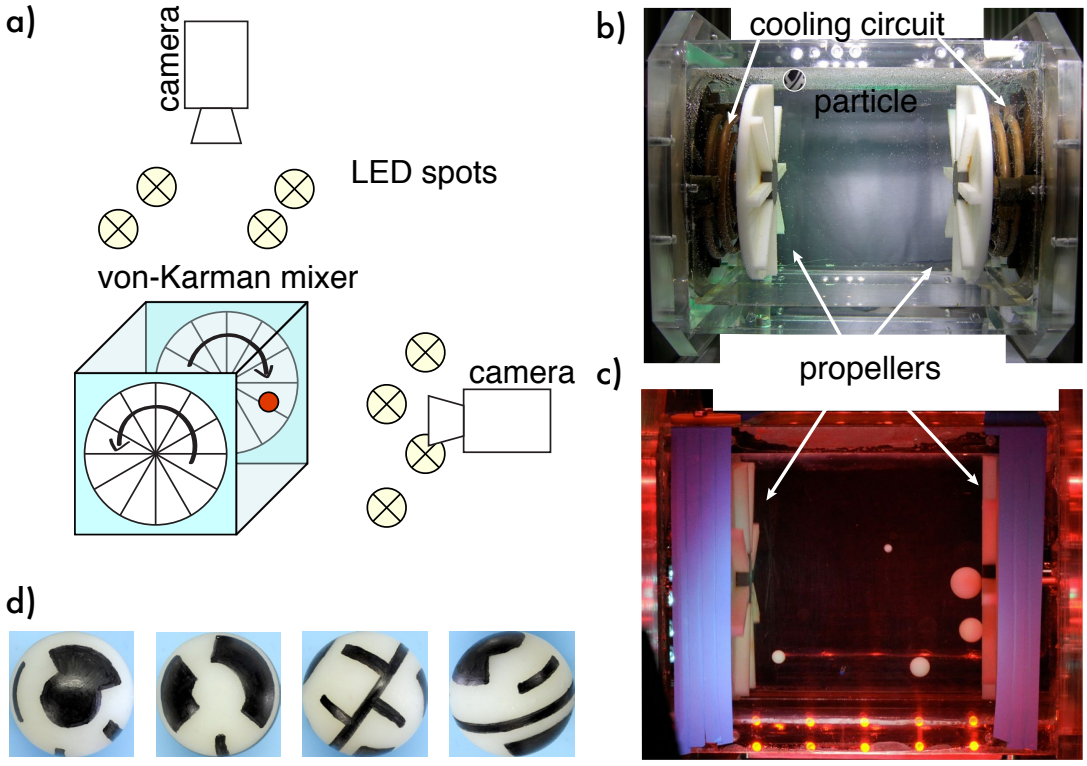

Figure 3.2: Sketch of the experimental setup: **a)** sketch of the camera arrangement; **b)** first version of the von Kármán mixer; **c)** upgraded stainless steal version, the cooling circuit is now integrated into the metal walls. **d)** a textured particle at different orientations

3.1 Experimental Setup

3.1.1 Von Kármán flow

A turbulent flow is generated in the gap between two either *co-* or *counter*-rotating impellers of radius $R = 9.5$ cm fitted with straight blades 1 cm in height. The flow domain in between the impeller has characteristic length $H = 2R = 20$ cm. In order to be able to perform direct optical measurements, the container is build with flat Plexiglas (Poly[methyl methacrylate]) side walls, so that the cross section of the vessel is square. The total volume is 11.4 l. A small opening at the top enables us to conveniently add or remove particles from the container. Parts of the apparatus served already in the thesis of Nicolas Mordant [44] and of Yoann Gasteuil [20]. More details on von Kármán swirling flow can be found in section 2.3. A sketch of the setup is provided in Fig. 3.2.

The working fluid – either de-ionized water or a finely tuned water-glycerol mixture – is chosen such that its density matches the density of the particle. A cryo-thermostat continuously pumps water of well-controlled temperature through a cooling circuit, thereby controlling the fluid's temperature. A fast degassing can be achieved by heating the fluid to 65 °C while the motors and the filter system are running. Our filter system consists simply of a centrifugal pump which pumps fluid from a bubble trap trough a filter back

into the apparatus; two high points of the vessel are connected back to the bubble trap. The plumbing consist mainly of standard garden hose from the DIY store and Gardena (quick connectors, valves, etc; all made of plastic).

It should be noted that the apparatus was upgraded: the first version [20] was built mainly with brass parts and the propellers were driven by DC-motors mounted to a $1 : 2.5$ reductor. However, this setup is limited to non-corrosive fluids. Therefore, all parts are now made of stainless steel. The propellers are now directly driven by brushless DC-motors (Leroy-Somer) each controlled by a variator. We house both in a control cabinet. The improved apparatus is easier to use and able to work with corrosive working fluids *e.g.* a potassium salt - water mixture, which is less viscous than the water-glycerol mixture.

A second apparatus is briefly used in this thesis: the *Lagrangian Exploration Module* (LEM). There, twelve independently driven impellers produce turbulence in a closed icosahedral water tank of 140 l and it was shown that this apparatus creates homogeneous isotropic turbulence with little mean flow. Further details are found in section A.1 and in [80, 85].

We estimate the energy injection rate ε by measuring the active power of the delivered motors in water and in air; the active power is a direct output of the variators. Fig. 3.3 shows the energy injection rate for co- and counter-rotating impellers. For comparison we further provide ε in the LEM. Here, $\varepsilon_{\mathrm{LEM}}$ was obtained from PIV measurements [15] in the center of the apparatus and independently from the active power injected by the twelve motors. The two energy injection rates differ by a factor of 20. Similar discrepancy between the two methods of determining ε has been noted in the apparatus in Göttingen [80], too.

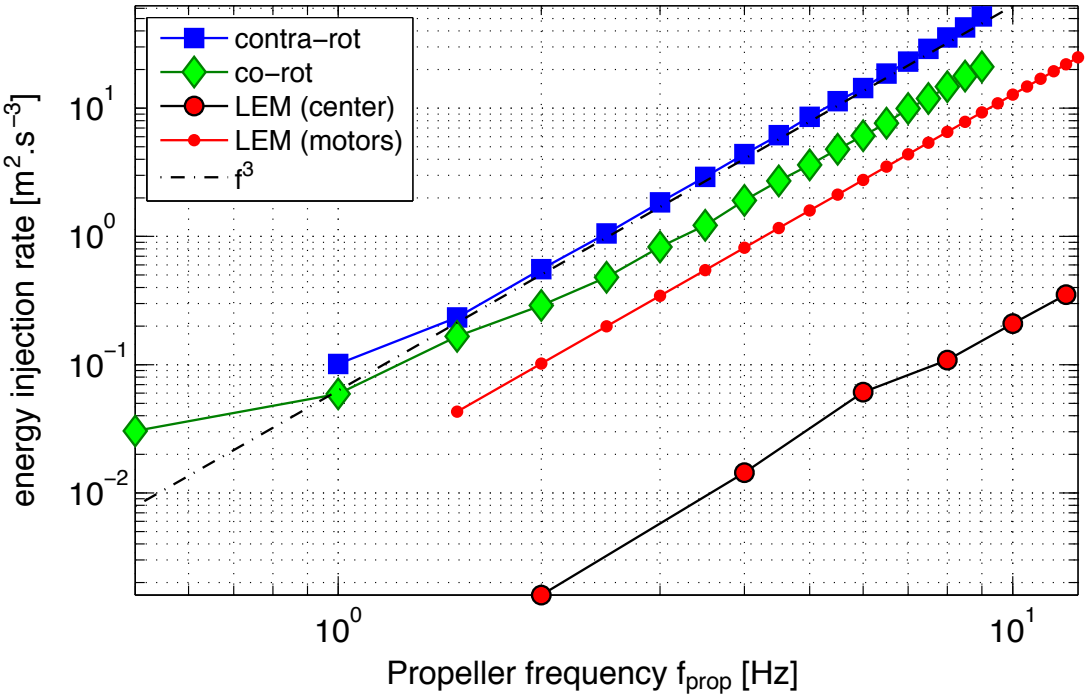

Figure 3.3: Energy injection rate, ε; for the KLAC ε is based on the energy consumption of the motors. In the Lagrangian Exploration Module (LEM) ε_{LEM} was obtained from PIV measurements in the center of the apparatus and independently from the total energy injected by the 12 motors. Similar discrepancy between the two methods of determining ε has been noted in the apparatus in Göttingen [80], too.

3.1.2 Particles

Two types of particles have been used:

PolyAmid spheres Solid, white PolyAmid (PA) spheres with the following diameters $D = 6$ mm, 10 mm, 15 mm, 18 mm, and 24 mm (accuracy 0.01 mm, Marteau & Lemarié, France) were used. Their density is $\rho_p = 1.14$ g. cm^{-3} and can be matched by addition of glycerol to water.

Instrumented particles The instrumented particle, which is explained in detail in chapter 7, consists of a PEEK[1]-capsule embarking a circuit which continuously transmits the signal of a 3D accelerometer to an exterior receiver. The capsule's color is light gray; its total density is close to that of water and can be adjusted by adding weight inside.

In both cases the density mismatch, measured from sedimentation speeds, is found to be of the order of $\Delta\rho/\rho = 10^{-4}$. In order to track the orientation, the particle is textured black and white by hand using black-ink permanent marker. Texture as well as suitable

[1] Polyether-ether-ketone

pens and nail polish[2] have been identified by trial and error methods. Best results were obtained with Edding #8300 industry permanent marker, but in general inks, which are not water-soluble, perform well. Fig. 3.2**d)** shows a textured PA sphere at four different views. The particles are left unpainted white if we just aimed on measuring the translation.

3.1.3 Image acquisition & processing

The motion is tracked by two high-speed video cameras (Phantom V12, Vision Research) which record synchronously two views at approximately 90 degree. The flow is illuminated by high power LEDs and sequences of 8–bit gray scale images are recorded at a sufficiently high frame rate (see table 3.4, page 48). It should be stressed that a short exposure time is crucial for observing a sharp round shape in the movies. Both, cameras and illumination are mounted to a custom-made structure made of aluminum profiles (Bosch-Rexrodt and Newport).

Both cameras observe the measurement region with a resolution of approximately 650×650 pixels, covering a volume of $15 \times 15 \times 15$ [cm^3] corresponding to 4.2 pixel/mm. Hence, the particle diameter ranges 25 to 110 pixels.

In our configuration, the camera can store on the order of 15 000 frames in on-board memory, thus limiting the duration of continuous tracks. The movies are downloaded to a PC, waiting to be processed. The processing is done on a gaming PC with a state of the art graphics card. The code is written in Matlab using the image and signal processing toolboxes as well as the Psychtoolbox extension [10, 51] which provide OpenGL wrappers for Matlab. Our image processing is mostly based on the documentation of the Matlab's image processing toolbox, the book *Morphological image analysis: principles and applications* [61]. Inspiration was further found on Peter Kovesi's web site[33] and Matlab Central [64].

[2] Nail polish was abandoned because it alters the surface roughness of the particle.

3.2 Position Tracking

Although the identification of a large sphere from the camera images causes no particular conceptual difficulty, the fact that the sphere is *textured* raises some practical issues. A simple thresholding returns only either the white or the black part of the particle. Reflections from the impellers continuously change the background, and small impurities in the flow and possible bubbles add sharp gradient noise to the images. Furthermore, the illumination of the flow is not perfectly uniform, and thus, shadows as well as reflections occur. As the experiment evolved over the time of this thesis light conditions, working fluid and unfortunately also the scratches on the box changed. Hence, the arrangement of light, camera and background as well as the image processing were carefully adjusted for each experiment. In either case, we compute the background view as the average of an equally distributed subset of its images for each movie of each camera.
Three different configurations were explored within the scope of this thesis[3]:

- several unpainted white particles with different diameters in front of a dark background
- *one* painted particle in front of a light background
- several painted particles in front of a light background, all particles having a clearly different diameter associated to a specific, unique texture.

Unpainted Particles In the case of the unpainted particles we estimate the area, A_{part}, covered by particles beforehand. For each frame we then subtract the background and threshold such that at least A_{part} pixels are white. For round, unconnected blobs we directly save their location, (x, y), on the image in pixels plus their diameter, $2\,r$; the deviation from the spherical shape serves as an error estimator. Connected blobs are split using the maxima of the distance transform [61] of the blob. A sketch of the blob-splitting is provided in Fig. 3.4.

One textured particle For one painted particle we first subtract the background and perform a *Difference of Gaussians* blob detection. The threshold is adjusted by hand for each camera and light arrangement. We then identify blobs with a round shape and a diameter close to that of the particle. Shadows, bubbles, and reflections might be found during blob detection because of their sharp separation from the background, but they are of uniform texture and hence characterized by a small value of the variance of light intensity across the blob. The blob with highest variance and closest resemblance to a sphere is considered to be the particle. The precise position of the particle is refined using a *Canny edge* detection or *standard deviation* filter in a tight region around the blob. Again, for each time step we record the position, (x, y), of the particle on the image (in pixels) plus its diameter, $2\,r$; the deviation from the spherical shape serves as an error estimator.

[3] The temporal order is slightly different: we first worked on one painted, then several unpainted and finally on multiple painted particles.

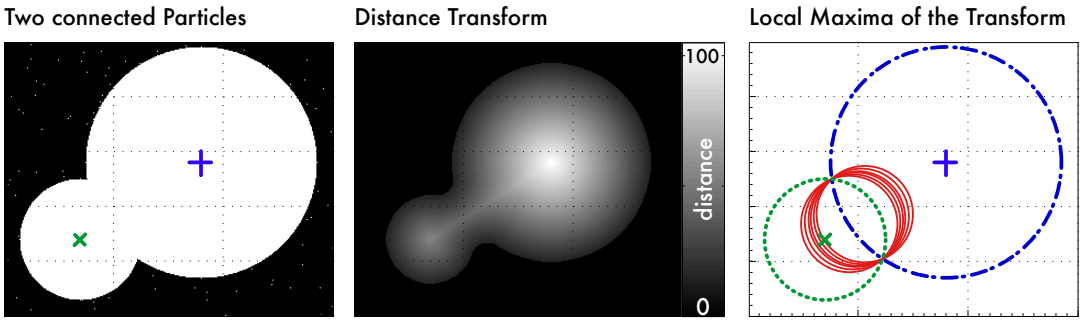

Figure 3.4: Sketch of the Blob-splitting technique. Overlapping particles form a blob. The distance transform then returns for each white pixel the euclidian distance to the closest black pixel. Cleaning can be achieved by rejecting all pixels with a distance smaller than the smallest expected particle radius. The local maxima of the distance transform are possible particle positions with their associated radii; often more maxima than particles are detected and one has to remove artifacts: Starting from the largest radius one iteratively excludes wrong detections which are within a bigger particle (solid red circles). One obtains position, (x, y), and radius, r, of the remaining, real particles (dotted and dashed circle).

It is further necessary to store a precise crop of the particle image in order to extract its orientation.

Several textured particles The technique for several painted particles combines ideas from the former two cases. Given that the texture strongly deviates from the background a sliding standard deviation filter returns regions of high contrast corresponding to the edges of the particle and its texture. A hysteresis thresholding based on an estimate of the area covered with particles yields the outlines of the spheres. Matlab then detects and fills closed outlines. If necessary the resulting blob is split. Position, diameter, images and error estimates are stored. From Fig. 3.5 it becomes clear that if particles overlap, no orientation can be determined. However, the image of the second camera is typically exploitable.

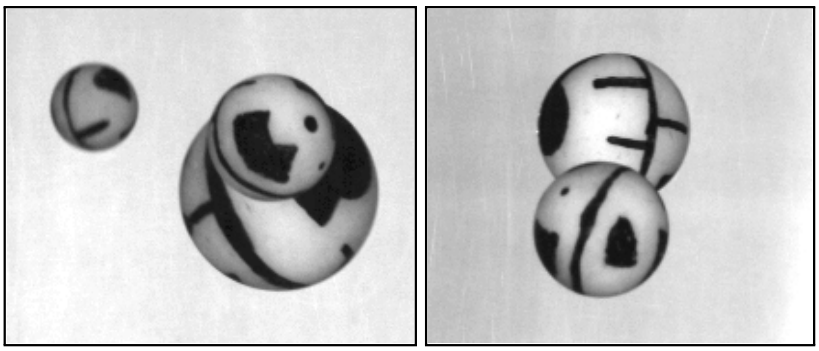

Figure 3.5: Overlapping particles: the position is extractable but not the orientation.

Stereo-matching To obtain the particle position in 3D a standard stereo-matching technique as sketched in Fig. 3.6 is employed: We model the cameras as pin-hole cameras with an additional radial distortion as proposed by Tsai [68]. The projection of a particle on the sensor of the cameras is projected back into 3D, where it forms a line-of-sight. The particle's position in 3D is the point, which has minimal distance to both lines-of-sight. For setups with two cameras this point can be computed analytically [13]. The calibration of the camera contains the position of the camera plus its rotation with respect to the lab coordinate system, which is needed later for the orientation processing.

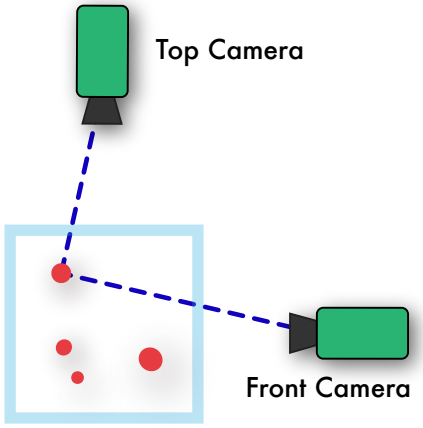

Figure 3.6: Stereo-matching. The particle position is the point which has minimal distance to both lines-of-sight.

Track assembly The track assembly is straight forward if exactly one particle is placed into the flow. The algorithm may temporarily loose the particle for short times (because of bad light reflection, blurs, ...); this is compensated by the large oversampling and gaps of less than 5 frames are interpolated to obtain longer tracks. Outliers are identified using a least-square spline and replaced by an interpolation.

If multiple particles are in the flow we still know the possible physical dimensions exactly. The cameras are placed such that their projected diameters covers well distinct ranges. This enables us to convert their observed diameter, $2r$ (in pixels) to their real particle diameter, D_{part} (in meter). Particles of the same diameter are then stereo-matched.

The tracking building is then done in two steps: First, particles of the identical size are connected using a Nearest-Neighbor track connection which allows short interpolations. The tracks break easily when trajectories cross in any of the two cameras, due to the large size of the particles. For that reason the reconnection algorithm suggested by Haitao Xu [77] is applied. It considers both, position and velocity at beginning and end of the tracks, thereby ensuring a little number misconnections. In our case the acceleration of the particle is neglected (that corresponds to $w_a = 0$ in [77]). We further modified the search area from a cylinder to a cone: the maximum distance between two tracks separated by Δt is $d_{\max}(\Delta t) = d_0 + \frac{\Delta t}{\Delta t_{\max}}$ ($d_{\max}(\Delta t) = \text{const.}$ was the choice in [77]). This modification was added by Haitao Xu (cf. page 37 in [80]) to take into account that the uncertainty

of the extrapolation increases with time. In a last step we identify and eliminate outliers with a least-square spline.
As a result we obtain less but significantly longer tracks. In most cases a particle track now ends when the particle leaves the observation volume.

3.3 Orientation Tracking

3.3.1 Math

The parametrization of an angular position in 3D space causes a number of difficulties which are briefly addressed in this section (see *e.g.* [36, 23, 62, 75] for a more complete presentation). One of them is caused by the degeneracy of the axes of rotation for certain orientations (the *gimbal lock* problem). Another is the choice of a suitable measure of distance between two orientations. An further issue is that mathematically two angular velocities exist: Whereas $\boldsymbol{\omega}^{\mathbb{P}}$ describes the rotation of the particle with respect to the fixed lab coordinate system, $\boldsymbol{\omega}^{\mathbb{L}}$ fixes the particle and rotates the lab system. This is somewhat similar to quantum mechanics where one has the choice between the Heisenberg and the Schrödinger picture to incorporate a dependency on time. We found no particular use for $\boldsymbol{\omega}^{\mathbb{L}}$ in our analysis, and name it here just for completeness. In the later chapters, which analyze and present the results, we focus only on the angular velocity which rotates the particle, $\boldsymbol{\omega}^{\mathbb{P}}$. Therefore, unless otherwise stated the superscript $^{\mathbb{P}}$ is omitted and we always rotate the particle.

It should be noted that throughout this manuscript the units of angle *degree* [°], *radiant* [rad] and *round* are equally employed. It is left to the reader to convert the units if needed. We (try to) specify the propeller frequency in round/s $=$ Hz and measured angles in degree.

3.3.1.1 Describing Orientations

As stated by the Euler rotation theorem, 3 parameters are needed to describe any rotation in 3D. We use here Euler angles with the Tait-Bryan convention as shown in Fig. 3.7. In the transformation from Lab to Particle coordinate system, we first apply a rotation around the $z-$axis of angle θ_z, followed by a rotation around the intermediate $y-$axis of angle θ_y and last a rotation of angle θ_x around the new $x-$axis. The rotations work on the object using a right handed coordinate system and right handed direction of rotation. We will denote an orientation triplet by an underscore, *e.g.* $\underline{\theta}$, in order to distinguish them from vectors (which are typeset in bold font, *e.g.* $\boldsymbol{\omega}$).

The orientation of the object is fully described by an orthogonal 3×3 matrix $\underline{\underline{\boldsymbol{R}}}$, obtained from the composition of the 3 elementary rotations:

$$\underline{\underline{\boldsymbol{R}}}(\theta_x, \theta_y, \theta_z) = \underline{\underline{\boldsymbol{R}}}_x(\theta_x)\underline{\underline{\boldsymbol{R}}}_y(\theta_y)\underline{\underline{\boldsymbol{R}}}_z(\theta_z) = \begin{bmatrix} c\theta_y\, c\theta_z & -c\theta_y\, s\theta_z & s\theta_y \\ s\theta_x\, s\theta_y\, c\theta_z + c\theta_x\, s\theta_z & -s\theta_x\, s\theta_y\, s\theta_z + c\theta_x\, c\theta_z & -s\theta_x\, c\theta_y \\ -c\theta_x\, s\theta_y\, c\theta_z + s\theta_x\, s\theta_z & c\theta_x\, s\theta_y\, s\theta_z + s\theta_x\, c\theta_z & c\theta_x\, c\theta_y \end{bmatrix} \tag{3.1}$$

with $c\cdot = \cos(\cdot)$ and $s\cdot = \sin(\cdot)$. Consequently, from any rotation matrix the 3 Euler angles can be extracted using

$$\underline{\theta} = \{\theta_x, \theta_y, \theta_z\} = \begin{pmatrix} \text{atan2}(-\underline{\underline{\boldsymbol{R}}}_{12}, \underline{\underline{\boldsymbol{R}}}_{11}) \\ \text{asin}(\underline{\underline{\boldsymbol{R}}}_{13}) \\ \text{atan2}(-\underline{\underline{\boldsymbol{R}}}_{23}, \underline{\underline{\boldsymbol{R}}}_{33}) \end{pmatrix}, \tag{3.2}$$

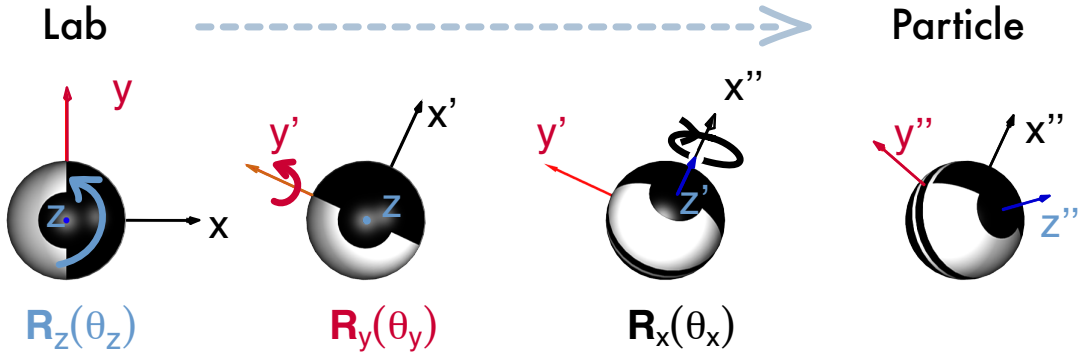

Figure 3.7: Tait-Bryan rotation sequence describing the sphere's orientation. The object is first rotated around the $z-$axis with angle θ_z, followed by a rotation around the intermediate $y-$axis of angle θ_y and last a rotation of angle θ_x around the new $x-$axis. We work on the object using a right handed coordinate system and right handed direction of rotation.

enforcing $\theta_x, \theta_z \in [0, 2\pi[$ and $\theta_y \in [-\pi/2, \pi/2]$. However, this choice is not unique because there is a second triplet with $\underline{\underline{\boldsymbol{R}}}\,(\theta_x + \pi, \mathrm{sign}(\theta_y)\cdot\pi - \theta_y, \theta_z + \pi) = \underline{\underline{\boldsymbol{R}}}\,(\theta_x, \theta_y, \theta_z)$. Needless to say, multiples of 2π can be added to each angle. An important practical consequence is that even for small changes in orientation the difference between two Euler angle triplets, $\underline{\theta}_1$ and $\underline{\theta}_2$, has formally four possible results. The unwrapping of a time series of Euler angles is explained in appendix B.1.

The curvilinear coordinate $\underline{\theta}$ is related to the angular velocity, $\boldsymbol{\omega}^{\mathbb{P}}$, (in the particle frame) by

$$\begin{aligned}\boldsymbol{\omega}^{\mathbb{P}}\left(\underline{\theta}(t)\right) &= \begin{bmatrix} 1 & 0 & s\theta_y \\ 0 & c\theta_x & -s\theta_x\, c\theta_y \\ 0 & s\theta_x & c\theta_x\, c\theta_y \end{bmatrix} \cdot \frac{\mathrm{d}}{\mathrm{d}t}\begin{pmatrix}\theta_x \\ \theta_y \\ \theta_z\end{pmatrix} \\ &= \underline{\underline{\boldsymbol{H}}}(\theta_x, \theta_y)\cdot\frac{\mathrm{d}}{\mathrm{d}t}\begin{pmatrix}\theta_x \\ \theta_y \\ \theta_z\end{pmatrix}\end{aligned} \tag{3.3}$$

For $\cos(\theta_y) \approx 0$, the determinant of the matrix $\underline{\underline{\boldsymbol{H}}}$, $\det(\underline{\underline{\boldsymbol{H}}})$, vanishes and its inverse is not defined. In other words, finite body rotations need infinite change in the Euler angles. This singularity is called a *gimbal lock* and is a well-known problem in robotics and aerospace engineering. Geometrically, the second rotation turns the first axis parallel to the third axis of rotation, and the rotation loses two degrees of freedom (an illustration and some more details can be found in appendix B.1). Unfortunately gimbal locks cannot be avoided by a wise choice of representation.

In order to meaningful compare orientations one needs to define a distance between two arbitrary orientations, which is immune to this type of singularity. A natural distance

between two arbitrary orientation matrixes, $\underline{\underline{\boldsymbol{A}}}$ and $\underline{\underline{\boldsymbol{B}}}$, is

$$\begin{aligned} \mathrm{Tr}\left(\left(\underline{\underline{\boldsymbol{A}}}-\underline{\underline{\boldsymbol{B}}}\right)\left(\underline{\underline{\boldsymbol{A}}}-\underline{\underline{\boldsymbol{B}}}\right)^{T}\right) &= 6-2\,\mathrm{Tr}\left(\underline{\underline{\boldsymbol{A}}}\underline{\underline{\boldsymbol{B}}}^{T}\right) \\ &= 4\big(1-\cos\left(\phi\right)\big) \end{aligned} \tag{3.4}$$

using $\underline{\underline{\boldsymbol{A}}}\,\underline{\underline{\boldsymbol{A}}}^{T} = \underline{\underline{\boldsymbol{B}}}\,\underline{\underline{\boldsymbol{B}}}^{T} = \underline{\underline{\mathbb{1}}}$ and that $\underline{\underline{\boldsymbol{A}}}\underline{\underline{\boldsymbol{B}}}^{T}$ is a rotation matrix with the eigenvalues $1, e^{i\phi}, e^{-i\phi}$. The distance is thus a growing function of ϕ. We measure here the distance between two rotation matrices by:

$$\mathrm{d}\left(\underline{\underline{\boldsymbol{A}}},\underline{\underline{\boldsymbol{B}}}\right) \equiv \mathrm{acos}\left(\frac{1}{2}\left[\mathrm{Tr}\left(\underline{\underline{\boldsymbol{A}}}\,\underline{\underline{\boldsymbol{B}}}^{T}\right)-1\right]\right) \tag{3.5}$$

Because it works directly on the orientation matrices, it is neither sensitive to gimbal locks nor to the choice of the representation and thus an important tool in our algorithm. It should be noted that $\mathrm{d}\left(\underline{\underline{\boldsymbol{A}}},\underline{\underline{\boldsymbol{B}}}\right)$ is the angle of the rotation which turned the orientation from $\underline{\underline{\boldsymbol{A}}}$ to $\underline{\underline{\boldsymbol{B}}}$.

In the search of the particle's orientation, one last inconvenience of Euler angles is that they are not locally orthogonal, in the sense that

$$\begin{aligned} &\mathrm{d}\big(\left\{\theta_x,\theta_y,\theta_z\right\},\left\{\theta_x+\Delta\theta_x,\theta_y+\Delta\theta_y,\theta_z+\Delta\theta_z\right\}\big)^2 \\ &\quad\approx \Delta\theta_x^2+\Delta\theta_y^2+\Delta\theta_z^2+2\,\Delta\theta_x\cdot\Delta\theta_z\cdot\sin\left(\theta_y\right) \end{aligned} \tag{3.6}$$

for a small variation $\underline{\Delta} = \{\Delta\theta_x, \Delta\theta_y, \Delta\theta_z\}$. As a consequence, a uniform spacing of the Euler angles in $\theta_x, \theta_y, \theta_z$ does not sample the space of possible orientations in an optimal way. In particular near gimbal locks, the sampling rate would be higher at no higher accuracy. The so-called Lattman angles [37]

$$\{\theta_+,\theta,\theta_-\} \equiv \{\theta_x+\theta_z,\theta_y,\theta_x-\theta_z\} \tag{3.7}$$

fulfill local orthogonality since they verify

$$\begin{aligned} &\mathrm{d}\big(\left\{\theta_+,\theta,\theta_-\right\},\left\{\theta_++\Delta\theta_+,\theta+\Delta\theta,\theta_-+\Delta\theta_-\right\}\big)^2 \\ &\quad\approx \Delta\theta_+^2\frac{1+\sin\theta}{2}+\Delta\theta^2+\Delta\theta_-^2\frac{1-\sin\theta}{2} \end{aligned} \tag{3.8}$$

As they are locally orthogonal, it is sufficient for sampling purposes to keep a constant stepping:

$$\Delta\theta = \Delta\theta_+\sqrt{\frac{1+\sin\theta}{2}} = \Delta\theta_-\sqrt{\frac{1-\sin\theta}{2}}$$

After a constant sampling of N values of θ with $\Delta_{\mathrm{Latt}} \equiv \Delta\theta = \pi/(N-1)$, the stepping in θ_+ and θ_- can be computed with $\Delta\theta_+(\theta) = \Delta_{\mathrm{Latt}}/\sin\left(\frac{\theta}{2}+\frac{\pi}{2}\right)$ and $\Delta\theta_-(\theta) = \Delta_{\mathrm{Latt}}/\sin\left(\frac{\pi}{2}-\frac{\theta}{2}\right)$. It should be stressed that $\theta_- \in [0, 2\pi[$ whereas $\theta_+ \in [0, 4\pi[$. The Lattman angles allow us to sample the set of orientations in an optimal way, in terms of

achieving the best resolution from the point of view of the metric given by Eq. (3.5), and also from an algorithmic point of view.

Finally, in several instances it is convenient to describe a rotation by the direction of an axis $\hat{\boldsymbol{n}}$ about which the system is rotated by an amount ϕ. The corresponding rotation matrix can be computed using the Rodrigues Formula [23, 75]

$$\underline{\underline{\boldsymbol{R}}}\left(\hat{\boldsymbol{n}},\phi\right)=\begin{bmatrix} c\phi+n_x^2A & -n_zs\phi+n_xn_yA & n_ys\phi+n_xn_zA \\ n_zs\phi+n_xn_yA & c\phi+n_y^2A & -n_xs\phi+n_yn_zA \\ -n_ys\phi+n_xn_zA & n_xs\phi+n_yn_zA & c\phi+n_z^2A \end{bmatrix} \tag{3.9}$$

with $A=(1-\cos\phi)$. Eq. (3.9) also allows us to extract the axis, $\hat{\boldsymbol{n}}$, and the angle, ϕ, from any arbitrary rotation matrix. As a result, changing the coordinate system or changing the representation of rotation can be done by expressing the orientation in its matrix form, applying the transformation which changes the coordinate system and extracting the desired representation.

3.3.1.2 Angular Velocity & Acceleration

Angular velocity and acceleration are often obtained by direct differentiation of a time-series of Euler angles, *e.g.* using Eq. (3.3). However, it is possible to obtain the angular velocity in the particle frame directly from the matrices. This technique is not sensitive to gimbal locks because of the uniqueness of the orientation matrices.

Let $\boldsymbol{e}_{x,y,z}^{\mathbb{P},k}$ be the particle coordinate system at time step k, whereas the fixed lab coordinate system is $\boldsymbol{e}_{x,y,z}^{\mathbb{L}}$. For two time-steps, k and $k+m$, we know the corresponding orientation matrices which rotate the particle:

$$\begin{array}{lcll} \underline{\underline{\boldsymbol{R}}}(\underline{\theta}_k) & : & \boldsymbol{e}_{x,y,z}^{\mathbb{L}} & \xrightarrow{\underline{\underline{\boldsymbol{R}}}(\underline{\theta}_k)} \quad \boldsymbol{e}_{x,y,z}^{\mathbb{P},k} \\ \underline{\underline{\boldsymbol{R}}}(\underline{\theta}_{k+m}) & : & \boldsymbol{e}_{x,y,z}^{\mathbb{L}} & \xrightarrow{\underline{\underline{\boldsymbol{R}}}(\underline{\theta}_{k+m})} \quad \boldsymbol{e}_{x,y,z}^{\mathbb{P},k+m} \\ \underline{\underline{\boldsymbol{T}}} & : & \boldsymbol{e}_{x,y,z}^{\mathbb{P},k} & \xrightarrow{\underline{\underline{\boldsymbol{R}}}(\underline{\theta}_{k+m})\ \underline{\underline{\boldsymbol{R}}}(\underline{\theta}_k)^T} \quad \boldsymbol{e}_{x,y,z}^{\mathbb{P},k+m} \end{array}$$

in which the matrix $\underline{\underline{\boldsymbol{T}}}$ is the change in orientation, in other words the matrix representation of the discrete angular velocity (for a given time difference). The change is with respect to the particle coordinate system at time k: $\boldsymbol{e}_{x,y,z}^{\mathbb{P},k}$. $\underline{\underline{\boldsymbol{T}}}$ expressed in the axis-angle convention (see Eq. (3.9)) returns a direction vector, $\hat{\boldsymbol{n}}$, of length unity and an angle, $\Delta\phi$ (meaning that between times k and $k+m$ the particles has rotated an angle $\Delta\phi$ around the vector $\hat{\boldsymbol{n}}$). The time difference, Δt, between the steps is a function of m. Therefore an estimator of angular velocity is

$$\boldsymbol{\omega}^{\mathbb{P}}\big(t(k)\big)=\frac{\Delta\phi}{\Delta t(m)}\left(n_x\cdot\boldsymbol{e}_x^{\mathbb{P},k}+n_y\cdot\boldsymbol{e}_y^{\mathbb{P},k}+n_z\cdot\boldsymbol{e}_z^{\mathbb{P},k}\right) \tag{3.10}$$

Averaging $\hat{\boldsymbol{n}}\frac{\Delta\phi}{\Delta t}$ over several separations, m, returns the angular velocity in the particle frame without a prior unwrapping nor problems near gimbal locks. The angular velocity which fixes the particle and rotates the lab coordinate system is defined as

$$\boldsymbol{\omega}^{\mathbb{L}}\big(t(k)\big)=\underline{\underline{\boldsymbol{R}}}\left(\underline{\theta}_k\right)^T\boldsymbol{\omega}^{\mathbb{P}}\big(t(k)\big) \tag{3.11}$$

The angular acceleration in either particle or lab frame is defined as

$$\boldsymbol{\alpha}^{\mathbb{L}/\mathbb{P}} = \frac{\mathrm{d}}{\mathrm{d}t}\boldsymbol{\omega}^{\mathbb{L}/\mathbb{P}} \tag{3.12}$$

In practice, it is obtained from a convolution of the angular velocity time series with the derivative of a gaussian kernel. This technique has proved to be efficient in removing noise [46]. We remind the reader here that we found no particular use for $\boldsymbol{\omega}^{\mathbb{L}}$ and $\boldsymbol{\alpha}^{\mathbb{L}}$; in the analysis the superscript $^{\mathbb{P}}$ is omitted and we work only with the angular variable rotating the object.

It should be pointed out that this algorithm can be applied to a set of particles attached to a rigid body which are tracked using standard particle tracking algorithms. If one records the positions in space of 3 or more points, $\boldsymbol{P}_1 \ldots \boldsymbol{P}_N$ at time t and $t + \Delta t$, their motion can be split up into a translation of their center of mass plus a rotation. Once the translation part is subtracted, one needs to determine the rotation matrix, $\underline{\underline{\boldsymbol{R}}}_{\text{kabsch}}$, which turns the points $\boldsymbol{P}_1 \ldots \boldsymbol{P}_N$ around their center of mass. Measurement uncertainties in the position of the particles render the system of equations degenerate *i.e.* no exact solution can be found. Furthermore, for more than 3 points this defines an overdetermined system of equations.
However, Kabsch's [31, 30] algorithm can efficiently compute an optimal solution[4]: $\underline{\underline{\boldsymbol{R}}}_{\text{kabsch}}$ is then the matrix representation of the change in orientation, and the angular velocity, $\boldsymbol{\omega}^{\mathbb{P}}$, (in the particle reference frame) at time t can be extracted as done here. It should be pointed out that, one does not gain access to neither the angular velocity in the lab reference frame, $\boldsymbol{\omega}^{\mathbb{L}}$, nor to the absolute orientation, $\underline{\theta}$.

[4] A brief sketch of his algorithm is given in annex B.5. Kabsch's algorithm is needed in our technique which determines the texture of a painted particle from a set of images.

3.3.2 Tracking

The algorithm used to process the camera images and obtain a time series of orientations (and angular velocities) can be split into three parts:

> By comparison of the sphere's picture with synthetic images, the algorithm identifies a set of possible orientations.

> From the set of possible candidates at successive instants, a *Flow* algorithm identifies a likely time series.

> A post-treatment adjusts remaining ambiguities.

These steps are described in details in this section.

Texturing a sphere In the choice of the particle texture, several features have to be considered:

> A single view should correspond to a unique orientation.

> Illumination inhomogeneities may cause regions to look similar in the camera images. Optically resembling views should correspond to clearly distinct orientations.

> The cameras are grayscale so the texture has to be of high lightness variation such that the gray scale image of the particle contains exactly two distinct colors: black and white. Painting with black ink on a whitish particle is the convenient choice.

> For image-processing reasons the number of black and white pixel should be approximately the same in every possible view.

> The ink/paint has to be resistant to the working fluid at temperatures up to 60 °C as well as to continuous impacts with the wall and the propellers. The surface roughness should be left unaltered.

3.3.2.1 Candidate Finding

Synthetic images. A first step is to obtain a 2D projection, $\underline{\underline{\boldsymbol{S}}}(\underline{\theta})$, of a sphere with known texture and size at an arbitrary orientation, $\underline{\theta}$. This rendering is achieved using OpenGL, *via* the Psychtoolbox extensions for Matlab – for a disk image of about 60 pixels, the algorithm can render several thousand orientations per second (see Fig. 3.10 for an illustration).

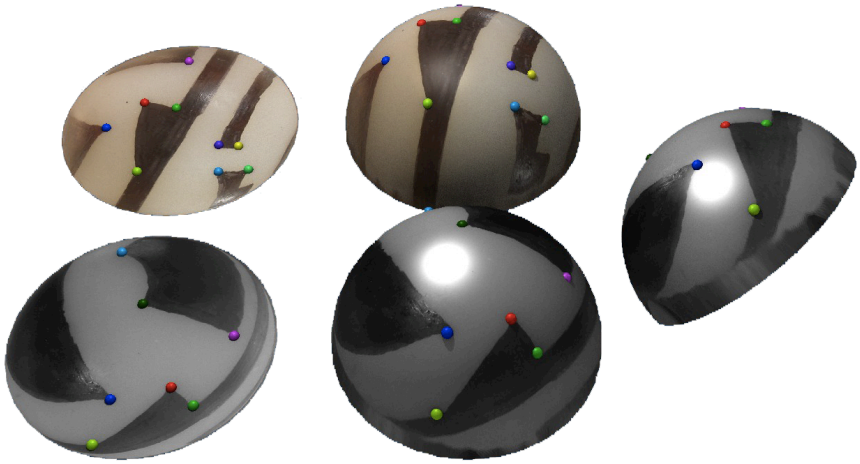

Figure 3.8: Computing the texture from a set of images: Two images are first projected onto a half sphere. The colored dots depict features; each feature has a unique name/color. Then the rotation matrix which turn the common features from the upper view to the lower view is computed and applied to the lower half-sphere. One can thus partially see behind the upper view.

Obtaining the texture for a set of images One can paint the particle according to a pattern already known to Matlab; however, the uncertainty in the texture is then dominated by the artistic skills of the painter. For this reason we developed a procedure to compute the texture of a sphere from a set of images.

We first paint the sphere and then add small dots with a different pen. These dots are so-called features and are removed before the actual experiment. We then take pictures of the particle at arbitrary orientations with a SLR camera and a high quality macro objective. The images are edited/cleaned in PhotoShop setting the background, the two colors of the texture and the dots/features to known, distinct colors.

Since every image is the 2D projection of textured half-sphere we can revert the projection. One thus obtains a set of colored 3D vectors. If each feature has a unique name we can identify the rotation which turns the view in image A to a second view B and thus look partially behind the sphere[5]. Typically 10 images have to be used to obtain a well resolved texture. A sketch of the procedure is provided in Fig. 3.8. The technique to assign unique feature names with user interaction is explained in the appendix.

The texture of each particle has to be known before inserting it into the apparatus, because its texture continuously degrades during the experiment (mainly due to impacts with the propellers). It lasts for several days and it is much faster to paint a new, fresh texture than wasting ones time on repairing a worn-out texture.

Texture extraction. Once the particle position and diameter are known, one extracts a disk subset of the image, centered on the particle, $\underline{\underline{G}}$. In a first step the contrast is

[5] This is like a superposition of rotated hedgehogs with colored spikes.

adjusted such that the global histogram of intensity contains at least b percent of black and w percent of white pixels (the algorithm only takes into account the disk / particle region in $\underline{\underline{\boldsymbol{G}}}$). The adjustable parameters b, w are fixed to $b = w \sim 30\%$ which is the minimum amount of black/white pixel in an arbitrary orientation. In a second step, the image is thresholded by using Otsu's method [49] for the global histogram. To refine this first rough thresholding we developed and tested successfully:

- Thresholding in smaller moving regions,
- hysteresis thresholding, and
- identifying the edges between black and white regions with either a Canny or standard deviation filter. Within each enclosed region the color is a priori uniform and therefore set to its medium value.

Either way, the thresholded image, $\underline{\underline{\boldsymbol{I}}}$, is adjusted such that pixels outside the particle / disk are set to 0 whereas black is -1 and white $+1$. These steps are shown in Fig. 3.9.

Figure 3.9: Texture extraction and comparison with a synthetic image. The resemblance between the image $\underline{\underline{\boldsymbol{I}}}$ and the synthetic projection $\underline{\underline{\boldsymbol{S}}}$ at angle $\underline{\theta}$ is estimated using Eq. (3.13).

Comparison, possible orientations. The image $\underline{\underline{\boldsymbol{I}}}$ (with diameter $2\,r$) obtained as above is ready for comparison with synthetic images. The resemblance to a rendered image $\underline{\underline{\boldsymbol{S}}}(\underline{\theta})$ with orientation $\underline{\theta}$ is estimated by

$$T(\underline{\underline{\boldsymbol{I}}}, \underline{\theta}) = \frac{1}{2} + \frac{1}{2\pi r^2} \sum_i \sum_j \underline{\underline{\boldsymbol{I}}}_{i,j} \cdot \underline{\underline{\boldsymbol{S}}}_{i,j}(\underline{\theta}) \,, \tag{3.13}$$

which is ratio of the number of correct pixels to the total number of pixels.

At this point we note that the computational cost of directly comparing an image $\underline{\underline{\boldsymbol{I}}}$ to synthetic ones $\underline{\underline{\boldsymbol{S}}}(\underline{\theta})$ covering the set of possible orientation $\{\underline{\theta}\}$ scales roughly as $\left(1/\Delta_{\text{Latt}}\right)^3$, where Δ_{Latt} is the grid spacing in the orientation space. There is also the additional difficulty that the particle apparent diameter changes slightly as the sphere moves in the flows. For efficiency and physical correctness, we use the following strategy: instead of finding at any time step the best images, we identify a set of possible candidates for all time steps and then extract globally the time series of orientations.

First, we render images, $\underline{\underline{\boldsymbol{S}}}(\{\underline{\theta}_{\text{coarse}}\})$, covering *all* possible orientations with a coarse grid – in practice $\Delta_{\text{Latt}} \approx 12°$. Lattman angles are locally orthogonal and thus more efficient

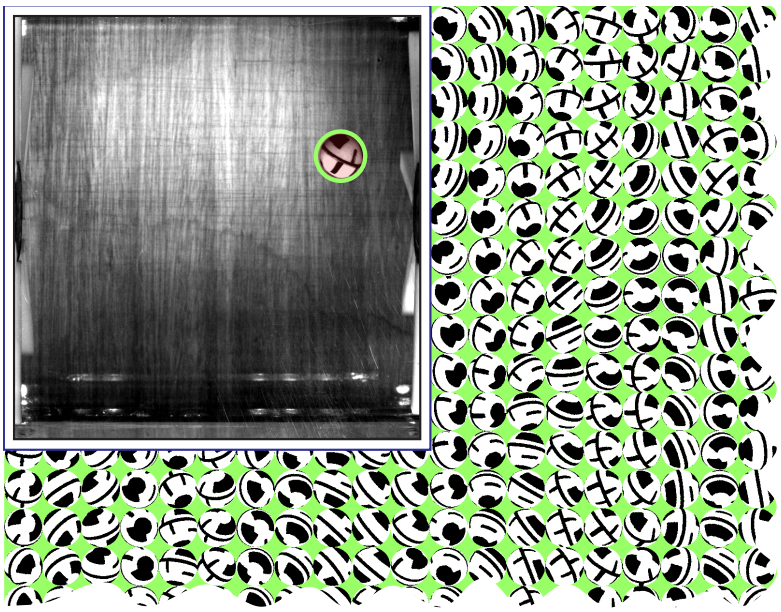

Figure 3.10: Synthetic 2D projections of the particle for a range of orientations, using OpenGL. A camera image of the moving particle is shown in the upper left corner (contrast enhanced; note the driving disks on either side).

in creating such grids. The size of the rendered images is fixed to approximately one half of the particle's real diameter. Since their size does not change, these images are kept in the computer memory and do not need to be recomputed for every new image.

The thresholded particle image, $\underline{\underline{I}}$, is then resized to the size of the renderings, $\underline{\underline{I}}_{\text{coarse}}$, and compared to all synthetic images, $\underline{\underline{S}}\left(\{\underline{\theta}_{\text{coarse}}\}\right)$ as shown in Fig. 3.10 using Eq. (3.13). All angles $\underline{\theta}$ satisfying $T(\underline{\underline{I}}_{\text{coarse}}, \underline{\theta}) > \max\left(T(\underline{\underline{I}}_{\text{coarse}}, \{\underline{\theta}_{\text{coarse}}\})\right) - \delta_{\text{coarse}}$ are considered to be possible orientations. Here δ_{coarse} is an arbitrary thresholding value, with inspection showing that a value equal to 0.1 gives good results.

Experience shows that the identified possible orientations usually cover several broad classes. They are thus separated into groups of images whose orientations differ by less than a rough threshold, approximately $30 - 45°$. For each group, synthetic images are further added using a fine grid spacing, $\Delta_{\text{fine}} = 3°$ (at this point 'bad' images may cause the code to runaway; they are dropped and the code advances to the next time step). The possible orientations are then rendered in real size and compared (using Eq. (3.13)) to the image $\underline{\underline{I}}$. For each group, the code returns the final best guess, *i.e.* the orientation with the maximum resemblance, thus drawing a list of *candidates*, see Fig. 3.11 for an example of a particle with its corresponding candidates.

3.3.2.2 Track Assembly

After identifying the candidates for each time step, the most likely orientation for each time step has to be determined. However, the candidate with the highest count of correct pixels is not necessarily the best choice. Although counterintuitive, the direct use of two

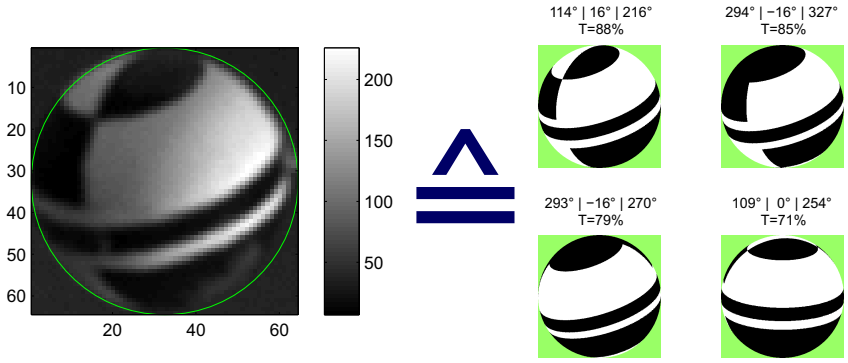

Figure 3.11: Particle camera image (left) and corresponding candidates, after analysis of the possible orientations.

cameras seeing the particle at different angles does not simplify the problem, because in the case of a bad image, one camera falsifies the choice of the candidates found by the other camera. Moreover, gimbal locks prevent the use of a predictor-corrector scheme for the prediction of the orientation. However, the norm of angular velocity is assumed to be smooth and we search the time series which globally minimizes the sum $\sum_t \xi(t)$ along the time series of the so called *direct neighbor distance function*:

$$\xi(t) \equiv \left|\boldsymbol{\omega}\left(\underline{\theta}(t), \underline{\theta}(t+\Delta t)\right)\right| = \frac{\mathrm{d}\left(\underline{\theta}(t), \underline{\theta}(t+\Delta t)\right)}{\Delta t} \quad . \tag{3.14}$$

A direct neighbor is the next valid time step at $t+\Delta t$. The distance between 2 orientations does not depend on the representation, ensuring the robustness of the algorithm even at gimbal locks. Minimizing $\sum_t \xi(t)$ is only meaningful for small changes in orientation between two time steps, another requirement for high (over)sampling rates.

Flow algorithms are highly efficient in finding a global optimum for a discrete set of candidates. The following is done for each camera without considering the extra information from the second camera. In a first step all candidates with a resemblance $T < s_{\text{quality}}$ are removed – in practice $s_{\text{quality}} = 0.5$. Then a directed graph is built which connects all candidates at time step t with all their direct neighbors at the non-empty time step $t+\Delta t$. The cost function is chosen such that it takes into account both the change in orientation and the quality of the matching:

$$C\left(\{\underline{\theta}_A, T_A\}, \{\underline{\theta}_B, T_B\}\right) = \mathrm{d}\left(\underline{\theta}_A, \underline{\theta}_B\right) \frac{2 - T_A - T_B}{\Delta t} \quad , \tag{3.15}$$

with $\{\underline{\theta}_A, T_A\}$ a candidate at time t and $\{\underline{\theta}_B, T_B\}$ a directly neighboring candidate at $t + \Delta t$.

A Dijkstra path finding algorithm returns the sequence of candidates having a global minimum of the total cost, *i.e.* the global minimum of change of orientation (weighted by the image quality) (cf. Fig. 3.11). In most cases this algorithm returns directly the time series of absolute orientation. Nevertheless, bad images introduce false candidates

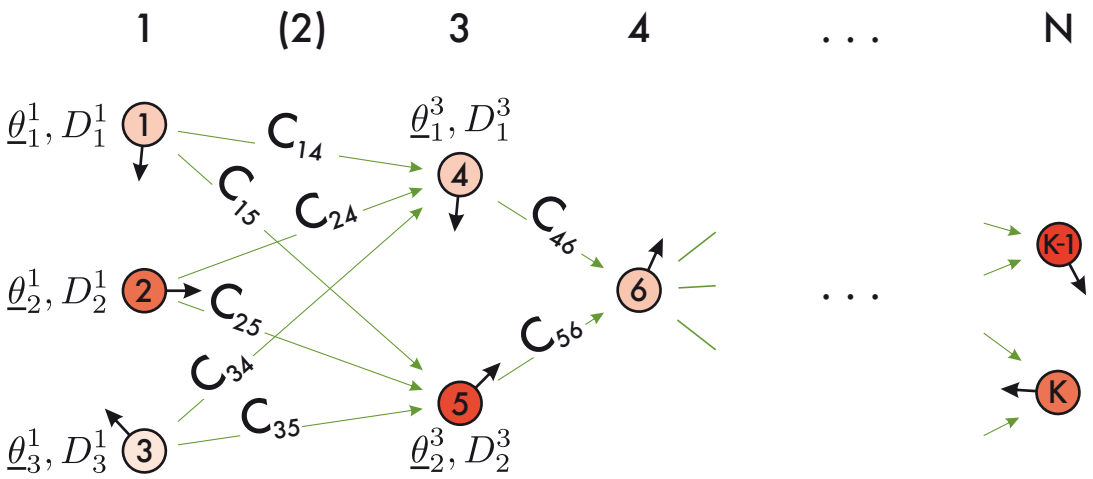

Figure 3.12: Sketch of a graph connecting the possible candidates using the cost function C (cf. Eq. (3.15)). For each time step t, we have $b(t)$ candidates with an orientation $\underline{\theta}_b^t$ and a resemblance D_b^t. In the time series $t = 1 \ldots N$, the candidates are labeled $k \in 1 \ldots K$. The directed graph C connects all candidates at t to all their next valid time step $t + \Delta t$; gaps are skipped as indicated for time step **2**.

forcing the path finding algorithm to take a different, non-physical path. These points manifest as spikes in the direct neighbor distance function, $\xi(t)$. After a spike, there is no guarantee that the path is still physical. Therefore, we segment the time-series based on the spikes. The second view (from the second camera) treated with the same algorithm contains the information to correct such wrong segments. The rotation matrix, which transforms the orientations seen by one camera into the coordinate system of the other one, is known from the camera calibration. Therefore, both views are expressed in an intermediate, common coordinate system where the segments with $\mathrm{d}\left(\underline{\theta}_{\mathrm{cam1}}, \underline{\theta}_{\mathrm{cam2}}\right) \gtrsim 30°$ can be corrected.

The algorithm presented so far assumes an orthographic view. This condition holds only true if the particle center is on the optical axis of the camera or in the case one uses telecentric lenses. In the present experiments we do not, and the perspective effect alters the measured orientation (note that the parallax displacement corresponds to a change in the 2D projection, and hence to a rotation). The distortion induced by the perspective is characterized by the position of the particle center in the camera image, $\boldsymbol{X}$, and the focal length, f. Common camera objectives allow only small angles, $\gamma_{\mathrm{persp}} \equiv \mathrm{atan}\left(\|\boldsymbol{X}\| / f\right) \lesssim 15°$. As a consequence we assume that the shape of the particle does not change and we introduce an orientation matrix $R_{\mathrm{persp.}}$ (taking advantage of the Rodrigues formula Eq. (3.9)):

$$\underline{\underline{R}}_{\mathrm{persp.}}\left(\boldsymbol{X} = (x, y), f\right) = \underline{\underline{R}}\left(\frac{(-y, x, 0)}{\sqrt{x^2 + y^2}}, \mathrm{atan}\left(\frac{\|\boldsymbol{X}\|}{f}\right)\right) \tag{3.16}$$

such that the measured orientation is related to the absolute orientation $\underline{\theta}_{\mathrm{abs}}$ by

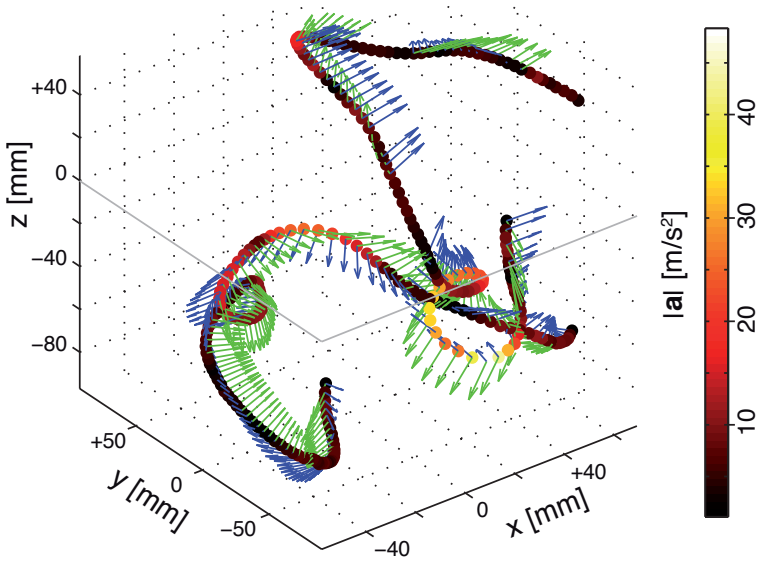

Figure 3.13: Example of particle tracks and orientations (the green and blue arrows mark North-South and East-West directions, respectively).

$\underline{\underline{R}} \cong \underline{\underline{R}}_{\text{persp.}}\, \underline{\underline{R}}(\underline{\theta}_{\text{abs}})$. The perspective distortion can then be removed from the orientation time series.

Finally, after correcting for perspective distortion, a combined time-series of orientation can be built using the information from both views, if they are expressed in the same coordinate system. Euler angles are not locally orthogonal, hence, we use the weighted mean of the orientation expressed in the axis-angle representation. The variance within a moving window of the direct neighbor distance function, $\xi(t)$, proves to be a good error estimator of the noise, since for short times the particle is assumed to rotate smoothly. A sample orientation track is shown in the upper panel of Fig. 3.14 and in 3D in Fig. 3.13.

3.3.3 Robustness

The accuracy and robustness of our technique depends mainly on the quality of the particle image and the texture. Although the resolution of the texture in the computer depends mostly on the carefulness of the researcher, the textures of the particle degrades due to the constant contact with the working fluid and impacts with the propellers or walls. A well chosen[6] ink and adaptive thresholding enable us to perform several experiments with the same particle. It is further advantageous to perform the experiments as fast as possible, which avoids/reduces the dissolving of the ink by the fluid. Computer, cameras and gigabit ethernet network are tweaked to support jumbo frames thereby decreasing the download time by a factor of 2. Additionally, the computer hosts 6 Terabytes of storage to continuously record over a few days.

[6] We tested (almost) all permanent markers available at RadioSpares and various office suppliers.

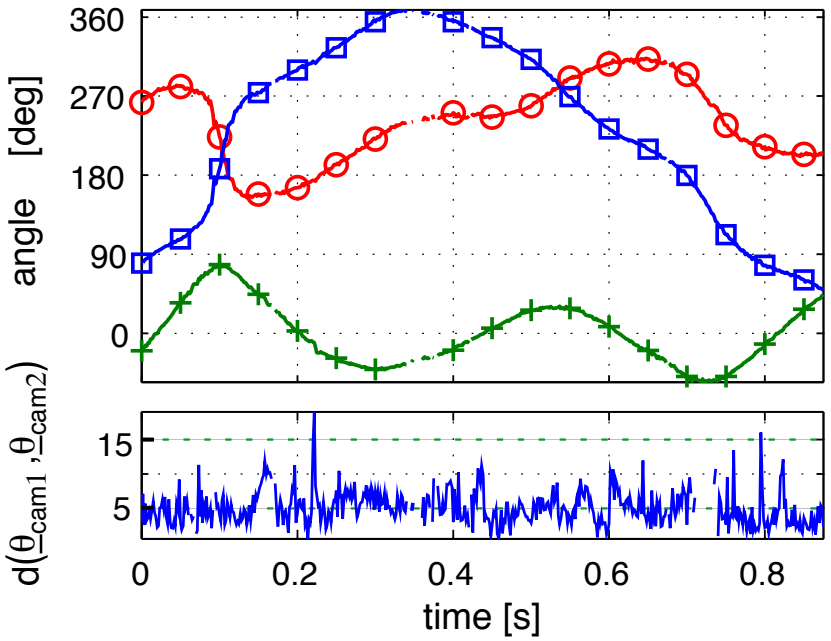

Figure 3.14: A sample orientation track; it is $\theta_x = \circ$, $\theta_y = +$, $\theta_z = \square$, the bottom plot shows the distance (in degrees) between the independent orientation measurements from the 2 cameras.

Problems with the images are mainly caused by reflections, shadows, and objects (such as bubbles or dirt particles) between the particle and the camera. The setup, light conditions and particle texture must be first tuned in order to optimize these parameters – by trial and error methods. It is further possible to run the filter system of the apparatus while the cameras are downloading.

For the orientation algorithm *per se*, we have used a series of synthetic images of known orientation. We found that the measurement error is 2°, which is smaller than the size of the fine grid ($\Delta_{\text{fine}} = 3°$) used in the image processing (cf. paragraph 3.3.2.1). A finer grid would improve the resolution for ideal images, but not for real images which, as stated above, always contain some amount of distortions or impurities. In addition, the fast dynamics of the particle and high frame rate ensure that wrong detection do not persist for longer than a few frames. As a result, most defects are detected and skipped or interpolated or handled as part of post-processing (wrong orientations correspond to jumps in the direct neighbor distance function).

We illustrate the accuracy of the detection on two examples. The first one concerns the agreement between the orientation as estimated from each camera measurement. In the upper panel of Fig. 3.14, the combined three angles with respect to the lab coordinate system are plotted. The lower panel shows the distance (in degrees of angle) between the two estimations, $\mathrm{d}\left(\underline{\theta}_{\text{cam1}}, \underline{\theta}_{\text{cam2}}\right)$. The probability density function (PDF) of these distances, computed with and without processing for perspective corrections are shown in Fig. 3.15. Correcting the systematic error induced by the perspective distortion reduces

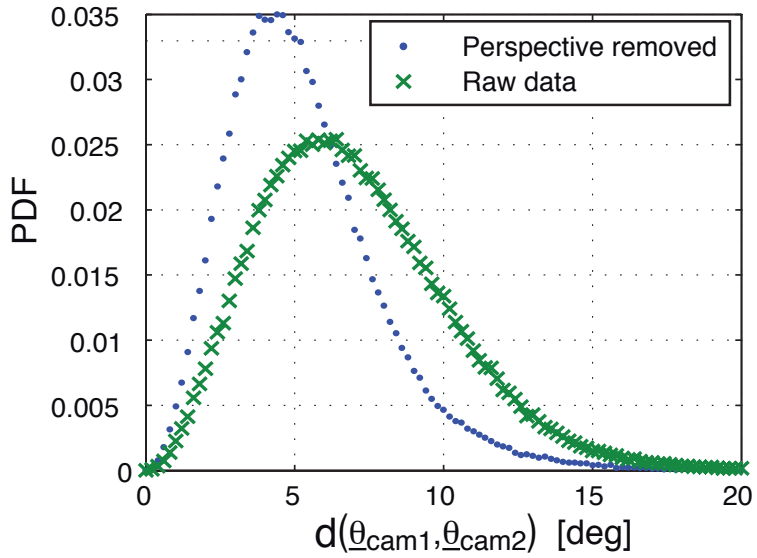

Figure 3.15: Probability density function (PDF) of the distance, d, between the orientations measured from cameras 1 and 2, with (○) and without (×) correction for perspective distortion.

the mean value and width of the distribution. The remaining error is of random nature. Combining the two independent views as described early leads to a weighted error of approximately 3°.

3.3.4 Efficiency & further development

On an off-the-shelf gaming PC processing a movie set containing two movies of 14 000 frames each, takes 2−3 hours to extract the position and 2−5 hours to find the orientation candidates. The first step is speed up by either the Parallel computing toolbox or by launching multiple instances of Matlab. The later step is harder to optimize: only one process can access the renderer due to limitations in the OpenGL wrappers for Matlab, and moreover, this process blocks one screen of the PC[7]. Thus the other computers in the office are used at night for helping. Time-wise the bottleneck in this step is the transfer of rendered images from the graphics card back to Matlab. This step could be avoided if one instead transfers the thresholded particle image, $\underline{\underline{I}}$, into the graphics card and then uses the heavy parallel computing capabilities of modern graphic cards to perform the comparison defined by Eq. (3.13). The CUDA or OpenCL framework seems suitable for such a task.

3.4 Data runs

The results are analyzed in detail in chapter 4 and 5. Table 3.4 lists the performed tracking experiments.

[7] Actually it looks like a psychedelic screen saver. By the way, it doesn't block the screen on a Mac.

run	propeller speed [Hz]	Particle sizes [mm]	frame rate [fps]	density [g/cm^3]	date
SP	2 3	25	500 800	1.0	Aug 2011
PA18	3	18	600	1.14	Jun 2010
PApaint	1.5 2.5 3.5	6, 10, 15, 18, 24 10, 15, 18, 24	500 850 1000	1.14	Feb 2012
PAmult	0.5 1 2 3 4 4.5 2 3	2×6, 2×10, 15, 18, 24	120 500 800 1000 1500 1800 700 900	1.14	Jan 2012

Table 3.1: Data runs, the particles were always neutrally buoyant. SP denotes the instrumented particle, *i.e.* we filmed and simultaneously recorded its accelerometer signal. The *PAmult* runs contain only the translation. If the density is 1 g/cm^3 water was used as working fluid whereas 1.14 g/cm^3 needed to be density matched with a water-glycerol mixture. The kinematic viscosity ν is approximately 8 times higher than pure water in that case.

4 How they move

Even when restricting to round dead objects, particles in turbulent flows come in a variety of densities and size: They can be either lighter (*e.g.* bubbles) or neutrally buoyant or heavy (*e.g.* sediments & droplets) than the carrier flow. Likewise, their size ranges from much smaller than the Kolmogorov scale, η, up to the integral scale, L_{int}. Particles which are smaller than the Kolmogorov scale, η, have drawn much attention due to their ability to follow the flow as tracers if they are neutrally buoyant and the available theoretical description [22, 41]. In 2002, Voth *et al.* [74] reported the first Lagrangian measurements which compared the dynamics of finite-sized particles to that of tracers. And in the last decade more and more experiments were done investigating particles of sizes up to the intermediate Taylor length scale, λ [67, 65]. For particle diameters $D_{\text{part}}/\eta \lesssim 40$ it has been established that upon increasing the ratio D_{part}/η the variance of the particle acceleration decreases as $(D_{\text{part}}/\eta)^{-2/3}$, but the fluctuations remain non–gaussian within this range [54, 65]. A comprehensive study on the one-particle statistics can be found in the dissertation of Nauman Qureshi [53].

However, the behavior of particles whose size is comparable to the largest scales of the flow, L_{int}, has still received little attention.

Particles & Flow-types In this chapter we present results on the translation of *neutrally buoyant* spheres in a von Kármán flow. The tested diameters are $D_{\text{part}} = 6$ mm, 10 mm, 15 mm, 18 mm, and 24 mm. The uncertainty in diameter is less the 0.02 mm and the sphericity 0.01 mm. The particles are made of white Poly-Amid (PA), which has a density of 1.14 g/cm^3. A density-adjusted water-glycerol mixture serves as working fluid, the side walls of the apparatus are temperature-controlled at 20 °C. The observation volume is approximately $15 \times 15 \times 15$ [cm^3] large.

Two different ways of driving are tested: the impellers are either *co-* or *counter*-rotating, but in all cases both impellers run at the same propeller speed, f_{prop}. We list the key parameters of the counter-rotating driving in table 4.1. The co-rotation is mostly used as a cross-check and we do not attempt to estimate the Kolmogorov scales or Reynolds number here. A picture of the experiment is provided in Fig. 4.1.

	f_{prop}[Hz]	Re	R_λ	ε[m^2/s^3]	η[µm]	τ_η[ms]	T_{int}[s]	D_{part}/η
counter-rot	0.5	4200	75	0.01	425	24.3	2.00	14 . . . 56
	1.0	8400	105	0.10	253	8.6	1.00	24 . . . 95
	2.0	16900	150	0.56	165	3.7	0.50	36 . . . 145
	3.0	25300	185	1.85	122	2.0	0.33	49 . . . 196
	4.0	33700	215	4.39	99	1.3	0.25	61 . . . 243
	4.5	37900	225	6.15	91	1.1	0.22	66 . . . 265

Table 4.1: Key-parameters of the counter-rotating flow configurations. The integral length scale is estimated to be $L_{\text{int}} = 3$ cm $\sim R/3$, consequently $D_{\text{part}}/L_{\text{int}} = 0.2 \ldots 0.8$. We use the following definition for the Reynolds numbers: $Re = 2\pi R^2 f_{\text{prop}}/\nu$ and $R_\lambda = \sqrt{\frac{15}{\nu} \cdot 2\pi L_{\text{int}}^2 f_{\text{prop}}}$. Note that we follow particles in a $15 \times 15 \times 15$ [cm^3] region, where the flow is known to be inhomogeneous and anisotropic. Thus, R_λ and the Kolmogorov scales are only rough estimates.

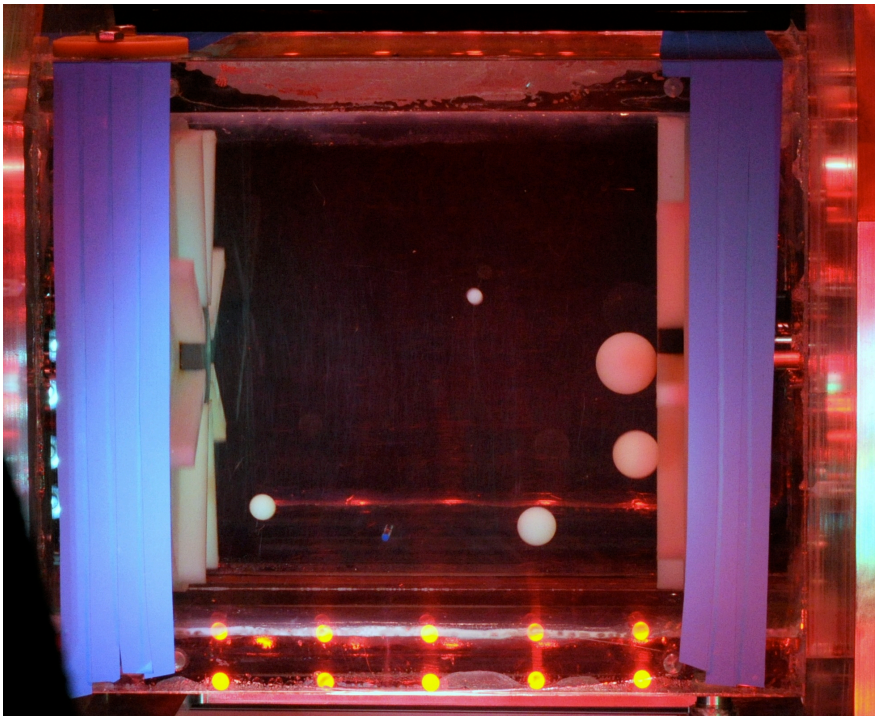

Figure 4.1: Large unpainted spheres in our von Kármán mixer; the red light stems from high-power LED illumination, the blue tape reduces reflections. The fluid is density-matched to 1.14 g/cm^3.

4.1 Motion

Dimensional arguments tell that particle velocity, $\boldsymbol{v}$, and acceleration, $\boldsymbol{a}$, are proportional to f_{prop} and f_{prop}^2, respectively. Fig. 4.2 shows the standard deviation (RMS) of the components of $\boldsymbol{v}$ and $\boldsymbol{a}$ for the co- and counter-rotation and different propeller frequencies. To take into account the dimensional arguments we normalize by the speed, $2\pi \cdot R \cdot f_{\text{prop}}$, and the centrifugal force, $4\pi^2 \cdot R \cdot f_{\text{prop}}^2$, at the tip of the propeller, R. We find that both acceleration and velocity are following well the propeller motion with an effective radius $R_{\text{eff}} \approx 0.15\,R$. In other words $\text{RMS}\,(v)\,/\left(2\pi f_{\text{prop}}\right) \sim \text{RMS}\,(a)\,/\left(4\pi^2 f_{\text{prop}}^2\right)$. This confirms that all measurement were performed in the fully turbulent flow regime [58].

Similar to conventions for cylindrical coordinates we denote y and z (which lie in the plane of the rotation) the *polar* and x the *longitudinal* component. We find that the polar components, y and z, collapse, whereas x, which is parallel to the rotation axis, is slightly weaker. As anticipated the co-rotation separates the velocity components stronger than a counter-rotation at the same propeller speed. However, the effect is less pronounced for the acceleration. This signature of the anisotropy of the von Kármán flow has been known for a long time, and as one may expect, the anisotropy is less pronounced for small scale quantities like the acceleration *e.g.* in [74, 57, 50, 72].

The motion diminishes with increasing particle diameter, *i.e.* smaller particle move faster and "shakier". For the velocity the change seems linear, but we observe a non-trivial spacing for the acceleration. We, therefore, plot the RMS as a function of the particle diameter in Fig. 4.3: The different frequencies collapse for each particle size and component. The velocity RMS diminishes linearly with D_{part}, the dependence is stronger for the longitudinal component, x. For the acceleration the dependence is most likely a power-law. Based on Kolmogorov scaling arguments, Voth *et al.* [74] extended the Heisenberg-Yaglom scaling to finite size particles

$$\left\langle a^2 \right\rangle = a_0\, \varepsilon^{3/2}\, \nu^{-1/2} \left(\frac{D_{\text{part}}}{\eta} \right)^{-2/3} = a_0\, \varepsilon^{4/3}\, D_{\text{part}}^{-2/3} \tag{4.1}$$

with $\eta = \left(\frac{\nu^3}{\epsilon}\right)^{1/4}$ the Kolmogorov length scale and a_0 a "constant"[1] of order 1. The energy injection rate, ε, is proportional to the propeller speed, $\varepsilon \propto f_{\text{prop}}^3$. Furthermore, we worked with the RMS of a, *i.e.* the square root of the acceleration variance, $\langle a^2 \rangle$. Thus

$$\frac{\text{RMS}(a)}{f_{\text{prop}}^2} \propto D_{\text{part}}^{-1/3} \tag{4.2}$$

In contrast to the prediction, we note that $\text{RMS}(a)/f_{\text{prop}}^2$ is better compensated with $D_{\text{part}}^{-0.53\pm0.06}$ than with $D_{\text{part}}^{-1/3}$ (illustrated by the thick black line in Fig. 4.3). This has partially been seen by Romain Volk *et al.* [72]. Also, one should keep in mind that Eq. (4.1) and Eq. (4.2) are based on the assumption of locally homogeneous and isotropic turbulence as well as smaller particles. That is clearly not the case in our experiment where

[1] In practice, a_0 varies weakly with flow, turbulence level and other things [74].

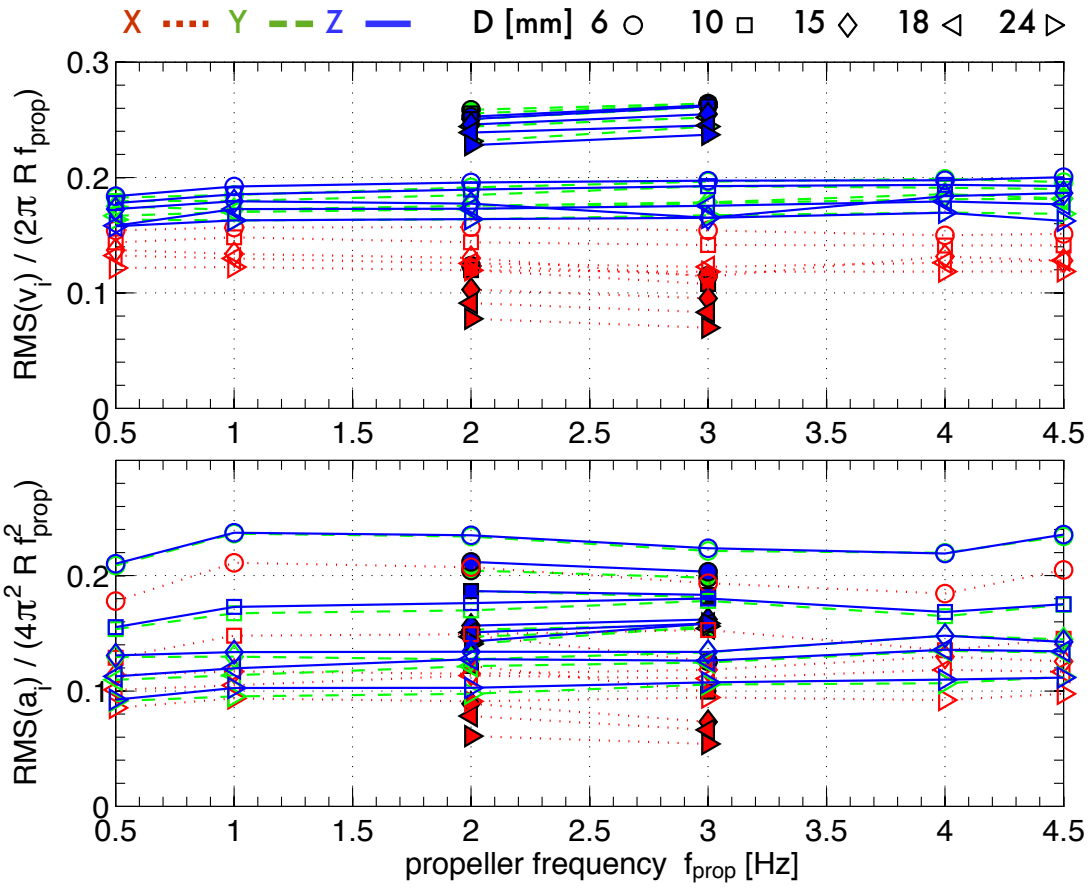

Figure 4.2: RMS of velocity, v_i, and acceleration, a_i, for different diameters normalized by the rotation of the propeller. Filled symbols indicate co-rotating driving. The motion of the particles is dominated by the propellers and one can define an effective propeller radius of $R_{\text{eff}} \approx 0.15\,R$. In a fully turbulent von Kármán flow the velocity variance is a fraction of the propeller tip speed [58]. Since $\text{RMS}\,(v)\,/\left(2\pi f_{\text{prop}}\right) \sim \text{RMS}\,(a)\,/\left(4\pi^2 f_{\text{prop}}^2\right)$ we conclude that the flow is fully turbulent. In contrast to a cylindrical von Kármán flow, one observes that co- and counter-rotating impellers create comparable turbulence. In all cases the components in the plane of the rotation, y and z, collapse, whereas x which is parallel to the rotation axis, is slightly weaker. The influence of the particle diameter is shown in Fig. 4.3.

larger particles are tracked over the whole flow domain. Furthermore, experiments show that a_0 varies weakly with the Reynolds number (see for example [74]).

It is interesting that the co-rotation produces acceleration fluctuations which are weaker but comparable to counter-rotating forcing. As reported by Catherine Simand [60], one expects a much bigger difference to counter-rotating driving in a smooth cylinder with co-rotating smooth disks. However, our apparatus has square cross-section which acts similar to baffles in a cylinder. In addition, the blades on the propellers induce centrifugal pump-

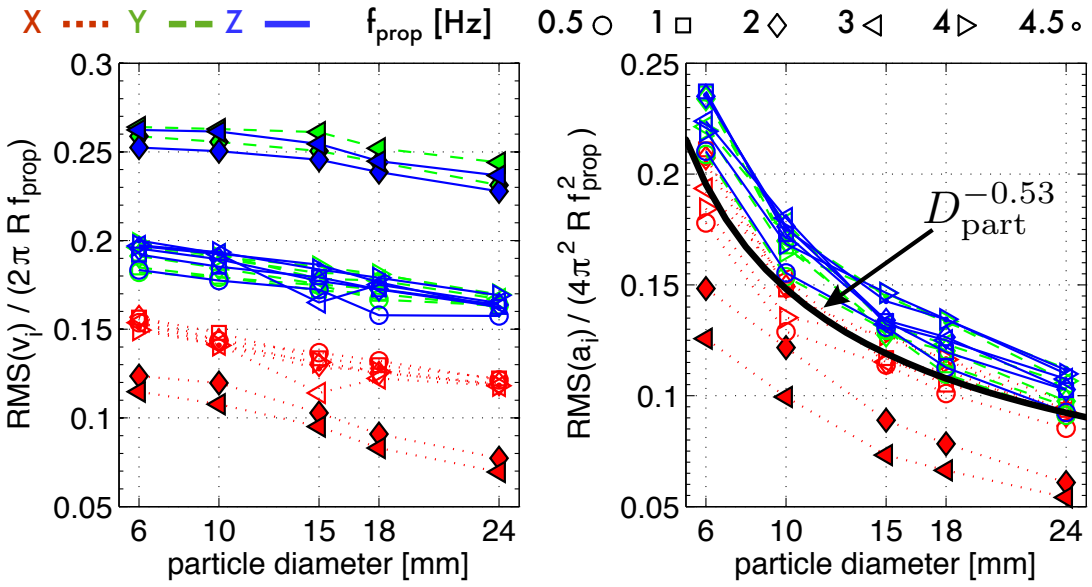

Figure 4.3: RMS of velocity, v_i, and acceleration, a_i, for different diameters normalized by the rotation of the propeller. Filled symbols correspond to co-rotating impellers. Note that in the right plot we shifted the co-rotation (filled symbols) by -0.1. The data is the same as in Fig. 4.2, only the arrangement changed. The solid line is a fit to the data: $\mathrm{RMS}(a)/\left(4\pi^2\, R\, f_{\mathrm{prop}}^2\right) = (0.5 \pm 0.1) \cdot D_{\mathrm{part}}^{-0.53\pm0.06}$. In contrast thereto, Heisenberg-Yaglom scaling predicts $\mathrm{RMS}(a)/f_{\mathrm{prop}}^2 \propto D^{-1/3}$.

ing and help producing a much more turbulent flow. One notices that in this apparatus the acceleration magnitude alone is not sufficient to distinguish co- from counter-rotating driving.

4.1.1 PDFs

Fig. 4.4 depicts the (normalized) probability density function (PDF) of the components of the velocity, $\boldsymbol{v}$ for the counter-rotating runs. The three components are approximately normal distributed. Moreover, the PDFs are independent of propeller speed and diameter. When comparing in detail, one notices a slight difference between polar and longitudinal components. In addition, the curves become sub-gaussian for values larger 3 standard deviations.

As shown in Fig. 4.5 the PDFs of the components of the acceleration, $\boldsymbol{a}$, for the counter-rotating runs superimpose independent of particle diameter and propeller frequency. The PDF themselves displays weakly stretched-exponential tails and clearly *no* Gaussian distribution. For a quantitative comparison to previous measurements (*e.g.* [55, 54, 11, 72])

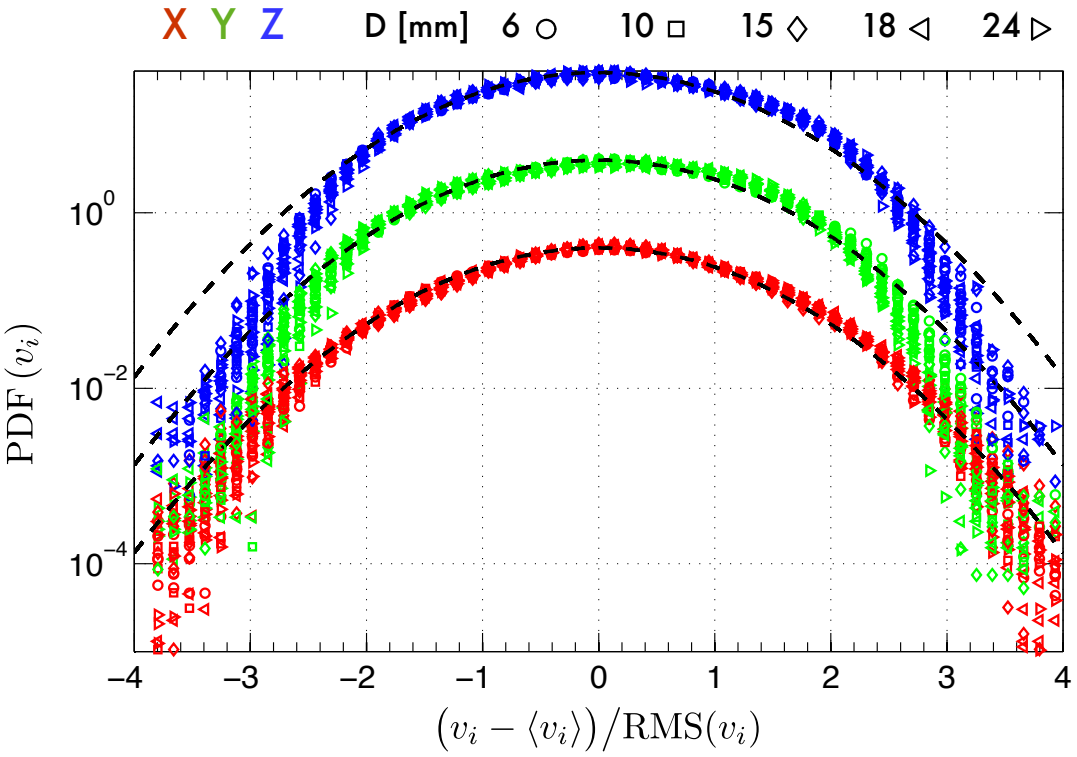

Figure 4.4: PDF (shifted) of the velocity components, all counter-rotating runs (with all diameters) are plotted. The PDFs are shifted and the order is x, y, z starting from the bottom. For comparison, the dashed lines indicate a normal distribution.

we use the fitting function:

$$\Pi_s(x) = \frac{e^{3s^2/2}}{4\sqrt{3}} \left(1 - \mathrm{erf}\left(\frac{\ln\left|x/\sqrt{3}\right| + 2s^2}{s\sqrt{2}}\right)\right) \tag{4.3}$$

which has been used extensively in the analysis of the intermittency of the translational motion of Lagrangian tracers [45] – it stems from the approximation that the norm of the acceleration has a log-normal distribution. The parameter s is related to the flatness F by

$$\mathrm{F}(s) = \frac{9}{5}\exp\left(4\,s^2\right) \quad \Leftrightarrow \quad s = \frac{1}{2}\sqrt{\ln\left(\frac{5}{9}\,\mathrm{F}\right)} \tag{4.4}$$

When determining s for each diameter, propeller speed and component we find that s increases with propeller speed. It slowly approaches $s \approx 0.62$ a value reported by Qureshi *et al.* [54]. A difference between polar and longitudinal components remains. As expected, bigger particles develop narrower tails in the PDF than smaller particles. The covered range of s corresponds to flatness values from 4.2 to 8.8 with $\mathrm{F}(\langle s \rangle) = 6.1$.

For the co-rotating driving we notice that the longitudinal component is almost unaltered. The polar components, however, show clear signs of the different flow: the velocity

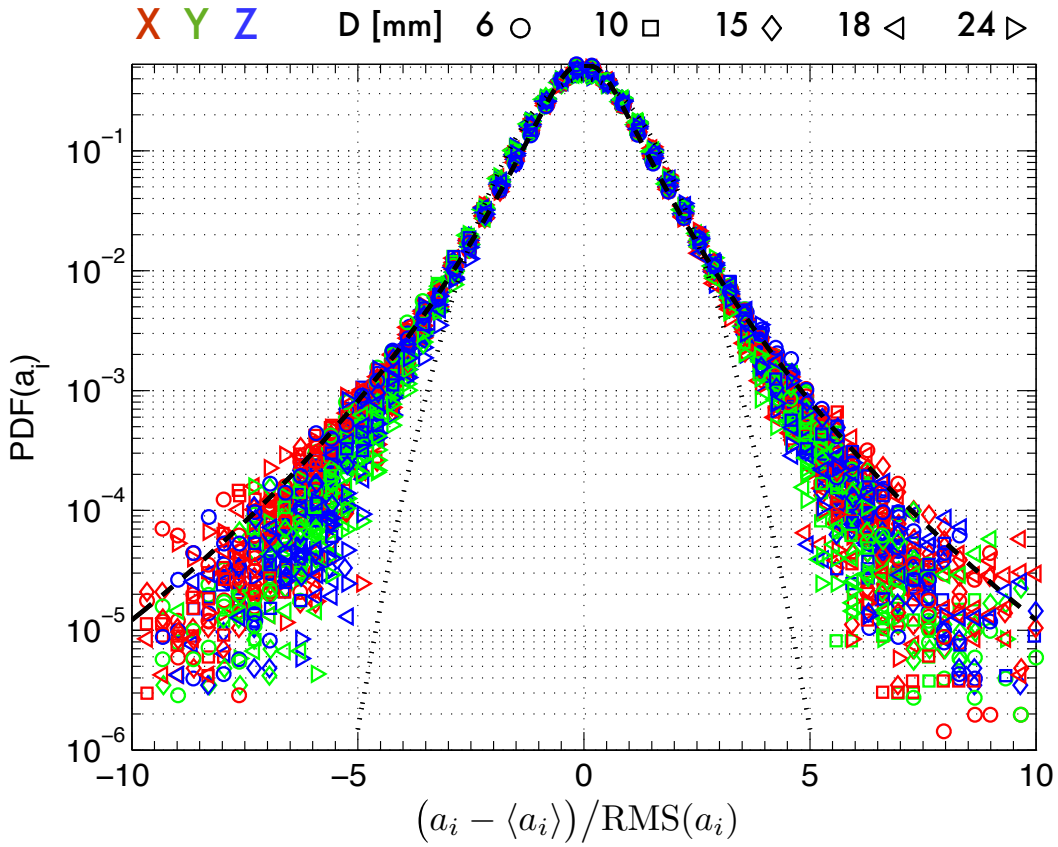

Figure 4.5: Probability density function (PDF) of the acceleration components, all counter-rotating runs (with all diameters) are plotted. The dotted line shows a Gaussian whereas the dashed line is a stretched-exponential $\Pi_s(x) = \frac{e^{3s^2/2}}{4\sqrt{3}}\left(1-\mathrm{erf}\left(\frac{\ln|x/\sqrt{3}|+2s^2}{s\sqrt{2}}\right)\right)$ with $s = 0.62$ as reported by Qureshi *et al.* [54].

PDF has a hat shape and the acceleration PDF shows two peaks[2] which are symmetric to 0. This is linked to the fact that we have centrifugal pumping: The poloidal component of the flow field is comparable for the two ways of driving the flow.

[2] A M-shaped PDF

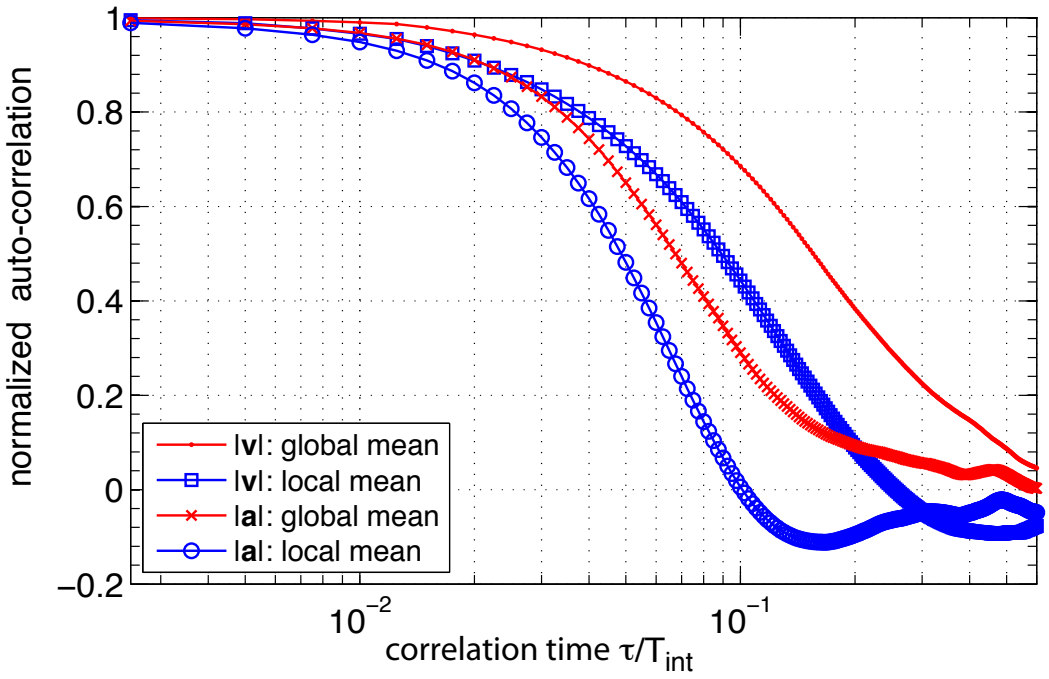

Figure 4.6: Influence of the subtraction of a local or global mean on the autocorrelation for $|\boldsymbol{v}|$ and $|\boldsymbol{a}|$. [18 mm, 2 Hz counter-rotating], the effect is less pronounced for quantities which can have both signs.

4.1.2 Auto-correlations

When computing autocorrelations one has several choices: On each track one can either subtract the global mean or its specific local mean. The difference between these two is illustrated for $|\boldsymbol{v}|$ and $|\boldsymbol{a}|$ in Fig. 4.6. Subtracting a local mean causes the positive quantities, $|\boldsymbol{v}|$ and $|\boldsymbol{a}|$, to drop faster and moreover to cross zero. In general, correlation time scales are found to be approximately twice as large when using the global mean.

It should be noted that one can furthermore choose between the biased and the unbiased definition of the autocorrelation, where the former is obtained from the inverse Fourier transform of the Power Spectrum and the latter from the $\langle s(t)s(t+\tau)\rangle$. Due to the way we handle tracks we always use the unbiased definition. More details can be found in appendix B.3.

We show here only the time-scale derived from the autocorrelation of velocity and acceleration; here, we discuss the unbiased correlation function with prior subtraction of the global mean. τ_{corr} is defined as the time when the autocorrelation passes below a threshold of $1/e$ for the first time. A threshold of 0 is not stable because the correlation might fall fast to 0 but not become negative. The timescales of the counter-rotating runs are provided in Fig. 4.7. For both, velocity and acceleration components, only little dependence of τ_{corr} on the propeller speed is found. Again, longitudinal and polar components are separated. For the velocity only the polar components seem to weakly depend on the diameter; they increase from $\tau_{\text{corr}}(\boldsymbol{v}, 6\text{ mm}) \approx 0.16\,T_{\text{int}}$ to $\tau_{\text{corr}}(\boldsymbol{v}, 24\text{ mm}) \approx 0.20\,T_{\text{int}}$.

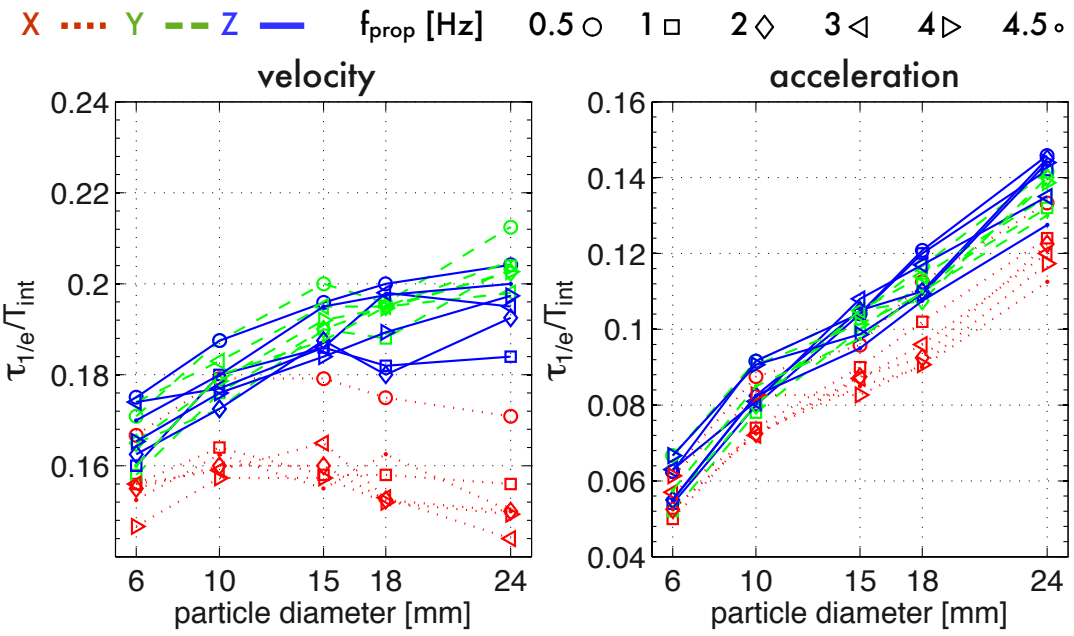

Figure 4.7: Correlation times for velocity and acceleration, [counter rotating forcing]. The unbiased correlation function with prior subtraction of the global mean was used. The time scales of velocity vary only little with propeller frequency, whereas the acceleration is approximately linear depended on f_{prop}.

The dependence on diameter is much clearer for the acceleration based time scales. Here, $\tau_{\text{corr}}(\boldsymbol{a})$ doubles from $D_{\text{part}} = 6$ mm to 24 mm. Moreover, the ratio between velocity and acceleration timescale, $\tau_{\text{corr}}(\boldsymbol{v})/\tau_{\text{corr}}(\boldsymbol{a})$, decreases from ~ 3 at $D_{\text{part}} = 6$ mm to ~ 1.5 at 24 mm.

4.1.3 Viscosity & density

The question arises to which extent the fluid viscosity and density determine the motion of large particles. In contrast to the measurements presented in this chapter the characterization of the instrumented particle was done in water, *i.e.* at a viscosity approximately 8 times lower than the here used water-glycerol mixture and a density of 1 g/cm^3 instead of 1.14 g/cm^3. Fortunately its diameter of 25 mm is close to the largest PA sphere ($D_{\text{part}} = 24$ mm). We, therefore, compare the runs with the solid 24 mm PA sphere to the instrumented particle. The forcing is counter-rotating propellers at $f_{\text{prop}} = 2$ Hz and $f_{\text{prop}} = 3$ Hz. Instrumented particle and solid sphere are indicated by **SP** and **PA** in the following equations. It should be noted that the instrumented particle deviates slightly from a rigid sphere: Mainly it has inhomogeneous inertia, a small imbalance and the gap between the two hemispheres might act as a trip wire. The technical details are found in chapter 7.

For both, velocity and acceleration, we find no difference in the normalized probability density functions (PDF) of the single components between the two particle. But as stated

in table 4.2, the instrumented particle has an acceleration RMS, which is ~ 1.25 times larger than that of the solid sphere. Similarly we find the longitudinal and polar velocity components to be 1.17 and 1.07 larger. We found in the previous section that the flow structure is independent of the propeller speed. Here the propeller frequency is identical for both particles and can thus not account for the change. The motion of tracers and small material particle is determined by viscosity and energy transfer rate. But it is remarkable that density and viscosity of the fluid are still playing a role for a particle this large.

One first notices that the density ratio $\rho\,(\text{glyc.–}H_2O)\,/\rho\,(H_2O) = 1.14$ is close to the increase in velocity RMS. If the particle is subject to Newton drag[3] instead of Stokes drag than the drag force is ~ 1.14 times higher for the solid sphere. Also, the square of the density change, $\left(\rho\,(\text{glyc.–}H_2O)\,/\rho\,(H_2O)\right)^2 = 1.29 \sim 1.25$ is close to the difference in the acceleration RMS. Stokes drag on the other hand is ruled out as it yields particle response times with $\tau_p^{\text{SP}}/\tau_p^{\text{PA}} \sim 8$. One can further experiment with an equation which stems from the motion of tracer: The Heisenberg-Yaglom equation (4.1) tells that the acceleration RMS of tracers is RMS $(a_i) \sim \varepsilon^{3/4}\nu^{-1/4}$. Accordingly the change in viscosity would increase the RMS by:

$$\frac{\text{RMS}\left(a_i^{\text{SP}}\right)}{\text{RMS}\left(a_i^{\text{PA}}\right)} \sim \left(\frac{\nu(\text{glyc.–}H_2O)}{\nu\,(H_2O)}\right)^{1/4} \sim 1.6 \neq 1.25$$

As expected the increased acceleration RMS cannot be explained by a formula derived for much smaller particles.

A possible explanation for the difference might lie in their preferential sampling of the flow (cf. the next section): Despite their close size the instrumented particles samples the flow in a more homogeneous way than the solid PA sphere. It might thus explore the more active regions of the flow leading to a higher acceleration variance.

To conclude more measurements at different viscosities are necessary.

Table 4.2: Ratios of the velocity and acceleration RMS of the instrumented particle to a solid 24 mm PA sphere. Both, viscosity and density, are smaller for the instrumented particle; its diameter is 25 mm.

RMS (instr. part.)/RMS (solid sphere)	v_x	v_y	v_z	a_x	a_y	a_z
$f_{\text{prop}} = 2$ Hz	1.17	1.10	1.09	1.28	1.37	1.23
$f_{\text{prop}} = 3$ Hz	1.19	1.07	1.07	1.22	1.24	1.24

[3] $F_D = \frac{1}{2}\,C_D\,\rho_f\,\boldsymbol{v}_{\text{slip}}^2\,A$ with A the reference area of the object and C_D a drag coefficient.

4.1.4 Sampling

Summing up, we see two reoccurring features:

- The motion scales well with the propeller frequency, and
- the motion depends in a nontrivial way on the particle size

One can thus ask if the motion changes because the particles "see" a reduced part of the turbulent spectrum or because they explore different regions of the flow. This preferential sampling of the flow has been observed for particles which are not neutrally buoyant: bubbles concentrate in regions of high vorticity whereas heavy particles tend to low-vorticity regions. Density effects can be neglected here, as the fluid is density-matched such that the settling velocity of each particle was less than 1 cm/s (the corresponding density mismatch is of the order 10^{-3} or better). We focus here on the influence of the complex large scale flow structure on the dynamics of the particles. Previous studies have mainly focused on the modification of small scale clustering in the presence of a homogeneous mean shear.

In order to evaluate the sampling of the flow, we bin the particle position (in cylindrical coordinates) into rings of diameter r and longitudinal position x with a width of Δr and Δx. Adequate normalization yields then the 2D PDF of the particle's longitudinal x and radial position r.

In agreement with our previous observations we notice no dependence of the sampling on the propeller frequency. However, by gradually increasing the diameter the PDFs change significantly from almost homogenous sampling at $D_{\text{part}} = 6$ mm to being located in two toruses near the propellers. Each torus core is situated at approximately $\frac{1}{2}R$ away from propeller and rotation axis. As an illustration we provide the PDF(x, r) at $f_{\text{prop}} = 3$ Hz for $D_{\text{part}} = 6$ mm, 15 mm, 24 mm in Fig. 4.8. It is noteworthy the preferential sampling of the 24 mm sphere is more pronounced than for the instrumented particle (cf. Fig. 7.22 on page 132). The two measurements differ mainly in their working fluid (the viscosity and density are 8 times and 0.87 times smaller for the latter), but the propeller speed was the same in both experiments. We plan on redoing the experiment with a different fluid viscosity (while keeping to particle neutrally buoyant) in order to understand this difference.

One can further compute the mean flow field, $\langle \boldsymbol{v} \rangle (r, x)$. Using the same binning, we then build the average velocity[4] $\langle v_x \rangle (r, x)$,$\langle v_r \rangle (r, x)$,$\langle v_\theta \rangle (r, x)$ for each ring.

The mean flow is almost identical to the flow structures described in section 2.3 (see also the sketch in Fig. 4.10) and to results for a cylindrical von Kármán flow [57]. $\langle v_\theta \rangle (r, x)$ shows two counter-rotating eddies with their vortex core at $R \sim 8$ cm and approximately 5 cm $= \frac{1}{2}R$ away from the impeller. Moreover, the flow is in average circulating around these eddies. By eye, the stagnation point is in the center of the apparatus at $x = r = 0$ and the flow is symmetric to $x = 0$, *i.e.*

$$\langle v_x \rangle (r, |x|) \approx - \langle v_x \rangle (r, -|x|) \quad \text{and} \quad \langle v_\theta \rangle (r, |x|) \approx - \langle v_\theta \rangle (r, -|x|)$$

[4] expressed in cylindrical coordinates

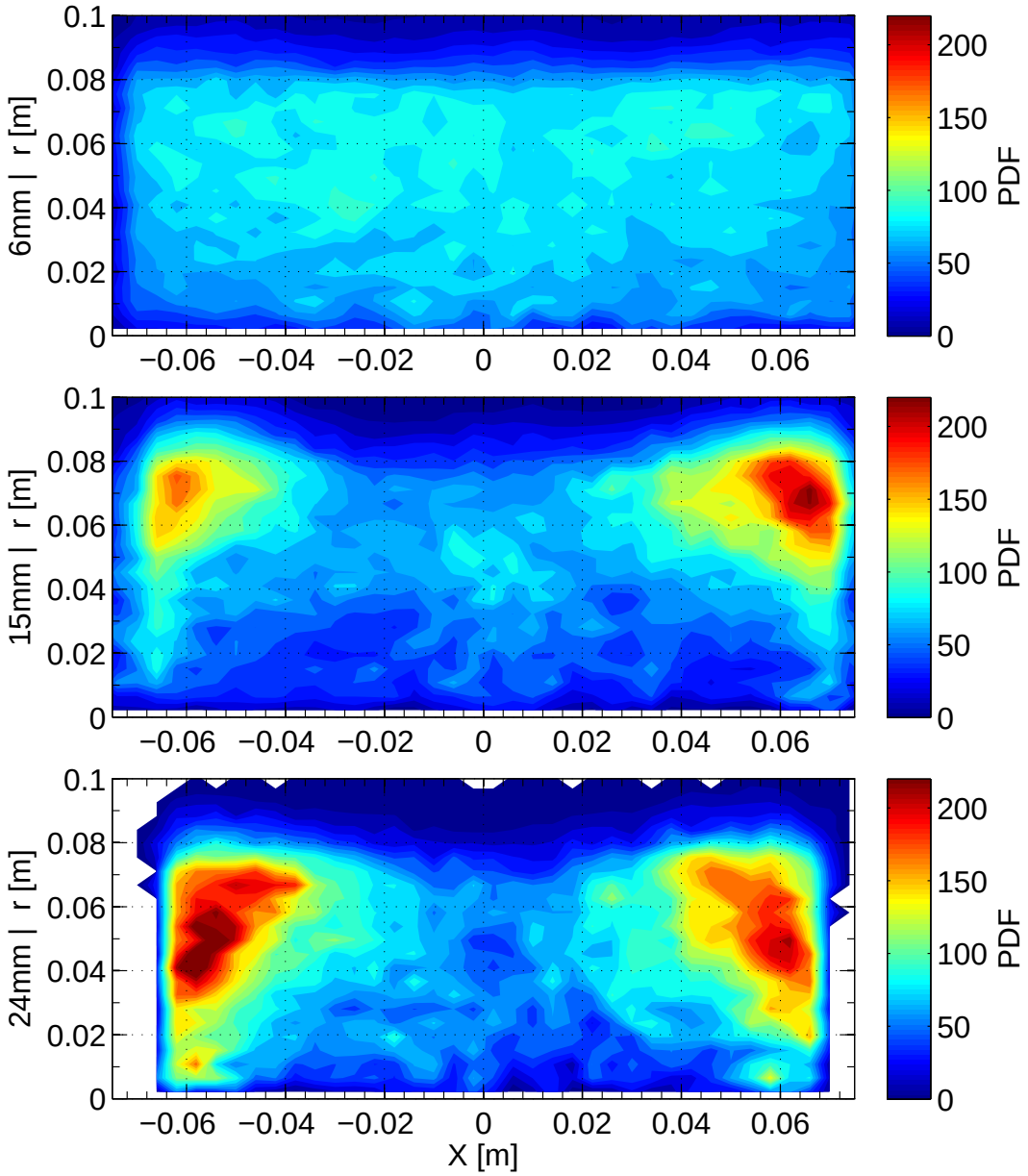

Figure 4.8: Preferential sampling of the different diameters. The sampling depends only little on the propeller speed, here we show counter-rotating propellers at $f_{\text{prop}} = 3$ Hz.

Comparing to the PDF of position, one notes that bigger particles stay preferably close to the eddy core. Surprisingly, the shape of the mean flow is not altered by the particle diameter. To compare the flow fields of different particle diameters we compare the toroïdal (v_θ) to the poloïdal ($\sqrt{v_r^2 + v_x^2}$) component along two lines the flow field. As shown in Fig. 4.9 we find that the dependence on the particle diameter is weak. Only close to the two big eddies (blue vectors in the sketch in Fig. 4.10) bigger particles exhibit a stronger toroidal motion. This analysis also reveals that the stagnation point of the flow is at $x \approx -1.5$ cm, *i.e.* it does not exactly coincide with geometric center of the vessel.

Co-rotating impeller form only one eddy in $\langle v_\theta \rangle (r, x)$ but the circulation in x and r towards the propellers persists. Its stagnation point is slightly off-center at $x = -1$ cm $\sim -0.1\,R$ and for $r < 4$ cm $\sim 0.4\,R$ the components $\langle v_x \rangle$ and $\langle v_x \rangle$ vanish. In total, the general structure of the co-rotating flow is in good agreement with the results reported in Catherine Simand's PhD thesis [60].

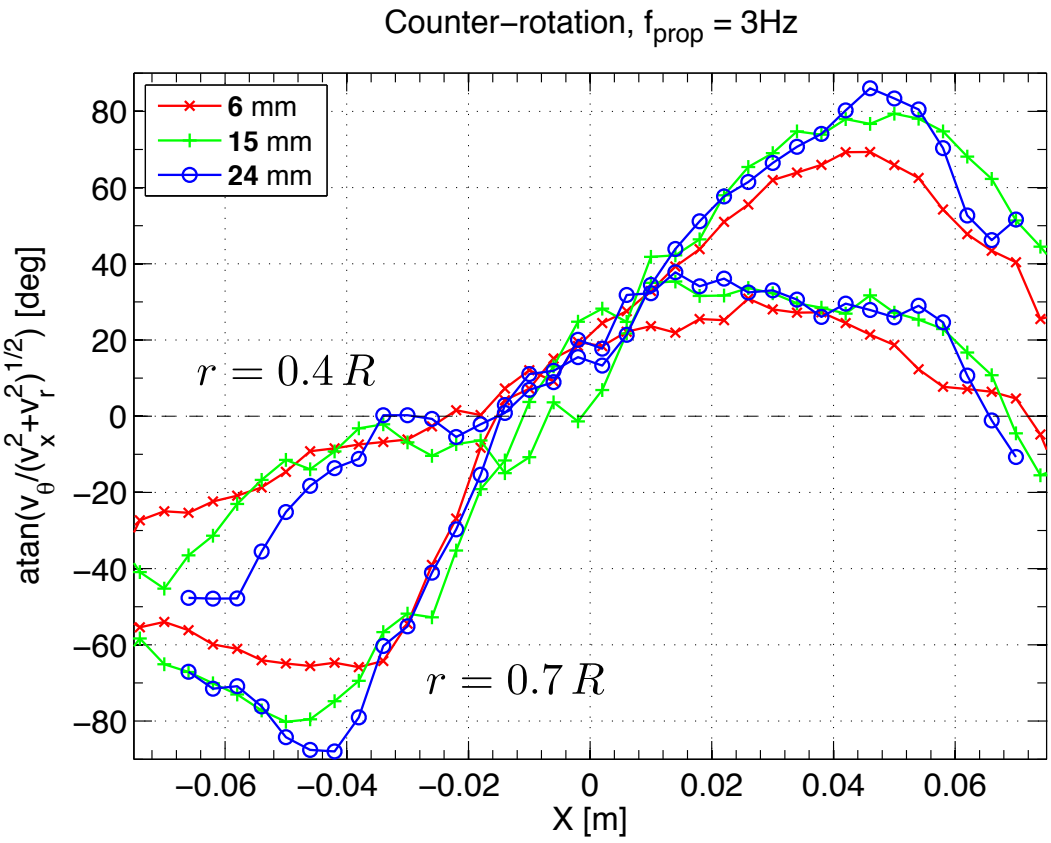

Figure 4.9: Dependence of the mean field on the particle size; we compare the toroidal v_θ to the poloidal $\sqrt{v_r^2 + v_x^2}$ component along a line trough the mean flow field at $r = 0.4R$ and $r = 0.7R$. Note that instead of simple ratio the arctan is used; atan is less sensitive if one component is close to 0. For both lines the maximum of the poloidal component is ~ 0.3 m/s, it varies only weakly with the particle diameter.

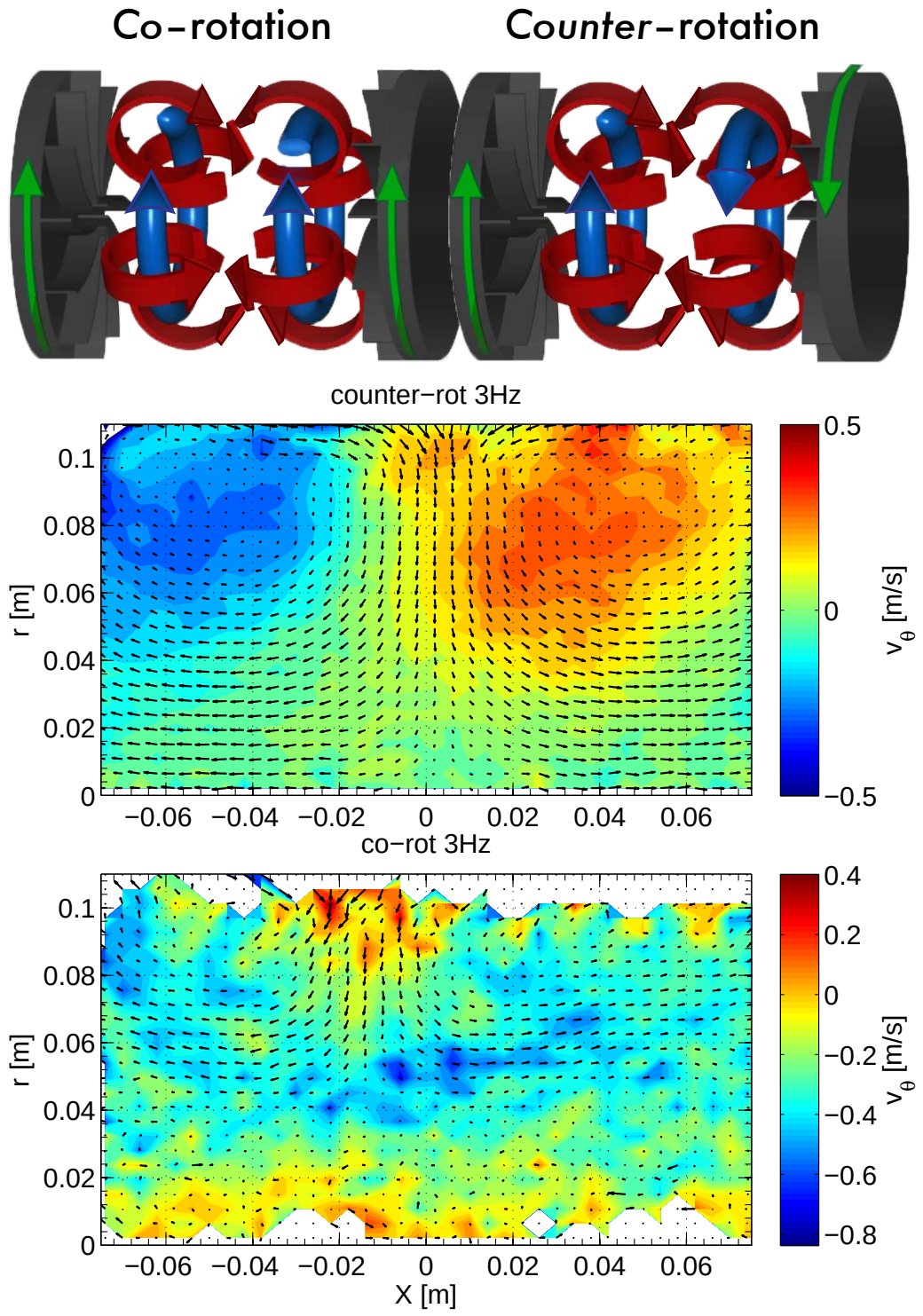

Figure 4.10: Mean flow field for co- and counter-rotation, here $f_{\text{prop}} = 3$ Hz. The top pictures sketches the large scale flow structure [image based on [57], co-rotation similar to [60]] and we observe the identical behavior for counter-rotation: $\langle v_\theta \rangle (r, x)$ shows two eddies with opposite rotation sense (sketch: blue vectors) and we see a circulation around these eddies similar to the red arrows in the sketch. For the co-rotation only one eddy in $\langle v_\theta \rangle (r, x)$ is formed, and circulation in x and r towards the propellers persists. The stagnation point is at $x \approx -1$ cm $\sim -0.1\, R$.

5 How they spin

In this chapter we focus on the rotational dynamics and their influence on the translation of the particle. Although we recently took data of multiple painted particles at different propeller speeds, we did not yet finish the processing. We therefore limit the evaluation to the data presented in a Physical Review Letters [82] and the two runs with the painted instrumented particle. As soon as my broken foot is healed the remaining data will be analyzed and added.

The motion of a sphere in a flow is defined by the Navier-Stokes equation of the flow, possibly buoyancy and the no-slip condition: At the surface the fluid velocity matches the particles velocity. If the Reynolds number based on the particle, Re_p, is small, one can derive its equation of motion [22, 41] (cf. chapter 2). For flows that creep around the particle ($Re_p \ll 1$), the translation and rotation decouple and the particle's rotation becomes a measure of the fluid's vorticity [18]. With increasing Re_p the separation between linear and angular motion disappears and one can observe a coupling between translation and rotation. That was first reported by Magnus [39] when he studied the motion of rotating artillery projectiles (and thereafter rotating cylinders in a windtunnel) in his article *Über die Abweichung der Geschosse, und: Über eine auffallende Erscheinung bei rotierenden Körpern*. In order to quantify the "Erscheinung" one therefore decomposes the hydrodynamics forces into contributions parallel and perpendicular to the relative velocity, $\mathbf{v}_{\text{slip}} \equiv \boldsymbol{v}_{\text{p}}(\boldsymbol{x}, t) - \boldsymbol{u}(\boldsymbol{x}, t)$, of the particle with respect to the flow. A generalization of the lift or Magnus force [39] acting on a body of volume $\mathcal{V}$, as derived in an inviscid, laminar flow of density ρ_f is then

$$\boldsymbol{F}_{\text{lift}} = \rho_f \mathcal{V} \cdot \left(C_{\text{lift}} \cdot \boldsymbol{v}_{\text{slip}} \times \boldsymbol{\omega}^{\mathbb{P}} \right) \tag{5.1}$$

and it appears as a natural possibility of a force acting perpendicular[1] to $\boldsymbol{v}_{\text{slip}}$ [6, 38]. It is worthwhile noting that the lift force is independent of the viscosity of the flow. The parameter C_{Lift} can be negative and positive; in general it depends on the (relative) linear and angular velocity but also on the surface roughness. This leads to astonishing trajectories in ball games; mastering the lift force can easily increase the income of a football player by a factor of 10 (or more).

A lift force has been observed where the flow is steady and laminar [79, 70, 56]. Turning to turbulent flows with high particle Reynolds numbers one encounters several problems as sketched in Fig. 5.1. In fact the very definition of the fluid velocity around the particle is very ambiguous. For this reason, we reduce the expression for the lift force to $\propto \boldsymbol{v} \times \boldsymbol{\omega}^{\mathbb{P}}$, where $\boldsymbol{v}$ is the particle velocity. It is, furthermore, not clear if and how the fluid drives

[1] The formula given by Auton [6] uses $\boldsymbol{u} - \boldsymbol{v} = -\boldsymbol{v}_{\text{slip}}$

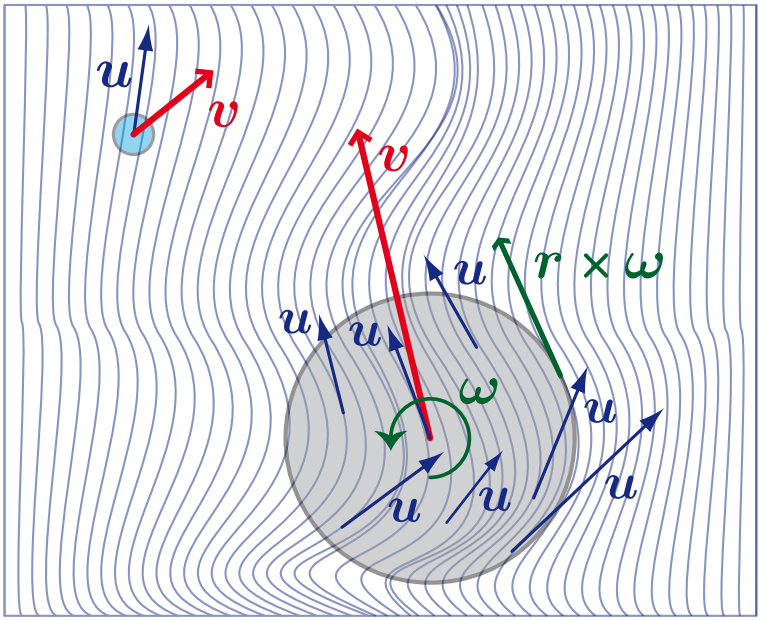

Figure 5.1: Sketch of particles of increasing sizes superimposed on local velocity gradients. Whereas the flow around the small particle is smooth, it exhibits significant spatial variations around the large particle.

the rotation of the sphere: An simple estimate of the particle's response time τ_p^{rot} from Eq. (2.12) tells[2] that the cases investigated here have a response time of several integral timescales T_{int}. The existence of a significant rotation and a lift force in such conditions is thus not evident.

Mathematically two angular velocities exist: Whereas $\boldsymbol{\omega}^{\mathbb{P}}$ describes the rotation of the particle with respect to the fixed lab coordinate system, $\boldsymbol{\omega}^{\mathbb{L}}$ fixes the particle and rotates the lab system. This is somewhat similar to quantum mechanics where one has the choice between the Heisenberg and the Schrödinger picture to incorporate a dependency on time. We found no particular use for $\boldsymbol{\omega}^{\mathbb{L}}$ in our analysis and will thus work only with the angular velocity which rotates the particle, $\boldsymbol{\omega}^{\mathbb{P}}$. The superscript $^{\mathbb{P}}$ is omitted in the following.

In this chapter we present data from two experiments which differ both in particle and working fluid:

> The first successful measurement of the 6D-tracking was done with a single homogenous Poly-Amid sphere in a density-adjusted water-glycerol mixture of viscosity $\nu = 8.5 \cdot 10^{-6}\,\text{m}^2/\text{s}$. The sphere is 18 mm in diameter. Thus the particle response time is $\tau_p^{\text{rot}}(\text{PA18}) = 0.8\,\text{s} = 2.5\,T_{\text{int}}$. We indicate the run by **PA18**.

> We also exploit the 6D tracking of the instrumented particle. Note that these runs were originally performed to better understand the instrumented particle; conse-

[2] $\tau_p^{\text{rot}} = J/8\pi\rho_f\,\nu\,a^3 = a^2/15\nu$

quently the amount of data points is less. Moreover, the fluid is water with a viscosity of $\nu = 1.004 \cdot 10^{-6}\,\mathrm{m}^2/\mathrm{s}$ and the particle is 25 mm in diameter with a non-homogeneous inertia. Although we adjusted the position of its center of mass such that is close to the geometrical center, there is as remaining small displacement between the two. Hence, the particle has a preferred direction of its pole. Additionally, it consists of two hemispheres which are screwed together, that adds a little deviation (< 0.5 mm) from a spherical shape. The remaining gap between the two capsules might furthermore act similar to a tripwire. We denote the two data sets **SP 2Hz** and **SP 3Hz**, respectively. The particle response time is $\tau_p^{\mathrm{rot}}(\mathrm{SP}) = 10.4\,\mathrm{s}$ which is 20 and 30 times larger than the integral time scale, T_{int}.

In all cases the impellers are counter-rotating and the particles are neutrally-buoyant.

The analysis is grouped into the following parts:

- We first present statistics on the angular velocity and acceleration. Further, the rotational and translational energy are compared.
- Next we investigate the coupling between rotation and translation (section 5.2). This is done in the spirit of the Magnus force, $\boldsymbol{F}_{\mathrm{lift}} = \rho_f \mathcal{V} \cdot \left(C_{\mathrm{lift}} \cdot \boldsymbol{v}_{\mathrm{slip}} \times \boldsymbol{\omega}\right)$. The so-called *Frenet* frame proved to be helpful in this investigation of the coupling between rotation and translation and is presented here at the beginning of section 5.2.

Parts of this chapter are close to the article published in Physical Review Letters [82] and the conference proceeding for the 13th European Turbulence Conference [84].

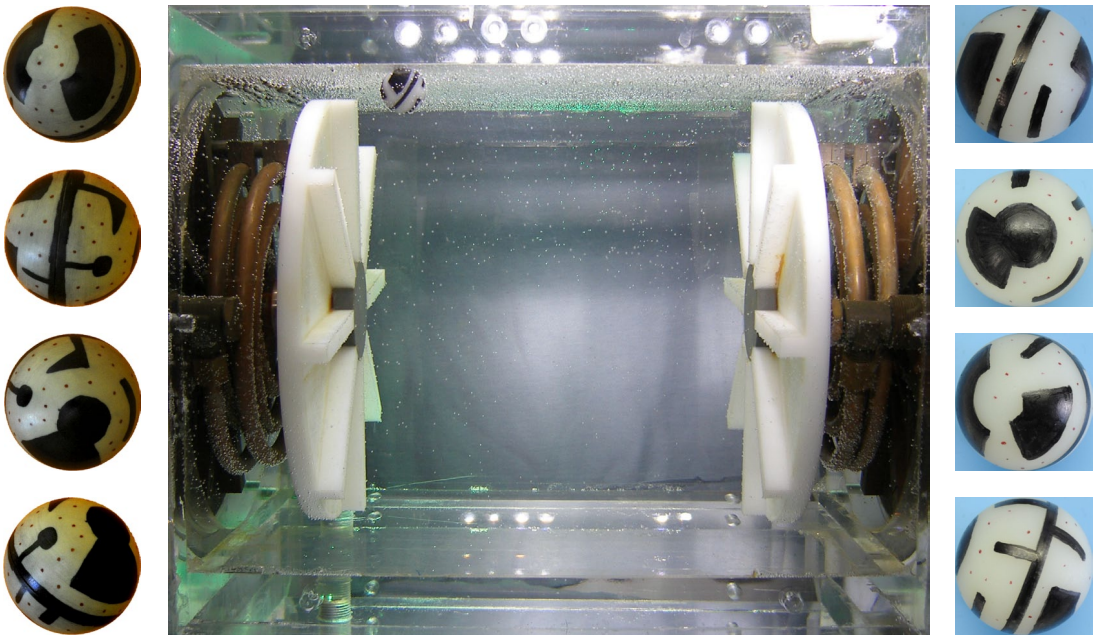

Figure 5.2: The employed mixer and particles in this chapter.

5.1 Rotational dynamics

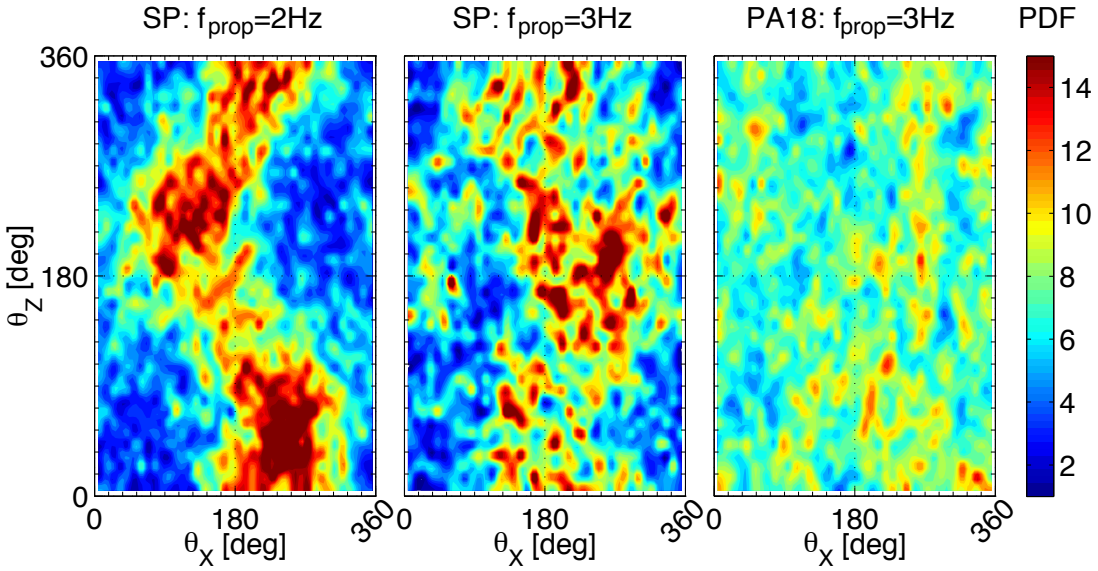

Figure 5.3: 2D-PDF of the absolute orientation (θ_x, θ_z) for the instrument particle (SP) at $f_{\text{prop}} = 2$ Hz & 3 Hz and the solid PA sphere ($f_{\text{prop}} = 3$ Hz). One can clearly see the preferred orientation of the instrumented particle.

Before focusing on the actual motion of the particle one can ask if the space of orientation is homogeneously sampled by the particle or if preferred alignments exist. We therefore plot the two-dimensional PDF of the absolute orientation (θ_x, θ_z) in Fig. 5.3. Whereas the solid particle samples the (θ_x, θ_z) plane in a homogenous way we spot regions of preferred orientations for the instrumented particle. The spots are more distinct at the lower propeller speed, f_{prop} which is in agreement with the signal from the accelerometer inside. The preferred direction is most likely caused by a small mismatch between its center of mass and its geometric center, as we adjust the mass of the particle by adding extra weight inside. The technical origin is explained in section 7.1.1.2.

We note that the PDF(θ_y) is in all three cases distributed close to $\cos(\theta_y)$ which is the shape for a homogeneous sampling (Eq. (3.8) in section 3.3.1.1).

5.1.1 Angular velocity & acceleration

We now turn to the angular velocity[3], $\boldsymbol{\omega}$. For both, solid particle and instrumented particle, the three components fluctuate around a zero mean value. Furthermore, their distributions are symmetric, and slightly non-Gaussian with a flatness F ~ 4. The PDFs reveal no preferred orientation, and their RMS amplitude is approximately $\frac{1}{3}$ of the propeller frequency, f_{prop}. It also corresponds to the rotation that would result from imposing a velocity difference of the order of u_{rms} across the particle diameter D. The PDF of angular

[3] Note, that we omit the indicator $^{\mathbb{P}}$ in the following

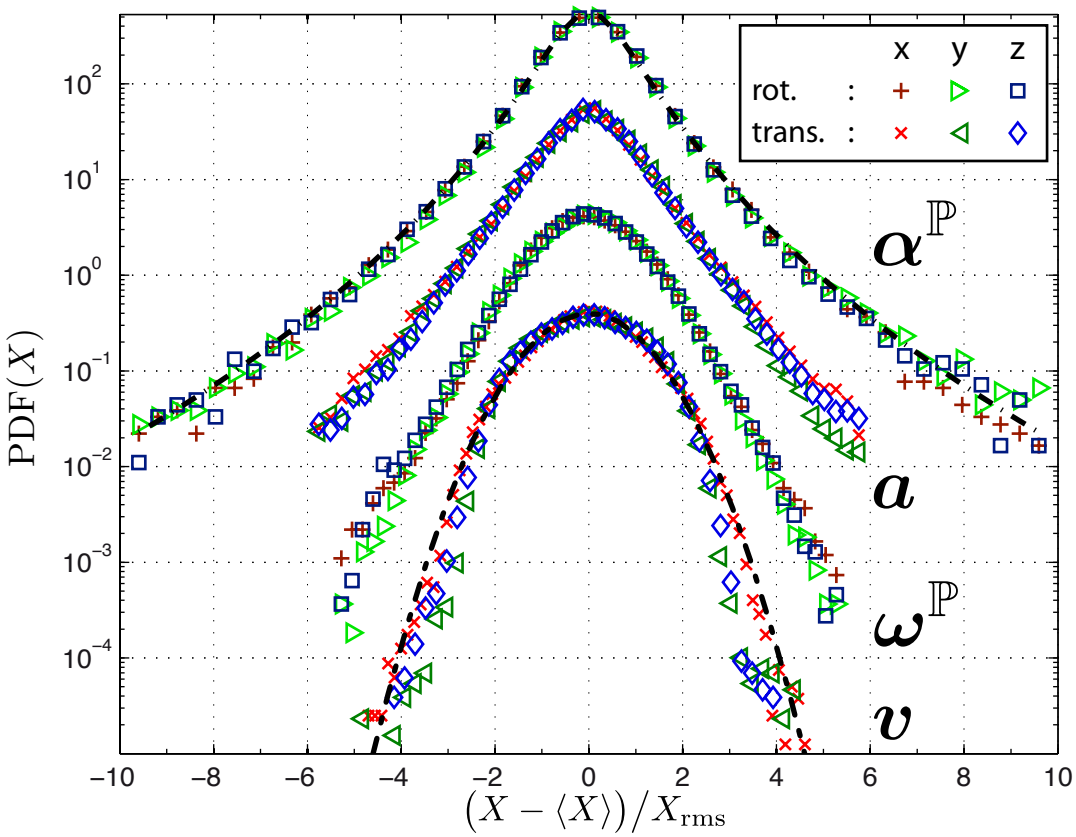

Figure 5.4: PDFs of the translational and rotational velocity and acceleration [run PA18, $f_{\rm prop} = 3$ Hz]. The PDFs are shifted for readability and the dashed lines show a gaussian and a stretched exponential, $\Pi_s(x) = \frac{e^{3s^2/2}}{4\sqrt{3}}\left(1 - \mathrm{erf}\left(\frac{\ln|x/\sqrt{3}|+2s^2}{s\sqrt{2}}\right)\right)$, with $s = 0.65$ (that corresponds to a flatness $\mathrm{F}(s) = 9.8$).

velocity components of the solid sphere are shown in Fig. 5.4. The RMS amplitude of the angular acceleration, $\boldsymbol{\alpha}$, is about 700 rad/s^2, again of the order of $(u_{\rm rms}/D_{\rm part})^2$. The PDF of $\boldsymbol{\alpha}$ is strongly non-Gaussian, the flatness is $F = 7 \pm 1$. Hence, the PDFs of the angular velocity increments become broader when the time-lag τ decreases from $\tau \sim T_{\rm int}$ to $\tau \sim \tau_\eta$: the angular dynamics is intermittent.

In agreement with the observation for the single components we further find that the magnitude of angular velocity is mostly depending on the propeller speed. Fig. 5.5 shows the PDF of $|\boldsymbol{\omega}| \,/\, (2\pi f_{\rm prop})$ for the solid and the instrumented particle at 2 propeller speeds. The average rotation rate for $f_{\rm prop} = 3$ Hz is $|\omega| \sim 0.60 \cdot 2\pi f_{\rm prop}$ and the 80% percentile is found at $0.83 \cdot 2\pi f_{\rm prop}$. At $f_{\rm prop} = 2$ Hz the values are $\sim 8\%$ lower ($|\omega| \sim 0.56 \cdot 2\pi f_{\rm prop}$ and $0.76 \cdot 2\pi f_{\rm prop}$).

The little difference between the three data sets is striking, since the instrumented particle is 40% larger than the solid particle, in fluid which a 8 times less viscid and has an in-homogenous mass distribution. Accordingly, they have particle Reynolds numbers of

$Re_p^{\mathrm{PA18}}\,(3\ \mathrm{Hz}) \sim 1200$, $Re_p^{\mathrm{SP}}\,(2\ \mathrm{Hz}) \sim 8400$, and $Re_p^{\mathrm{SP}}\,(3\ \mathrm{Hz}) \sim 12500$. Despite the fact that viscosity and Reynolds number are varied by an order of magnitude we do *not* observe any significant difference in their angular motion. Additionally, we find that the response time of a particle to a torque, τ_p^{rot}, is 2.5 to 30 times larger than the integral time scale, T_{int}. This is in contrast to the observed rotation rates. It becomes evident that formulas derived for the motion of small spheres do no longer apply to the case of large particles.

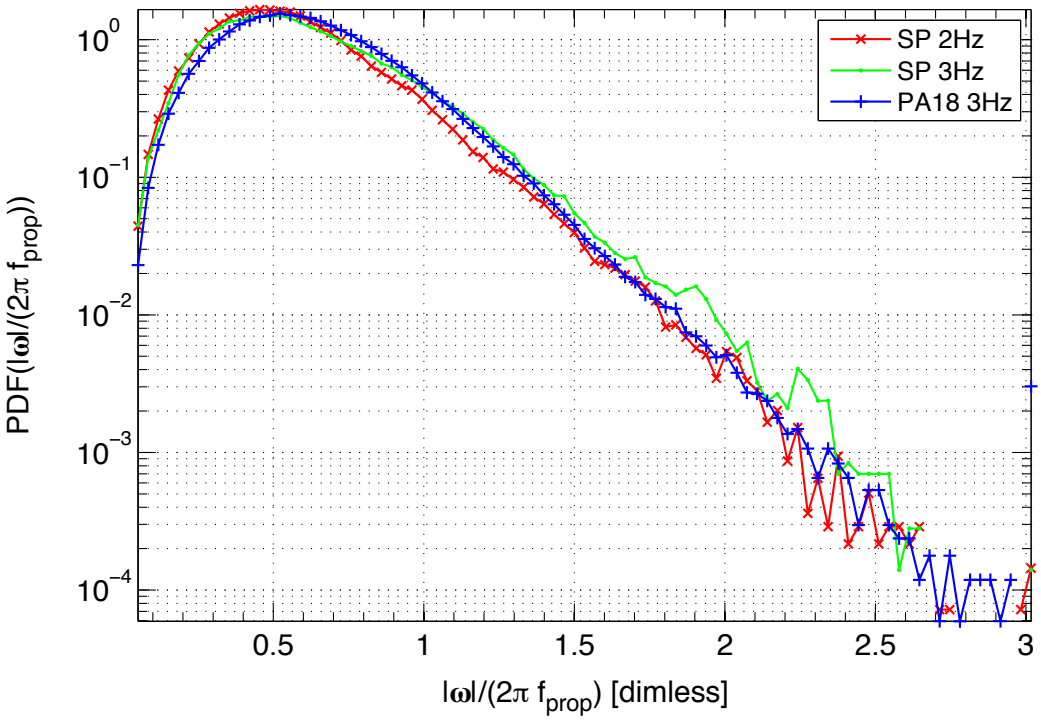

Figure 5.5: PDF of the magnitude of angular velocity $|\boldsymbol{\omega}|$ normalized by the propeller speed, f_{prop}. It should pointed out that instrumented particle (SP) and solid particle (PA18) differ by 40% in diameter, a factor 8 in viscosity and their mass distribution. It is $|\boldsymbol{\omega}| \sim 0.6 \cdot 2\pi f_{\mathrm{prop}}$ and the 80% percentile is at $0.8 \cdot 2\pi f_{\mathrm{prop}}$.

5.1.2 Energy

We now investigate the kinetic energy of the particle. Since the particle's translation and rotation is in average well approximated by the propeller speed, one can estimate $E_{\text{trans}} = \frac{1}{2} m\, \boldsymbol{v}^2$ and $E_{\text{rot}} = \frac{1}{2} J\, \boldsymbol{\omega}^2$ beforehand. In the case of a solid particle of diameter D_{part} their ratio is:

$$\frac{E_{\text{trans}}}{E_{\text{rot}}} = \frac{\frac{1}{2} m\, \boldsymbol{v}^2}{\frac{1}{2}\left(\frac{1}{10} m\, D_{\text{part}}^2\right) \boldsymbol{\omega}^2} \approx 10 \cdot \left(\frac{C_{\text{trans}} \cdot 2\pi\, f_{\text{prop}}}{C_{\text{rot}} \cdot 2\pi\, f_{\text{prop}}} \frac{R}{D_{\text{part}}} \cdot \right)^2 \tag{5.2}$$

C_{trans} and C_{rot} are factors which relate $|\boldsymbol{v}|$ and $|\boldsymbol{\omega}|$ to the propeller speed, R is the propeller radius. Based on chapter 4 and Fig. 5.5 it is $C_{\text{trans}}/C_{\text{rot}} \sim 1/2$. Therefore

$$\frac{E_{\text{trans}}}{E_{\text{rot}}} \sim 2.5 \cdot \left(\frac{R}{D_{\text{part}}} \right)^2 \tag{5.3}$$

The largest particle has a diameter of $D_{\text{part}} = 1/4R$, hence, $E_{\text{trans}} \gg E_{\text{rot}}$. The inhomogeneous inertia of the instrumented particle complicates E_{rot} to $E_{rot} = \frac{1}{2} \boldsymbol{\omega}^T \underline{\underline{\boldsymbol{J}}}\, \boldsymbol{\omega}$. In addition the inertia tensor is changing its orientation. But the inertia tensor has only two unique eigenvalues (cf section 7.2.3), one 50% smaller and one 50% larger than the inertia of a solid sphere of the same diameter $D_{\text{part}} = 25$ mm. Consequently, the statement $E_{\text{trans}} \gg E_{\text{rot}}$ holds also for the instrumented particle.

The left plot of Fig. 5.6 shows the PDF of the translation as well as the rotation energy. In agreement to the estimate above, we find that the ratio of $E_{\text{rot}}/\left(E_{\text{rot}} + E_{\text{trans}}\right)$ is in average 2.7% with the 80% percentile at 3.5% – the rotational energy is negligible compared to the translation. We also investigated the auto correlation of both parts of the kinetic energy (right plot in Fig. 5.6).

In all three experiments we find that the normalized autocorrelation of E_{trans} follows approximately an exponential decay which passes $1/e$ at $\tau_{\text{corr}} \sim 0.16\, T_{\text{int}}$. We further find the rotational energy to stay about twice as long correlated. For the solid particle we notice that the auto-correlation of E_{rot} shows two different time scales. We need here to process the remaining data runs to be sure that this is not an artifact. However, Alain Pumir and Michael Wilkinson modeled the tumbling of a spherical particle and also find two timescales in the auto-correlation [76].

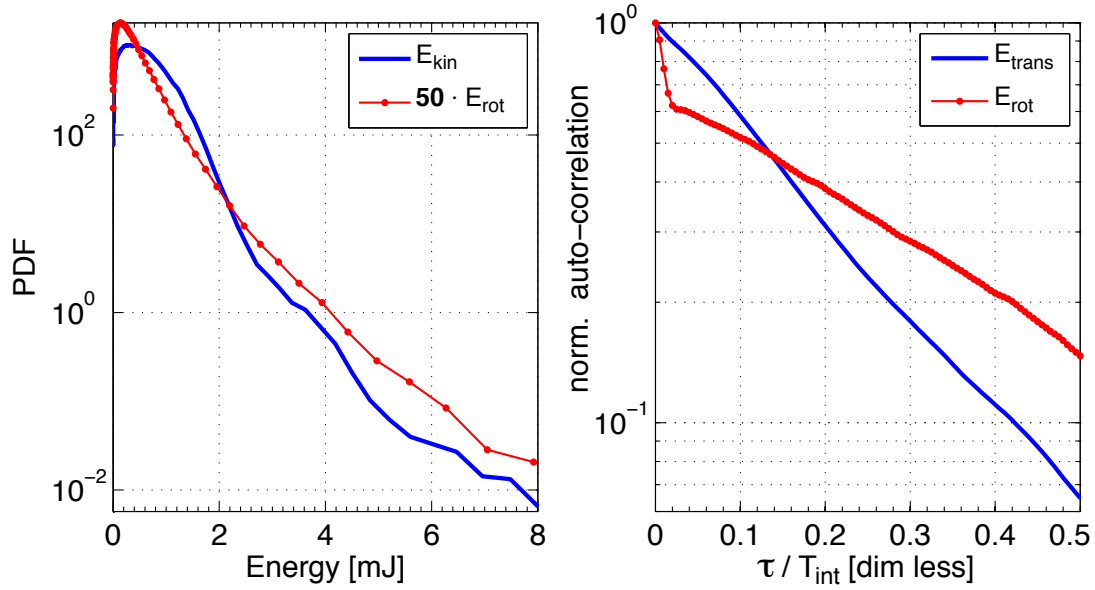

Figure 5.6: Rotational ($E_{\text{rot}} = \frac{J}{2}\boldsymbol{\omega}^2$) and translational ($E_{\text{trans}} = \frac{m}{2}\boldsymbol{v}^2$) energy of the solid particle [PA18].
Left: PDF of E_{rot} and E_{trans}. Note that $\mathbf{50} \times E_{\text{rot}}$ is compared to E_{trans}. The ratio of $E_{\text{rot}}/\left(E_{\text{rot}} + E_{\text{trans}}\right)$ is in average 2.7% and the 80% percentile is at 3.5% – the rotational energy is negligible compared to the translation.
Right: Auto correlation of E_{rot} and E_{trans}

5.2 Coupling between rotation & translation

5.2.1 Frenet frame

The Frenet formulas define a local coordinate system which is attached to and moving with the trajectory, $\boldsymbol{x}(t)$.

$$\boldsymbol{T}(t) = \frac{\dot{\boldsymbol{x}}(t)}{|\dot{\boldsymbol{x}}(t)|} \tag{5.4a}$$

$$\boldsymbol{N}(t) = \boldsymbol{B}(t) \times \boldsymbol{T}(t) = \frac{\dot{\boldsymbol{x}} \times \ddot{\boldsymbol{x}}}{|\dot{\boldsymbol{x}} \times \ddot{\boldsymbol{x}}|} \times \frac{\dot{\boldsymbol{x}}}{|\dot{\boldsymbol{x}}|} \tag{5.4b}$$

$$\boldsymbol{B}(t) = \frac{\dot{\boldsymbol{x}} \times \ddot{\boldsymbol{x}}}{|\dot{\boldsymbol{x}} \times \ddot{\boldsymbol{x}}|} \tag{5.4c}$$

$(\boldsymbol{T}, \boldsymbol{N}, \boldsymbol{B})$ are the so-called tangent, normal, and bi-normal (unit) vectors. Expressing the trajectory in the Frenet frame, $(\boldsymbol{T}, \boldsymbol{N}, \boldsymbol{B})$, yields

$$\boldsymbol{v}(t) = |\boldsymbol{v}(t)| \cdot \boldsymbol{T}(t) \tag{5.5}$$

and for the acceleration

$$\boldsymbol{a}(t) = \frac{\mathrm{d}}{\mathrm{d}t}\big(|\boldsymbol{v}(t)| \cdot \boldsymbol{T}(t)\big) = \frac{\mathrm{d}\ |\boldsymbol{v}(t)|}{\mathrm{d}t}\boldsymbol{T}(t) + \kappa\,|\boldsymbol{v}(t)|^2\,\boldsymbol{N}(t) \tag{5.6}$$

$1/\kappa$ is the radius of the circle in the $(\boldsymbol{T}-\boldsymbol{N})-$plane which approximates the trajectory at $\boldsymbol{x}(t)$ best. Consequently, $a_N = \kappa\,|\boldsymbol{v}(t)|^2$ is the well-known centrifugal acceleration. In addition, the acceleration vector lies in the $(\boldsymbol{T}-\boldsymbol{N})-$plane and the velocity is pointing with $\boldsymbol{T}$. An illustration of the equations is given in Fig. 5.7 and further details can be found in appendix B.4 and in [34, 75].

5.2.2 Preferential alignment

By construction (5.6) all forces expressed in the Frenet frame lie in the $(\boldsymbol{T}-\boldsymbol{N})-$plane. A lift force of the form $\boldsymbol{F}_{\text{lift}} = C_{\text{lift}}\,\boldsymbol{v}_{\text{slip}} \times \boldsymbol{\omega}$ is perpendicular to v_{slip} and as a consequence, it can only contribute to a_N *i.e.* in direction of $\boldsymbol{N}$. Unfortunately, our measurement technique can not measure the flow around the particle and we cannot access the relative velocity, $\boldsymbol{v}_{\text{slip}}$, but only its absolute velocity, $\boldsymbol{v}$. To check for an alignment of the angular velocity to the trajectory one can express the direction of $\boldsymbol{\omega}$ in the $(\boldsymbol{T}, \boldsymbol{N}, \boldsymbol{B})$ frame by spherical coordinates (ϕ, θ) as sketched in Fig. 5.7.

The two-dimensional probability density function(PDF) of the direction of $\boldsymbol{\omega}$ within the Frenet frame is depicted for the solid particle in Fig. 5.8 and a three-dimensional visualization thereof is provided in Fig. 5.7.

In the following we define $\omega_B \equiv \boldsymbol{\omega} \cdot \boldsymbol{B}$: We find that $\langle \omega_B \rangle > 0$, with the peak of the PDF being at $\theta \approx 30°$. By construction it is $\boldsymbol{v} = |\boldsymbol{v}| \cdot \boldsymbol{T}$ and $\boldsymbol{B} \times \boldsymbol{T} = \boldsymbol{N}$, therefore $\langle \omega_B \rangle > 0$ implies that the parameter C_{lift} of the lift force is positive.

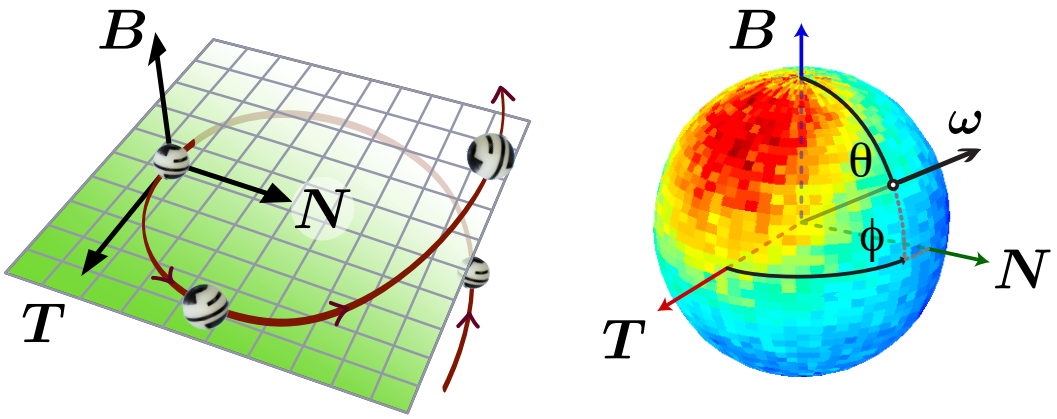

Figure 5.7: **Left**: Sketch of the co-moving Frenet coordinate system as defined by the particle trajectory. By definition all forces are in the $\boldsymbol{T}-\boldsymbol{N}$ plane. The curvature κ measures the bending of the trajectory in that plane.
Right: Direction of angular velocity $\boldsymbol{\omega}$ of the particle with respect to the Frenet frame. The texture of the sphere presents the PDF of alignment for run PA18.

Moreover, $\boldsymbol{\omega}$ is aligned perpendicular to $\boldsymbol{N}$. Consequently, $\boldsymbol{\omega}\times\boldsymbol{v}$ lies in the $(\boldsymbol{T},\boldsymbol{N})$-plane and is parallel with $\boldsymbol{N}$. This observation is consistent with a Magnus force $a_{\text{lift}}\cdot\boldsymbol{N}$; however, the fairly sharp distribution of the direction of $\boldsymbol{\omega}$ on the sphere is remarkable.

The von Kármán flow is known for its large scale inhomogeneities (cf *e.g.* [57, 50]). Therefore, we verified our observations by using only data points within a box of edge length d in the center (cf. the middle and right plot in Fig. 5.8). Despite a significant reduction in the amount of data we find that preferential alignment is robust and not an artifact of the large scale flow of the apparatus. In Fig. 5.6 we showed that the kinetic energy de-correlates within $\sim\frac{1}{2}T_{\text{int}}$. Within this time the particle moved approximately one propeller radius R along its (non-straight) trajectory. Thus, for the smaller observation volumes the particle lost all possible trace of the impellers.

We further test if the alignment persists in the case of the instrumented particle. Despite its inhomogeneous inertia, the lesser viscosity and the preferential orientation of the particle as such we still find an alignment of $\boldsymbol{\omega}$ with the trajectory. But as shown in Fig. 5.9 it is much weaker than for the solid particle. In agreement with the findings in section 7.2.2, the sampling becomes more uniform with increasing propeller frequency.

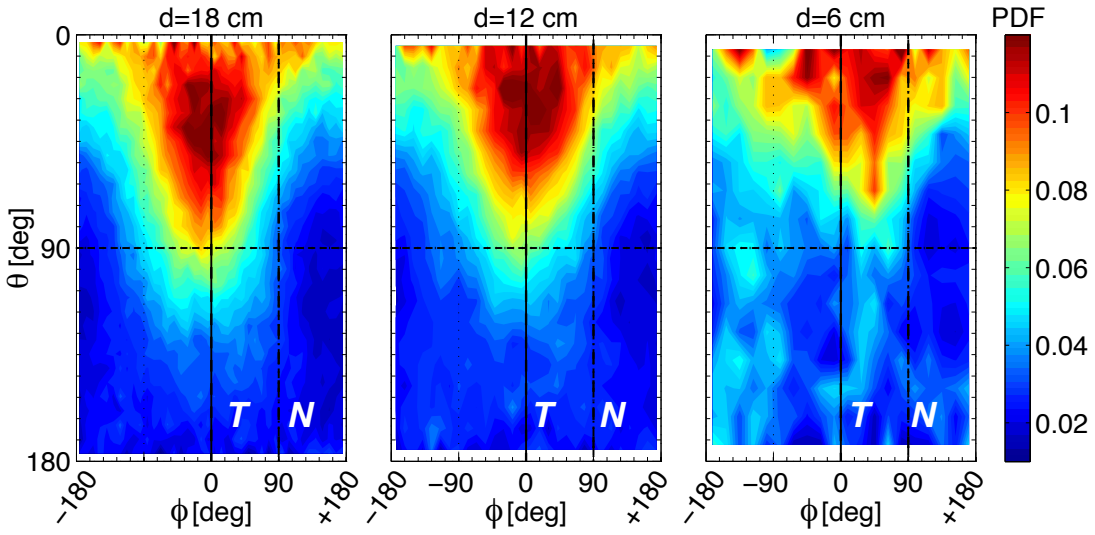

Figure 5.8: Alignment of the angular velocity ω with the Frenet frame, here we show the solid particle. To ensure that the alignment is not due to contacts with walls and impellers, the PDF is calculated for the whole volume as well as in two smaller boxes in the center. A 3D rendering is provided in Fig. 5.7.

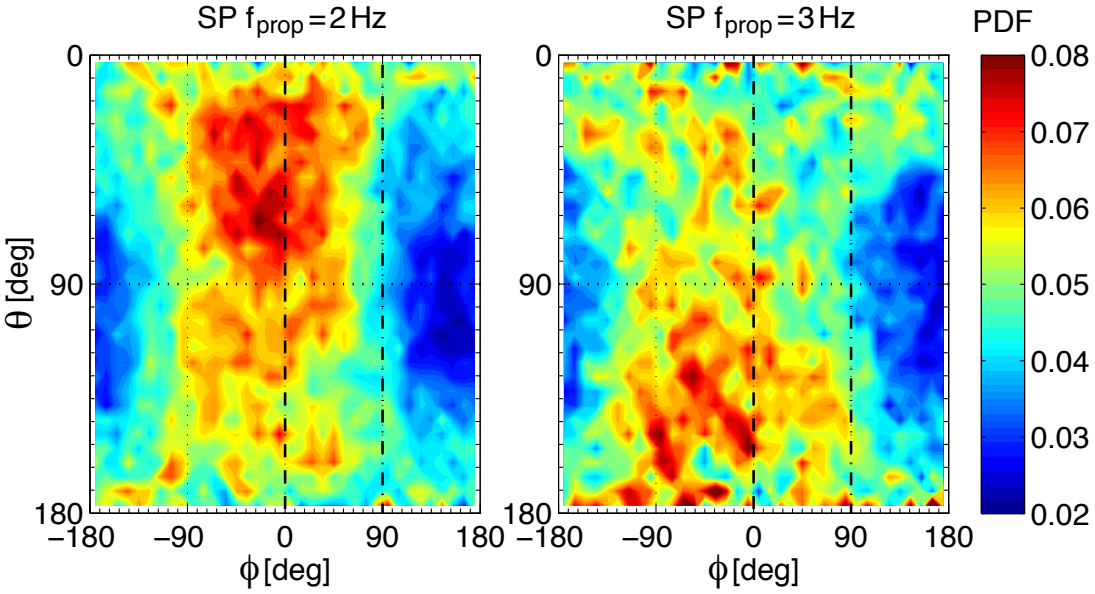

Figure 5.9: Alignment of the angular velocity ω with the Frenet frame, in the case of the instrumented particle at 2 propeller frequencies. One still observes a preferential alignment although the particle is known to be inhomogeneous and in a less viscid fluid than the solid particle.

5.2.3 Influence on the centrifugal force

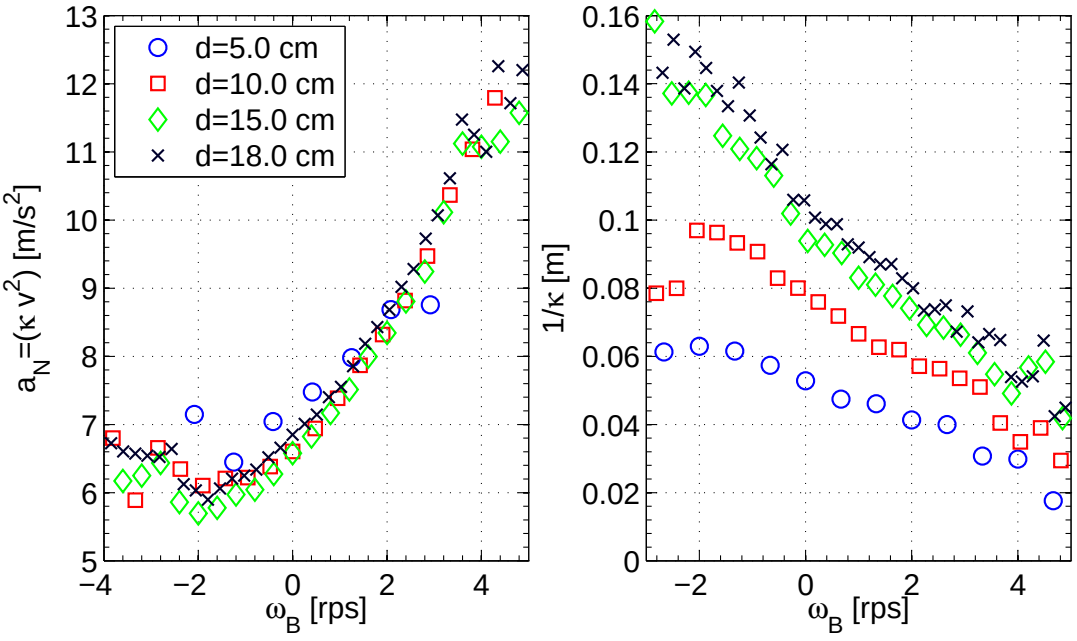

Figure 5.10: Influence of the rotation on the centrifugal force
Left: Normal acceleration, a_N, conditioned on the component of angular velocity parallel to the bi-normal Frenet vector, $\omega_B \equiv \boldsymbol{\omega} \cdot \boldsymbol{B}$.
Right: Average bending of the trajectory, $1/\kappa$, conditioned on ω_B. Note that the variations in radius are much larger than average.
In both cases we test the robustness by restricting the data to smaller boxes of edge length d in the center.

The lift force $\boldsymbol{F}_{\text{lift}} \propto \boldsymbol{\omega} \times \boldsymbol{v}$ expressed in the Frenet coordinate system, suggests a contribution of $|\boldsymbol{v}| \times \omega_B$ to the acceleration(*i.e.* force), a_N. Fig. 5.10 shows the amplitude of the acceleration, a_N, conditioned on the amplitude of ω_B. The averaged normal acceleration conditioned on ω_B increases by 50% from 6 to 9 m/s^2 when the particle rotation varies in the range ± 2 Hz ($= 12$ rad/s). The effect is stronger if ω_B is positive, however, this observation might be biased due to the fact that much less data is available for $\omega_B < 0$ (cf. Fig. 5.8). By restricting the data to smaller regions in the center of the apparatus, we verified that the dependence of a_N on ω_B does not depend on the large scale mean flow of the apparatus (Fig. 5.10). It should be noted that the ratio of normal to lift force

$$\frac{a_N}{a_{\text{Lift}}} = \frac{\kappa\,|\boldsymbol{v}|^2}{\boldsymbol{\omega} \times \boldsymbol{v}} = \frac{\kappa\,|\boldsymbol{v}|}{\omega_B}$$

probes the dependence of curvature κ on ω_B. We therefore investigate the dependence of the bending radius[4] of the trajectory, $1/\kappa$, on ω_B. Over the range $\omega_B = -3$ Hz $\ldots +5$ Hz

[4] Averaging κ corresponds to building the inverse of the harmonic mean of the bending radius.

a clear decrease of the bending radius with increasing ω_B is observed. In other words the particle moves in a tighter spiral trajectory if the rotation is in the sense of the Magnus force.

In agreement with their weak preferential alignment, no clear influence of the rotation on the centrifugal force is found for the instrumented particle.

6 How they fluctuate

A material particle which is advected in flow is *a priori* interacting with the flow. The basic interaction of a material particle can be illustrated by a person's movement in a crowd of people (as they are for example found at German christmas markets or French train stations). In such environments moments alternate where one is being pushed by other people and where one pushes back.

Turning back to the particle, if it is moving faster than the surrounding fluid it has to push it away and decelerates. Likewise, if the particle is slower than flow, it is accelerated. By changing its speed it is exchanging energy with the flow.

In the limit of particle small compared to the smallest scales, the (neutrally-buoyant) particle behaves as a tracer of the fluid motion: Its dynamics are close to that of the flow. For particles (*e.g.* those presented in this thesis), which are much larger than the smallest eddies, the situation becomes complicated. We demonstrate in chapter 5 that the rotation and translation couple in agreement with the lift force $\boldsymbol{F}_{\text{lift}} \propto \boldsymbol{v} \times \boldsymbol{\omega}$. Additionally, a large particle is no longer a tracer of the fluid motions: It has a relative velocity (and acceleration) with respect to its surroundings. As a result, it is sometimes pushes the surrounding fluid and conversely sometimes it looses momentum to the fluid: Energy flows in both directions and we will show that this exchange is characterized by large deviations from its mean.We approach the particle's complex motions from a statistical physics point of view: the *fluctuation theorem* can be used to describe the particle in a turbulent flow as a system in interaction with a heat source and a heat sink.

Our investigation is strongly motivated by an article by Sergio Ciliberto *et al.* [12], where it was shown that the forces acting on an obstacle inside a von Kármán swirling flow obey the fluctuation theorem. In the following we first discuss the kinetic energy of the particle. Then, we test if the dynamics of the particle's kinetic energy are governed by the theorem. We therefore follow tightly the mentioned article.

The fluctuation theorem stems from the mathematical theory of large deviations which has strong links to thermodynamics and the description of chaotic systems [66]. A descriptive analogon of entropy and phase space contraction rate in turbulent flows has yet to be found.

6.1 Kinetic Energy

The total kinetic energy of the particle as such has two contributions: One associated with the translation

$$E_{\text{trans}} = \frac{1}{2} m \boldsymbol{v}^2 \tag{6.1}$$

and one for the rotation

$$E_{\text{rot}} = \frac{1}{2}\boldsymbol{\omega}^T \underline{\underline{\boldsymbol{J}}}\boldsymbol{\omega} \tag{6.2}$$

For a solid, homogeneous sphere of mass m and diameter D_{part} the latter simplifies to $E_{\text{rot}} = \frac{1}{20}\, m\, D_{\text{part}}^2\, \boldsymbol{\omega}^2$ and we showed in section 5.1.2 that their ratio is:

$$\frac{E_{\text{trans}}}{E_{\text{rot}}} = \frac{\frac{1}{2} m\, \boldsymbol{v}^2}{\frac{1}{2}\left(\frac{1}{10} m\, D_{\text{part}}^2\right) \boldsymbol{\omega}^2} \approx 2.5 \left(\frac{R}{D_{\text{part}}}\right)^2 \tag{6.3}$$

Even for the largest particle it is $D_{\text{part}} = \frac{1}{4}R$. Hence, we neglect the contribution of the rotation to the total kinetic energy.

A change in kinetic energy translates to energy being exchanged with the flow. One can thus define an instantaneous *energy exchange rate* $\varepsilon_{\text{v.a}}$:

$$\varepsilon_{\text{v.a}}(t) \equiv \frac{1}{m}\frac{\mathrm{d}}{\mathrm{d}t} E_{\text{trans}}(t) = \boldsymbol{v}(t) \cdot \boldsymbol{a}(t) \tag{6.4}$$

Several questions arise from this equation. The apparatus can be modeled as a thermodynamic system in contact to two thermal reservoirs – the propellers (a heat source) and dissipation (a heat sink). At equilibrium the energy injected equals the energy transferred equals the dissipated energy. One, therefore, expects that the integral over the whole apparatus $\frac{\mathrm{d}}{\mathrm{d}t}\int_{\mathcal{V}} \boldsymbol{v}^2 \mathrm{d}\boldsymbol{x} = 0$ if the flow is homogeneous. In contrast thereto, we focus here on the Lagrangian motion of large particles in a finite measuring volume, where the energy is injected by the propellers outside this region. The particle gains energy in active regions of the flow and along their ensuing trajectory the kinetic energy is dissipated back to the flow until the particle gets pushed by the flow again. In other words, the particle is mostly loosing energy during its motion but we will see strong fluctuations around a small mean value.

It should be pointed out that $\varepsilon_{\text{v.a}}$ is *no* substitute for the common methods based on structure functions as discussed in detail *e.g.* in [52, 24]. We aim here only at investigating the energy exchange of one moving particle with its surrounding fluid by means of the fluctuation theorem and do not propose a new method for obtaining the energy transfer rate. Reginald Hill [24] proposed a method, which computes the mean energy transfer rate from Lagrangian trajectories of tracer particles. However, we are interested in the fluctuations and consequently, his method cannot be used in our context.

6.1.1 Distribution of $\varepsilon_{\text{v.a}}$

We first notice that for all runs $\langle \varepsilon_{\text{v.a}} \rangle < 0$, *i.e.* the particle is in average loosing energy. The mean is small compared to the fluctuations: Its RMS is approximately ten-times the average value $\text{RMS}\,(\varepsilon_{\text{v.a}}) \sim 10\, \langle \varepsilon_{\text{v.a}} \rangle$. When looking on the probability distribution of $\varepsilon_{\text{v.a}}$ we remark that it differs strongly from a Gaussian distribution: it has wide tails and the skewness is order -1. Hence, the particle experiences large fluctuations in kinetic energy

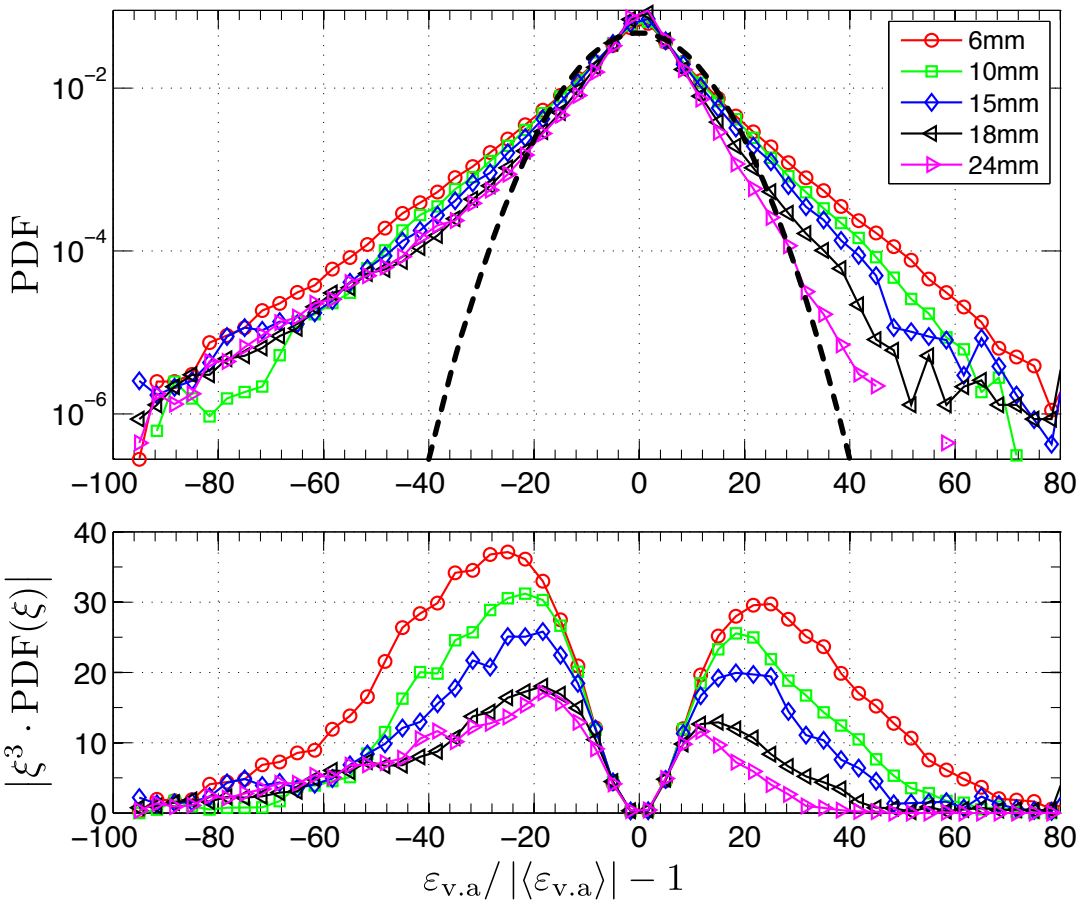

Figure 6.1: Distribution of the energy exchange rate, $\varepsilon_{\mathrm{v.a}} = \boldsymbol{v} \cdot \boldsymbol{a}$, for different particle diameters. The propellers are counter-rotating at $f_{\mathrm{prop}} = 4$ Hz. The dashed curve displays a gaussian distribution, $\varepsilon_{\mathrm{v.a}}$ is has a non-gaussian distribution with wide tails. Note that we plot here the centered PDFs which are normalized in an uncommon way: As suggested by the fluctuation theorem, $\varepsilon_{\mathrm{v.a}}$ is rescaled by its mean instead of its RMS value. Thus, the tails appear ~ 10 times wider than the common normalization.
To demonstrate the skewness ($\langle \varepsilon_{\mathrm{v.a}} \rangle$ is negative) its absolute value is taken: $\varepsilon_{\mathrm{v.a}} / |\langle \varepsilon_{\mathrm{v.a}} \rangle| - 1$. In the lower plot we show $|\xi^3 \cdot \mathrm{PDF}\, \xi|$ in order to demonstrate that the PDF of $\varepsilon_{\mathrm{v.a}}$ is skewed.

along it's trajectory, and it is more likely to push the fluid and thereby loose kinetic energy. Although trivial, this also implies that the particle stops moving shortly after one switches off the motors. In other words, the interaction with the flow drives the particle out of equilibrium. A typical distribution of $\varepsilon_{\mathrm{v.a}}$ is shown in Fig. 6.1.

One can further compare the energy exchange rate, $\varepsilon_{\mathrm{v.a}}$, to the energy injection rate based on the power injected by the motors $\varepsilon_{\mathrm{motors}}$. The latter has been measured at frequencies from $f_{\mathrm{prop}} = 1 \ldots 10$ Hz (cf. Fig. 3.3 in chapter 3). It should be noted that we set $\varepsilon_{\mathrm{motors}} > 0$. As shown in Fig. 6.2 we find that $\langle \varepsilon_{\mathrm{v.a}} \rangle / \varepsilon_{\mathrm{motors}} \sim -0.1$. We further find

that RMS $(\varepsilon_{\text{v.a}})\,/\varepsilon_{\text{motors}}$ is of order 1 with a dependency on the particle diameter and a weak dependency on the propeller frequency f_{prop}. That is consistent with the previous findings for the translation of large spheres, which showed that smaller spheres have a higher acceleration RMS.

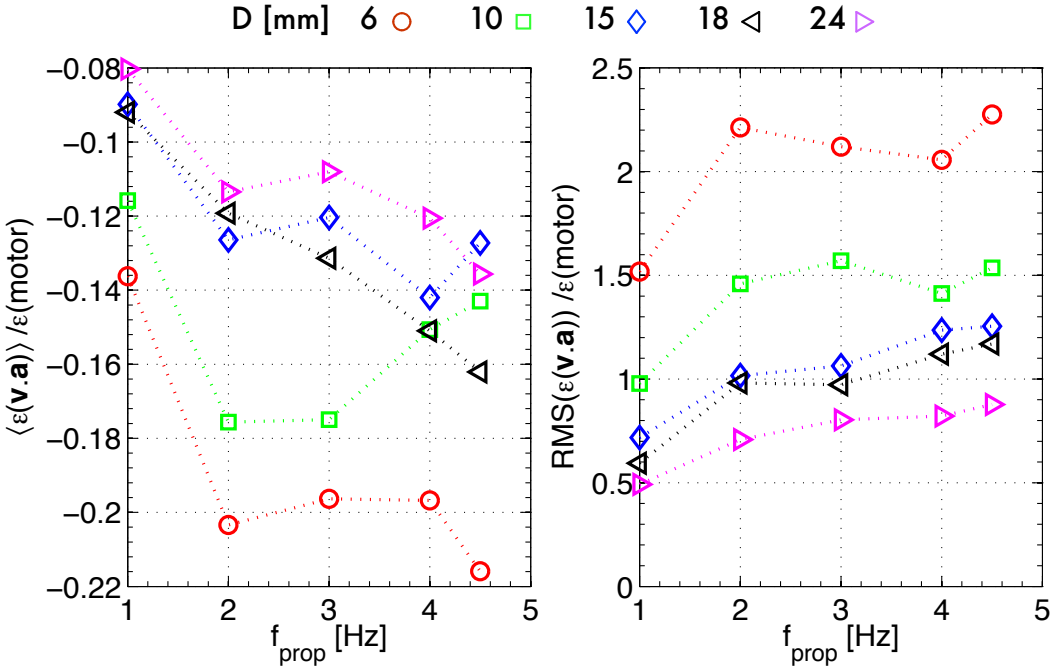

Figure 6.2: Energy exchange rate, $\varepsilon_{\text{v.a}} = \boldsymbol{v} \cdot \boldsymbol{a}$ for different propeller speeds, f_{prop}, and particle diameters.

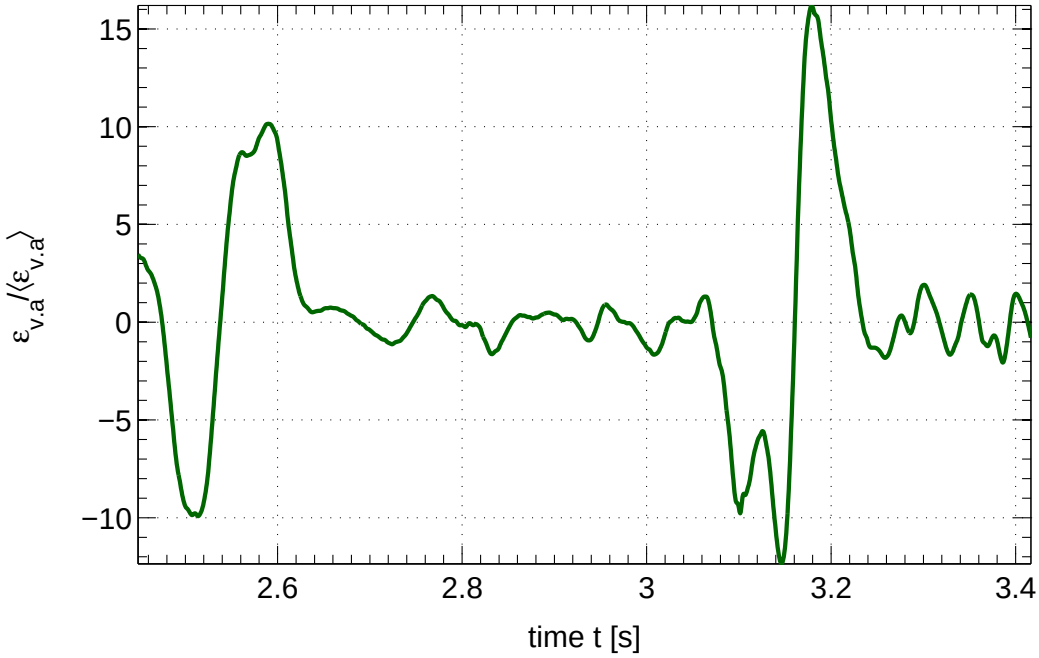

Figure 6.3: A typical time-series of $\varepsilon_{\text{v.a}}(t)$ (normalized by its mean value). The used particle diameter is $D_{\text{part}} = 10$ mm and the propellers are counter-rotating at $f_{\text{prop}} = 4$ Hz. One can see that the energy is flowing in both directions, with a short correlation time and strong events.

6.1.2 Time scales

We now turn to the correlation time of the energy exchange rate, $\varepsilon_{\text{v.a}}$. A typical time-series of $\varepsilon_{\text{v.a}}(t)$ is provided in Fig. 6.3. We observe that energy is flowing in both directions, with a short correlation time and isolated strong events. Also, no significant asymmetry between receiving and giving energy is perceived.

In chapter 4, we saw that the time, $\tau^a_{1/e}$, for which the auto-correlation of acceleration passes $1/e$, increases linear from $\tau^a_{1/e}(6\text{ mm}) = 0.06\,T_{\text{int}}$ to $\tau^a_{1/e}(24\text{ mm}) = 0.13\,T_{\text{int}}$. However, even for the largest diameter $\tau^a_{1/e}$ is smaller than the correlation time of velocity ($\tau^v_{1/e} \sim 0.18$). Now, $\varepsilon_{\text{v.a}}$ is the product of velocity and acceleration: One thus expects that it decorrelates faster than both acceleration and velocity. This is the case: We find that the time when the auto-correlation of $\varepsilon_{\text{v.a}}$ crosses 0 is (almost) the time $\tau^a_{1/e}$ when the correlation function of acceleration passes $1/e$. Similar to the auto-correlation it depends on the particle size, too. As a representative example we plot in Fig. 6.4 the autocorrelation of $\varepsilon_{\text{v.a}}$ for counter-rotating propellers running at $f_{\text{prop}} = 4$ Hz. Summing up, the characteristic time scale of the variations of the energy exchange rate is $\tau_0(\varepsilon_{\text{v.a}}) \sim 0.1\,T_{\text{int}}$.

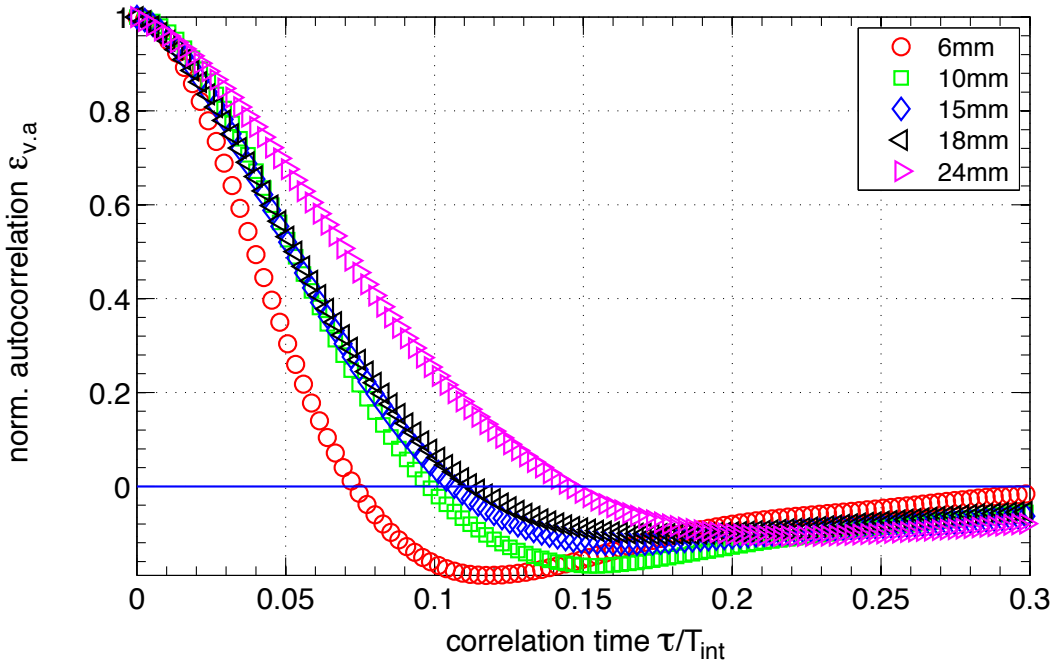

Figure 6.4: Autocorrelation of $\varepsilon_{\text{v.a}}$ for the five particle diameters; here, we show counter-rotating propellers with $f_{\text{prop}} = 4$ Hz. The time when the auto-correlation of $\varepsilon_{\text{v.a}}$ crosses 0 is (almost) the time $\tau_{1/e}$ when the correlation function of acceleration, $\boldsymbol{a}$, passes $1/e$.

6.2 A step-by-step test of the fluctuation theorem

One knows that one has to constantly stir to keep a fluid in motion, and that the flow (in *e.g.* a bowl of soup or a cup of coffee) stops fast after the forcing was stopped. In other words, a flow is only at equilibrium when it does *not* move. On the other hand, turbulence is a far-from equilibrium state, where permanent forcing establishes a stationary flow of energy from the large scales to the small scales. Although the energy injection as such is steady, one observes the well known large variations in velocity and acceleration. However, it is legit to ask if energy can also flow for short times in the reverse direction, *i.e.* going from the small scales to the large scales. This problem is for example addressed (in a readable manner) in [4].

From a more abstract point of view, the second law of thermodynamics tells that no process is possible whose sole result is the transfer of heat from a body of lower temperature to a body of higher temperature[1]. Statistical physics extended this statement such that for short times the second law can be violated and one can observe energy flowing from the cold to the warm. The Gallavotti and Cohen fluctuation theorem considers the dynamics of the energy flux fluctuations in a driven dissipative far-from-equilibrium system [19]. Dissipation causes the phase space of such a system to contract and the rate of contraction is related to the rate at which energy, heat or momentum flows out of the system. As the reversed (cold-to-warm) energy flux is forbidden in the long time average, it investigates the possibility of such a reversed flux by looking at averages computed for larger and larger time scales. It should be noted that the theorem is related to stochastic differential equations. As we saw earlier the energy exchange of large material spheres in a turbulent flow is dissipative with large deviations. We will investigate now if its dynamics are governed by this theorem.

Simple version of the theorem Let j denote a variable related to this energy flux; in our case $j \equiv \varepsilon_{\text{v.a}}$. One then defines the sliding average of the flux normalized by its mean, *i.e.* :

$$Y_\tau = \frac{1}{\tau}\int_t^{t+\tau} \frac{j(t')}{\langle j \rangle}\mathrm{d}t' \tag{6.5}$$

Note that we non-dimensionalize the filter width, τ, by the integral length scale, T_{int}. The probability density function of the filtered flux Y_τ is then defined as:

$$\pi_\tau(Y) = \mathrm{PDF}\left(Y_\tau\right) \tag{6.6}$$

Note that the second law of thermodynamics dictates $\pi_\infty(Y) = \delta\left(Y-1\right)$, with δ the Delta function. The theorem now states that if τ is larger than a characteristic time scale of the system the shape of the PDF comports as

$$\ln\left(\frac{\pi_\tau(+Y)}{\pi_\tau(-Y)}\right) = \tau\,\sigma\,Y \tag{6.7}$$

[1] Rudolf Clausius: "Es gibt keine Zustandsänderung, deren einziges Ergebnis die Übertragung von Wärme von einem Körper niederer auf einen Körper höherer Temperatur ist."

where σ is related to the phase space contraction rate and its inverse is sometimes called a temperature. The proportionality $\ln\left(\pi_\tau(+Y)/\pi_\tau(-Y)\right) \propto Y$ is thus imposing the general shape of the PDF of the energy flux for a given filter width τ. Eq. (6.7) further tells that the PDF becomes linearly narrower and more skewed with increasing filter width, τ. Rearranging Eq. (6.7) yields

$$\sigma = \frac{1}{\tau Y} \ln\left(\frac{\pi_\tau(+Y)}{\pi_\tau(-Y)}\right) \tag{6.8}$$

If the theorem is satisfied, σ is independent of Y and τ, *i.e.* $\sigma(Y,\tau) = \sigma$.

6.2.1 π_τ

We first investigate how the PDF of the energy exchange rate, $\varepsilon_{\text{v.a}}$, evolves with filtering. In order to avoid showing 40 plots, we illustrate the procedure on the 10 mm particle in a counter-rotating flow at $f_{\text{prop}} = 4$ Hz. It was verified that the other runs behave in a similar manner.
Inserting $\varepsilon_{\text{v.a}}$ into Eq. (6.5) and Eq. (6.6) yields the PDF of the filtered $\varepsilon_{\text{v.a}}$:

$$\pi_\tau(Y) = \text{PDF}\left(\frac{1}{\langle\varepsilon_{\text{v.a}}\rangle\ \tau}\int_t^{t+\tau} \varepsilon_{\text{v.a}}(t')\mathrm{d}t'\right) \tag{6.9}$$

In our setup we have many trajectories of different length, and a priori one should apply the sliding average to each track that is longer than the filter width and reject all data biased by the track ends. Unfortunately, this leads to a strong reduction in data and we test also a "quick&dirty" method, where all trajectories are concatenated to one large track. To check if this concatenating does not introduce artifacts, we further apply the procedure after shuffling the concatenated track. The implications are discussed soon.

Fig. 6.5 depicts the PDF $\pi_\tau(Y)$ with $\tau = 0.2$ and $1\,T_{\text{int}}$ for the three different ways of filtering/handling the data. Since $\langle\varepsilon_{\text{v.a}}\rangle < 0$, the PDF is mirrored and has now positive skewness. In agreement with Eq. (6.7) and intuition, $\pi_\tau(Y)$ becomes narrower with increasing filter width. Furthermore, we observe a clear reduction in data for the trajectory wise filtering and statistical convergence is not given for trajectory-wise filtering with $\tau > T_{\text{int}}$, but one integral time scale is still accessible. The theorem mentions a characteristic time scale which is close to the correlation time of the energy exchange rate: $\tau_0(\varepsilon_{\text{v.a}}) \sim 0.1\,T_{\text{int}}$. Thus, one integral time scale corresponds to about ten characteristic time scales.

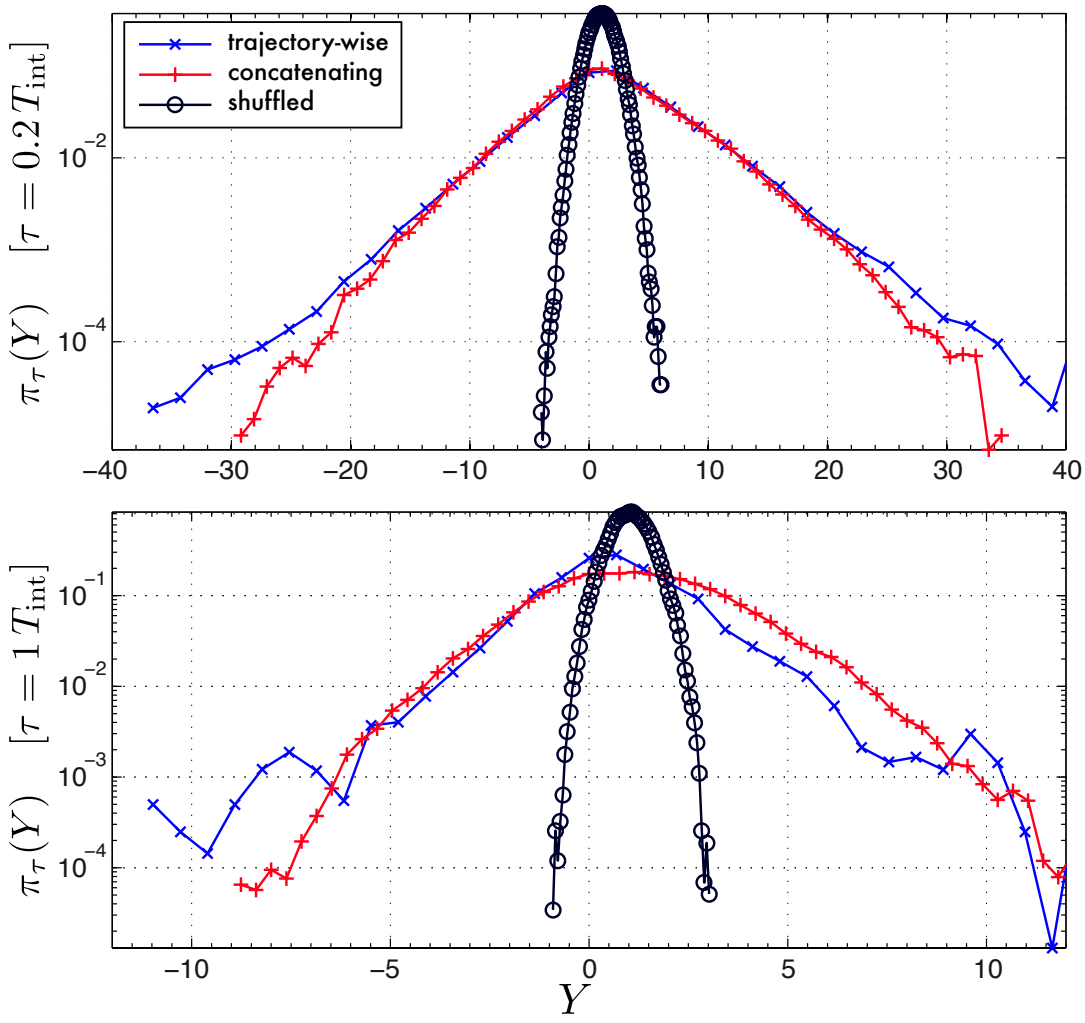

Figure 6.5: The PDF $\pi_\tau(Y)$ of the filtered energy exchange rate for a filter width of $\tau = 0.2\,T_{\mathrm{int}}$ and $1\,T_{\mathrm{int}}$ [counter-rotating propellers, $D_{\mathrm{part}} = 10$ mm, $f_{\mathrm{prop}} = 4$ Hz]. Three ways of handling to the data are tested:

– The sliding average is applied to each track that is sufficiently long leading to a strong reduction in data.

– The trajectories are concatenated to one large track.

– The data of the concatenated track is shuffled.

Adequate binning was chosen to achieve converged statistics. In all three cases, we observe that the PDF become narrower and more skewed with increasing filter width, τ. However, trajectory-wise and concatenating method deviate stronger with increasing filter width.

6.2.2 FIR filter and their implications on Lagrangian data

The sliding average of window length τ belongs to the family of finite impulse response filters. That means nothing which happens before the beginning of the filter window, does influence its output. A lower cutoff frequency (*i.e.* more smoothing) can only be achieved by increasing the filter width. This is different to Infinite Impulse Response (IIR) low-pass filters (*e.g.* Butterworth filters), where one adjusts the cutoff frequency without changing the filter width.
It is trivial that a filter necessitates a number of data points larger than its window length. In other words, for a filter width of $1\,T_{\text{int}}$ only tracks, which are longer than $1\,T_{\text{int}}$, can be used. Although this does not pose a problem for many Eulerian measurement techniques, where one traces a quantity (*e.g.* pressure, velocity or temperature) locally over extremely long times, it is suboptimal for Lagrangian tracking techniques. There, the acquisition time is mainly limited by the time a particle stays in the observation volume. Thus, one can have an ensemble of tracks with different (temporal) length. But without periodic boundary conditions it is (almost) impossible to follow one particle over very long time. Filtering with a window length of $\tau = T_{\text{int}}$ removes one integral time from each track and all tracks which are shorter than $1\,T_{\text{int}}$ are excluded from the data set. We find that in general the probability of a track length decays exponentially and that tracks longer than $3\,T_{\text{int}}$ are extremely rare. To illustrate that we provide the histogram of counter-rotating forcing with $f_{\text{prop}} = 4$ Hz in Fig. 6.6. In our experiment the maximum filter width is limited to $\lesssim 1\,T_{\text{int}}$.
In order to overcome this limitation, one can also concatenate all the trajectories, construct one giant trajectory and then compute the moving average on this track. Obviously, much more data is available in this method. This "quick & dirty" method works suspiciously well. Thus, one has to verify if concatenating is legit and does not introduce artifacts. An extreme way of concatenating is to shuffle the data points. It is clear that this operation leaves PDF($\varepsilon_{\text{v.a}}$) unaltered but removes all correlation (and thus the underlying information of the flow) within $\varepsilon_{\text{v.a}}$, *i.e.* the dataset becomes delta-correlated. Consequently, the PDF of the filtered dataset will differ from the other two methods, which are both not delta-correlated.

The terms *trajectory-wise*, *concatenating* and *shuffled* are employed for the three different ways of filtering/handling the data.

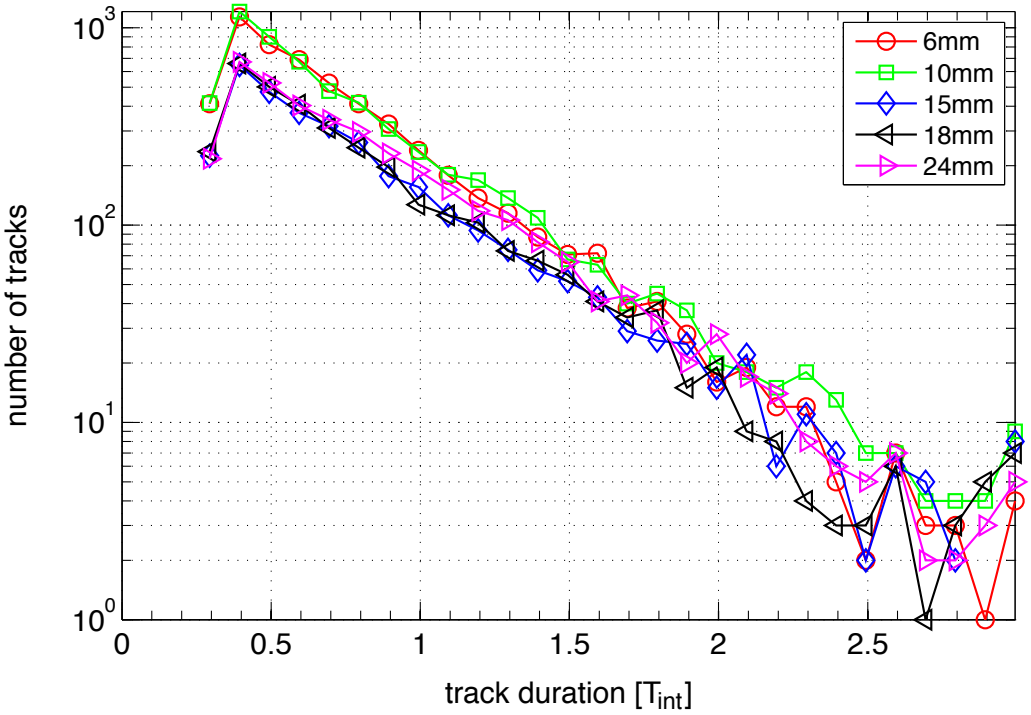

Figure 6.6: Histogram of the track length, [counter-rotating propellers, $f_{\text{prop}} = 4$ Hz]. The probability of a track length decays exponentially. The moving average filter, which is needed for the fluctuation theorem, can use less and less data with increasing window width.

6.2.3 Shape of π_τ

We now test the fluctuation theorem on the 10 mm particle in a counter-rotating flow at $f_{\text{prop}} = 4$ Hz. The PDF for two different filter widths were depicted earlier in Fig. 6.5. Rearranging Eq. (6.7), the fluctuation theorem states for τ larger a characteristic time that:

$$\Xi(Y,\tau) \equiv \frac{T_{\text{int}}}{\tau} \ln\left(\frac{\pi_\tau(+Y)}{\pi_\tau(-Y)}\right) = \sigma \cdot Y = \Xi(Y) \tag{6.10}$$

Consequently:

$$\sigma = \frac{1}{Y}\frac{T_{\text{int}}}{\tau} \ln\left(\frac{\pi_\tau(+Y)}{\pi_\tau(-Y)}\right) \tag{6.11}$$

In other words, the fluctuation theorem requires that $\Xi(Y,\tau)$ is a straight line passing through 0 and $\sigma(Y,\tau) = \Xi(Y,\tau)/Y$ is independent of Y and τ.

Fig. 6.7 provides $\Xi(Y,\tau)$ for the trajectory-wise and concatenating method. It further contains an estimate of σ for the latter method.

For both methods $\Xi(Y)$ forms an (approximately) straight line which passes through 0. However, the slope depends strongly on the way the data is handled: For $\tau \geqslant \frac{1}{2}T_{\text{int}}$ we

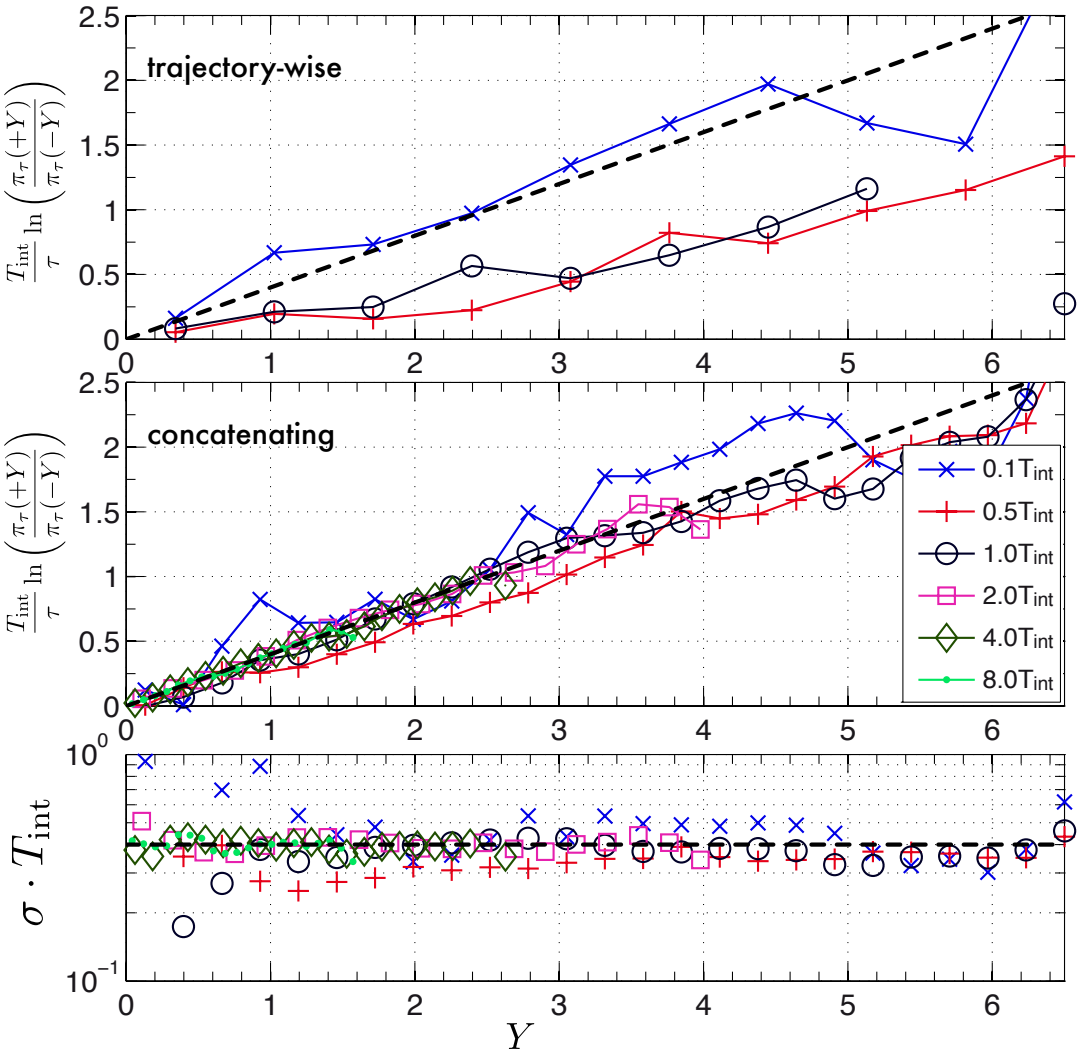

Figure 6.7: Evolution of the shape of π_τ with the filter width [counter-rotating propellers, $D_{\mathrm{part}} = 10$ mm, $f_{\mathrm{prop}} = 4$ Hz]. The dashed line corresponds to $\sigma = 0.4$ in all 3 subfigures.

find slopes of 0.2, 0.4 and 10 for trajectory-wise, concatenating and shuffled, respectively. Hence, concatenating is not a legit work-around to access longer filter widths.

We applied the procedure to all (co- and counter-rotating) runs: Unfortunately the statistics did not converge in some runs and in general only rough estimates of the slope can be obtained. Nevertheless, we observe that:

> The fluctuation theorem is *not* satisfied for co-rotating impellers.

> But for counter-rotating driving we find evidence that the dynamics of $\varepsilon_{\mathrm{v.a}}$ are governed by the fluctuation theorem.

> When normalizing σ with the propeller speed (*i.e.* the integral time scale), it is

$\sigma \cdot T_{\text{int}} \approx 0.1 - 0.4$. In other words, $\sigma \propto f_{\text{prop}}$.

> The fluctuation theorem is clearer and more pronounced for smaller particles diameters and unfortunately the results for the 24 mm particle did not allow any conclusion. Partially, this size effect can be attributed to the higher amount of data points for smaller particles (cf. Fig. 6.6). Surprisingly, no significant dependency of σ on the particle diameter is found.

6.3 Summary

In this chapter, we investigated the dynamics of the kinetic energy of the particle. We find that the energy exchange rate is non-gaussian distributed: The PDF shows wide tails, negative skewness, small negative mean and a standard deviation 10 times larger than the mean. Additionally, the energy exchange rate decorrelates within $\sim \frac{1}{10}$ of the integral time scale. Thus, the energy exchange of the sphere with the fluid falls within the mathematical theory of large deviations [66]. We, therefore, tested if the dynamics of the energy exchange are governed by the fluctuation theorem [19, 4, 12, 28]. Our procedure was similar to [12], where it was demonstrated that the force acting on a fixed obstacle in a von Kármán flow fluctuates as stated in the theorem. Here, we investigated a freely moving sphere in a turbulent flow, which conceptually different from the force acting on a fixed object as the sphere explores the whole volume. Two ways – co and counterrotating – of driving the flow were tested. We find that the fluctuation theorem is not satisfied for co-rotating impellers, but we have first positive evidence for the counter-rotating driving – *i.e.* the energy exchange of the sphere with the fluid is governed by the fluctuation theorem if the propellers are counter-rotating. We estimate the phase space contraction rate, σ, as about $0.2\,T_{\text{int}}^{-1}$ – *i.e.* $\sigma \propto f_{\text{prop}}$. Moreover, no significant influence of the particle diameter is observed but it became evident that more data and more importantly longer trajectories are needed. Also, we did not perform a stringent analysis if the energy exchange is coupled to the other particles which were in the box at the same time. Though, a first inspection revealed nothing remarkable.

It is remarkable that albeit both flow configurations are clearly turbulent, the theorem is only observed for the counter- but not for the co-rotating propellers. At the same time, we know that the mean flow differs strongly between the forcings. We thus suspect that the fluctuation theorem is related to the large scale structure.

The fluctuation theorem states that σ is related to the phase space contraction rate. To illustrate that rather abstract quantity one can ask what happens if the forcing suddenly stops: If the motors are running, the injected energy equals the dissipation and the phase space does not contract. However, it contracts the moment the forcing disappears. Assuming a simple exponential decay $\mathcal{V}(t) \sim \mathcal{V}_0 \exp(-\sigma \cdot t) \approx \mathcal{V}_0 \exp(-0.2/T_{\text{int}} \cdot t)$ tells that the flow stops within 20 to 30 integral time scales. This is close to our observations.

7 An instrumented particle measuring Lagrangian acceleration

Fundamental fluid dynamics research in the lab consists of an interplay of suitable flow generation devices, working fluids, measurement techniques and analysis. However, in the world outside the lab one is often limited: The apparatus comes as it is, providing no or little access for probing the flow. Even if the fluid is transparent, the injection of tracer particles might be still not allowed or unsuitable due to bio-medical- or food regulations, or the chemical properties of the fluid.

At the same time a good understanding of the flow and the mixing within the apparatus is crucial for optimizing both its output and energy consumption. Although Eulerian measurements are well-known and largely available, Lagrangian measurement techniques have proven to give insights on the flow from a different, promising perspective [65].

Historically, similar problems where encountered in oceanography and meteorology: A simple local measurement on ground level or the surface of the sea does tell little about the ocean or the atmosphere. Therefore, in these fields ocean floaters and weather balloons were developed. These instrumented vessels float in air or water , respectively and they contain a series of instruments (*e.g.* for temperature and pressure) plus a transmission system and a battery to work autonomously. As one can imagine, they hardly fit on a lab bench; nevertheless, they are small compared to the large scales of the targeted flow.
In 2007 Jean-François Pinton, Yoann Gasteuil, Woodrow Shew and others [59, 21] presented an *instrumented particle* measuring temperature that is suitable for convection experiments in the lab. Its working principle is close to an ocean floater: A small plastic capsule with embarked electronics has thermistors on its surface whose resistance is modulated on a carrier radio frequency. The signal is then received with an antenna outside the experiment, demodulated and converted into the measured physical temperature. The ensemble of capsule, thermistors, battery, and transmission circuitry is $\sim$ 16 mm large, neutrally buoyant in water, operates autonomously for several hours and transmits the temperature in real time as it is advected with the flow. Hence, it falls into the family of Lagrangian measurement techniques.

Here, we present a new instrumented particle, which continuously transmits its Lagrangian three-dimensional acceleration – *i.e.* it measures the forces acting on it. In contrast to the swimming thermometer, which was designed for convection experiments, this particle is intended for turbulent flows and more specifically for the characterization of devices where optical measurement techniques are not applicable. Nevertheless, the basic construction is similar: a round, leak-tight plastic capsule contains battery, digitizing and radio transmission system and a 3D accelerometer. The density of the ensemble can be adjusted in

a range of $0.8 - 1.4$ g/cm^3 and the sphere is 25 mm in diameter. Thanks to its radio transmission it is suitable for opaque fluids or apparatuses without access for optical measurement techniques. Its continuous operation is advantageous over Particle Tracking Techniques which have to operate in chunks as the memory of the tracking cameras is necessarily limited. Moreover, the particle might be allowed in pharmaceutical mixers if it passes the regulations of the CE mark for medical devices[1].

However, as the particle is advected in a flow it rotates and consequently continuously changes its orientation with respect to the laboratory frame. Thereby the signals of the accelerometer are altered in a non-trivial way. One is therefore in need of a detailed characterization and methods which extract meaningful information about the flow from its acceleration signals. This is addressed twofold: We demonstrate how some quantities such as correlation times and the moments of the acceleration can be derived directly from the signals. As a cross-check these quantities are compared against the motion of large, solid spheres.
In order to get a better understanding of its motion and to verify that its transmitted acceleration is well related to its motion, we apply our six-dimensional tracking method to track the particle's position and absolute orientation while simultaneously acquiring its Lagrangian acceleration signal. The absolute orientation is a crucial step here, as it enables us to re-express the Lagrangian acceleration in the coordinate system of the tracking system. Hence, we can compare these independent measurements.

This chapter is organized as follows:

- First, we present the instrumented particle and additional techniques needed for its characterization (section 7.1).
- We then present an analysis of the results obtained in two different mixers. Here, the necessary methods are developed and tested (section 7.2).
- Finally, we show results of the tracking of position and orientation of the instrumented particle while simultaneously recording its acceleration signal (section 7.4).

Two mixers – a von Kármán mixer (**KLAC**) and the Lagrangian Exploration Module (**LEM**) – are used in this chapter. They are described briefly in Fig. 7.1 and in more detail in chapter 3.1 and annex A.1.

In contrast to the experiments with Poly-Amid spheres, we adjust the weight of the particle instead of the density of the fluid. Thus, the working fluid in this chapter is de-ionized *water* at 20 °C.

[1] Parts of the requirements are that the particle is always extractable in one piece from the mixer and that it survives sterilization. The approval procedure concerns only smartINST and is not further discussed in this document.

KLAC

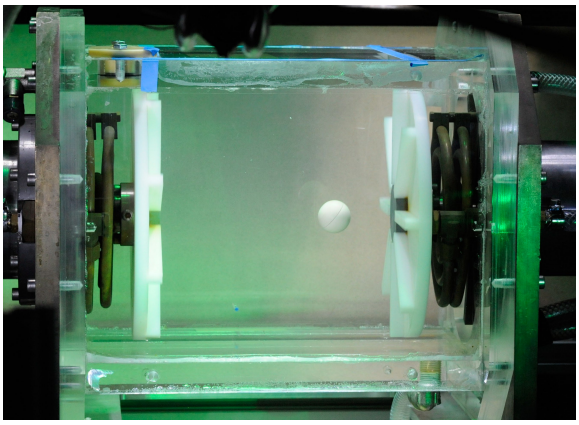

LEM

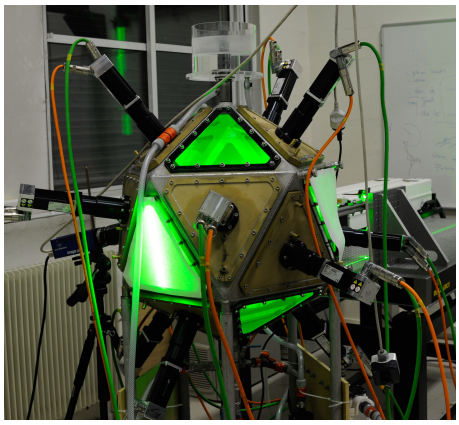

Figure 7.1: The mixers used for the characterization of the instrumented particle. Most experiments (including the combined measurement with the 6D-tracking) were performed in a square von Kármán flow, the so-called **KLAC**; the sphere in the image is a smartPart. The flow was driven with *counter*-rotating and *co*-rotating impellers. An instrumented particle was injected into the Lagrangian Exploration Module (**LEM**), too. The green light in the picture stems from a laser which was switched on only for its beauty.

7.1 An instrumented particle

The apparatus described in the following is designed and built by smartINST S.A.S., a young startup situated on the ENS de Lyon campus. It builds mainly on the work of Yoann Gasteuil during his thesis [20], the particle which measures temperature [21, 59] as well as developments carried out in the ENS Lyon. The device consists of:

- an instrumented particle (the so-called *smartPART*): a spherical particle which embarks an autonomous circuit with 3D-acceleration sensor, a coin cell and a wireless transmission system, and
- an antenna, which is connected to
- a data acquisition center (the so-called *smartCENTER*), which acquires, decodes, processes and stores the signal of the smartPART.

The system smartPART and smartCENTER enables us to measure the three dimensional acceleration vector acting on the particle in the flow. The received signals can be displayed, analyzed and stored for further processing.

7.1.1 Design & Technical Details

7.1.1.1 Sensor

The central component of the particle is the ADXL 330 (Analog Device) – a three axis accelerometer. It belongs to the category of micro-electro-mechanical systems (MEMS). Each of the three axes returns a voltage proportional to the force acting on a small, movably mounted mass-load suspended by micro-fabricated springs (see Fig. 7.3). The three axes of the ADXL 330 are decoupled and form an orthogonal coordinate system attached to the chip package. From this construction arises a permanent measurement of the gravitational force/acceleration $\boldsymbol{g} \equiv 9.8\ \mathrm{m/s^2} \cdot \hat{\boldsymbol{e}}_g = g \cdot \hat{\boldsymbol{e}}_g$. Each axis has a guaranteed minimum full-scale range of $\pm 3g$; however, we observe a typical range of $\pm 3.6g = 35\ \mathrm{m/s^2}$ per axis. By design the $x-$ and $y-$axis have an internal cutoff frequency of 1.6 kHz whereas the $z-$axis filters at 0.5 kHz. The sensor has to be calibrated to compute the physical accelerations from the voltages of the accelerometer.

7.1.1.2 smartPART

The signals from the ADXL 330 are first-order low-pass filtered at $f_c = 160$ Hz and then digitized at 12 bits and 316 Hz sampling rate. A multiplexer prior the signal digitization induces a small time shift between the components of 0.64 ms. The output is then reshaped into small packets and send via radio frequency. A free ISM[2] band at 433.9 MHz is used as the carrier frequency. The ensemble is powered by a coin cell. A voltage regulator ensures a stable supply voltage and thus a constant quality of the measurement. A

[2] That are radio frequency bands which are reserved for industrial, scientific and medical equipment. Devices operating in this range must tolerate the radio signals from other devices.

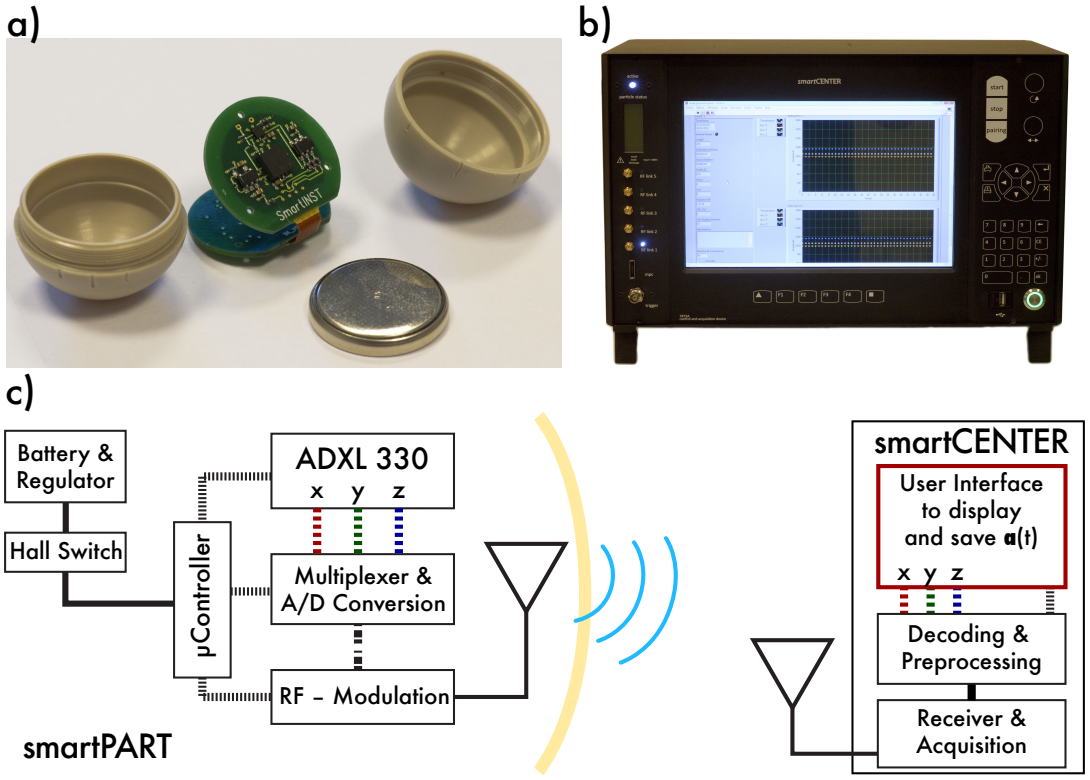

Figure 7.2: **a)** & **b)**: the instrumented particle (so-called *smartPART*) and its data control acquisition unit (so-called *smartCENTER*). The coin cell is 20 mm in diameter. Cables and antenna are not shown here. The diagram below sketches how the acceleration measurement is transmitted to and processed at the smartCenter.

Hall switch allows one to power-down most components and thereby drastically increase the life time of the battery. A sketch explaining how the different components are related is provided in Fig. 7.2.

The ADXL 330 is soldered to the printed circuit board such that it is situated close to the geometrical center of the particle. The particle itself is spherical with a diameter of 25 mm. The walls are made of Polyether-ether-ketone (PEEK) which is known for its excellent mechanical and chemical robustness. It is leak-proof and its density can be matched by adding extra weight to the interior to fluids to a range of $0.8 - 1.4$ g/cm^3. A relative density match of better than 10^{-4} is achievable. The particle is thus suited for most experiments in water and water-based solutions. Depending on the power needed to transmit the acceleration signals, the life time ranges from 12 to 36 hours.

Summing up, the smartPART transmits in real-time the accelerations acting on the particle as it is advected in the flow. The accelerations are observed in a moving and rotating coordinate system and consist of four contributions: gravity, translation, noise and possibly a weak contribution of the rotation around the center of the particle itself.

It should be noted that the mass distribution inside the particle is neither homogeneous nor isotropic. Additionally, the density matching is achieved by adding Tungsten paste to

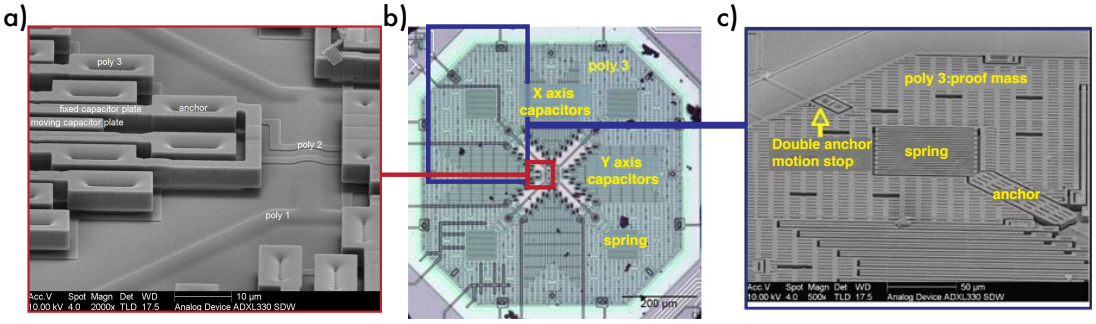

Figure 7.3: Interior of the ADXL 330 accelerometer [image based on [1, 2]], a mass load is supported by springs (parts **b** & **c**). The x and y digitated sense capacitors measure lateral movement (part **a**), whereas the $z-$axis is formed between the proof mass and the underlying plate. That is also the reason for the lower resolution in z.

the inside of the two capsules. It is therefore possible that the particle is out-of-balance, *i.e.* the center of mass does not coincide with the geometrical center. The imbalance can be adjusted to some extent as sketched in Fig. 7.4. A particle, which is out-of-balance, has a strong preferred orientation and wobbles similar to a kicked physical pendulum. We therefore assume (and prove later) that its movement deviates from the classical case of solid homogenous particles. For that reason most experiments are performed with a well balanced particle which rotates easily in the flow. In section 7 we show that the free rotation is actually desirable. The particle's inertia is best described by a heavy disk of 20 mm diameter (the battery), a spherical shell and patches of tungsten paste. One of the eigen-axes of inertia coincides (approximately) with the $z-$axis of the accelerometer. The other two are within the $x-y$ plane due to the rotational symmetry.

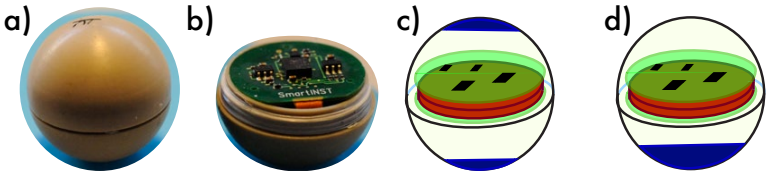

Figure 7.4: Possible mass distributions of the particle. Its inertia consists mainly of a disk and a spherical shell; however, the density adjustment also sets the imbalance of the particle (parts **c** & **d**). Most of the experiments with the smartPART are done in configuration **c**.

7.1.1.3 smartCENTER

The signals from the smartPART are received by an antenna connected to a radio reception, processing and display unit: the so-called *smartCENTER*. Once the raw signal is acquired the smartCENTER decodes in real-time the packets to obtain the raw voltages of the ADXL 330. The physical acceleration, $\boldsymbol{a}_{SP}$, sensed by the smartPart can then be

computed according to Eq. (7.1):

$$\boldsymbol{a}_{SP} = \begin{pmatrix} a_1 \\ a_2 \\ a_3 \end{pmatrix} = \begin{pmatrix} (A_1 - O_1)/S_1 \\ (A_2 - O_2)/S_2 \\ (A_3 - O_3)/S_3 \end{pmatrix} \tag{7.1}$$

where A_i, O_i and S_i are the measured raw signal, the offset and the sensitivity of each axis, respectively. Offset and sensitivity have to be calibrated beforehand; the procedure is described in section 7.1.2. The resulting time-series are saved for further processing.

7.1.1.4 Contributions to the Acceleration

The acceleration sensor measures the forces acting on it as it moves in the flow. The following contributions can be identified:

Gravity By construction, gravity $\boldsymbol{g}$ is always contributing to $\boldsymbol{a}$. Since the particle is a priori oriented arbitrarily in space, $\boldsymbol{g}$ is projected to all 3 axes. Rotations of the sensor around the axis of gravity do not change the measured signal.

Translation The Lagrangian acceleration $\boldsymbol{a}_{trans} = \frac{d^2}{dt^2}\boldsymbol{x}(t)$ will be projected onto the sensor. However the projection changes if the sensor is rotating.

Rotation If the sensor is placed by $\boldsymbol{r}$ outside the geometrical center of the sphere one observes two centrifugal forces: $\boldsymbol{a}_{cf} = \boldsymbol{\omega} \times (\boldsymbol{\omega} \times \boldsymbol{r})$ and $\boldsymbol{a}_{cc} = \left(\frac{d}{dt}\boldsymbol{\omega}\right) \times \boldsymbol{r}$. According to the technical drawing it is $\boldsymbol{r} \approx 3 \text{ mm} \cdot \hat{e}_z$.

Coriolis The construction of the ADXL 330 and the fact that the circuit is fixed within the sphere ensure that the Coriolis force is zero.

Noise & spikes In ideal situations the smartPart has a noise of less than $0.01g$ for each axis, which can be handled by a low pass filter. Wrong detections appear as strong deviations from the signal and are hard to distinguish from high acceleration events due to the turbulent flow or contacts with *e.g.* the propellers.

Orientation of the sensor The orientation of the particle is a priori changing as it is advected in the flow. The orientation of the sensor can be described by an absolute orientation with respect to a reference coordinate system, $\underline{\underline{\boldsymbol{R}}}(\underline{\theta}(t))$, plus a constant rotation matrix, $\underline{\underline{\boldsymbol{R}}}_{\text{TS}}$, which handles the orientation of the sensor with respect to an outer texture as well as the arbitrary choice of the reference frame. If needed one can incorporate $\underline{\underline{\boldsymbol{R}}}_{\text{TS}}$ into the time-series of absolute orientation $\underline{\underline{\boldsymbol{R}}}(\underline{\theta}(t))$. For simplicity $\underline{\underline{\boldsymbol{R}}}_{\text{TS}} = \underline{\underline{\mathbb{1}}}$ in most cases.

Combining the different terms yields:

$$\boldsymbol{a}_{SP} = \underline{\underline{\boldsymbol{R}}}_{\mathrm{TS}}^{T}\, \underline{\underline{\boldsymbol{R}}}\left(\underline{\theta}\right)^{T} \left[\boldsymbol{g} + \frac{\mathrm{d}^2}{\mathrm{d}t^2}\left(\boldsymbol{x}(t) + \boldsymbol{r}\right) + \boldsymbol{\omega} \times \left(\boldsymbol{\omega} \times \boldsymbol{r}\right) + \frac{\mathrm{d}\boldsymbol{\omega}}{\mathrm{d}t} \times \boldsymbol{r}\right]$$

and

$$\underline{\underline{\boldsymbol{R}}}\left(\underline{\theta}\right) \underline{\underline{\boldsymbol{R}}}_{\mathrm{TS}}\, \boldsymbol{a}_{SP} = \boldsymbol{g} + \frac{\mathrm{d}^2}{\mathrm{d}t^2}\left(\boldsymbol{x}(t) + \boldsymbol{r}\right) + \boldsymbol{\omega} \times \left(\boldsymbol{\omega} \times \boldsymbol{r}\right) + \frac{\mathrm{d}\boldsymbol{\omega}}{\mathrm{d}t} \times \boldsymbol{r} \tag{7.2}$$

Extracting meaningful information on the flow from the smartPart is explained later in section 7.2.

7.1.2 Calibration & Resolution

The offset and sensitivity of the ADXL 330 have to be calibrated in order to convert the measured voltages into a physical acceleration. The axes of the accelerometer form an orthogonal coordinate system according to Eq. (7.1). At rest one always observes gravity projected on the sensor at an arbitrary orientation. The observed raw values define consequently a translated ellipsoid :

$$\boldsymbol{a}_{SP} \cdot \boldsymbol{a}_{SP} = \frac{(A_x - O_x)^2}{S_x^2} + \frac{(A_y - O_y)^2}{S_y^2} + \frac{(A_z - O_z)^2}{S_z^2} = |\boldsymbol{g}|^2 = 1 \tag{7.3}$$

For simplicity $|\boldsymbol{g}| \equiv 1$. Eq. (7.3) can be arranged to

$$1 = \zeta_1\, A_x^2 + \zeta_2\, A_y^2 + \zeta_3\, A_z^2 - 2\zeta_4\, A_x - 2\zeta_5\, A_y - 2\zeta_6\, A_z \tag{7.4}$$

with $\zeta_1 \ldots \zeta_6$ six parameters containing offset and sensitivity. A sufficient number of measurements with different orientation defines a set of equations which is solved using a linear least squares technique. 20 to 30 data points are necessary to certainly obtain stable results. Offset and sensitivity are then computed from the resulting $\zeta_1 \ldots \zeta_6$. The calculations can be found in appendix B.6.
We found that a particle at rest has an average noise of $\sigma_x = \sigma_y \approx 2.3[q]$ and $\sigma_z \approx 3.5[q]$. $1\,q$ is the quantization of the digitizer. In physical units that corresponds to $\sigma_x = \sigma_y = 0.006g$ and $\sigma_z = 0.008g$ and $|\boldsymbol{\sigma}| = \sqrt{\sum_i \sigma_i^2} = 0.012g$. An analysis using the residuals showed an slightly higher resolution of

$$\sigma_x = \sigma_y = 0.005g\ ,\ \sigma_z = 0.003g \quad \text{and} \quad |\boldsymbol{\sigma}| = 0.008g\ . \tag{7.5}$$

These values are, thus, the absolute errors of our measurement. A second, different calibration method based on geometrical construction results in a comparable resolution.

7.1.2.1 Reproducibility & Robustness

The temperature in an experiment is not necessarily fixed. When for example monitoring an industrial mixer, the temperate can vary within short time by several Kelvin. Moreover, the slowly discharging of the battery might induce a slow drift.

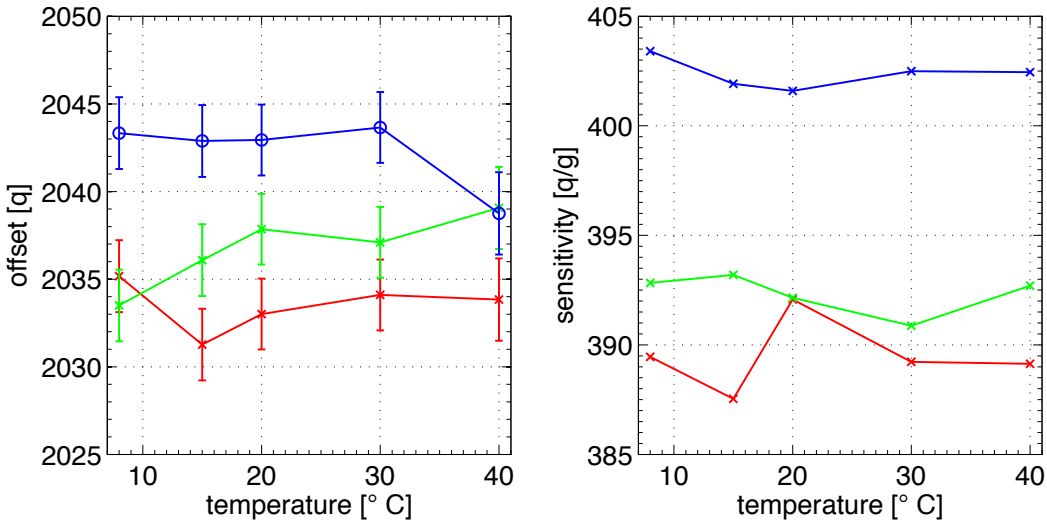

Figure 7.5: Temperature dependence of a sample smartPART; the x, y, z component are red, green, and blue, respectively.

The ADXL 300 has amongst other things been chosen for its weak temperature dependance: its offset varies by typically $1\frac{\mathrm{m}g}{^\circ C} \approx 0.4\frac{q}{^\circ C}$ and its sensitivity by $0.015\frac{\%}{^\circ C}$. To check that the smartPART – *i.e.* the ensemble of accelerometer, digitizing and radio emission circuitry – works comparably, we calibrated after it swam for several minutes in a water bath of known temperature. Fig. 7.5 shows that the temperature dependence is non-zero but comparable to the specifications of the ADXL 330. However, for high precision measurements it is advised to calibrate at experiment temperature shortly before doing the experiment.

Fig. 7.6 shows the long time behavior of the particle at rest. Here, the radio emission power was set to medium, which corresponds to capturing its signal at up to 10m in air and 0.5m in de-ionized water. The $x-$ and $y-$ axes do not stay constant and show only little increase in noise as the coin cell slowly discharges. The $z-$axis has a slow drift of the order of $2\frac{q}{\mathrm{h}}$. The usable life time is 32 hours followed by a few hours with significantly higher noise until the particle fully stops working. The particle is that sensitive that ground vibrations (caused by people walking in the office/lab) are detected.

A stronger radio emission power can be required if:

- The apparatus builds a Faraday cage, *i.e.* an electrically-connected metal structure surrounds the flow.
- Electro-Magnetic noise is present *e.g.* caused by badly isolated motors or electromagnetic shakers.
- The signal has to pass a longer distance in more water in a bigger apparatus.
- Solutions with a high conductivity (*e.g.* salt water) are likely to damp the radio signal.

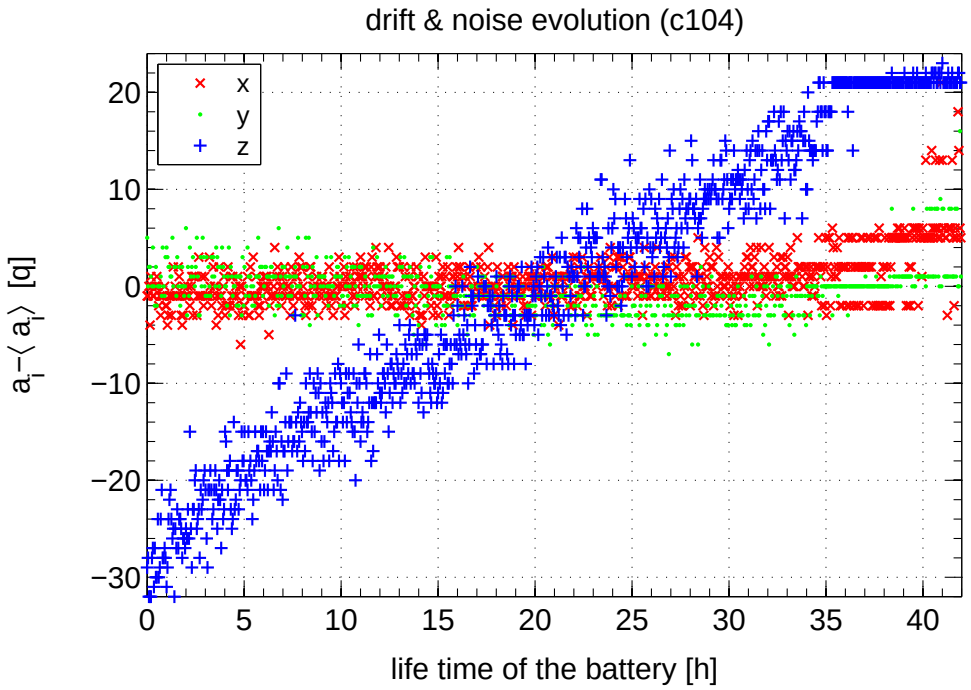

Figure 7.6: Long time behavior of a sample smartPART.

The receiver/demodulation unit of the smartCenter works best within a range of radio power, *i.e.* particles which are emitting either too strong or too weak are undesirable. Whereas medium power was optimal in the KLAC, strong radio emission has to be used in the LEM in order to continuously receive the particle's signal. Nevertheless, particles with stronger radio emission still last 6 to 12 hours, which is sufficient in most cases.

Considering the mechanical robustness, the smartPART "survived" several hours in the KLAC and the LEM. Both have impellers which are equipped with sharp edged blades in order to achieve an inertial forcing. But the shell cracked once when the edge of a blade damaged the underlying thread. It then filled with water and sank to the bottom; the circuit was fully functional after drying.

7.1.3 Orientation of the sensor within the capsule

The sensor is fixed within the capsule such that it doesn't move. However, the circuit is inserted by hand between the two half spheres. Thus, its orientation with respect to an outer texture is not known and has to be determined if one wishes to perform simultaneous acquisitions of its signal and its six-dimensional trajectory.

The following is an extension of the procedure to find the texture: as stated in paragraph 3.3.2.1 pictures of the particle at arbitrary orientations are taken. To determine the position of the sensor, it is additionally necessary to simultaneously acquire its signal and to know the exact orientation of $\boldsymbol{g}$ (its magnitude is well-known). The latter can be achieved by placing the camera such that its optical axis coincides with the axis of gravity

and the particle center. For simplicity we set $\boldsymbol{g} = g \cdot \boldsymbol{e}_z$ which tells us how to re-project $\boldsymbol{g}$ on the half sphere for each image[3].

Thus, we have N tuples, each consisting of an image, its measured acceleration, $\boldsymbol{a}(k)$, and its orientation, $\underline{\theta}(k)$ with respect to a base view. The accelerometer can be seen as three independent sensors, each measuring the projection of $\boldsymbol{g}$ on axis $\boldsymbol{c}_i$. $\boldsymbol{c}_i$ is fixed with respect to the texture. For simplicity, we focus on only one sensor at a time: $a_i(k)$ is then the projection of $\boldsymbol{g}$ onto $\boldsymbol{c}_i$ at the $k-$th image:

$$a_i(k) \equiv \boldsymbol{g}(k) \cdot \boldsymbol{c}_i \tag{7.6}$$

All points $\boldsymbol{\xi}$ with

$$\boldsymbol{g}(k) \cdot \boldsymbol{\xi} = a_i(k) \tag{7.7}$$

are possible candidates for $\boldsymbol{c}_i$, because of rotations around the axis of gravity do not alter the measured acceleration (Eq. (7.6)). These points form a circle on the surface of a sphere[4].

For more than one measurement, the circles cross at $\boldsymbol{c}_i$ because it is the only point which fulfills Eq. (7.7) for multiple measurements. A sketch is provided in Fig. 7.7.

Thus, we can determine where the three axes of the accelerometer point on the texture. Measurement errors might cause that the three axes are not perfectly orthogonal, and thereby resulting in a "bad" rotation matrix. Kabsch's algorithm (cf. appendix B.5) is then used to compute a valid rotation matrix $\underline{\underline{\boldsymbol{R}}}_{\mathrm{TS}}$ verifying $\underline{\underline{\boldsymbol{R}}}_{\mathrm{TS}} \underline{\underline{\boldsymbol{R}}}_{\mathrm{TS}}^T = \underline{\underline{1}}$ and $\det(\underline{\underline{\boldsymbol{R}}}_{\mathrm{TS}}) = 1$.

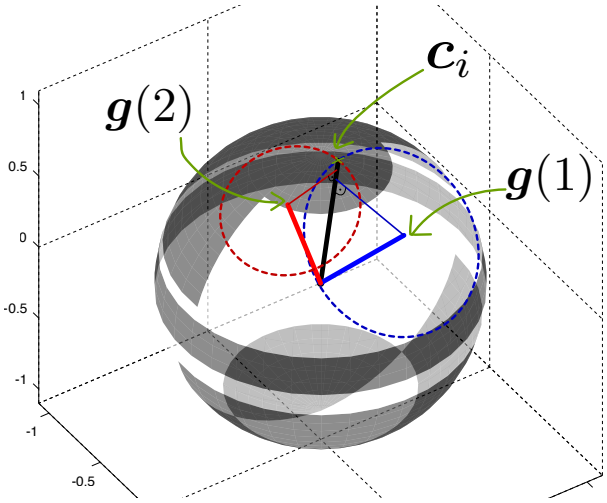

Figure 7.7: Sketch explaining how to find the position of the sensor. The circles are $\boldsymbol{g}(1) \cdot \boldsymbol{\xi} = a_i(1) = \boldsymbol{g}(1) \cdot \boldsymbol{c}_i$ and $\boldsymbol{g}(2) \cdot \boldsymbol{\xi}' = a_i(2) = \boldsymbol{g}(2) \cdot \boldsymbol{c}_i$ respectively. The circles cross at $\boldsymbol{c}_i$

[3] For an image k with an arbitrary but known orientation, $\underline{\theta}(k)$, its position with respect to an unrotated sphere (and therefore on the texture) can be computed by $\boldsymbol{g}(k) = \underline{\underline{\boldsymbol{R}}}(\underline{\theta}(k))^T \, \boldsymbol{e}_z$.

[4] Visualizing them in the ϕ, θ coordinates of the texture is less intuitive.

7.1.4 Runs

Measurements were performed in a von Kármán flow (the KLAC) and the Lagrangian Exploration Module (LEM); in all the runs presented we kept the propeller frequency, f_{prop}, constant during the measurement and the density of the particle was adjusted to that of water. A list of the runs where we only recorded its signal is provided in table 7.1. We also performed two experiments where we acquired the particle's acceleration signal and simultaneously tracked its position and absolute orientation. They were done in the KLAC counter-rotating impellers running at a speed of 2 Hz and 3 Hz.

	runs	particle	infos	frequencies [Hz]
KLAC	c104	c104	counter-rotating impellers	0.25, 0.33, 0.66, 1, 1.25, 1.5, 1.66, 2, 2.33, 2.5 , 2.75, 3, 3.25, 3.5, 4
	corot	c104	co- rotating impellers	1, 1.5, 2
	c102	c102	counter-rotating impellers, strong imbalance	0.5, 1, 1.5
LEM	LEM	c101	all motors	1, 2, 3, 4, 5

Table 7.1: data runs with *only* the smart particle, the working fluid was always water. All runs were done in August 2011 and all particles except *c102* are well balanced.

7.2 Directly accessible quantities

As explained in section 7.1.1.4 we have to deal with the orientation of the sensor in addition to the gravitational, translational and rotational forces acting on the particle when describing/understanding the particle's signal. According to Eq. (7.2) one measures

$$\boldsymbol{a}_{\mathrm{SP}} = \underline{\underline{\boldsymbol{R}}}_{\mathrm{TS}}^{T}\, \underline{\underline{\boldsymbol{R}}}\left(\underline{\theta}\right)^{T} \left[\boldsymbol{g} + \frac{\mathrm{d}^2}{\mathrm{d}t^2}\left(\boldsymbol{x}(t) + \boldsymbol{r}\right) + \boldsymbol{\omega} \times \left(\boldsymbol{\omega} \times \boldsymbol{r}\right) + \frac{\mathrm{d}\boldsymbol{\omega}}{\mathrm{d}t} \times \boldsymbol{r}\right] \tag{7.8}$$

with $\boldsymbol{r} = 3\ \mathrm{mm} \cdot \hat{e}_z$ the displacement with respect to the geometrical center of the particle. Experiments on the rotation of solid spheres in a von Kármán flow showed that the angular velocity, ω, of the particle is of the order of the propeller frequency, f_{prop}. The rotational forces are of order $r\,\omega^2 \sim r \cdot (4\pi^2\, f_{\mathrm{prop}}^2) \lesssim \frac{1}{10}\, \boldsymbol{a}_{\mathrm{trans}}$ and Eq. (7.2) reduces to

$$\boldsymbol{a}_{\mathrm{SP}} \approx \underline{\underline{\boldsymbol{R}}}\left(\underline{\theta}\right)^{T} \left[\boldsymbol{g} + \boldsymbol{a}_{\mathrm{trans}}\right] \qquad \Leftrightarrow \qquad \underline{\underline{\boldsymbol{R}}}\left(\underline{\theta}\right) \boldsymbol{a}_{\mathrm{SP}} \approx \boldsymbol{g} + \boldsymbol{a}_{\mathrm{trans}} \tag{7.9}$$

As the particle is advected by the flow, it also rotates freely and more important in a *a priori* unknown way. Consequently one has to investigate how common quantities, mainly mean and variance of the acceleration time series as well as auto correlation functions, are altered by the continuously changing orientation of the sensor, $\underline{\underline{\boldsymbol{R}}}\left(\underline{\theta}\right)$. In the following the abbreviations $\underline{\underline{\boldsymbol{R}}} = \underline{\underline{\boldsymbol{R}}}\left(\underline{\theta}(t)\right)$ and $\boldsymbol{a}_t = \boldsymbol{a}_{\mathrm{trans}}(t)$ are applied for readability.

7.2.1 "Shakiness"

Taking the average of Eq. (7.9) yields:

$$\langle \boldsymbol{a}_{\mathrm{SP}} \rangle = \langle \underline{\underline{\boldsymbol{R}}}\boldsymbol{g} \rangle + \langle \underline{\underline{\boldsymbol{R}}}\boldsymbol{a}_t \rangle \tag{7.10}$$

If the particle explores continuously all the possible orientations, the mean vanishes; whereas a fixed orientation (*i.e.* no rotation) yields $\langle \boldsymbol{a}_{\mathrm{SP}} \rangle = \underline{\underline{\boldsymbol{R}}}\,(\boldsymbol{g} + \langle \boldsymbol{a}_t \rangle)$. However, this situation is highly unlikely: Even if the mass distribution induces a preferred direction, the particle can rotate freely around this axis. Contacts with impellers, walls, eddies, etc overpower any preferred direction easily and force the particle to rotate.

Fig. 7.8 shows $\langle \boldsymbol{a}_{\mathrm{SP}} \rangle$ as a function of the propeller speed, f_{prop} and the forcing. As expected the mean accelerations are becoming smaller with increasing propeller frequency. Although it is trivial it should be pointed out that

$$|\boldsymbol{a}_{\mathrm{trans}}| \geq |\boldsymbol{a}_{\mathrm{SP}}| - g \tag{7.11}$$

In other words, $|\boldsymbol{a}_{\mathrm{SP}}|$ is not a justifiable quantity to estimate the mean acceleration (*i.e.* force) seen by the particle.

Similar arguments show that the variance of $\boldsymbol{a}_{\mathrm{SP}}$ (and therefore the standard deviation (RMS)) is altered by the rotation, too. Moreover, the variance of a component, $\boldsymbol{a}_{\mathrm{SP},i}$, of

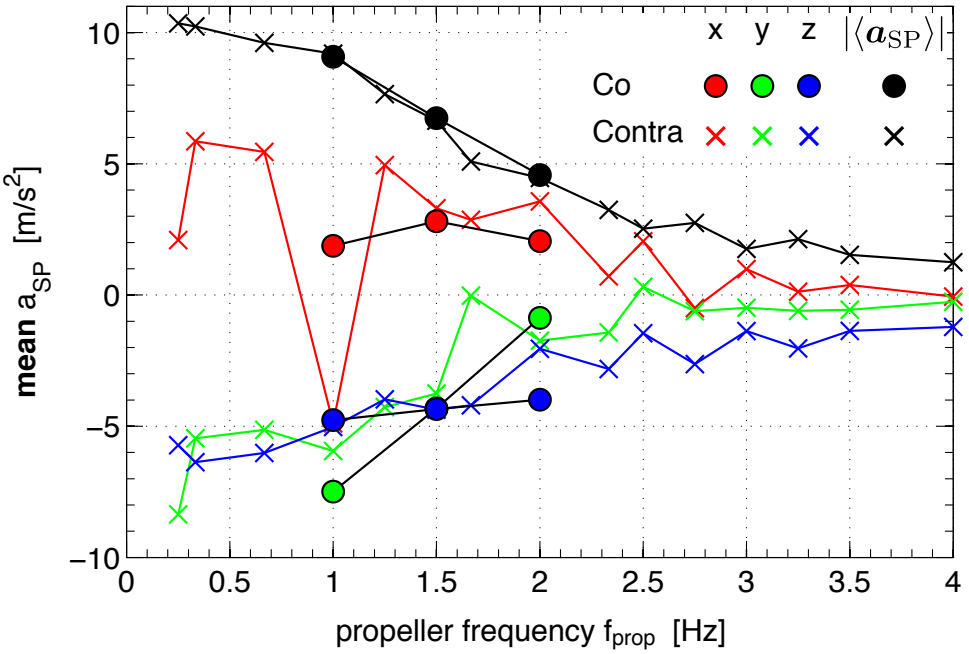

Figure 7.8: Evolution of $\langle \boldsymbol{a}_{\mathrm{SP}} \rangle$ with the propeller speed f_{prop}; filled symbols (○) indicate co-rotating propellers. In all cases the particle explored the flow for a sufficient amount of time for the statistics to converge. In good agreement with Eq. (7.10), $|\langle \boldsymbol{a}_{\mathrm{SP}} \rangle|$ continuously decreases from $1g$ to $0g$ as the propeller frequency increases.

$\boldsymbol{a}_{\mathrm{SP}}$ depends strongly on its mean value, $\langle \boldsymbol{a}_{\mathrm{SP,i}} \rangle$. As shown before, gravity renders $\langle \boldsymbol{a}_{\mathrm{SP,i}} \rangle$ non-negligible. Additionally, we observed at weak turbulence levels ($f_{\mathrm{prop}} \lesssim 1$ Hz) that particles are able to stay in an orientation for several seconds. Hence, a global mean of the complete time-series is not a meaningful quantity. Although subtracting a moving average with a window length of several 10 s performs well in estimating the variance, it is not efficient in a computational sense. Instead we apply a low-order band-pass filter with $f_{\mathrm{low}} \approx \frac{1}{10}$ Hz and $f_{\mathrm{high}} \approx 100$ Hz to the time series. f_{low} is chosen such that it is much smaller that the expected slow timescales of the flow or a possible rotation of the particle. High frequency noise associated to the electronics is handled by f_{high}. This technique also works if a global mean is applicable.

Fig. 7.9 shows the dependence of the RMS of the components, $\boldsymbol{a}_{\mathrm{SP},i}$, of $\boldsymbol{a}_{\mathrm{SP}}$ on the propeller speed, f_{prop}. We found no preferred direction in any of the axes. Dimensional arguments and the results from chapter 4 tell that, $\boldsymbol{a}_{\mathrm{trans}} \propto f_{\mathrm{prop}}^2$. In contrast thereto, we observe a linear or (in the case of the LEM) even sub-linear scaling with the propeller frequency. We further investigated $|\boldsymbol{a}_{\mathrm{SP}}|$ and noticed that RMS of the norm is always smaller than the RMS of the components. This confirms experimentally the simple inequality of Eq. (7.11).

One can further look at the PDF of the components of $\boldsymbol{a}_{\mathrm{SP}}$: Fig. 7.10 provides as an example the PDF of the balanced particle ($c104$) at low and high turbulence. Whereas at

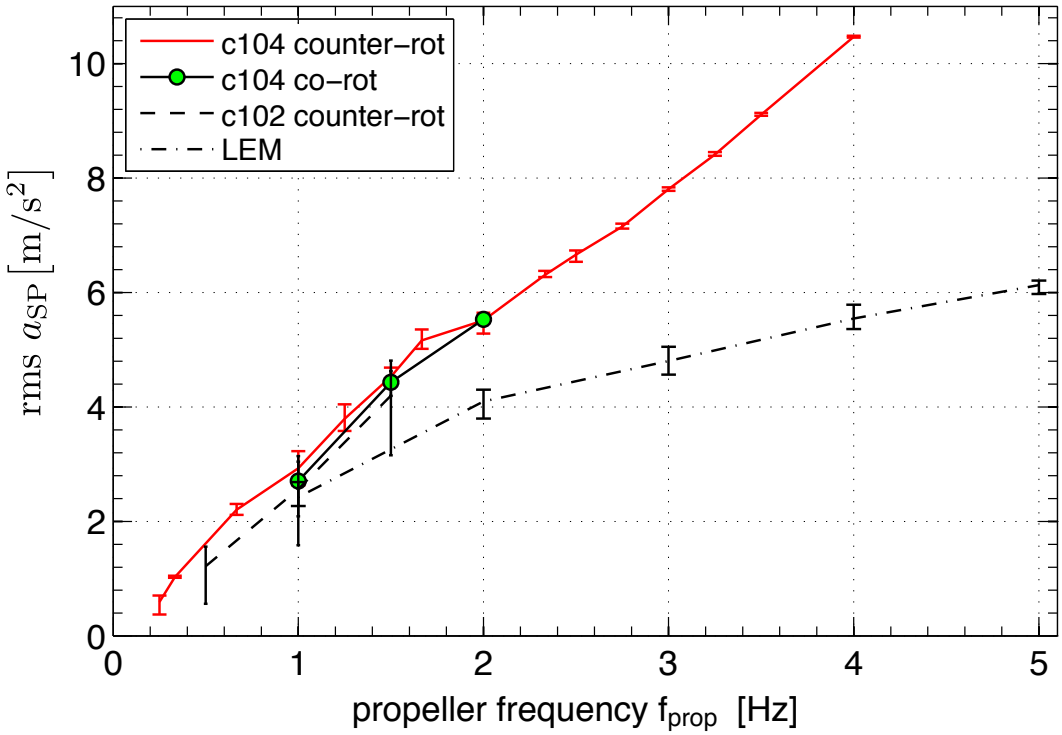

Figure 7.9: Evolution of the RMS of the components of $\boldsymbol{a}_{\mathrm{SP}}$ with the propeller speed, f_{prop}; a band-pass filter is used to subtract the mean. The error bars indicate the spread within the three components. Although not shown here, RMS($|\boldsymbol{a}_{\mathrm{SP}}|$) is always smaller than the RMS of the single components of $\boldsymbol{a}_{\mathrm{SP,i}}$.
In opposition to dimensional arguments and results for solid spheres in the similar flow conditions, the RMS is *not* proportional to f_{prop}^2.

low propeller speeds the PDF are skewed and shifted, they become centered and symmetric with increasing propeller speed. The ADXL 330 saturates if the accelerations exceed $\pm 3.6g$, we exclude these points from the analysis. This removal diminishes the observed acceleration and the bias increases with the forcing. In the case of Fig. 7.10, almost 3% of all data points were removed at $f_{\mathrm{prop}} = 4$ Hz. That is two orders of magnitude more than for $f_{\mathrm{prop}} = 1$ Hz. As we will see in the following the saturation of the accelerometer lead to an underestimation of the moments of the PDF of $\boldsymbol{a}_{\mathrm{trans}}$.
Excluding data points with $a_i > 3.6g$ alters the observable variance and flatness.

Résumé: Recapitulating, both mean and variance of the raw signals do contain only little information on the flow. That means that naive/direct approaches on raw signals risk to evaluate the shakiness of the signals instead of the underlying physics. Hence, well-adapted methods are needed to extract informations on the flow from the instrumented particles. In the next section we will develop these methods.

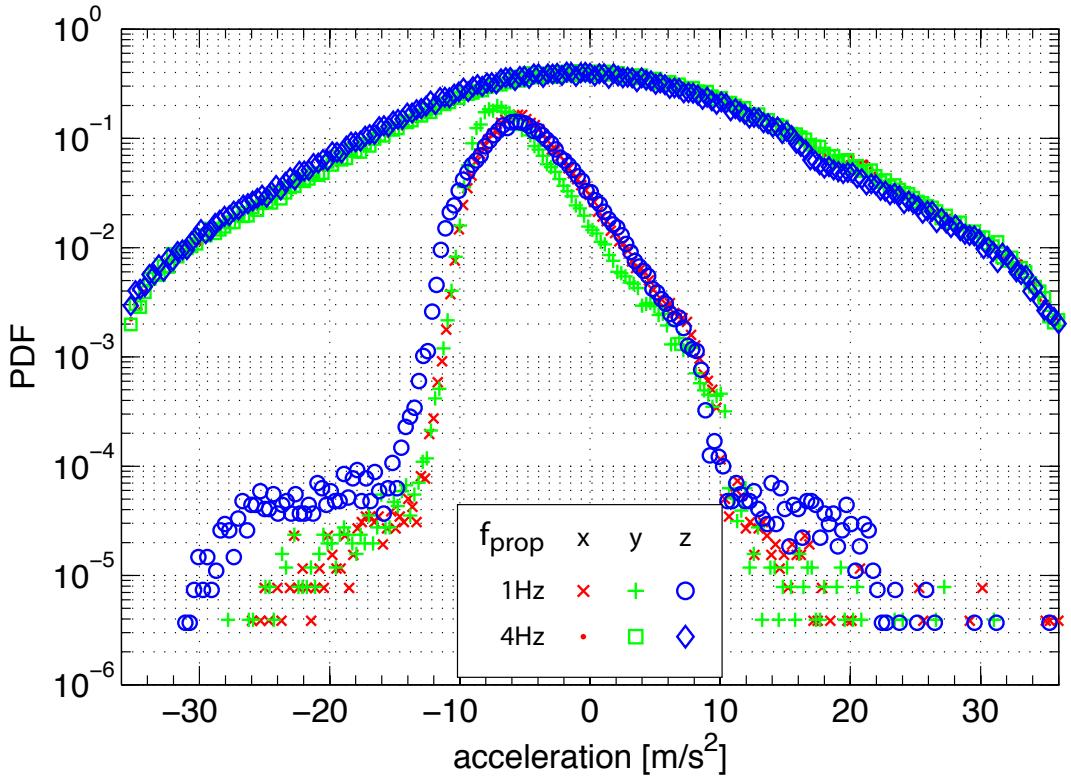

Figure 7.10: PDF of the components of $\boldsymbol{a}_{\mathrm{SP}}$ at low (1 Hz) and high (4 Hz) turbulence. The latter has been shifted for readability. Points where axes of the accelerometer saturated are deactivated and not used in the analysis. The saturation of the accelerometer leads to an underestimation of the moments of the PDF of $\boldsymbol{a}_{\mathrm{trans}}$.

7.2.2 Moments of a_{trans}

In most flows one expects $\langle \boldsymbol{a}_{\text{trans}} \rangle \approx 0$. One is therefore interested in the PDF of $\boldsymbol{a}_{\text{trans}}$. Although, we don't have direct access to $\boldsymbol{a}_{\text{trans}}$ and its PDF, we can compute the even (central) moments of its PDF.

Variance The variance of $\boldsymbol{a}_{\text{SP}}$ is[5]:

$$\begin{aligned} \left\langle \boldsymbol{a}_{\text{SP}}^2 \right\rangle &= \langle \underline{\underline{\boldsymbol{R}}} \boldsymbol{g} \cdot \underline{\underline{\boldsymbol{R}}} \boldsymbol{g} \rangle + \langle \underline{\underline{\boldsymbol{R}}} \boldsymbol{a}_t \cdot \underline{\underline{\boldsymbol{R}}} \boldsymbol{a}_t \rangle + 2 \langle \underline{\underline{\boldsymbol{R}}} \boldsymbol{g} \cdot \underline{\underline{\boldsymbol{R}}} \boldsymbol{a}_t \rangle \\ &= g^2 + \left\langle \boldsymbol{a}_t^2 \right\rangle + 2g \left\langle a_t^z \right\rangle \\ &\simeq g^2 + \left\langle \boldsymbol{a}_t^2 \right\rangle \end{aligned} \tag{7.12}$$

$a_t^z \equiv \boldsymbol{g} \cdot \boldsymbol{a}_t$ has zero mean in most flows if the particle is neutrally buoyant. We therefore define

$$a_{\text{magn}} \equiv \sqrt{\left\langle \boldsymbol{a}_t^2 \right\rangle} = \sqrt{\left\langle \boldsymbol{a}_{\text{SP}}^2 \right\rangle - g^2} \tag{7.13}$$

as measure of the magnitude of $\boldsymbol{a}_{\text{trans}}$. a_{magn} is independent of gravity. Nevertheless, a bad calibration (*e.g.* caused by longterm drift or temperature change) can introduce a systematic offset to a_{magn}. It is thus advised to always recalibrate before doing the actual experiment. The left plot in Fig. 7.11 depicts the evolution of a_{magn} with the driving. One first notices, that a_{magn} depends on the mixer: the acceleration is much smaller in the LEM than in the KLAC. This observation agrees well with the fact, that the energy injection rate (at the same propeller speed) is smaller in the LEM, too.
In agreement with dimensional analysis, $a_{\text{magn}}\left(f_{\text{prop}}\right)$ describes a parabola, however, one could also argue that $a_{\text{magn}}\left(f_{\text{prop}}\right)$ is linear for f_{prop} larger some threshold. It should be kept in mind, that each axis of the smartPart's accelerometer is limited to $\pm 3.6g$. Even if the flow induces events of higher acceleration these are not be detectable (cf. Fig. 7.10) and therefore not included in the observed variance. If one likes to investigate the behavior at large f_{prop} the ADXL 330 has to be replaced with a different model supporting higher accelerations. One also has to ensure, that both apparatus and particle mechanically support the forces occurring at higher propeller speeds.

Flatness In the spirit of Eq. (7.12) one can estimate the higher moments of $\boldsymbol{a}_{\text{trans}}$, which we demonstrate here for the forth central moment, the *flatness*[6].

$$\begin{aligned} \left\langle \left|\boldsymbol{a}_{\text{SP}}\right|^4 \right\rangle &= \left\langle \left[g^2 + a_t^2 + 2\,\boldsymbol{g} \cdot \boldsymbol{a}_t\right] \left[g^2 + a_t^2 + 2\,\boldsymbol{g} \cdot \boldsymbol{a}_t\right] \right\rangle \\ &= \left\langle \left|\boldsymbol{a}_t\right|^4 \right\rangle + g^4 + 2g^2 \left\langle \left|\boldsymbol{a}_t\right|^2 \right\rangle + 4g^2 \left\langle \left|a_t^z\right|^2 \right\rangle + 4\,g^3 \left\langle a_t^z \right\rangle + 4g \left\langle \left|\boldsymbol{a}_t\right|^2 a_t^z \right\rangle \\ &\approx \left\langle \left|\boldsymbol{a}_t\right|^4 \right\rangle + g^4 + \frac{10}{3} g^2 a_{\text{magn}}^2 \end{aligned} \tag{7.14}$$

[5] The dot product of two vectors, in other words the angle between them, is invariant to choice of the coordinate system. Therefore $\left(\underline{\underline{\boldsymbol{R}}}_1 \boldsymbol{a}\right) \cdot \left(\underline{\underline{\boldsymbol{R}}}_2 \boldsymbol{b}\right) = \left(\underline{\underline{\boldsymbol{R}}}_2^T \underline{\underline{\boldsymbol{R}}}_1 \boldsymbol{a}\right) \cdot \boldsymbol{b} = \boldsymbol{a} \cdot \left(\underline{\underline{\boldsymbol{R}}}_1^T \underline{\underline{\boldsymbol{R}}}_2 \boldsymbol{b}\right)$ for $\underline{\underline{\boldsymbol{R}}}_1, \underline{\underline{\boldsymbol{R}}}_2$ arbitrary rotation matrixes.

[6] Also known as *kurtosis*.

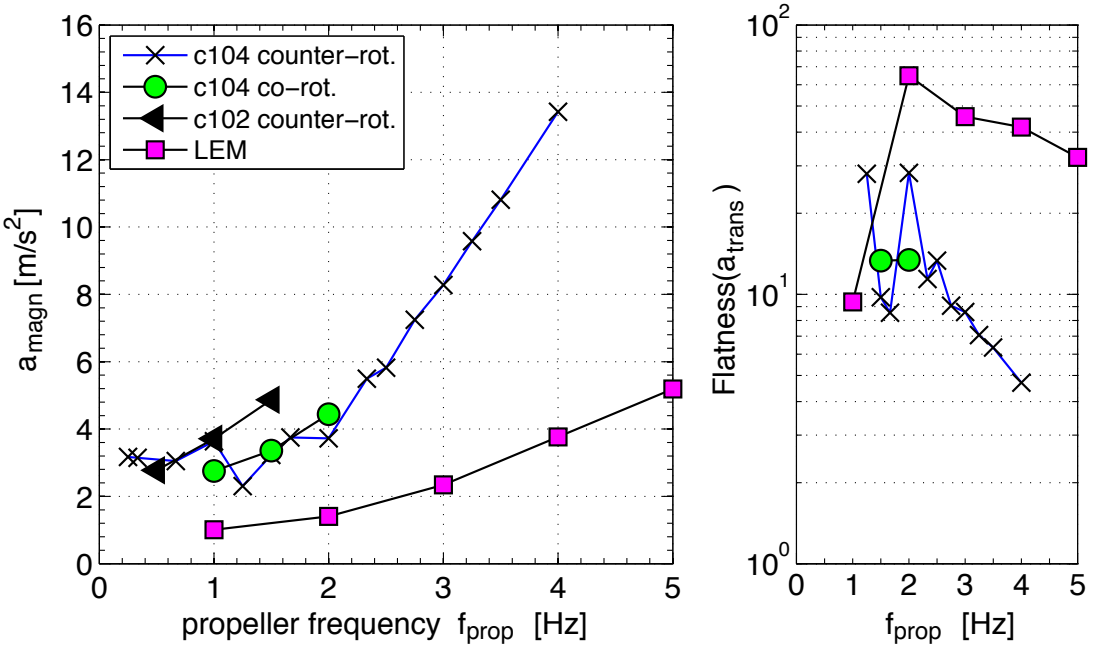

Figure 7.11: Magnitude and Flatness of $\boldsymbol{a}_{\text{trans}}$
Left: $a_{\text{magn}}(f_{\text{prop}}) = \text{RMS}(\boldsymbol{a}_{\text{trans}}) = \sqrt{\left\langle \boldsymbol{a}_{\text{SP}}^2(f_{\text{prop}}) \right\rangle - g^2}$
Right: estimate of the flatness of $\boldsymbol{a}_{\text{trans}}$.

Assuming no preferred direction in $\boldsymbol{a}_t$ it is $4g^2 \left\langle |a_t^z|^2 \right\rangle \approx 4/3\, g^2\, a_t^2$. Again, the terms $4\, g^3 \left\langle a_t^z \right\rangle$ and $4g \left\langle |\boldsymbol{a}_t|^2\, a_t^z \right\rangle$ are expected to have zero mean. The flatness, $F(a_t)$, is then

$$F\left(a_{\text{trans}}\right) = \frac{\left\langle a_t^4 \right\rangle}{\left\langle a_t^2 \right\rangle^2} = \frac{\left\langle |\boldsymbol{a}_{\text{SP}}|^4 \right\rangle - g^4 - \frac{10}{3} g^2 a_{\text{magn}}^2}{a_{\text{magn}}^4} \tag{7.15}$$

As shown in Fig. 7.11 we observe a flatness of the order of 10 in the KLAC, which is close to our finding for solid particles. In the LEM we find $F \sim 40$ which is open to doubt. The uncertainty in the flatness can partially be attributed to a uncertainty in g and stems from the resolution, noise and measurement range of the smartPart but also from the particle's weak temperature dependence and drift. It is furthermore biased by contacts with the impellers and walls. More surprisingly, the flatness decreases in both apparatuses with the forcing. This decline is due to the measurement range of the ADXL 330: At high accelerations the sensor saturates and thereby sets PDF $\left(\boldsymbol{a}_{\text{trans}} \,\middle|\, |a_i| > 3.6g\right) = 0$. Since the flatness is the forth moment of the PDF and as such highly sensitive to high accelerations, we find a decrease although solid large spheres in the same flow have an increasing flatness (cf. chapter 4).

Possibly the uncertainty in the flatness estimate can be reduced by filtering or improved electronics. However, it is evident that calculating moments of even higher order is out of reach.

7.2.3 Influence of inertia & imbalance

As explained in section 7.1.1.2 the imbalance of the particle is adjustable to some extent. The runs *c102* correspond to a particle which is strongly out of balance whereas the other particles *c101* and *c104* shows little imbalance. The inertia can be approximated as the sum of a spherical shell (the capsule), a cylinder (the battery and circuit) and two point masses (the added weight). The ensemble has one axis of symmetry which by construction coincides with the $z-$axis of the accelerometer. Hence, the smartPart's inertia has exactly two unique moments – J_z for rotations around the $z-$axis and J_{xy} for the perpendicular case. Simple estimates based on the technical drawings yield $J_z \approx 2 \cdot 10^{-7} \mathrm{kg} \cdot \mathrm{m}^2$ and $J_{xy} \approx 3.5\, J_z$. The resonance frequency of a physical pendulum with displacement r_{disp} and mass m is approximately[7]

$$T = 2\,\pi \sqrt{\frac{J}{g\, m\, r_{\mathrm{disp.}}}} \tag{7.16}$$

An imbalanced particle behaves similar to such a physical pendulum, which in addition it is driven/kicked by the flow. Assuming a difference between center of mass and geometrical center of $r_{\mathrm{disp}} = 2$ mm one finds $T(J_z) \approx 0.2$s and $T(J_{xy}) \approx 0.4$s. The resonance frequencies are thus $f(J_{xy}) \approx 2.5$ Hz and $f(J_z) \approx 5$ Hz; they are in a first approximation independent on the forcing.

Fig. 7.12 shows the power spectral density of the imbalanced particle *c102* at propeller speeds of 0.5 Hz, 1 Hz, and 1.5 Hz. The x and y axes coincide and differ clearly from the $z-$axis. One peak for x and y and two clear peaks for the $z-$axis can be identified; in either case their position is independent of the forcing. Moreover, the peak position correspond to the 2 resonant frequencies, $f(J_{xy})$ and $f(J_z)$, which were estimated from the technical drawings. A well-balanced smartPart at the same propeller speed shows neither the distinct peaks nor do the axes differ. It is clear that the peaks alter the autocorrelation functions in an unwanted way.

[7] small angle approximation

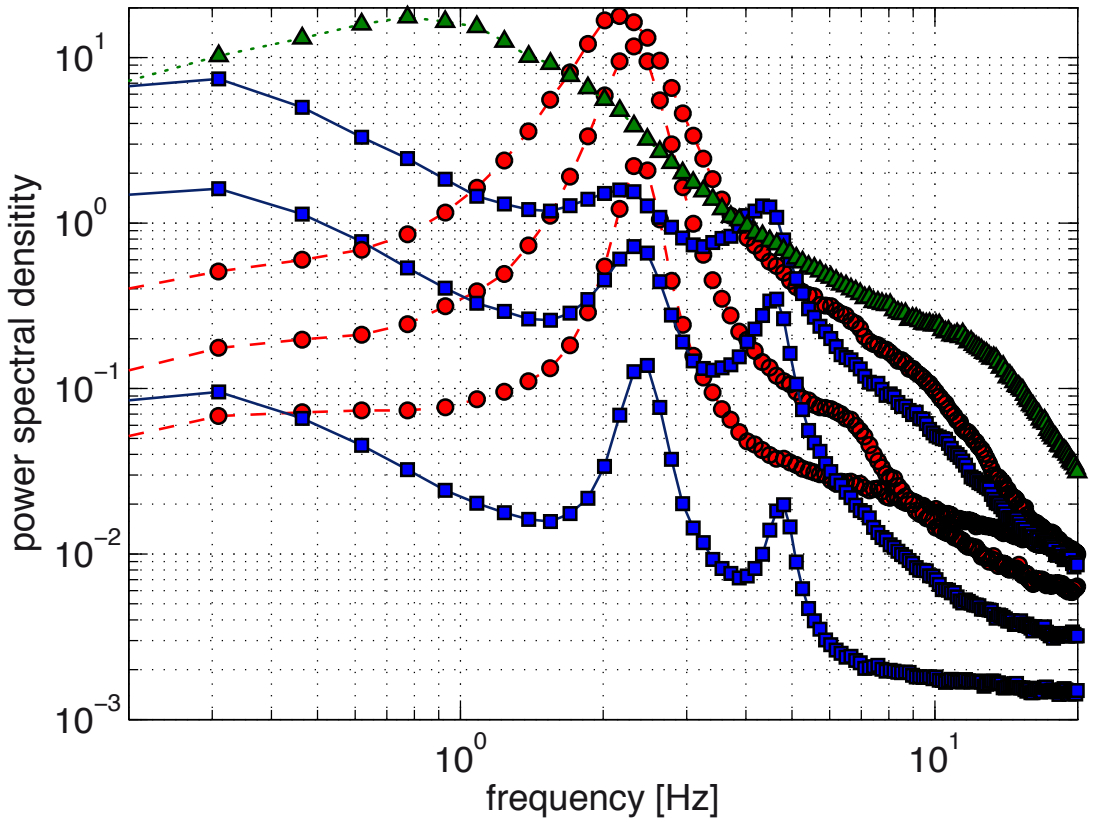

Figure 7.12: Power spectral density of imbalanced particle (*c102*) at propeller speeds of 0.5 Hz, 1 Hz, & 1.5 Hz. x coincides with y (●) and is not plotted for readability. One peak for x and y and two clear peaks for z (□) can be identified; in either case their position is independent of the forcing. Moreover, the peak position can be estimated from the technical drawings. No peaks and no difference in the three components is found for a well-balanced particle (▲, *c104*).

7.2.4 Auto-correlations

It is remarkable, that based only on a_{magn} one cannot clearly distinguish between a counter-rotating and a co-rotating flow although it is known that these two forcings induce two clearly different flow types. Ideally, one would want to compute the auto-correlation of the translational force, $\langle a_t\,(t)\cdot a_t\,(t+\tau)\rangle$, to estimate correlation time scales of the flow. Again, the constantly changing orientation of the smartPart blocks any direct access to $a_t\,(t)$ and quantities derived thereof. We therefore need to find quantities which are either not altered by the orientation of the smartPart or extract information on its rotation.

7.2.4.1 An Auto-correlation invariant to the rotation of the sensor

In the spirit of Eq. (7.12) and Eq. (7.14) one can construct the auto correlation function of the magnitude of $|\boldsymbol{a}_{\text{SP}}|^2$:

$$
\begin{aligned}
&\left\langle |\boldsymbol{a}_{\text{SP}}(t)|^2\,|\boldsymbol{a}_{\text{SP}}(t+\tau)|^2\right\rangle \\
&\quad= \left\langle \left[g^2+a_t^2(t)+2\,\boldsymbol{g}\cdot\boldsymbol{a}_t(t)\right]\left[g^2+a_t^2(t+\tau)+2\,\boldsymbol{g}\cdot\boldsymbol{a}_t(t+\tau)\right]\right\rangle \\
&\quad= \left\langle |\boldsymbol{a}_t(t)|^2\,|\boldsymbol{a}_t(t+\tau)|^2\right\rangle + g^4 + g^2\left(\left\langle |\boldsymbol{a}_t(t)|^2\right\rangle + \left\langle |\boldsymbol{a}_t(t+\tau)|^2\right\rangle\right) \\
&\qquad + 2\,g^2\left(\langle \boldsymbol{g}\cdot\boldsymbol{a}_t(t+\tau)\rangle + \langle \boldsymbol{g}\cdot\boldsymbol{a}_t(t)\rangle\right) + 2\left\langle |\boldsymbol{a}_t(t)|^2\,\boldsymbol{g}\cdot\boldsymbol{a}_t(t+\tau)\right\rangle \\
&\qquad + 2\left\langle |\boldsymbol{a}_t(t)|^2\,\boldsymbol{g}\cdot\boldsymbol{a}_t(t+\tau)\right\rangle + 4\left\langle \left(\boldsymbol{g}\cdot\boldsymbol{a}_t(t+\tau)\right)\left(\boldsymbol{g}\cdot\boldsymbol{a}_t(t)\right)\right\rangle \\
&\quad= \left\langle |\boldsymbol{a}_t(t)|^2\,|\boldsymbol{a}_t(t+\tau)|^2\right\rangle + g^4 + 2g^2\left\langle |\boldsymbol{a}_t|^2\right\rangle + 4g^2\left\langle a_t^z(t)\,a_t^z(t+\tau)\right\rangle \\
&\qquad + 4\,g^3\left\langle a_t^z\right\rangle + 2g\left\langle |\boldsymbol{a}_t(t+\tau)|^2\,a_t^z(t)\right\rangle + 2g\left\langle |\boldsymbol{a}_t(t)|^2\,a_t^z(t+\tau)\right\rangle \\
&\quad\approx \left\langle |\boldsymbol{a}_t(t)|^2\,|\boldsymbol{a}_t(t+\tau)|^2\right\rangle + g^4 + 2\,g^2 a_{\text{magn}}^2 + 4g^2\left\langle a_t^z(t)\,a_t^z(t+\tau)\right\rangle
\end{aligned}
\tag{7.17}
$$

Again, the terms containing $a_t^z \equiv \boldsymbol{g}\cdot\boldsymbol{a}_t$ are expected to have zero mean. However, $4g^2\left\langle a_t^z(t)\,a_t^z(t+\tau)\right\rangle = 4g^2\left\langle |a_t^z|^2\right\rangle$ for $\tau\approx 0$. Assuming no preferred direction in a_t this can be approximated as $4/3\,g^2\,a_{\text{magn}}^2$. In contrast to Eq. (7.17), we preferably compute the autocorrelation of the fluctuations[8] around the mean[9] $\langle \boldsymbol{a}_{SP}^2\rangle$. Hence, the autocorrelation of the norm can be negative. We further normalize the auto-correlation such that it is 1 at $\tau = 0$. For more details please see appendix B.3.

Fig. 7.13 displays $\left\langle |\boldsymbol{a}_{\text{SP}}(0)|^2\,|\boldsymbol{a}_{\text{SP}}(\tau)|^2\right\rangle$ for three different configurations at a propeller speed of 1.5 Hz. A balanced and an imbalance particle in the same flow configuration show only little difference in the auto-correlation function. That is in contrast to paragraph 7.2.3, which demonstrated that imbalance causes distinct peaks in the power spectrum of the single components of $\boldsymbol{a}_{\text{SP}}$. Despite their different rotational dynamics, particles extract almost identical time scales of the flow. Their auto-correlation should be

[8] "Every American should have above average income, and my Administration is going to see they get it.", Bill Clinton on the campaign trail

[9] $\left\langle \left(|\boldsymbol{a}_{\text{SP}}(t)|^2-\mu\right)\left(|\boldsymbol{a}_{\text{SP}}(t+\tau)|^2-\mu\right)\right\rangle$ with $\mu = \langle \boldsymbol{a}_{SP}^2\rangle$

well approximated by a sum of exponential decays or the transient function of a critical damped oscillator.

In contrast to the counter-rotating flow, we observe that co-rotating impellers correspond to an auto-correlation function which resembles a weakly-damped oscillator. This means that this forcing creates more coherence in the large scale motion of the co-rotating flow. Moreover, this difference in the flow structure is observable with an instrumented particle. This is in agreement with Eulerian measurements [71], where pressure probes were mounted in a von Kármán flow: Whereas the counter-rotating flow produces typical pressure spectra, the same probe in the co-rotating case yields a spectrum which peaks at multiples of the propeller frequency. Similar behavior has been reported for the magnetic field in a von Kármán flow [73] filled with liquid Gallium.

Summing up, $\left\langle |\boldsymbol{a}_{\mathrm{SP}}(t)|^2 \, |\boldsymbol{a}_{\mathrm{SP}}(t+\tau)|^2 \right\rangle$ is insensitive to the particular rotational dynamics of the particle. It gives necessary information to determine the type of flow.

7.2.4.2 An Auto-correlation related to the tumbling of the particle

One can further focus on the rotation of the particle by considering the *dot* product of $\boldsymbol{a}_{\mathrm{SP}}(t) \cdot \boldsymbol{a}_{\mathrm{SP}}(t+\tau)$:

$$
\begin{aligned}
&\langle \boldsymbol{a}_{\mathrm{SP}}(t) \cdot \boldsymbol{a}_{\mathrm{SP}}(t+\tau) \rangle \\
&= \left\langle \left[\underline{\underline{\boldsymbol{R}}} \left(\underline{\theta}(t)\right)^T \left(\boldsymbol{g} + \boldsymbol{a}_t(t)\right) \right] \cdot \left[\underline{\underline{\boldsymbol{R}}} \left(\underline{\theta}(t+\tau)\right)^T \left(\boldsymbol{g} + \boldsymbol{a}_t(t+\tau)\right) \right] \right\rangle \\
&= \left\langle \left[\underline{\underline{\boldsymbol{R}}}\big(\underline{\theta}(t+\tau)\big) \cdot \underline{\underline{\boldsymbol{R}}}\big(\underline{\theta}(t)\big)^T \left(\boldsymbol{g} + \boldsymbol{a}_t(t)\right) \right] \cdot \left[\left(\boldsymbol{g} + \boldsymbol{a}_t(t+\tau)\right) \right] \right\rangle \\
&= \langle \boldsymbol{g} \cdot \left[\underline{\underline{\boldsymbol{T}}}(t,\tau) \boldsymbol{g} \right] \rangle + \langle \left[\underline{\underline{\boldsymbol{T}}}(t,\tau) \boldsymbol{a}_t(t) \right] \cdot \boldsymbol{a}_t(t+\tau) \rangle \\
&\qquad + \langle \left[\underline{\underline{\boldsymbol{T}}}(t,\tau) \boldsymbol{g} \right] \cdot \boldsymbol{a}_t(t+\tau) \rangle + \langle \left[\underline{\underline{\boldsymbol{T}}}(t,\tau) \boldsymbol{a}_t(t) \right] \boldsymbol{g} \rangle \\
&\approx g^2 \langle \hat{\boldsymbol{e}}_z \cdot \left[\underline{\underline{\boldsymbol{T}}}(t,\tau) \hat{\boldsymbol{e}}_z \right] \rangle + \langle \left[\underline{\underline{\boldsymbol{T}}}(t,\tau) \cdot \boldsymbol{a}_t(t) \right] \boldsymbol{a}_t(t+\tau) \rangle
\end{aligned}
\tag{7.18}
$$

The term $\underline{\underline{\boldsymbol{T}}}(t,\tau) \equiv \underline{\underline{\boldsymbol{R}}}\big(\underline{\theta}(t+\tau)\big) \underline{\underline{\boldsymbol{R}}}\big(\underline{\theta}(t)\big)^T$ is a rotation matrix related to the instantaneous angular velocity, $\boldsymbol{\omega}$, of the particle as explained in section 3.3.1.2. Again, the two terms containing products of $\boldsymbol{g}$ and $\boldsymbol{a}$ vanish if the particle is neutrally buoyant. The term $g^2 \langle \hat{\boldsymbol{e}}_z \cdot \left[\underline{\underline{\boldsymbol{T}}}(t,\tau) \hat{\boldsymbol{e}}_z \right] \rangle$ is related to the tumbling of a spherical particle [76].

In contrast to the other auto-correlation Eq. (7.17), one cannot subtract a mean value prior computing $\langle \boldsymbol{a}_{\mathrm{SP}}(t) \cdot \boldsymbol{a}_{\mathrm{SP}}(t+\tau) \rangle$. To estimate the ratio between $g^2 \langle \hat{e}_z \cdot \left[\underline{\underline{\boldsymbol{T}}}(t,\tau) \hat{e}_z \right] \rangle$ and $\langle \left[\underline{\underline{\boldsymbol{T}}}(t,\tau) \boldsymbol{a}_t(t) \right] \cdot \boldsymbol{a}_t(t+\tau) \rangle$ it is helpful to normalize by g^2. If $\langle \boldsymbol{a}_{\mathrm{SP}}(t) \cdot \boldsymbol{a}_{\mathrm{SP}}(t+\tau) \rangle$ becomes uncorrelated is does not necessarily vanish. If uncorrelated:

$$
\begin{aligned}
g^2 \langle \hat{\boldsymbol{e}}_z \cdot \left[\underline{\underline{\boldsymbol{T}}}(t,\tau) \hat{\boldsymbol{e}}_z \right] \rangle &= g^2 \left\langle \underline{\underline{\boldsymbol{R}}} \left(\underline{\theta}(t)\right)^T \hat{\boldsymbol{e}}_z \cdot \underline{\underline{\boldsymbol{R}}} \left(\underline{\theta}(t+\tau)\right)^T \hat{\boldsymbol{e}}_z \right\rangle \\
&= g^2 \left\langle \underline{\underline{\boldsymbol{R}}}^T \hat{\boldsymbol{e}}_z \right\rangle^2 \geqslant 0
\end{aligned}
\tag{7.19}
$$

That means $\langle \boldsymbol{a}_{\mathrm{SP}}(t) \cdot \boldsymbol{a}_{\mathrm{SP}}(t+\tau) \rangle$ approaches a plateau whose height is determined by the average orientation of the particle.

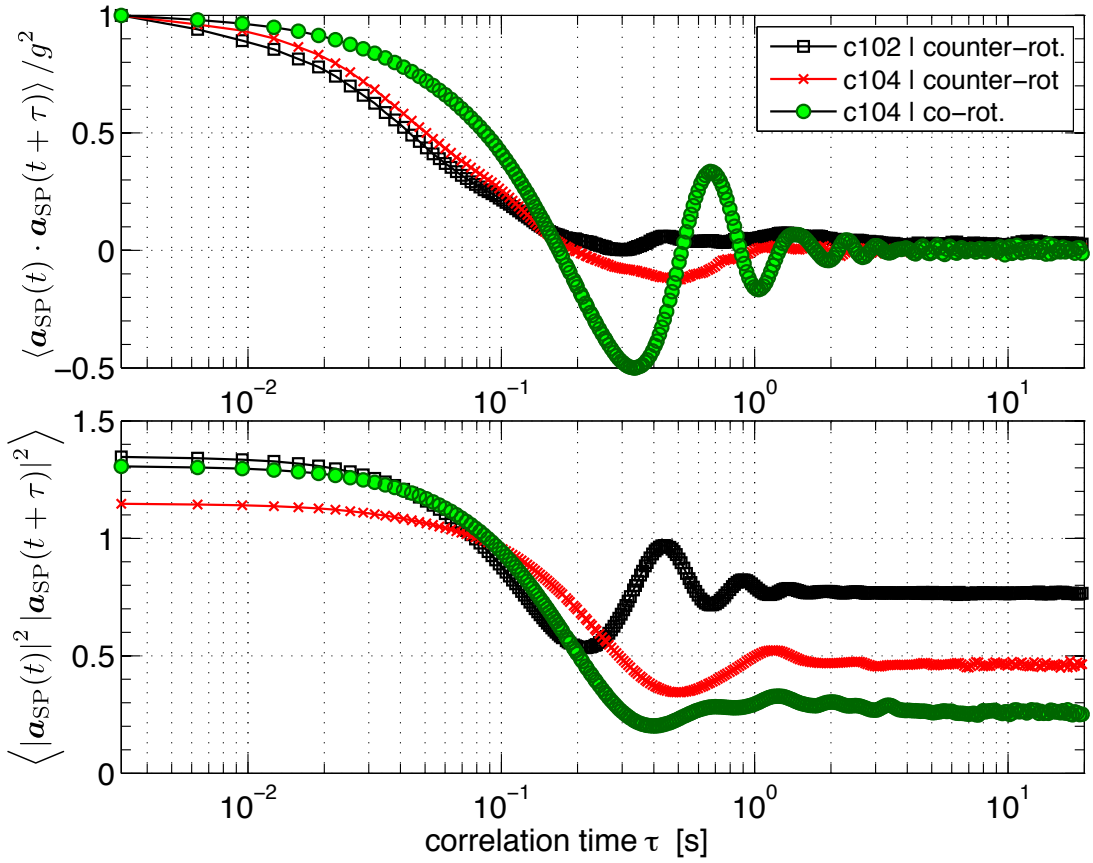

Figure 7.13: Rotation-invariant and rotation-sensitive auto-correlation functions, $\left\langle |\boldsymbol{a}_{\mathrm{SP}}(t)|^2 |\boldsymbol{a}_{\mathrm{SP}}(t+\tau)|^2 \right\rangle$ and $\langle \boldsymbol{a}_{\mathrm{SP}}(t) \cdot \boldsymbol{a}_{\mathrm{SP}}(t+\tau) \rangle$. In all cases the propeller speed is 1.5 Hz. A logarithmic scale was chosen for the abscissae as it displays both short and long time contributions to the correlations.
For the rotation invariant $\left\langle |\boldsymbol{a}_{\mathrm{SP}}(0)|^2 |\boldsymbol{a}_{\mathrm{SP}}(\tau)|^2 \right\rangle$ we find that the imbalanced particle *c102* shows only little difference to the balanced one (*c104*), which is in contrast to paragraph 7.2.3. Additionally, the autocorrelation significantly differs between counter- and co-rotating impellers.
$\langle \boldsymbol{a}_{\mathrm{SP}}(t) \cdot \boldsymbol{a}_{\mathrm{SP}}(t+\tau) \rangle$ shows a clear impact of the balance.

The lower plot in Fig. 7.13 depicts $\langle \boldsymbol{a}_{\mathrm{SP}}(t) \cdot \boldsymbol{a}_{\mathrm{SP}}(t+\tau) \rangle$ for three different configurations at a propeller speed of 1.5 Hz. For comparison to $\left\langle |\boldsymbol{a}_{\mathrm{SP}}(t)|^2 |\boldsymbol{a}_{\mathrm{SP}}(t+\tau)|^2 \right\rangle$ only the autocorrelation function changed; the configuration and f_{prop} are the same. In contrast to the rotation-invariant function, all three curves are different and reach a plateau for $\tau \gtrsim 1$s.
To investigate the role of the plateau we plot the auto-correlation of the well-balanced particle for increasing f_{prop} in Fig. 7.14. For $f_{\mathrm{prop}} \lesssim 1$ Hz one finds little change with the plateau at almost 1. For $f_{\mathrm{prop}} \approx 2$ Hz the plateau drops but is still non-zero. Further increase in f_{prop} the plateau vanishes. At the same frequency range we observe that the PDF of the components of $\boldsymbol{a}_{\mathrm{SP}}$ becomes centered and symmetric.

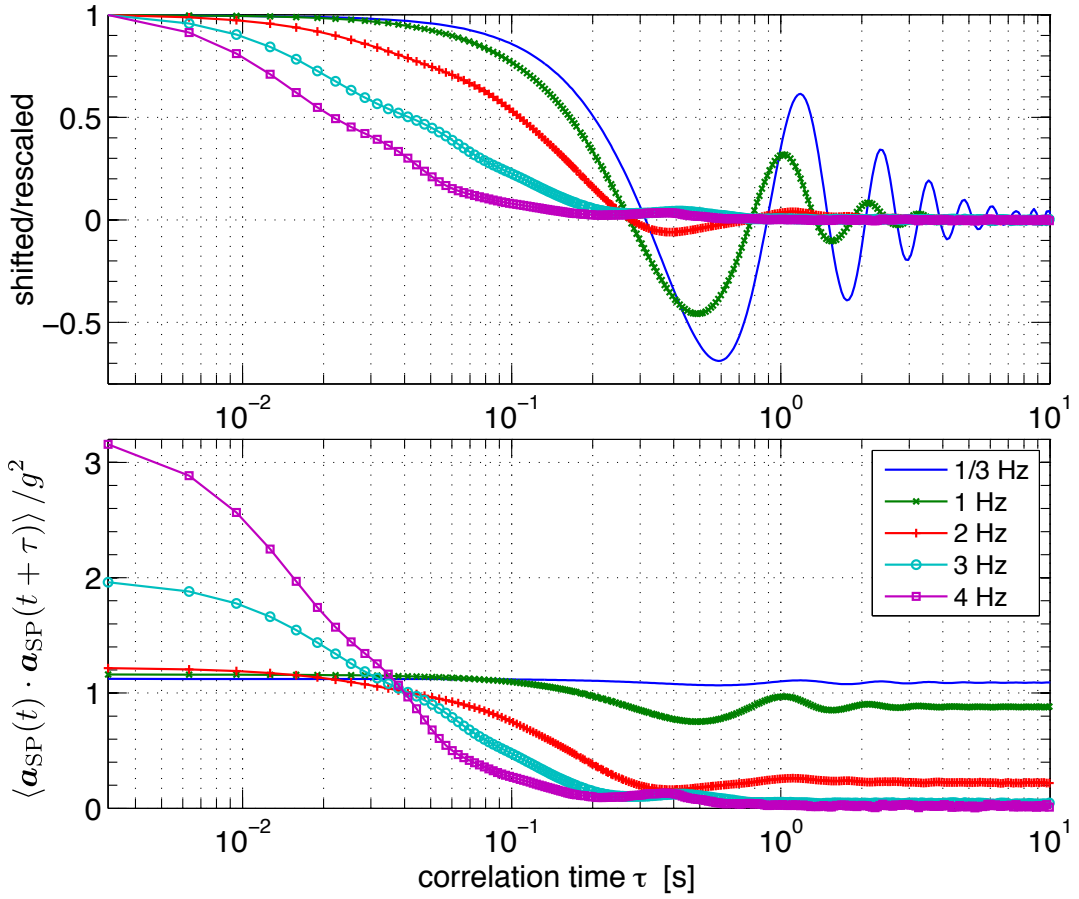

Figure 7.14: Dependence of $\langle \boldsymbol{a}_{\mathrm{SP}}(t) \cdot \boldsymbol{a}_{\mathrm{SP}}(t+\tau) \rangle$ on the propeller speed (balanced particle *c104*, counter-rotating propellers). The top plot shows the same data after subtracting the plateau and rescaling $\langle \boldsymbol{a}_{\mathrm{SP}}(t) \cdot \boldsymbol{a}_{\mathrm{SP}}(t+\tau) \rangle$.

In order to gain access to the fluctuations around a mean value, $\boldsymbol{\mu}$, one can subtract the plateau and then rescale. This is done for in the top plot of Fig. 7.14.

It becomes clear that a more detailed investigation of the particle's trajectory is needed. In section 7.4 we present results from the acquisition of the signal and the simultaneous 6-dimensional tracking of the instrumented particle.

7.2.5 Time scales

The auto-correlation functions contain one (or more) time-scale which are related to the movement of the particle in the flow. The functions resemble transient functions of a harmonic oscillator: Fig. 7.13 demonstrates the two scenarios of (weakly) damped and over-damped oscillation. We therefore tried the following techniques to extract meaningful time-scales of a sample auto-correlation function, $A(\tau)$:

value-crossing This straightforward ansatz determines when $A(\tau)$ is smaller some threshold A_0 for the first time. The resulting time-scale, τ_{corr}, strongly depends on the choice of the threshold. Moreover, in some runs $A(\tau)$ falls close to 0 but stays positive, one should thus not set $A_0 \approx 0$. This method underestimates the correlation time of the oscillating case.

fit Since $A(\tau)$ reminds one of the (driven) harmonic oscillator, we fit the weakly damped:

$$f_o(\tau) = a_0 \, \exp\left(-\tau/\tau_{\text{corr}}\right) \cdot \sin\left(2\pi f_{\text{osc}} + \phi_0\right) \tag{7.20}$$

and the critically damped transient function:

$$f_d(\tau) = \exp\left(-\tau/\tau_{\text{corr}}\right) \cdot \left(a_0 + a_1\,\tau\right) \tag{7.21}$$

to $A(\tau)$; τ_{corr}, f_{osc} and a_0, a_1, ϕ_0 are fit-parameters. We return τ_{corr} from the test function which performs better in approximating $A\left(\tau\right)$. f_{osc} enables us to estimate the tumbling frequency of the particle. We also tested the over-damped case (which is a sum of exponential decays), but it showed to be not numerically robust.

slope One can further determine the slope of $A(\tau)$ near $\tau = 0$ *i.e.* the derivative at $\tau \approx 0$. For the strongly-damped case this corresponds to fitting an exponential decay $f_e(\tau) = \exp\left(-\tau/\tau_{\text{corr}}\right)$ to $A\left(\tau\right)$. However, in the case of an oscillating $A\left(\tau\right)$ one obtains a value proportional to the frequency of the oscillation but not to de-correlation.

Mittag-Leffler We stumbled upon the Mittag-Leffler function, which performs surprisingly well in approximating $A(\tau)$. It is related to fractional differential equations. However, we do not (yet) understand its full meaning and how to extract timescales.

integral The integral of the auto-correlation function gave no valid results.

The fit method performs best and is thus selected.

Fig. 7.15 shows τ_{corr} as a function of the propeller speed and driving. For the rotation invariant function $\left\langle \left|\boldsymbol{a}_{\text{SP}}(t)\right|^2 \left|\boldsymbol{a}_{\text{SP}}(t+\tau)\right|^2 \right\rangle$ we find that τ_{corr} of the balanced particle in a counter-rotating flow or the LEM follows roughly a $f_{\text{prop}}^{-1.5}$ power-law as suggested by the scaling of the Kolmogorov time scale, $\tau_\eta \propto \varepsilon^{-1/2}$ and $\varepsilon \propto f_{\text{prop}}^3$. Moreover, it is

as expected τ_{corr}(counter-rotation)$<\tau_{\text{corr}}$(co-rotation). It should be pointed out, that co-rotating impellers induce only small variations in τ_{corr}, but an oscillation frequency following the propeller speed with $f_{\text{osc}} \sim \frac{2}{3} f_{\text{prop}}$ (not shown in figure). Surprisingly, the imbalance particle behaves completely different than its balanced counterpart.

After removing the plateau and re-normalizing one can apply the same method to the rotation sensitive function, $\langle \boldsymbol{a}_{\text{SP}}(t) \cdot \boldsymbol{a}_{\text{SP}}(t+\tau) \rangle$: whereas this method performs poorly for the LEM data, we note the runs in the KLAC are almost alike and follow the same $f_{\text{prop}}^{-1.5}$ power-law.
Furthermore, one gains access to the tumbling frequency, f_{osc} (cf. right plot in Fig. 7.15). f_{osc} varies only little with propeller speed. In the case of the imbalanced smartPart we find $f_{\text{osc}} \approx 2.4$ Hz which is close to the resonance frequency found earlier. Further, it is f_{osc}(imbalanced)$\sim 2.5 f_{\text{osc}}$(balanced). With $T = 2\pi\sqrt{J/\left(g\, m\, r_{\text{disp.}}\right)}$ (Eq. (7.16)) one thus estimates, that the displacement between center of mass and geometric center of balanced particles is 6 times smaller than for the imbalanced particle.

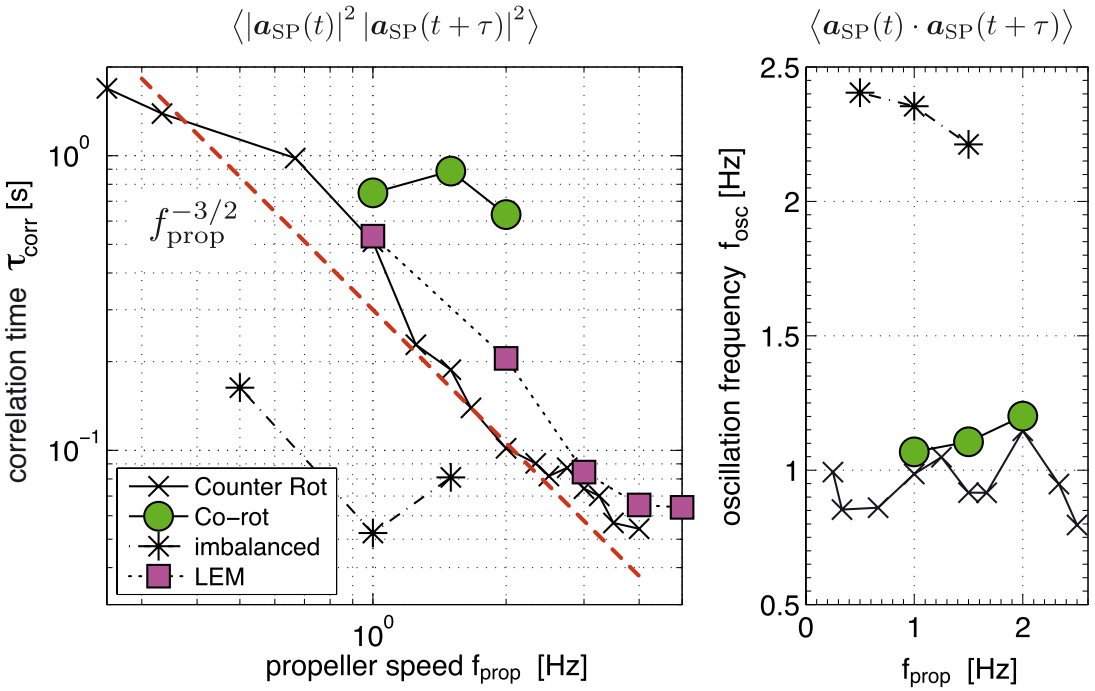

Figure 7.15: Time scales of flow and particle tumbling. τ_{corr} is determined from the rotation invariant auto-correlation and the tumbling of the particle, f_{osc}, from the rotation-sensitive function. The dashed line (left plot) indicates a $f_{\text{prop}}^{-1.5}$ power-law, which stems from the scaling of the Kolmogorov time scale ($\tau_\eta \propto \varepsilon^{-1/2}$ and $\varepsilon \propto f_{\text{prop}}^3$).

7.3 Estimating flow parameters

If key parameters of the flow can be estimated with an instrumented particle, this novel apparatus becomes a promising tool for engineers. In order to compare between simulations and mixers one would like to know the energy transfer rate ε, eddy diffusivity ν_{eddy}, correlation time scales, τ_{corr} and the turbulence level. In the section before we gained access to the moments of the translation and times scales of the flow.

In the following we develop suitable approximations based thereon.

7.3.1 Energy transfer rate

Based on the particle diameter D_{SP}, its acceleration a_{magn}, and a time, τ_{corr}, one can construct[10] an estimate of the energy transfer rate ε. The following four combinations of these three quantities yield the unit $[\text{m}^2/\text{s}^3]$ of the energy injection rate:

$D_{\text{SP}} \cdot a_{\text{magn}} \cdot \tau_{\text{corr}}^{-1}$ Although this estimate is not based on Kolmogorov-type arguments, it considers both motion of the particle and the flow structure. However, we found that $D_{\text{SP}} \cdot a_{\text{magn}} \cdot \tau_{\text{corr}}^{-1}$ delivers an acceptable approximation for tracer particles in the Göttingen LEM (cf. section A.1), too.

$D_{\text{SP}}^{2/3} \cdot a_{\text{magn}}^{3/2}$ is motivated by an extension of the Heisenberg-Yaglom scaling to finite size particles [74]:

$$\left\langle a^2 \right\rangle = a_0 \, \varepsilon^{3/2} \, \nu^{-1/2} \left(\frac{D}{\eta} \right)^{-2/3} \tag{7.22}$$

Inserting $\eta = \nu^{3/4} \, \varepsilon^{-1/4}$ and $a_0 \approx 1$ yields $\varepsilon = D^{1/2} \, \left\langle a^2 \right\rangle^{3/4}$

$a_{\text{magn}}^2 \cdot \tau_{\text{corr}}$ The Heisenberg-Yaglom scaling further tells that $\left\langle a^2 \right\rangle \cdot \tau_\eta \sim \varepsilon$ in the case of tracers. For large spheres ($D \gg \eta$) this is unlikely to hold.

$D_{\text{SP}}^2 \cdot \tau_{\text{corr}}^{-3}$ is just named for completeness, as it is only based on the flow structure but not the particle motion.

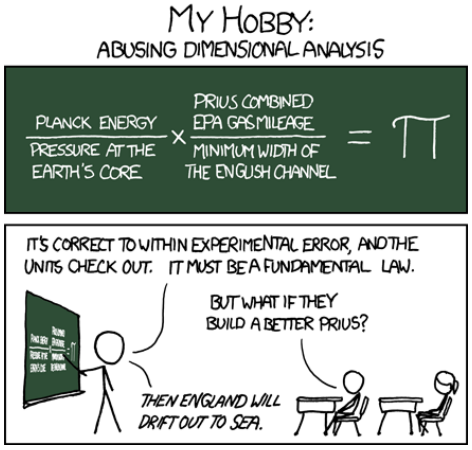

10 http://xkcd.com/687/

Based on previous observations we can rule out some of the combinations:
– a_{magn} is almost the same for co- and counter-rotating forcing. One therefore concludes that combinations, which do not contain τ_{corr}, cannot distinguish between the two forcings and are mostly likely wrong.
– Furthermore, τ_{corr} is larger in the co-rotating than in the counter-rotating case. Consequently and in contrast to measurements of ε, $a_{\mathrm{magn}}^2 \cdot \tau_{\mathrm{corr}}$ is larger for the co-rotating driving, too.

In the LEM and the KLAC we have knowledge of ε by either measuring the mechanical power injected by the motors or from PIV data in the center of the LEM. We can thus test the four combinations. In the case of counter-rotating impellers, all estimates are comparable for $f_{\mathrm{prop}} > 2$ Hz. However, for lower propeller speeds and for co-rotating driving the estimates cover three orders of magnitude. Only $D_{\mathrm{SP}} \cdot a_{\mathrm{magn}} \cdot \tau_{\mathrm{corr}}^{-1}$ gives an approximation close to the measured ε for both drivings; it is provided in Fig. 7.16. The estimator performs similar in the LEM when comparing to ε based on the power injected by the motors. It should be pointed out, that ε(motor) is 20 times the value measured in the center by PIV. The discrepancy between the two ways of estimating ε has been noted for the Göttingen LEM, too.

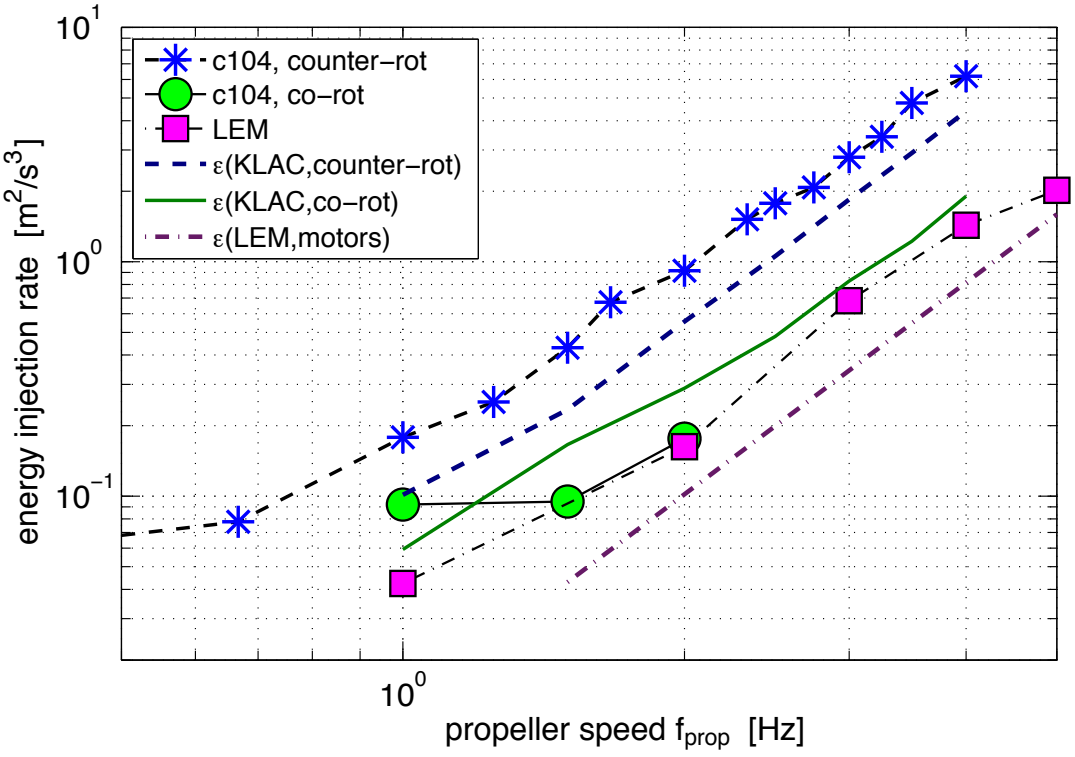

Figure 7.16: Estimating the energy injection rate, ε, from $D_{\mathrm{SP}} \cdot a_{\mathrm{magn}} \cdot \tau_{\mathrm{corr}}^{-1}$.
ε(KLAC) and ε(LEM) denotes measurements based on the power injection of the motors. Note that ε(LEM) is 20 times larger than ε calculated from PIV measurement in the center of the apparatus.

7.4 Simultaneous Tracking & Acquisition

In order to better understand the instrumented particle and to verify that its observed Lagrangian acceleration is related to the flow, we applied our six-dimensional tracking technique[11]. That means that we synchronize the smartCenter with high-speed cameras to acquire the particle's signal while simultaneously filming it.

The experiment is performed as follows:

- One first adjust the density, mounts a fresh coin cell and closes the capsule. It is wise to check that the particle is leak-tight and in stand-by mode. Here we use the particle with circuit *c104*.
- The painting of the texture follows. To determine the texture and the orientation of the acceleration sensor with respect to the texture one then takes images-signal pairs at several arbitrary orientations as described in 7.1.3. Because the procedure to compute texture and calibration takes too long, it is left for after the experiment. The smartPart is now ready for the measurement and can be injected in the mixer.
- For the actual measurement the control PC triggers both cameras and the smartCenter to start the acquisition of a movie-signal pair. Once the memory of the camera is full it starts the transfer to a hard drive. When the downloading is finished, it also stops the acquisition of the smartCenter. This procedure is repeated until the particle's battery is empty.
- After calibration, the movies and raw acceleration signal are processed and one obtains the trajectories. Each track contains the particle's 3D position as well as its absolute orientation and additionally the acceleration signal of the instrument particle. The small time shift (cf. section 7.1.1.2) between the three axes is taken into account.

7.4.1 Agreement between 6D tracking & acceleration signal

The two measurement techniques observe the motion of the instrumented particle in two completely different reference frames:

lab frame The 6D tracking uses a fixed, non-rotating coordinate system.

particle frame As the particle is advected and turned in the flow, it and the embarked accelerometer constantly rotate their coordinate system with respect to the lab frame. The acceleration signal is thus measured in a frame, which is rotating and not fixed.

With help of $\boldsymbol{a}_{SP} = \underline{\underline{\boldsymbol{R}}}_{\mathrm{TS}}^{T}\, \underline{\underline{\boldsymbol{R}}}\left(\underline{\theta}\right)^{T} \left[\boldsymbol{g} + \frac{\mathrm{d}^2}{\mathrm{d}t^2}\left(\boldsymbol{x}(t) + \boldsymbol{r}\right) + \boldsymbol{\omega} \times \left(\boldsymbol{\omega} \times \boldsymbol{r}\right) + \frac{\mathrm{d}\boldsymbol{\omega}}{\mathrm{d}t} \times \boldsymbol{r}\right]$ (Eq. (7.2)) it is possible to compute the forces acting on a point inside the particle and then project these into the rotating particle frame. We can also express the signal of the

[11] At the beginning the orientation tracking was mostly motivated by instrumented particles.

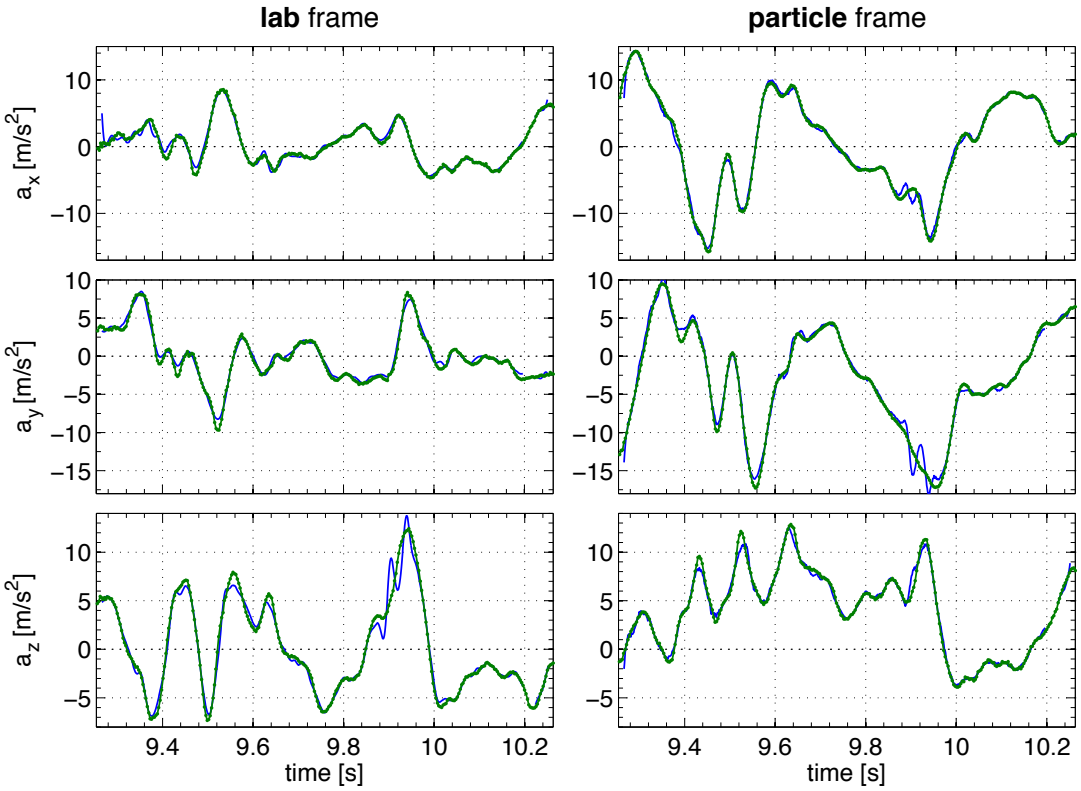

Figure 7.17: A sample trajectory of the instrumented particle seen by the camera (—) or smartPart (•), it is $f_{\text{prop}} = 3$ Hz. The absolute orientation enables us to re-express the camera measurement in the moving frame of the particle or the particle in the lab frame. In the latter gravity is subtracted.

smartPart in the lab frame by rotating it such that it corresponds to a non-rotating particle. To distinguish the different coordinate systems and techniques, we use $\boldsymbol{a}_{\text{6D}}$ for the optical technique and $\boldsymbol{a}_{\text{SP}}$ for the accelerometer data. $^{\mathbb{L}}$ and $^{\mathbb{P}}$ denote lab and particle frame, respectively.

Fig. 7.17 shows a sample trajectory in both coordinate systems. The agreement between the two techniques is remarkable. Unfortunately, after comparing several different trajectories, it becomes clear that no easy transformation is available to get rid of the rotation of the particle.

Deviations between the two techniques stem from

position measurement: Bubbles, reflections and other impurities alter the measured position of the particle. The acceleration is the second derivate and thus highly sensitive to such events.

orientation measurement: The absolute orientation is needed to change between the reference frames. The uncertainty in the absolute orientation is typically $3\,^\circ$ (cf. paragraph 3.3.3); that results in a wrong projection of gravity of ± 0.5 m/s^2. It further biases the rotational forces, as they are derivatives of the orientation time-series.

matrix relating sensor and texture: This matrix is constant and thus a systematic contribution. The uncertainty is less than 2° – *i.e.* the error in projecting gravity is < 0.3 m/s^2.

The observed agreement, $\Delta\boldsymbol{a} = \boldsymbol{a}^{\mathbb{L}}_{\mathrm{SP}} - \boldsymbol{a}^{\mathbb{L}}_{\mathrm{6D}}$, between the two techniques is as follows: All three components of $\Delta\boldsymbol{a}$ have the same PDF. Surprisingly, the (absolute) uncertainty almost doubled by increasing f_{prop} from 2 Hz to 3 Hz. Nevertheless, for 80% of the data the agreement is better than 0.8 m/s^2 and 1.6 m/s^2, respectively. That corresponds to a relative error, $|\Delta\boldsymbol{a}| \,/\, |\boldsymbol{a}_{\mathrm{6D}}|$, of less than 38% and 35%. However, this estimate is strongly biased by small values of $|\boldsymbol{a}_{\mathrm{6D}}|$.

The signal of the particle is thus corresponding to the flow, however, its interpretation is not simple.

7.4.2 Contribution of the different forces

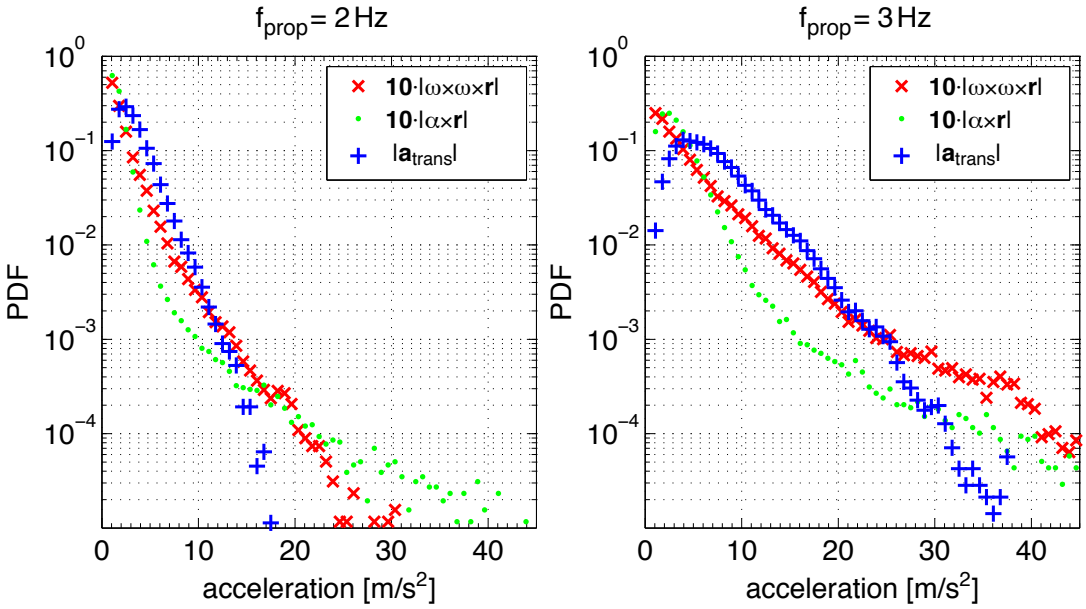

Figure 7.18: Contribution of the different forces to the motion of the smartPart. Note that the rotational forces are multiplied by **10**.

At the beginning of this chapter we reasoned that the rotational forces, $\boldsymbol{\omega} \times \boldsymbol{\omega} \times \boldsymbol{r}$ and $\boldsymbol{\alpha} \times \boldsymbol{r}$, are small compared to the translational forces[12]. The argument was based on the distance between the sensor and the particle's center of $|\boldsymbol{r}| = 3$ mm as well as the experience that $|\boldsymbol{\omega}| \sim 0.6 \cdot 2\pi\, f_{\mathrm{prop}}$. The 6D-tracking enables us to compute the different forces acting on a point at $\boldsymbol{r} = 3$ mm $\cdot\, \hat{\boldsymbol{e}}_z$ inside the sphere. As shown in Fig. 7.18, one has to multiply the PDFs of $|\boldsymbol{\omega} \times \boldsymbol{\omega} \times \boldsymbol{r}|$ and $|\boldsymbol{\alpha} \times \boldsymbol{r}|$ by a factor of **10** in order to

[12] $\boldsymbol{\alpha} \equiv \frac{\mathrm{d}\boldsymbol{\omega}}{\mathrm{d}t}$ denotes the angular acceleration.

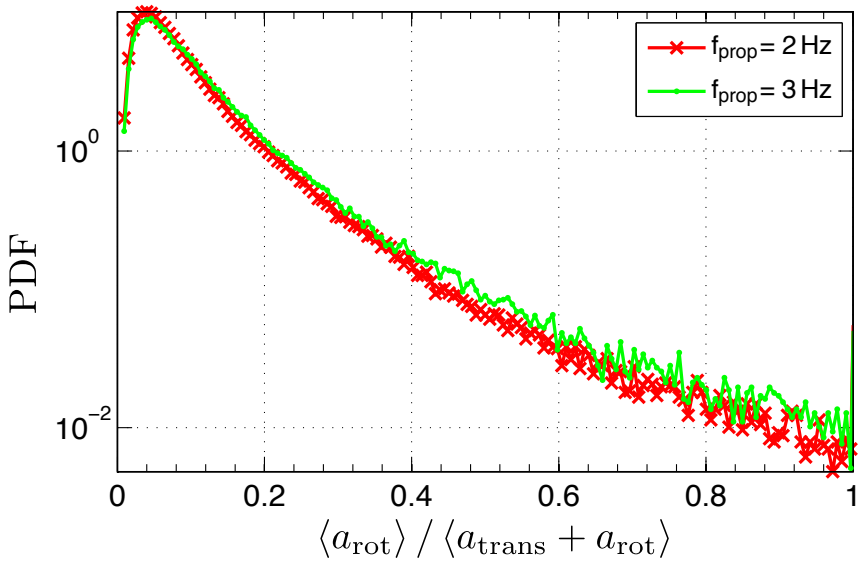

Figure 7.19: Ratio of the rotational forces to the total force acting on the particle. The 80% percentile is found at a ratio of 0.14 and 0.16, respectively.

compare them to the translation.
To fully conclude we plot the ratio of the rotational acceleration, $\boldsymbol{a}_{\text{rot}} = \boldsymbol{\omega}\times\boldsymbol{\omega}\times\boldsymbol{r}+\boldsymbol{\alpha}\times\boldsymbol{r}$ to the total acceleration, $\boldsymbol{a}_{\text{total}}$, (without gravity) in Fig. 7.19. Dimensional arguments and the results from the previous chapter tell that $a_{\text{total}} \propto f_{\text{prop}}^2$ and $a_{\text{rot}} \propto f_{\text{prop}}^2$. Consistently, the PDF of the ratio $|\boldsymbol{a}_{\text{rot}}| \,/\, |\boldsymbol{a}_{\text{total}}|$ differs only little for the two propeller frequencies. Moreover, it is peaked at 5% and the 80% percentile is at a ratio of 13.9% and 15.5%, respectively. Our ansatz to neglect the rotational forces if no 6D tracking is available is therefore legitimate.

7.4.3 Auto-correlations

7.4.3.1 Rotation-invariant auto-correlations

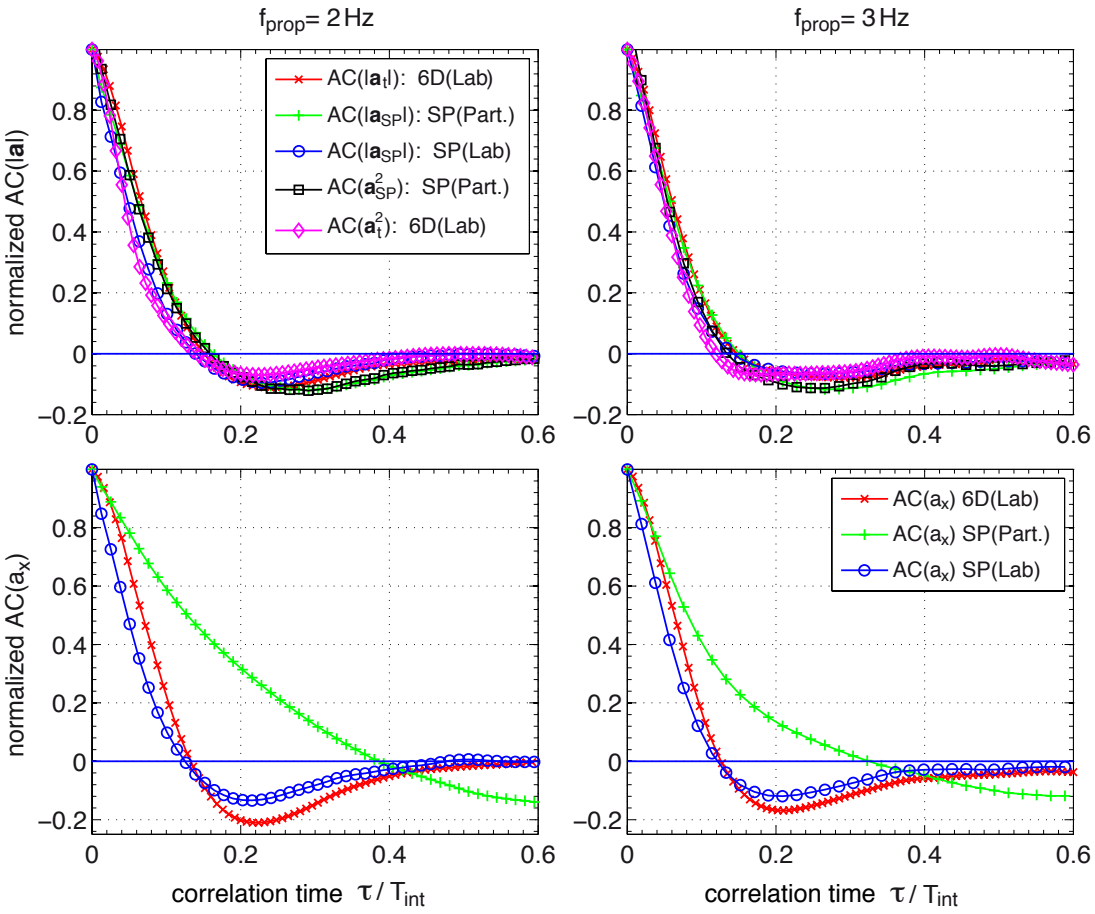

Figure 7.20: Upper plots show auto-correlations of $\left|\boldsymbol{a}^{\mathbb{L}}_{\mathrm{6D}}\right|$,$\left|\boldsymbol{a}^{\mathbb{L}}_{\mathrm{SP}}\right|$, $\left|\boldsymbol{a}^{\mathbb{P}}_{\mathrm{SP}}\right|$, $\left|\boldsymbol{a}^{\mathbb{P}}_{\mathrm{SP}}\right|^2$, and $|\boldsymbol{a}_{\mathrm{6D}}|^2$: As expected they resemble and are independent of the frame.
The lower plots show correlations for $\boldsymbol{a}^{\mathbb{L}}_{\mathrm{6D}x}$, $\boldsymbol{a}^{\mathbb{P}}_{\mathrm{SP}x}$, and $\boldsymbol{a}_{\mathrm{6D}x}$, we observed no different behavior for the y and z axis. Changing from particle frame ($\boldsymbol{a}^{\mathbb{P}}_{\mathrm{SP}x}$) to lab frame ($\boldsymbol{a}^{\mathbb{L}}_{\mathrm{6D}x}$ and $\boldsymbol{a}^{\mathbb{L}}_{\mathrm{SP}x}$) modifies strongly the observed shape.

As explained earlier in paragraph 7.2.4.1, $\langle \boldsymbol{a}^2_{\mathrm{SP}}(t)\ \boldsymbol{a}^2_{\mathrm{SP}}(t+\tau)\rangle$ is insensitive to the rotation of the particle and related to the correlation of the pure translation by

$$\left\langle \boldsymbol{a}^2_{\mathrm{SP}}(t)\ \boldsymbol{a}^2_{\mathrm{SP}}(t+\tau)\right\rangle = \left\langle \boldsymbol{a}^2_{\mathrm{trans}}(t)\ \boldsymbol{a}^2_{\mathrm{trans}}(t+\tau)\right\rangle + 4g^2\left\langle a^z_t(t)\ a^z_t(t+\tau)\right\rangle + const$$

Linear algebra tells that the norm of $\boldsymbol{a}_{\mathrm{trans}}$ and $\boldsymbol{a}_{\mathrm{SP}}$ is also insensitive to the rotation. The two top plots in Fig. 7.20 shows for the two propeller speeds the auto-correlations[13] of the norm $\left\langle |\boldsymbol{a}^{\mathbb{L}}_{\mathrm{6D}}(t)|\cdot|\boldsymbol{a}^{\mathbb{L}}_{\mathrm{6D}}(t+\tau)|\right\rangle$, $\left\langle |\boldsymbol{a}^{\mathbb{L}}_{\mathrm{SP}}(t)|\cdot|\boldsymbol{a}^{\mathbb{L}}_{\mathrm{SP}}(t+\tau)|\right\rangle$, and

[13] We plot the unbiased auto-correlation with a prior subtract of the local mean.

$\left\langle |\boldsymbol{a}^{\mathbb{P}}_{\mathrm{SP}}(t)| \cdot |\boldsymbol{a}^{\mathbb{P}}_{\mathrm{SP}}(t+\tau)| \right\rangle$ as well as the quantities derived earlier, $\left\langle |\boldsymbol{a}^{\mathbb{L}}_{\mathrm{SP}}(t)|^2 \cdot |\boldsymbol{a}^{\mathbb{L}}_{\mathrm{SP}}(t+\tau)|^2 \right\rangle$ and $\left\langle |\boldsymbol{a}^{\mathbb{L}}_{\mathrm{6D}}(t)|^2 \cdot |\boldsymbol{a}^{\mathbb{L}}_{\mathrm{6D}}(t+\tau)|^2 \right\rangle$.
They all cross 0 at the same time of $\tau \sim 0.15\, T_{\mathrm{int}}$ and their shape resembles (with a slight improvement for $f_{\mathrm{prop}} = 3$ Hz). That means that they are independent of the coordinate system.

In other words, they only depend on the translation, $\boldsymbol{a}_{\mathrm{trans}}$, and not on the rotation of the particle.

7.4.3.2 Rotation-sensitive auto-correlations

On the other hand, the single components of the smartPart are altered by the rotation. The lower plots of Fig. 7.20 illustrate that the auto-correlation of a single component strongly depends on its reference frame *i.e.* changing from particle frame ($\boldsymbol{a}^{\mathbb{P}}_{\mathrm{SP}x}$) to lab frame ($\boldsymbol{a}^{\mathbb{L}}_{\mathrm{6D}x}$ and $\boldsymbol{a}^{\mathbb{L}}_{\mathrm{SP}x}$) modifies strongly the observed shape of the function. In the particle frame we observed longer correlations; however, the effect seems to decrease with propeller frequency. In contrast to experiments with tracer particle, the components, $a^{\mathbb{L}}_i$, in the lab frame de-correlate comparable to the norm of the acceleration $|\boldsymbol{a}|$. One further notices that the autocorrelation in the lab frame cross 0 at the same fraction of the integral time scale, T_{int}.

Tumbling To get a better understanding of the auto-correlation of the tumbling (cf. Eq. (7.18)), we now investigate the two contributions to

$$\langle \boldsymbol{a}_{\mathrm{SP}}(t) \cdot \boldsymbol{a}_{\mathrm{SP}}(t+\tau) \rangle = g^2 \left\langle \hat{e}_z \cdot [\underline{\underline{\boldsymbol{T}}}(t,\tau)\hat{e}_z] \right\rangle + \left\langle [\underline{\underline{\boldsymbol{T}}}(t,\tau)\boldsymbol{a}_t(t)] \cdot \boldsymbol{a}_t(t+\tau) \right\rangle$$

As shown in Fig. 7.21, the term, $\left\langle [\underline{\underline{\boldsymbol{T}}}(t,\tau)\boldsymbol{a}_t(t)] \cdot \boldsymbol{a}_t(t+\tau) \right\rangle$, falls fast to 0 and is strongly depending on the forcing.

The left term $\left\langle \hat{e}_z \cdot [\underline{\underline{\boldsymbol{T}}}(t,\tau)\hat{e}_z] \right\rangle$ dominates $\langle \boldsymbol{a}_{\mathrm{SP}}(t) \cdot \boldsymbol{a}_{\mathrm{SP}}(t+\tau) \rangle$ and does not significantly change with propeller speed. It stays correlated several times longer than $\left\langle [\underline{\underline{\boldsymbol{T}}}(t,\tau)\boldsymbol{a}_t(t)] \cdot \boldsymbol{a}_t(t+\tau) \right\rangle$. Unfortunately we do not have a sufficient number of long tracks to determine the long term behavior of $\left\langle \hat{e}_z \cdot [\underline{\underline{\boldsymbol{T}}}(t,\tau)\hat{e}_z] \right\rangle$. Alain Pumir and Michael Wilkinson [76] used a spherical Ornstein-Uhlenbeck process to estimate $\left\langle \hat{e}_z \cdot [\underline{\underline{\boldsymbol{T}}}(t,\tau)\hat{e}_z] \right\rangle$. Their derivation is characterized by one dimensionless number, which they call the persistence angle. It describes the typical angle of rotation of the object during the correlation time of the angular velocity. The motion of our particle strongly resembles plots in their article describing the case of a large persistence angle.

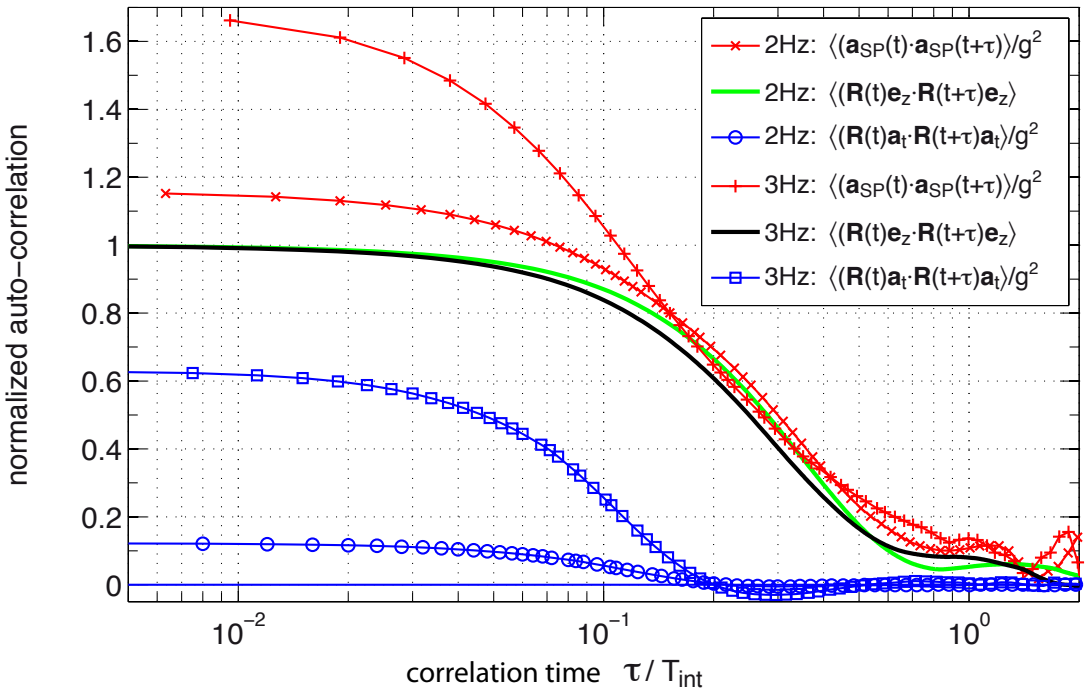

Figure 7.21: Contributions to the auto-correlation of the tumbling (see also Fig. 7.14). In agreement with Eq. (7.18), it is $\langle \boldsymbol{a}_{\rm SP}(t)\cdot\boldsymbol{a}_{\rm SP}(t+\tau)\rangle = g^2\,\langle \hat{e}_z\cdot[\underline{\underline{\boldsymbol{T}}}(t,\tau)\hat{e}_z]\rangle + \langle[\underline{\underline{\boldsymbol{T}}}(t,\tau)\boldsymbol{a}_t(t)]\cdot\boldsymbol{a}_t(t+\tau)\rangle$. The right term, $\langle[\underline{\underline{\boldsymbol{T}}}(t,\tau)\boldsymbol{a}_t(t)]\cdot\boldsymbol{a}_t(t+\tau)\rangle$, falls fast to 0, but the tracks were not sufficiently long to determine if $\langle \hat{e}_z\cdot[\underline{\underline{\boldsymbol{T}}}(t,\tau)\hat{e}_z]\rangle$ vanishes for $\tau > T_{\rm int}$.

7.4.4 Quantities accessible only to the tracking

Some properties of the movement of the particle are only accessible to the tracking. In the following we briefly show common parameters in order to related them to the movement of solid spheres. The rotational dynamics of the smartPART are discussed in detail in chapter 5 and its translation is compared to that of solid 24 mm spheres in a more viscous fluid in section 4.1.3.

We first note that at both propeller speeds the motion of the particle compares well to the motion of large solid spheres: In both cases the PDF of single components of the velocity $\boldsymbol{v}$ is approximately gaussian whereas the acceleration components are non-gaussian distributed. The particle Reynolds number, $R_p = \frac{D|\boldsymbol{u}|}{\nu}$, is 8400 ± 3500 and 12500 ± 5100, respectively.

The PDF of the magnitude of angular velocity, $|\boldsymbol{\omega}|/(2\pi)$, is peaked at $\frac{1}{2} f_{\text{prop}}$, but rotation rates up to $2.5 \cdot f_{\text{prop}}$ are observed. We further notice that PDF $\left(|\boldsymbol{\omega}|/(2\pi\, f_{\text{prop}})\right)$ is almost identical for the two propeller frequencies.

A summary of the particle motion is given in table 7.2.

		f_{prop} [Hz]	x	y	z	Norm
$\boldsymbol{v}$	[m/s]	2	-0.0 ± 0.18	0.0 ± 0.23	-0.0 ± 0.23	0.3 ± 0.1
		3	-0.0 ± 0.26	0.0 ± 0.34	-0.0 ± 0.34	0.5 ± 0.2
$\boldsymbol{a}$	[m/s^2]	2	-0.1 ± 1.8	-0.0 ± 2.1	0.0 ± 2.0	2.9 ± 1.8
		3	0.1 ± 4.1	-0.1 ± 4.6	-0.0 ± 4.7	6.6 ± 4.1
$\boldsymbol{\omega}$	[rad/s]	2	0.1 ± 4.7	0.2 ± 4.4	-0.0 ± 4.5	7.0 ± 3.5
		3	-0.5 ± 7.8	-0.2 ± 7.0	-0.2 ± 7.2	11.3 ± 5.9

Table 7.2: Characteristic values (mean±RMS) of the instrumented particle's motion.

7.4.4.1 Preferential sampling

Despite the fact that the instrumented particle is neutrally buoyant, we observe that it stays close to the impellers, in general. This effect manifests even more in the LEM: We tried particle tracking in a 20 cm region in the center of the apparatus with simple webcams but the particle did never pass through this region in preliminary tests. Fig. 7.22 shows the PDF of position for smartPart. Independent of the propeller speed it is mostly situated in a torus shape around the propeller. This agrees with the findings in section 4.1.4, where we observed preferential sampling for large, solid neutrally buoyant spheres. It should be noted that the viscosity is ~ 8 times higher for these solid spheres.

The particle, thus, samples the flow in a non-uniform way.

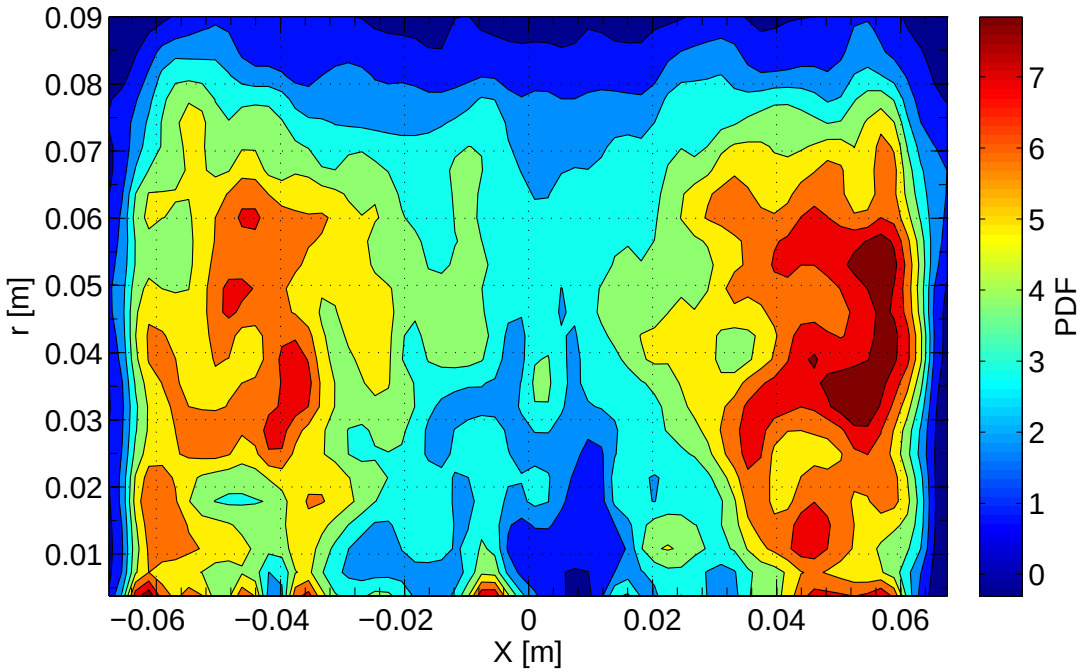

Figure 7.22: Preferred position of the instrumented particle: independent of the propeller speed it is mostly situated in a torus shape around the propeller. The same behavior is found in section 4.1.4 for large neutrally buoyant spheres.

7.5 Summary & Ideas

In this chapter we first presented the working principle of the instrumented particle, characterized its electronic performance and established a simple, fast calibration technique. We can show that an imbalance of the particle is *not* desirable, too. A weak drift and temperature dependence is noticed and we strongly advice to calibrate shortly before each experiment. We also noticed that the sampling rate can be pushed from 316 Hz to almost 400 Hz by adjusting the transmission sequence of the data packets. This requires a simple change in the program of the micro-controller.

Furthermore, we developed methods which are either invariant or adapted to the rotation of the sensor in the flow. These methods perform well within the wide range of tested turbulence levels and moreover in two different mixers. With a smartPART one gets access to correlation time scales of the flow, the variance and flatness of the (translational) acceleration and one can estimate the energy injection rate.

We limited our analysis to the extraction of global flow features. However, work on adaptive filtering techniques is ongoing. A promising candidate for such a filtering is the *Empirical Mode Decomposition*, which might be able to separate the different contributions of the signal. While investigating the auto-correlation functions we stumbled upon the Mittag-Leffler function. This function is related to fractional differential equations and the question, how a particle with inhomogeneous inertia tumbles in a turbulent flow.

On top of that we applied the 6D tracking to the particle. We find that the particle in general behaves almost identical to solid spheres of the same size in the same mixer. Similar to solid large spheres the instrumented particle samples the flow preferentially near the driving propellers.

We were further able to show that the Lagrangian acceleration of the smartPART corresponds well to its actual motion and the assumptions used to develop the earlier mentioned methods were verified. The data is further useful to test if by adding a second, well-placed accelerometer one can estimate two components of the particle's angular velocity $\boldsymbol{\omega}$ at sufficient rotation rates.

This instrumented particles can shed some light into mixers which were not or hardly accessible up to now. Due to its continuous transmission one flow configuration can be characterized within $\sim$ 30 min. Apart from its appeal for chemical and pharmaceutical industry, it might be an interesting tool to quantify flows in (*e.g.* biology) labs, too.

8 Conclusion

The cornerstone of this thesis is the novel tracking technique enabling us to follow the three dimensional position and the absolute orientation of painted, solid spheres in time. Having access to the six degrees of freedom of a particle in a turbulent flow allowed us to address important questions on the dynamics of the forces and torques acting on it. We applied this to gain insights into the motion and rotation of solid particles in a turbulent flow. Furthermore a new instrumented particle continuously transmitting its 3D Lagrangian acceleration is presented and characterized.

Solid Particles We first made use of the technique to study the linear and rotational motion of solid, neutrally-buoyant spheres; their size is a fraction of the integral length scale but large compared to the smallest scales of the flow. Expressing all physical quantities in their non-dimensional form using propeller frequency and propeller size, we find that the RMS of velocity and acceleration are determined by the propeller speed, with a non-trivial dependency on the particle size. Likewise, the spheres rotate with a rotation rate comparable and proportional to the propeller frequency. Despite the particles' large size of almost one integral length scale their acceleration statistics do not tend towards a gaussian distribution, their behavior stays intermitted. Likewise, the angular velocity and acceleration are both non-gaussian, too. We then investigated wether translation and rotation couple. Such behavior has been observed in laminar or simple shear flow configuration, but it was unclear if a coupling would persist in a fully turbulent environment. We discovered that despite the turbulent environment, translation and rotation couple in the agreement with the Magnus (or lift) force.

We remark that in contrast to small ones large spheres stay preferably in a torus-like structure near the impellers: They sample the flow preferentially. While such behavior is well-known for small particles whose density deviates from that of the fluid it has so far not been observed for neutrally-buoyant objects. However, the particles investigated in this dissertation are significantly larger than those reported in previous experiments. We are currently investigating wether this effect can be attributed to the observed lift force.

As the particle moves through the fluid it exchanges momentum with the surrounding carrier flow, the variations in kinetic energy are shown to be large compared to its small negative mean. We demonstrate that the dynamics of the energy exchange falls within the mathematical theory of large deviations and we have first evidence that the fluctuations in energy exchange satisfy a stationary state fluctuation theorem. However, more data and longer trajectories are needed to understand how the dynamics depend on the driving and on the particle diameter.

Starting from these results and our novel measurement technique new questions and topics

open up. All experiments in this dissertation were done with neutrally-buoyant particles at one viscosity. However, we recently started taking data with spheres of the same size but which are either heavier or lighter than the fluid. We plan on changing the viscosity while keeping the particle neutrally buoyant, too. This should give new insights into the role of viscous and inertial forces. One can further explore how more complex objects behave. With the instrumented particle we demonstrated that our technique can be applied to spheres of inhomogeneous inertia; an extension to ellipsoidal particles is feasible. The surface roughness (which was neglected so far) falls probably also in this question.

Also, in some of the experiments we tracked several particles simultaneously but we did not (yet) investigate their interaction. A very interesting question is if and how particles collide. One can further investigate the two-way coupling of large spheres by significantly increasing the number of spheres in the apparatus. This can either be investigated either by using one instrumented particle and many solid particles or by adding transparent gel spheres around one painted sphere.

Instrumented Particle In the second part we presented, characterized and developed methods a new instrumented particle which transmits its Lagrangian acceleration as it is advected through the flow. Having access to the absolute orientation enabled us to perform a rigorous examination of the forces acting on the particle. Comparing its results to motion of solid spheres helped further in benchmarking this novel measurement technique.

We demonstrate that this instrumented particle is simple to use and efficient for a fast characterization of flows and apparatuses; within approximately 30 min enough data is taken for one flow configuration. In addition, owing to its wireless transmission system it does not require transparent fluids nor optical access. Therefore, it can shed some light on flows, which are not (or hardly) accessible to other measurement techniques. Recent experiments by Sylvain Joubaud [29] show its applicability to granular flows, too. Apart from its appeal for chemical and pharmaceutical industry, it might be an interesting tool to quantify flows as they are found for example in biology labs, too.

The analysis was limited to the extraction of global/average flow features, but we are working on adaptive techniques. Also, statistical sampling techniques such as bootstrapping should be easily adaptable to our developed methods.

Sidetracks Two sidetracks were followed during this thesis: A second Lagrangian Exploration Module has been built and we carried out a promising feasibility study for a pH probe adapted for the study of chemical mixing in flows.

A Sidetracks

A.1 The second Lagrangian Exploration module

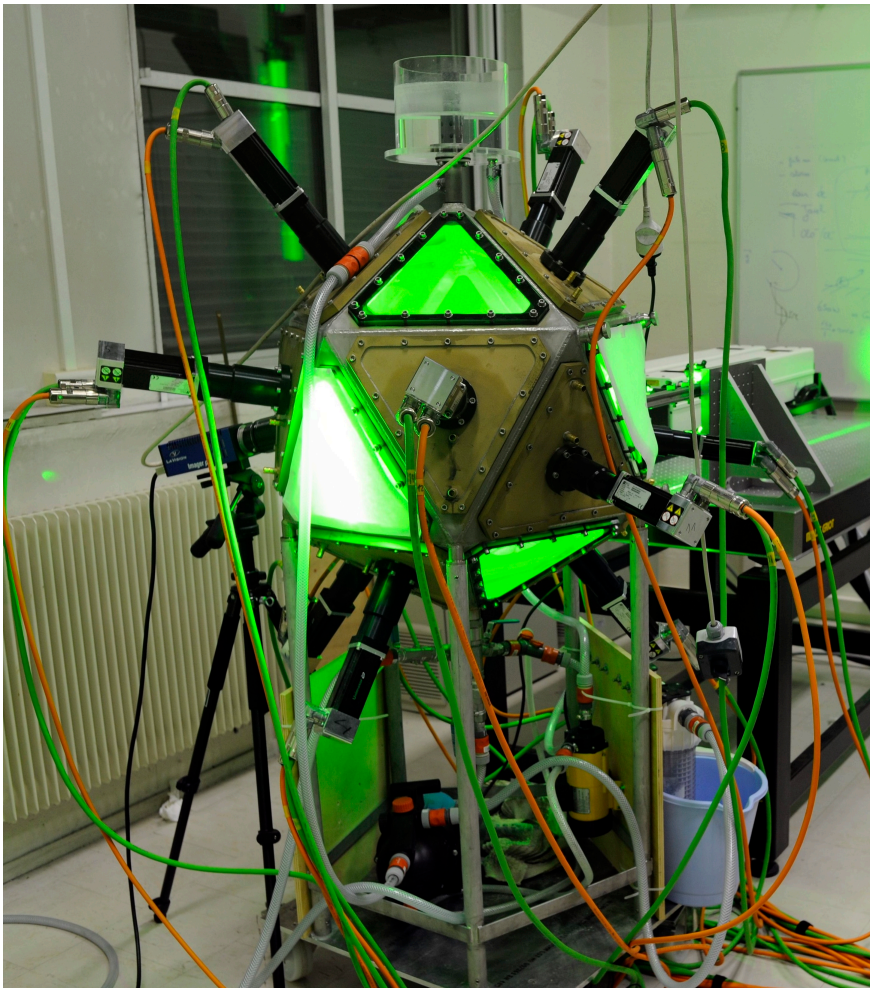

Figure A.1: Picture of the Lyon LEM illuminated by a green laser beam.

The *Lagrangian Exploration Module* (LEM) has been built and designed in a collaboration between the ENS Lyon and the Max-Planck-Institut für Dynamik und Selbstorganisation in Göttingen. Two apparatuses were manufactured[1], one at each side, the flow is described in detail in my Diplomarbeit[80] and in [85].

[1] and assembled by the same guy

The LEM produces turbulence in a closed water flow driven by twelve impellers. A picture is provided in Fig. A.1 and CAD drawings in Fig. A.2. In both versions the edge length of the icosahedron is 40 cm, giving a volume of 140 l water. The Lyon LEM is rotated with respect to the Göttingen LEM as shown in Fig. A.2 and the two version differ in the choice of motors, impellers and the placement of the impellers. In Lyon the 12 impeller units are mounted to 12 of the 20 faces of the icosahedron whereas in Göttingen these units are mounted to the 12 vertices. Also, the Lyon LEM uses stronger brushless motors (Unidrive, Emerson Industrial): each delivers up to 600W of mechanical energy at a maximum torque of 1.5 Nm. However, the electronics are not integrated in the motor, they have to be supplied with three-phase current. We, therefore, house them in a electrical panel and connect their analog in- and outputs to a USB acquisition card (National Instruments) linked to a control computer. Both LEMs are thus rather big USB devices. A Labview program then controls the motor independently; additionally it tracks torques and instantaneous propeller frequencies.

This apparatus has served for the characterization of the instrumented particle (chapter 7); Lionel Fiabane [15] characterized the flow by means of PIV measurements. He further uses the LEM for research on the clustering of particles [16].

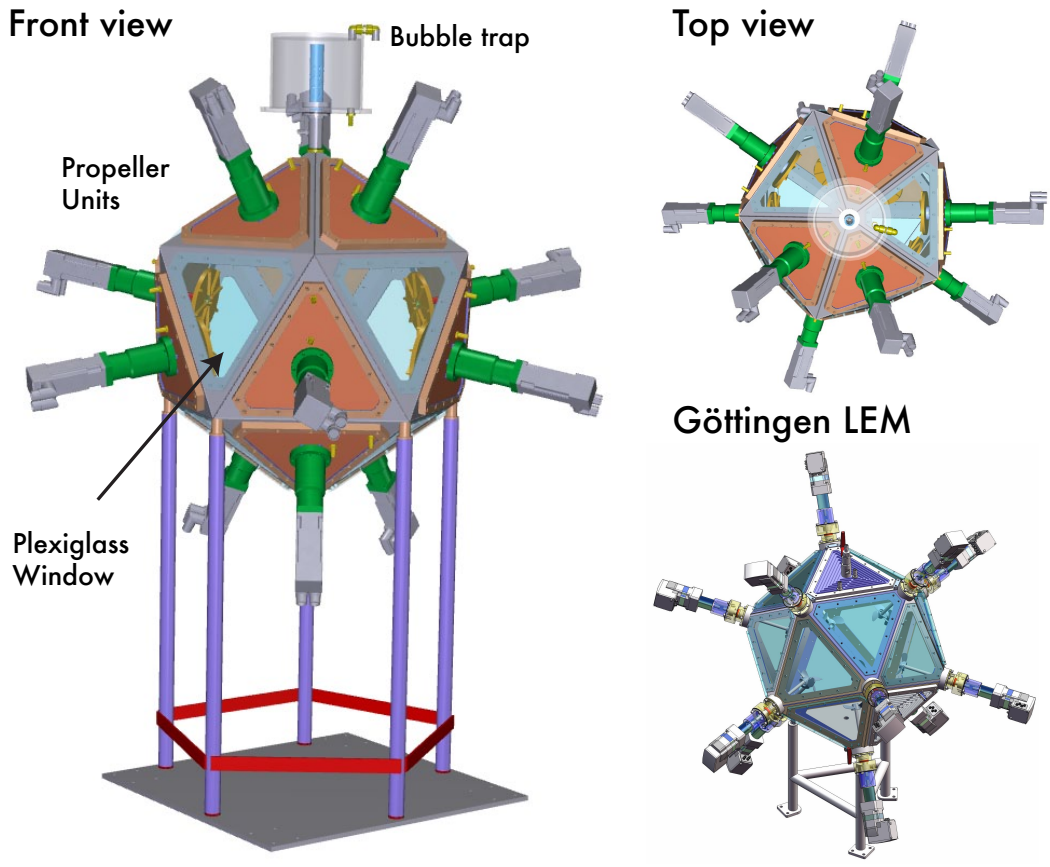

Figure A.2: CAD drawings, for comparison a CAD drawing of the Göttingen version is shown, too.

A.2 Mixing in chemical reaction: first results of a fast, local, and continuously-operating pH-probe

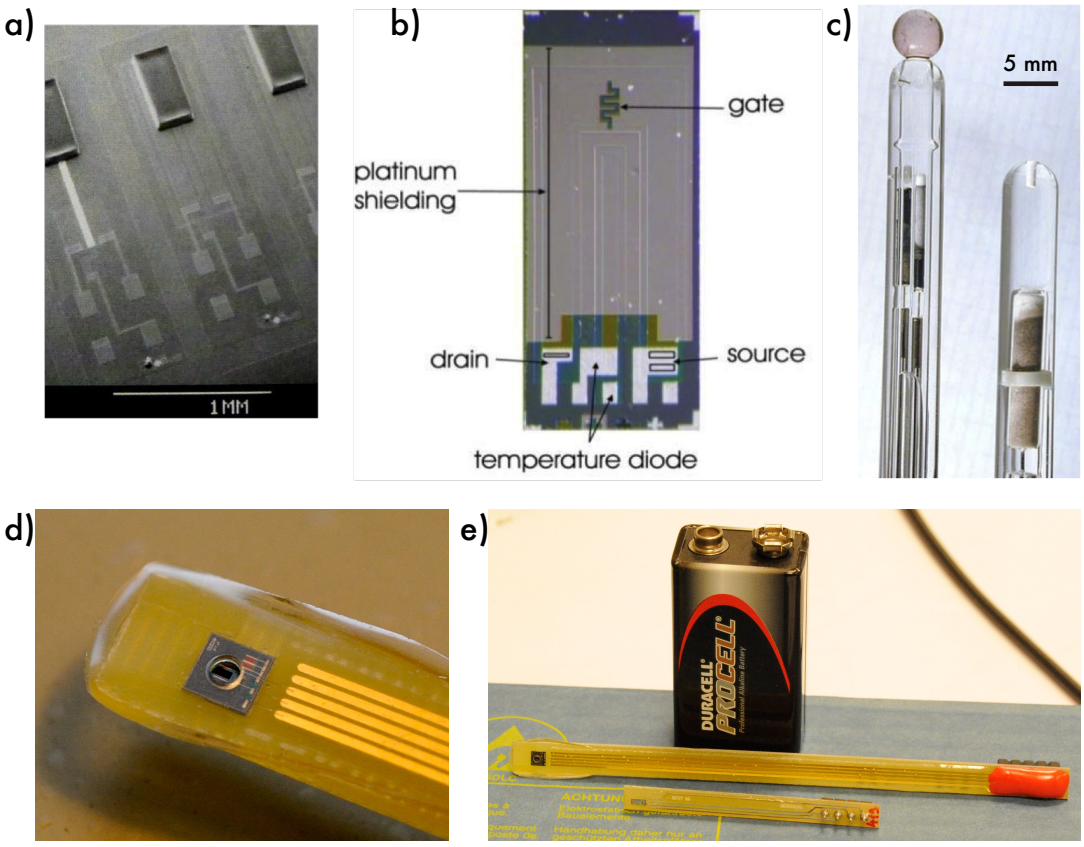

Figure A.3: **a)** electron microscope image of an ISFET **b)** typical ISFET die **c)** typical reference electrodes **d)** & **e)** pictures of our test ISFETs.

In the study of mixing most experiments are done in flows without *any* additional chemical reaction. However, in chemical or pharmaceutical industry but also in biological systems one often finds chemicals which flow into each other. When these react they form new products, release or consume energy and change the composition of the flow. Hence, the reactions add new timescales to already known time and length scales of the flow. In order to observe a chemical reaction and the mixing one would like to measure one (or more) characteristic property of the reaction as fast as possible. Moreover, the measurement should be local and not influence the reaction. Conductivity, chemical potential and ion-concentration (*i.e.* the acidity of a solution) are possible candidates and we show here a feasibility study of an *Eulerian pH-probe* for use in agitated flows. Unfortunately the classical glass electrode[2] has a reaction time of approximately one minute. Furthermore, it is rather fragile and large. We identified *Ion-Sensitive Field Effect Transistors* (ISFET) as a promising alternative. ISFETs measure locally with an active surface

[2] as discussed for example in Atkins' book *Physical Chemistry* [3]

smaller than 1 mm^2 and show response times of the order of $1/10$ s. In cooperation with smartInst we verified that the sensor can be integrated into an instrumented particle, too.

In the following we sketch their working principle, circuitry and a first promising measurement. Since this sidetrack does not fit into the storyline of the manuscript, we just outline the basic idea. For further reading the reader is referred to J. Janata's book *Principles of chemical sensors* [27] and a review article by P. Bergveld *Thirty years of ISFETOLOGY: What happened in the past 30 years and what may happen in the next 30 years* [8] and the references therein.

Working principle Field effect transistors [25] change the conductance between its drain and source contact in function of the electric field at the gate contact. In contrast to bipolar transistors no current flows through the gate. In 1970 P. Bergveld discovered that a field effect transistor can measure small variations in the ion concentration (of a solution) if one replaces the gate contact with an ion-sensitive membrane which is in contact with a solution; the *Ion-Sensitive Field Effect Transistor* (ISFET) was born.

An ISFET in contact to a solution is sketched in Fig. A.4. In the simplest case it can be described as a sandwich of six different layers (see Fig. A.4) and one can write the chemical potentials at each interface:
Ions can move from the solution into the membrane and back. Thus, the electro-chemical potentials, μ^{ion}, at the interface membrane/solution equal and the potential difference is given by the Nernst equation:

$$\frac{\mu_2^{\text{ion}} - \mu_3^{\text{ion}}}{z_{\text{ion}}\mathcal{F}} = \pi_0 + \frac{\mathcal{R}\,T}{z_{\text{ion}}\mathcal{F}} \ln a_2^{\text{ion}} \tag{A.1}$$

$\mathcal{R}$ and $\mathcal{F}$ are universal gas and Faraday constant, π_0 a constant potential, and T is the temperature. The ion has a (chemical) activity a_2^{ion} in the solution and is z_{ion}-times charged. That means that potential at the membrane is determined by the temperature and the activity of the ion in the solution. The pH-value (*i.e.* the acidity) of a solution is defined as

$$\text{pH} = -\log_{10}\left(a\left[H^+\right]\right) \tag{A.2}$$

Hence, a membrane, which is sensitive to hydrogen H^+, has a potential difference which depended on the pH-value of the solution. Membrane sensitive to different ions (*e.g.* K^+) work in a similar fashion.

The conductivity of the drain-source channel of a field effect transistor (and thus the ISFET) depends on the potential difference between gate and source. Analyzing the remaining interfaces yields:

$$\phi(3) - \phi(5) = U_{GS} + \phi_0 + T\,\frac{\mathcal{R}}{z_{\text{ion}}\mathcal{F}} \ln a_2^{\text{ion}} \tag{A.3}$$

U_{GS} is the applied potential difference between reference electrode and solution, and ϕ_0 contains constant terms[3]. Unfortunately, Eq. (A.3) is depending on the temperature, too.

[3] contact potentials, reference electrode and the constant activities

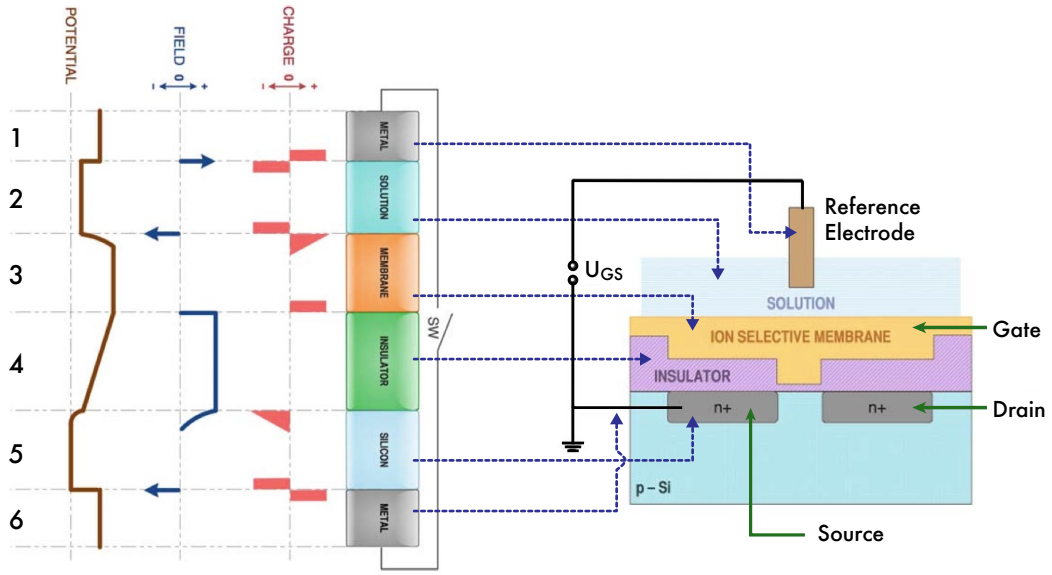

Figure A.4: Schematic of an ISFETs [adapted from [27], chapter 6.2]:
A reference electrode (**1**) without liquid junction is in contact with a solution (**2**) which contains a small amount of ions that can partition into the potassium-selective membrane (**3**). Therefore, the interface between the solution and the membrane is non-polarized. The insulator (**4**) is assumed to be ideal; that is, no charge can cross it and it is thicker than electron tunneling distance. Layer (**5**) is the semiconducting substrate of the transistor. For simplicity, the metal (**6**) is identical to metal (**1**) of the reference electrode.
The layers Membrane, Insulator, Semiconductor (**3,4,5**) form a capacitor. However, if the reference electrode is removed from the solution (by opening the circuit (**SW**)) a second capacitor between the two metals (**1**) and (**6**) is formed; the system becomes unpredictable.
Analysis of the chemical potentials yields that the voltage at the capacitor (**3,4,5**) is: $\phi(3) - \phi(5) = \phi_0 + T \cdot \frac{\mathcal{R}}{z_{\text{ion}}\mathcal{F}} \ln a_2^{\text{ion}}$. $\mathcal{R}$ and $\mathcal{F}$ are gas and Faraday constant, T is the temperature and the ion of interest has an activity a_2^{ion} in the solution and z_{ion} charges. The potential difference $\phi(3) - \phi(5)$ modulates the gate voltage and thereby the Drain-Source current.

The term $T \frac{\mathcal{R}}{z_{\text{ion}}\mathcal{F}}$ is called the sensitivity of the ISFET. In our case we wish to measure pH: Eq. (A.3) tells that the sensitivity is 59.1mV/pH at room temperature ($25\,^\circ\text{C}$). It should be noted that ISFETs always need a reference electrode in the same solution to meaningful measure the ion concentration.

Summing up, the electro-chemical interaction of ions in the solution with the membrane modulates the gate voltage, U_{GS} and thereby the conductivity/current between the source and the drain contact. An ISFET (including its circuit) has to be calibrated before being operation.

Reality As shown in Fig. A.3 ISFETs have a small form factor of < 1 mm^2 active surface. They further share the basic properties of MOSFETs including their well-known manufacturing processes. The reference electrodes on the other hand are several times larger than an ISFET and typically made of glass which renders them fragile. Nowadays, miniaturized reference electrodes are available and were used in our tests. Fig. A.3 shows different pictures of the ISFETs we used.

In the literature and after first tests the following questions arise:

Temperature The sensitivity of the ISFET changes linear with temperature, but chemical activities, reaction equilibrium and the transistor depend on temperature, too. Most commercial ISFET pH-meters measure additionally the temperature.

Light sensitivity Photons can create charges within the membrane, the ISFET is sensitive to light.

Ion-selectivity Real membranes are sensitive to a variety of ions in the solution. One therefore needs good knowledge of the chemicals beforehand. Especially salts are known to alter the sensitivity.

Drift & Hysteresis The ISFET show multiple timescales when reacting to a sudden change in pH. Whereas the fastest timescale of the response are better than 1 ms, a longterm drift with a time scale of several minutes is also observed. At present no physical description of the drift is available.

Electrostatic sensitive device ISFET have to be handled with care, a simple electrostatic discharge can destroy the membrane. Some companies therefore add a Platinum wire close to the membrane to provide shielding (cf. Fig. A.3).

Most of the properties depend on the membrane; for pH-sensitive ISFETs more than three different types (Al_2O_3, Si_3N_4, Ta_2O_5) are commercially available.

Electronics Several types of circuits for ISFETs are known in the literature [47, 27], the so-called *constant-voltage constant-current* (CVCC) circuit imposes a constant current I_{DS} and constant voltage U_{DS} between source and drain while keeping the source potential U_S floating. The basic principle is illustrated in Fig. A.5. For technical/historical reasons we measure $U_{SG} = -U_{GS}$.

Because of the limitations of commercially available current source one cannot integrate the circuit shown in Fig. A.5 into an instrumented particle. Two additional circuits, which are able to operate with one 3 V coin cell, were developed; they are not shown here for intellectual property reasons. In all cases the circuits were soldered by hand and we acquired the signal with a 16-bit USB data acquisition card (USB-6251 BNC, National Instruments) and Labview.

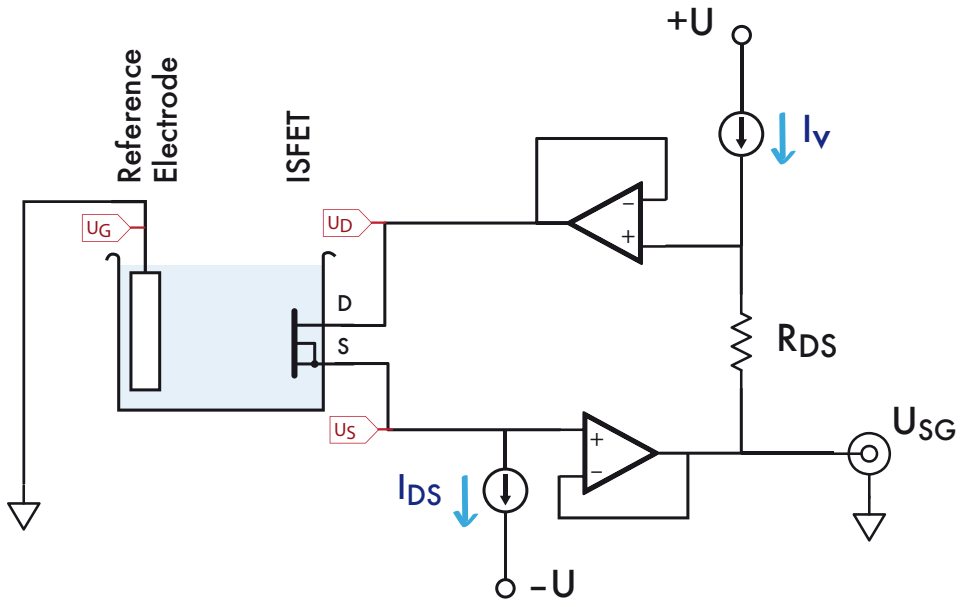

Figure A.5: *constant-voltage constant-current* (CVCC) circuit for ISFET measurements. The current source, I_V, imposes a constant potential difference $U_{DS} = I_V \cdot R_{DS} = 0.5\,\mathrm{V}$ between source and drain. In addition, a constant current $I_{DS} = 100\mu\mathrm{A}$ is established by a current sink while the source potential U_S is floating. The difference between gate potential U_G and U_S is then directly proportional to the pH of the solution. The sensitivity of ISFETs is less than $59\mathrm{mV/pH}$. In consequence the signal has to be amplified.

A.2.1 First Measurements

We found (and bought from) three companies, which sell small quantities. Surprisingly only one company was responding to technical questions and highly interested in a cooperation. Thus, we abandoned the solutions of the other two companies and discuss here result obtained with the ISFETs made by MicroSens SA (Lausanne, Switzerland). From a technical point of view their product is sound: the membrane is Tantalum-oxide (Ta_2O_5) with platinum wire shielding and the ISFET is conveniently encapsulated on a "finger" as shown in Fig. A.3. However, we noticed that the connector was not water-proof: They corroded and thereby randomly short-circuited the ISFET. We protect the contacts with nail polish.

Calibration & Observations ISFETs have to be calibrated shortly before the actual measurement, which is done with standard buffer solutions at pH values of $2, 4, 7, 10$ (Fisher Scientific). The spread between ISFET dies is large: for five dies U_{GS}(pH=7) covers almost $2\,\mathrm{V}$. The variation in sensitivity is weaker, the dies show a slope of $54 \pm 2\,\mathrm{mV/pH}$, which is less than the theoretic value of $59\mathrm{mV/pH}$. In order to perform measurements in solutions which change temperature one would have to calibrate at different temperatures and different pH.

In general, we observe that ambient light changes the output of the ISFET by $\lesssim 5\,\mathrm{mV}$

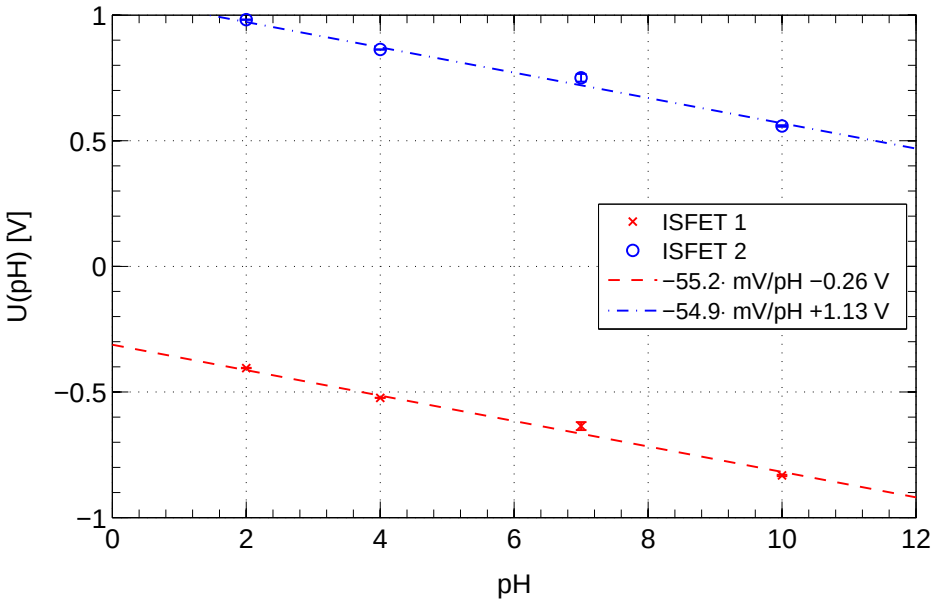

Figure A.6: Calibration of two ISFETs in the same buffer solution. The measured sensitivity is less than the theoretic value of $-59\mathrm{mV/pH}$.

($= 0.1$ pH). However, we found a complicated drift behavior after injecting reference electrode and ISFET into a buffer solution. The first response is instantaneous and within $\sim \pm 2pH$ of the buffer solution, then the signal approaches a plateau within 2 minutes. The plateau is not stable and drifts with $\lesssim 2\,\mathrm{mV/h}$ ($= 0.03$ pH/h). This behavior is mentioned in the literature and often modeled by a sum of exponential decays. Y. Ito [26] attributes the effect to light and impurities in the Tantalum-oxide layer.

It should be pointed out that a drift can induce a hysteresis of the ISFET. That would significantly alter the response to steps in pH. On the other hand common glass electrode pH-meters have a response time of 1 minute and are not specified for steps in pH at all. Preliminary tested identified Flourescein as a possible optical indicator of pH, unfortunately, photobleaching alters its response with time. A stringent test of its response time is therefore rather complicated and perhaps something for the next PhD student.

Mixing In order to observe a chemical reaction and the mixing one would like to measure a characteristics property of the reaction as fast as possible. Conductivity and pH are possible candidates and we sketch here the possible application of pH-sensitive ISFETs for following the mixing in a chemical reaction. The reaction is rather simple: Hydrochloric acid (HCl) is added into a beaker filled with a phosphate buffer. The solution is agitated by a magnetic stirrer and placed in temperature controlled heat bath at 25 °C. Two ISFETs attached to a miniature reference electrode are placed opposite to a nozzle (connected to a syringe pump) that injects small quantities of HCl. The ensemble is depicted in Fig. A.7. ISFET signal acquisition and injections are controlled in Labview. 0.5 ml of HCl (concentration 1 M) is added every 25 s, a drop of HCl needs thus some time (~ 3 s) to be advected to the ISFETs. Moreover, the ISFETs measure at slightly different positions.

Both ISFETs follow the same curve but differ by 0.05 pH. This offset is caused by the uncertainty in the calibration. They further capture the dynamics of a passing HCl drop, the shortest reaction times are of the order of 1/10 s.

Even tough many questions are still open, we identified pH sensitive ISFETs as a promising tool for monitoring mixing in simple chemical reactions. Although not discussed here, we further successfully tested circuits which consume 0.5 mA at 2 V. Hence, they can be integrated into an instrumented particle.

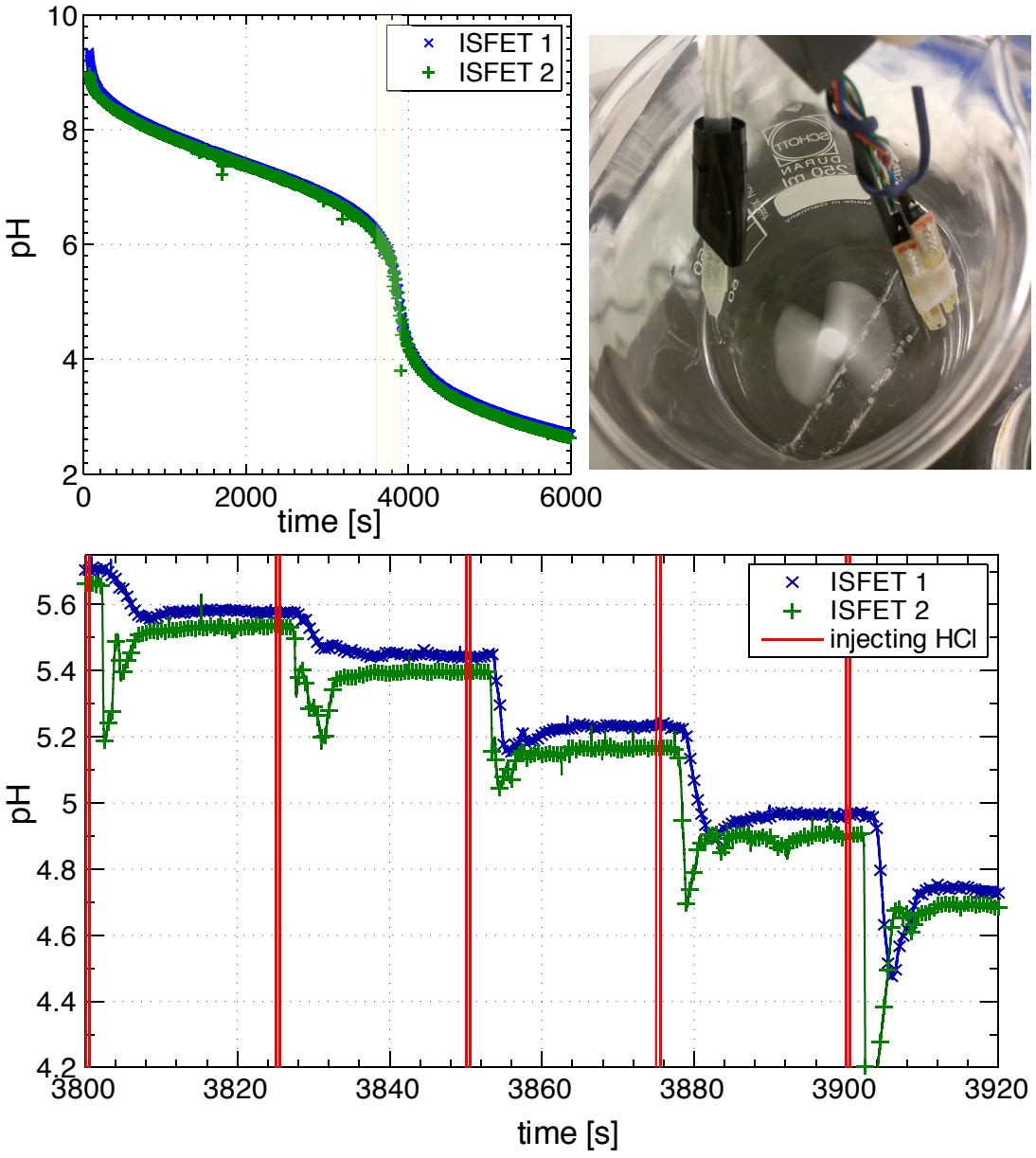

Figure A.7: Two ISFET sensors in a beaker with phosphate buffer, every 25 seconds a small quantities of HCl is injected. The picture shows the position of nozzle and ISFETs, the (miniature) reference electrode is behind the ISFETs and fixed with scotch tape. The nozzle is placed at the other side of the beaker, which is agitated by a magnetic stirrer. A drop of HCl needs thus some time ($\sim$ 3s) to arrive at the ISFETs. Moreover, the ISFETs measure at slightly different positions. The evolution of pH measured independently by the two ISFETs is depicted in the upper plot and a zoom is provided in the lower plot.

B Appendix

B.1 Unwrapping & Differences

Each Euler angle along a trajectory is bounded $\theta_x, \theta_z \in [0, 2\pi[$ and $\theta_y \in]-\frac{\pi}{2}, \frac{\pi}{2}[$ as defined in Eq. (3.2). However, this choice is not unique because there is a second triplet with

$$\theta'_x = \theta_x + \pi \tag{B.1a}$$
$$\theta'_y = (\pi - |\theta_y|) \cdot \text{sign}(\theta_y) = \text{sign}(\theta_y) \cdot \pi - \theta_y \tag{B.1b}$$
$$\theta'_z = \theta_z + \pi \tag{B.1c}$$

As a consequence the difference, $\underline{\Delta} = \underline{\alpha} - \underline{\beta}$, between two Euler angle triplets, $\underline{\alpha}$ and $\underline{\beta}$, has four valid results. Unwrapping a time trace is, thus, counterintuitive as illustrated in Fig. B.2. This problem is called a *gimbal lock*; a sketch is shown in Fig. B.1. In the following the second representation is marked by superscript ^{G}.

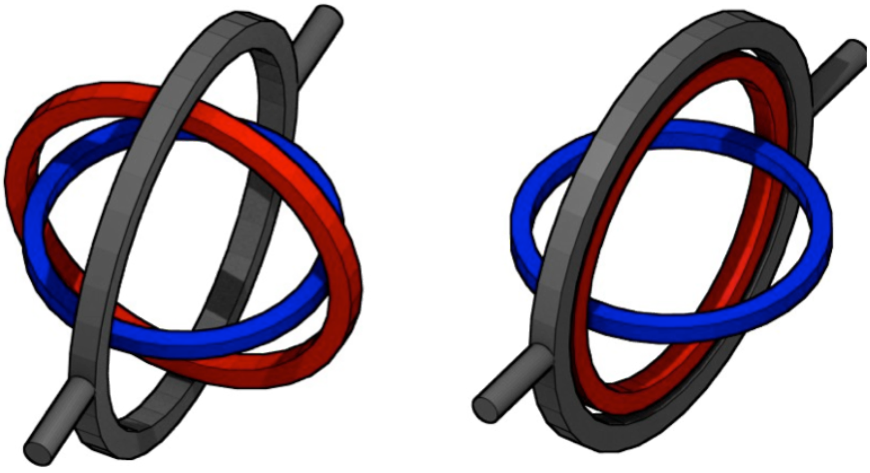

Figure B.1: Illustration of the gimbal lock problem: at $\theta_y = \pm 90°$ the first rotation is turned into the axis of the third rotation, and one is left with only one degree of freedom.

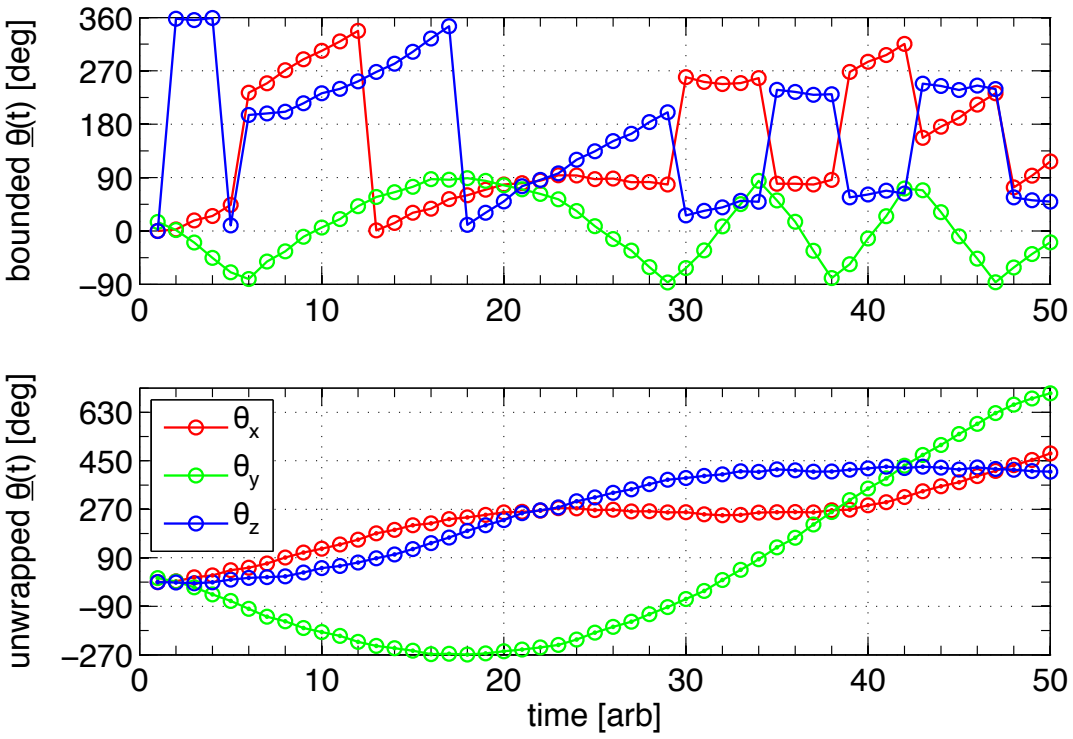

Figure B.2: Illustration of the difference between a bounded time-series of $\underline{\theta}(t)$ and its unwrapped time trace. Jumps of $\approx 180°$ in θ_x, θ_z correspond to passing a gimbal lock.

Difference between two orientations To compute derivates based on the Euler angles one needs continuous time series of the orientation.Therefore, the raw, bounded time series has to be unwrapped. Whereas this process is straightforward for one angular variable[1], we don't know the representation of $\underline{\alpha}$ and $\underline{\beta}$ in the case of Euler angles. $\underline{\Delta}$ is needed to compute derivates and to unwrap the signal.

Assuming that the change in angle is small, *i.e.* less than $90°$, we obtain accurate results for Δ_x and Δ_z[2]. Thus, the following four cases are possible :

$$\underline{\alpha} = \underline{\beta} + \underline{\Delta}_1 \quad \Rightarrow \quad \Delta_x = \alpha_x - \beta_x \tag{B.2a}$$

$$\underline{\alpha}^G = \underline{\beta}^G + \underline{\Delta}_2 \quad \Rightarrow \quad \Delta_x = (\alpha_x + \pi) - (\beta_x + \pi) \quad = \alpha_x - \beta_x \tag{B.2b}$$

$$\underline{\alpha}^G = \underline{\beta} + \underline{\Delta}_3 \quad \Rightarrow \quad \Delta_x = (\alpha_x + \pi) - (\beta_x) \quad = \alpha_x - \beta_x + \pi \tag{B.2c}$$

$$\underline{\alpha} = \underline{\beta}^G + \underline{\Delta}_4 \quad \Rightarrow \quad \Delta_x = (\alpha_x) - (\beta_x + \pi) \quad = \alpha_x - \beta_x + \pi \tag{B.2d}$$

Naturally, the formulas are the same for $\Delta_z, \alpha_z, \beta_z$. That means passing a gimbal lock corresponds to $\Delta_x \approx \Delta_z \approx \pi$.

[1] One just adds multiples of 2π whenever the absolute difference is greater π.

[2] We should keep in mind that we can add or subtract 2π whenever it is necessary. Consequently, it is $\xi - \pi = \xi + \pi$.

In order to determine Δ_y one has to know :
– the representation of one of the triplets, as well as
– if a gimbal lock was passed;
and then choose accordingly:

$$\text{Eq. (B.2a)} \quad : \quad \Delta_y = \alpha_y - \beta_y \tag{B.3a}$$
$$\text{Eq. (B.2b)} \quad : \quad \Delta_y = (\text{sign}(\alpha_y)\,\pi - \alpha_y) - (\text{sign}(\beta_y)\,\pi - \beta_y) = -(\alpha_y - \beta_y) \tag{B.3b}$$
$$\text{Eq. (B.2c)} \quad : \quad \Delta_y = (\text{sign}(\alpha_y)\,\pi - \alpha_y) - \beta_y = -(\alpha_y + \beta_y) + \pi \tag{B.3c}$$
$$\text{Eq. (B.2d)} \quad : \quad \Delta_y = \alpha_y - (\text{sign}(\beta_y)\,\pi - \beta_y) = (\alpha_y + \beta_y) + \pi \tag{B.3d}$$

Unwrapping a time series Let $\underline{\alpha}_1, \ldots, \underline{\alpha}_n$ be a time series of raw, bounded Euler angles. For each time step we can compute

$$\underline{\alpha}_k = \underline{\alpha}_{k-1} + \underline{\Delta}_k \tag{B.4}$$

The unwrapped signal, $\underline{\beta}_1, \ldots, \underline{\beta}_n$, is then

$$\underline{\beta}_k = \underline{\beta}_{k-1} + \underline{\Delta}_k \quad \text{with } \underline{\beta}_1 = \underline{\alpha}_1 \text{ and } \underline{\Delta} = \underline{\alpha}_k - \underline{\beta}_{k-1}. \tag{B.5}$$

Following (B.2) one has to chose the equation for Δ_y among equations (B.3).

The unwrapped orientation at step k is thus fully determined by the representation of $\underline{\alpha}_1$, $\underline{\beta}_{k-1}$, $\Delta_x(k)$ and $\Delta_z(k)$. Once the signals are unwrapped, they can be smoothed and their derivatives can be computed *e.g.* using the derivatives of a gaussian kernel approach.

B.2 Angular Velocity & Acceleration

The angular velocity and acceleration were derived as described in [23]. Here, we note just the final equations because our choice of the Tait-Bryan representation might be unknown to the reader.

$$\boldsymbol{\omega}^{\mathbb{L}}\left(\{\theta_x,\theta_y,\theta_z\},\{\dot{\theta}_x,\dot{\theta}_y,\dot{\theta}_z\}\right)=\begin{bmatrix}+\,c(\theta_z)\,c(\theta_y)\dot{\theta}_x+\,s(\theta_z)\dot{\theta}_y\\-\,s(\theta_z)\,c(\theta_y)\dot{\theta}_x+\,c(\theta_z)\dot{\theta}_y\\\dot{\theta}_z+\,s(\theta_y)\dot{\theta}_x\end{bmatrix} \tag{B.6}$$

$$\boldsymbol{\omega}^{\mathbb{P}}\left(\{\theta_x,\theta_y,\theta_z\},\{\dot{\theta}_x,\dot{\theta}_y,\dot{\theta}_z\}\right)=\begin{bmatrix}\dot{\theta}_x+\,s\,(\theta_y)\,\dot{\theta}_z\\c\,(\theta_x)\,\dot{\theta}_y-\,s\,(\theta_x)\,c\,(\theta_y)\,\dot{\theta}_z\\s\,(\theta_x)\,\dot{\theta}_y+\,c\,(\theta_x)\,c\,(\theta_y)\,\dot{\theta}_z\end{bmatrix} \tag{B.7}$$

For the angular acceleration one finds

$$\boldsymbol{\alpha}^{\mathbb{L}}=\frac{\mathrm{d}}{\mathrm{d}t}\boldsymbol{\omega}^{\mathbb{L}}=\begin{bmatrix}\ddot{\theta}_y\,s(\theta_z)+\ddot{\theta}_x\,c(\theta_z)\,c(\theta_y)+\dot{\theta}_y\dot{\theta}_z\,c(\theta_z)-\dot{\theta}_x\dot{\theta}_z\,s(\theta_z)\,c(\theta_y)-\dot{\theta}_x\dot{\theta}_y\,c(\theta_z)\,s(\theta_y)\\\ddot{\theta}_y\,c(\theta_z)-\ddot{\theta}_x\,s(\theta_z)\,c(\theta_y)-\dot{\theta}_y\dot{\theta}_z\,s(\theta_z)-\dot{\theta}_x\dot{\theta}_z\,c(\theta_z)\,c(\theta_y)+\dot{\theta}_x\dot{\theta}_y\,s(\theta_z)\,s(\theta_y)\\\ddot{\theta}_z+\ddot{\theta}_x\,s(\theta_y)+\dot{\theta}_x\dot{\theta}_y\,c(\theta_y)\end{bmatrix} \tag{B.8}$$

and

$$\boldsymbol{\alpha}^{\mathbb{P}}=\frac{\mathrm{d}}{\mathrm{d}t}\boldsymbol{\omega}^{\mathbb{P}}=\begin{bmatrix}\ddot{\theta}_x+\ddot{\theta}_z\,s(\theta_y)+\dot{\theta}_y\dot{\theta}_z\,c\,(\theta_y)\\\ddot{\theta}_y\,c(\theta_x)-\ddot{\theta}_z\,s(\theta_x)\,c(\theta_y)-\dot{\theta}_x\dot{\theta}_y\,s(\theta_x)-\dot{\theta}_x\dot{\theta}_z\,c(\theta_x)\,c(\theta_y)+\dot{\theta}_y\dot{\theta}_z\,s(\theta_x)\,s(\theta_y)\\\ddot{\theta}_y\,s(\theta_x)+\ddot{\theta}_z\,c(\theta_x)\,c(\theta_y)+\dot{\theta}_x\dot{\theta}_y\,c(\theta_x)-\dot{\theta}_x\dot{\theta}_z\,s(\theta_x)\,c(\theta_y)-\dot{\theta}_y\dot{\theta}_z\,c(\theta_x)\,s(\theta_y)\end{bmatrix} \tag{B.9}$$

B.3 Autocorrelations & Structure-functions

In experiments with a very small observation volume (*e.g.* acoustic or Laser Doppler velocimetry) the track length is reciprocal proportional to the particle velocity: Slower particles stay longer in the observation volume. But the experiments presented within the scope of this thesis surveil almost the whole box, and no simple weighting based on the length of a tracks can be constructed.
Measurement uncertainties and other problems might introduce errors. Therefore, we set points which are unlikely/missing/wrong to NaN, which introduces gaps into the tracks. The correlations and structure functions[3] are computed as follows:

autocorrelation The unbiased autocorrelation of a quantity s is:

$$R_s(\tau) = \frac{1}{\sigma^2 (L-\tau)} \sum_{k=1}^{L-\tau} \left[(s(k) - \mu) (s(k+\tau) - \mu) \right] \tag{B.10}$$

with $\tau = [1, \ldots, L-1]$, μ being the mean along the track and the variance $\sigma^2 = R_s(\tau = 0)$. The Fourier transformation is not used, however, its result, the biased version, can be computed $R'_s(\tau) = R_s(\tau) \cdot \frac{N_0 - \tau}{N_0}$ with N_0 the number of data points used. In our experiments the probability distribution of the tracks has the shape of an exponential decay, *i.e.* there is exponentially less data for larger τ. Therefore, the biased autocorrelation looks like a damped unbiased auto-correlation. The auto-correlation with and without a prior subtraction of the mean μ are related by

$$\langle (s(t) + \mu) (s(t+\tau) + \mu) \rangle = \langle (s(t)) (s(t+\tau)) \rangle + 2\mu \langle s \rangle + \mu^2 \tag{B.11}$$

One has further the choice between subtracting either the global mean of all tracks or at each track its local mean.

second-order structure function The multi trajectory mean similar to (B.10) yields the second-order structure function:

$$D_2(\tau) = \frac{1}{N_\tau} \sum_{\substack{j=1 \\ L_j > \tau}}^{N_{\text{trks}}} \sum_{t=1}^{L_j - \tau} \left[s(t+\tau) - s(t) \right] \tag{B.12}$$

The second-order structure function $D_2(\tau) = \left\langle (s(t+\tau) - s(t))^2 \right\rangle$ is less sensitive to mean flows or a remaining mean. If the signal is stationary, it is:

$$D_2(\tau) = 2\sigma^2 (1 - R(\tau)) \quad \Leftrightarrow \quad R(\tau) = 1 - \frac{D_2(\tau)}{2\sigma^2} \tag{B.13}$$

We verify that auto-correlation functions converged with Eq. (B.13).

[3] The corresponding code is VHT_AcSfFunc(STRUCT,field,[settings]).

B.4 Frenet formulas

The Frenet formulas define a local coordinate system which is attached to and moving with the trajectory [34, 75]:

$$\boldsymbol{T}(t) = \frac{\dot{\boldsymbol{x}}(t)}{|\dot{\boldsymbol{x}}(t)|} \tag{B.14a}$$

$$\boldsymbol{N}(t) = \boldsymbol{B}(t) \times \boldsymbol{T}(t) = \frac{\dot{\boldsymbol{x}} \times \ddot{\boldsymbol{x}}}{|\dot{\boldsymbol{x}} \times \ddot{\boldsymbol{x}}|} \times \frac{\dot{\boldsymbol{x}}}{|\dot{\boldsymbol{x}}|} \tag{B.14b}$$

$$\boldsymbol{B}(t) = \frac{\dot{\boldsymbol{x}} \times \ddot{\boldsymbol{x}}}{|\dot{\boldsymbol{x}} \times \ddot{\boldsymbol{x}}|} \tag{B.14c}$$

Consequently it is:

$$\boldsymbol{v} \cdot \boldsymbol{N} = 0 \qquad \boldsymbol{v} \cdot \boldsymbol{B} = 0$$
$$\boldsymbol{a} \cdot \boldsymbol{B} = 0 \qquad \boldsymbol{a} \cdot \boldsymbol{N} \geq 0$$

In other words, the acceleration vector is bound to the $\boldsymbol{T} - \boldsymbol{N}$ plane.
One further defines *curvature* $\kappa = \dfrac{|\dot{\boldsymbol{x}} \times \ddot{\boldsymbol{x}}|}{|\dot{\boldsymbol{x}}|^3}$ and *torsion* $\tau = \dfrac{(\dot{\boldsymbol{x}} \times \ddot{\boldsymbol{x}}) \cdot \dddot{\boldsymbol{x}}}{|\dot{\boldsymbol{x}} \times \ddot{\boldsymbol{x}}|^2}$.
The evolution of the Frenet frame is given by the Frenet-Serret formula[4]:

$$\frac{1}{|\dot{\boldsymbol{x}}|}\frac{\mathrm{d}}{\mathrm{d}t}\begin{pmatrix}\boldsymbol{T}\\ \boldsymbol{N}\\ \boldsymbol{B}\end{pmatrix} = \begin{pmatrix}0 & \kappa & 0\\ -\kappa & 0 & \tau\\ 0 & -\tau & 0\end{pmatrix}\begin{pmatrix}\boldsymbol{T}\\ \boldsymbol{N}\\ \boldsymbol{B}\end{pmatrix} \tag{B.15}$$

Eq. (B.15) defines the so-called Darboux (rotation) vector $\boldsymbol{\omega}_D = |\boldsymbol{v}|\,(\tau\boldsymbol{T} + \kappa\boldsymbol{B})$ which interprets curvature κ as a rotation around $\boldsymbol{B}$ and the torsion τ as measure of the twisting of the curve. It should be pointed out that the higher order derivatives necessitate careful filtering. We, therefore, employ the gaussian kernel technique. The corresponding code is VHT_Frenet.

[4] Many books express the trajectory as a function of the arc length, s, instead of time, t. They are related by $\frac{ds}{dt} = \left|\frac{d\boldsymbol{x}(t)}{dt}\right| = |\dot{\boldsymbol{x}}|$ and $\frac{d}{ds} = \frac{dt}{ds}\frac{d}{dt} = \frac{1}{|\dot{\boldsymbol{x}}|}\frac{d}{dt}$.

B.5 Texture

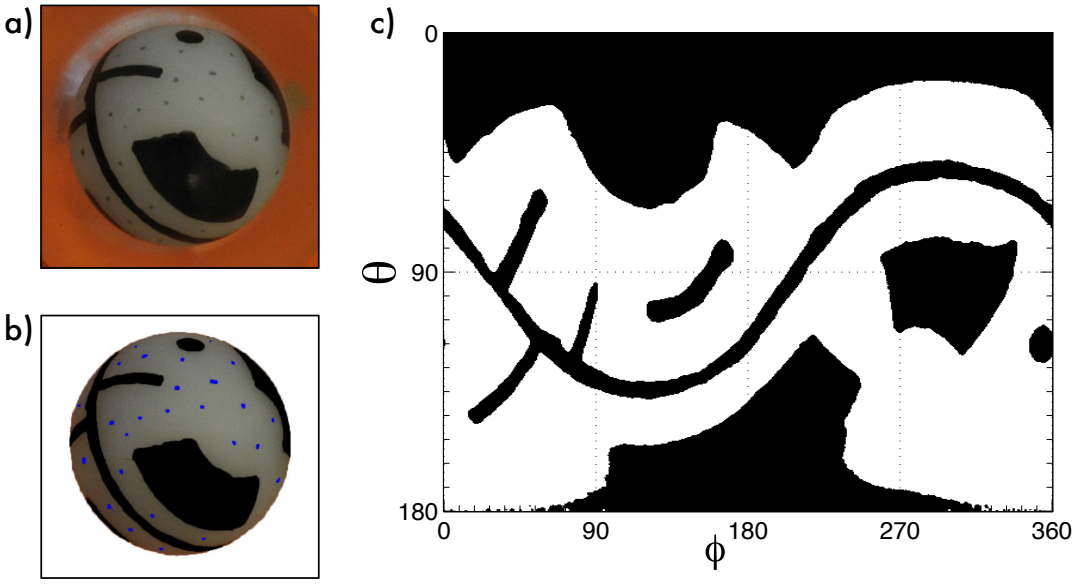

Figure B.3: **a)** raw image of the freshly textured particle **b)** image cleaned using PhotoShop's "magic selection tool": blue dots mark the features and can be easily found with Matlab **c)** computed texture of the same particle after applying the algorithm

Art First we add features as small dots to the sphere, they are removed after computing the texture. A fine marker or a pencil work well. Camera and particle are in fixed places, thus all images can be pre-cropped; the final adjustment is done with Photoshop [5]. Black regions are painted to black, the background is painted white and features are marked with blue. A Matlab code[6] then selects the biggest sphere, fetches the black/unpainted (*i.e.* white texture) points and the centroid of each feature.

Math The location of a pixel or a feature in the image can be projected to 3D:

$$x = X_p/r - 1 \tag{B.16a}$$
$$y = Y_p/r - 1 \tag{B.16b}$$
$$z = \sqrt{1 - x^2 - y^2} \tag{B.16c}$$

with $r = \text{size}\,(\text{image},1)/2$ and $\{X_p, Y_p\}$ the position in pixels.

If two images share a minimum number of features, there is a rotation matrix which turns image A into the orientation of image B. Two sets of feature vectors[7] $\underline{\underline{\boldsymbol{P}}}$ and $\underline{\underline{\boldsymbol{Q}}}$ have the covariance matrix $\underline{\underline{\boldsymbol{K}}} = \underline{\underline{\boldsymbol{P}}}^T\,\underline{\underline{\boldsymbol{Q}}}$. If there is *no* measurement error, the matrix $\underline{\underline{\boldsymbol{K}}}$ rotates

[5] In that case one marks the background in a known color and tells Matlab to extract the biggest sphere.
[6] getpoints.m
[7] It is clear that $\underline{\underline{\boldsymbol{P}}}$ and $\underline{\underline{\boldsymbol{Q}}}$ are of the same size.

the points $\underline{\underline{P}}$ to $\underline{\underline{Q}}$. Kabsch proposed [31, 30] a fast technique to compute an optimal solution of this problem when working with real data. The main idea is that the singular value decomposition of $\underline{\underline{K}}$ is svd $(\underline{\underline{K}}) = \underline{\underline{V}}\ \underline{\underline{S}}\ \underline{\underline{W}}^T$. The nearest orthonormal matrix to $\underline{\underline{K}}$ is then $\underline{\underline{V}}^T\ \underline{\underline{W}}$. In other words, the optimal rotation matrix $\underline{\underline{M}}$ from $\underline{\underline{P}}$ to $\underline{\underline{Q}}$ is given by $\underline{\underline{V}}^T\ \underline{\underline{W}}$.

First, for all images which share at least N_{feat} features the transformation matrixes, $\underline{\underline{M}}_{A\to B}$, are computed. Then, we build the connection matrix, which notes if two views share more than N_{feat} features. These views are thus directly connected by a rotation matrix $\underline{\underline{M}}$. Views, which are not directly connected can (in most cases) be reached by passing through an intermediate view: If we know the rotation matrix from view B to view C and from A to B then C can be reached from A by $\underline{\underline{M}}_{A\to C} = \underline{\underline{M}}_{B\to C}\ \underline{\underline{M}}_{A\to B}$.

All images are converted to sets of 3D vectors with an additional color and a view is selected as base view with orientation $\underline{0}°$. The vector sets for which a transformation to the base view exists, are then rotated and superposed.[8]. A sketch of the procedure is provided in figure 3.8.

OpenGL defines textures as equally spaced in in azimutal and polar angle. Each vector is therefore expressed in spherical coordinates, (ϕ, θ) and we build the average color of the vectors lying within grid cells on equally spaced grid in ϕ, θ. This is done for several grid resolutions which are then combined to one high resolution texture. Small parts of texture can be altered by hand if necessary (*e.g.* for a very small sphere). A typical texture is rendered on a 512×512 grid, the resolution in ϕ and θ is better than $1\,°$. An example is shown in figure B.3**c)**.

Semi-automatic feature naming & other improvements In the first version of the code the user needed to identify where and in which image a feature was located[9]. This process was extremely tedious, lengthy and frustrating. For the sanity of the PhD student we therefore developed a procedure which semi-automatically associates names to the features. It is still necessary to mark (with Photoshop) the exact position of features. Matlab then extracts these mark and their 2D and 3D position; for each image we have a set of of feature point each with a yet empty name.

Once we know that a sufficient number, $N_{\text{minCommon}}$ of features is shared between 2 images, the rotation matrix can be computed using a *brute force ansatz*.

Therefore, we first ask the user to click/identify features in image B which are also shown in a reference view A. Once a few features (≥ 4) are shared we try all reasonable rotations which turn the (feature) point cloud from B into a larger cloud A [10]. We thus have a set of features $\boldsymbol{b}_{1\ldots M}$ which after a rotation coincides with a subset of the features in view A, $\boldsymbol{a}_{1\ldots N}$. Clearly, it is $M \leq N$. We further know that angles and distances between features/vectors are rotation-invariant. Consequently, the rotation from B to A can be split into two parts.

In a first step, all identified vectors $\boldsymbol{b}_{1\ldots M}$ are rotated such that $\boldsymbol{b}'_1$ coincides with a

[8] Basically, we are superposing rotated hedgehogs with colored spikes
[9] At the beginning even the position was entered by hand!
[10] findFeatureRotation.m

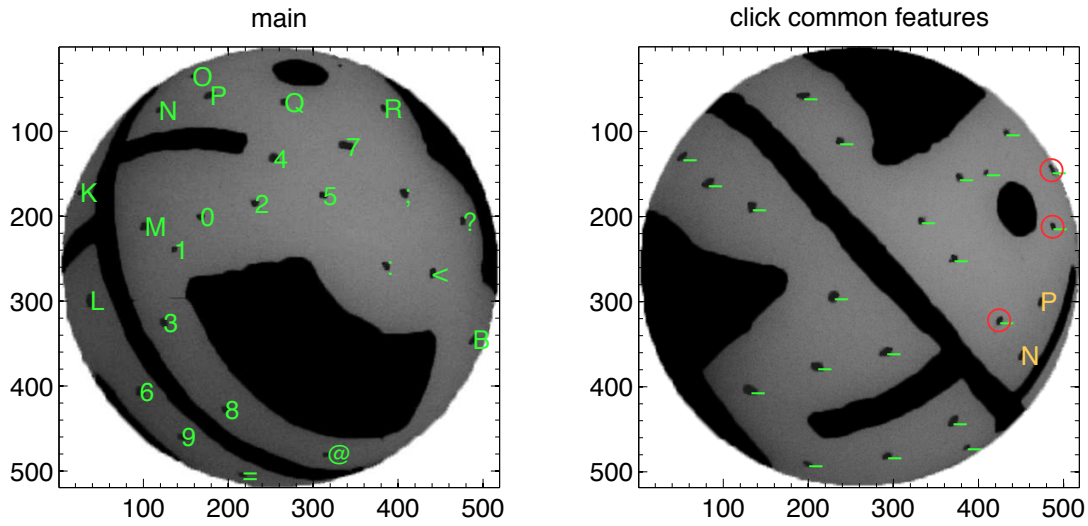

Figure B.4: User interface to determine which features are found in both images. The symbols indicate the unique name of each feature, – and # indicate unidentified features, the yellow letters on the right side are points which are already known from a previous image pair. The user clicks the features in the right image which are also found in the left image. It is not necessary to find all, 5 to 7 features are usually sufficient. Nevertheless, adding features which are not shared yields unpredictable results.

feature vector $\boldsymbol{a}_k$ in image A:

$$\boldsymbol{b}'_{1\ldots M} = \underline{\underline{\boldsymbol{R}}}\left(\boldsymbol{b}_1 \times \boldsymbol{a}_k, \angle\left(\boldsymbol{a}_k, \boldsymbol{b}_1\right)\right)\ \boldsymbol{b}_{1\ldots M} \tag{B.17}$$

But, the remaining features $\boldsymbol{b}'_{2..M}$ do not yet coincide with the $\boldsymbol{a}_{1..N}$.
Therefore, a second rotation then matches the remaining ones: all points are now turned around $\boldsymbol{b}'_1 = \boldsymbol{a}_k$ such that the direction vector $\boldsymbol{b}'_1 \times \boldsymbol{b}'_2$ which describes the direction of the point cloud (approximately) coincides with $\boldsymbol{b}'_1 \times \boldsymbol{a}_j$. In other words:

$$\begin{aligned}\boldsymbol{b}''_{1\ldots M} &= \underline{\underline{\boldsymbol{R}}}\left(\boldsymbol{b}'_1, \angle\left(\boldsymbol{b}'_1 \times \boldsymbol{a}_j\ ,\ \boldsymbol{b}'_1 \times \boldsymbol{b}'_2\right)\right)\ \boldsymbol{b}'_{1\ldots M} \\ &= \underline{\underline{\boldsymbol{R}}}\left(\boldsymbol{b}'_1, \angle\left(\boldsymbol{b}'_1 \times \boldsymbol{a}_j\ ,\ \boldsymbol{b}'_1 \times \boldsymbol{b}'_2\right)\right)\ \underline{\underline{\boldsymbol{R}}}\left(\boldsymbol{b}_1 \times \boldsymbol{a}_k, \angle\left(\boldsymbol{a}_k, \boldsymbol{b}_1\right)\right)\ \boldsymbol{b}_{1\ldots M}\end{aligned} \tag{B.18}$$

Now the quality of matching has to be determined. This is done with a greedy distance[11] between the point clouds: for each rotated feature $\boldsymbol{b}''_k$ we find

$$d_k = \min\left(\angle\left(\boldsymbol{b}''_k, \{\boldsymbol{a}\}\right)\right) \tag{B.19}$$

with $\{\boldsymbol{a}\}$ the still unmatched vectors of $\boldsymbol{a}_{1..N}$. Matched points are marked and not used twice. The function keeps also track of the pairs, such that we can later transfer/copy feature names.

[11] cloudDist.m

We determine the best rotation by testing the agreement for all combinations of $\boldsymbol{b}_1$ to the $\boldsymbol{a}_{1..N}$. As we might have missed features[12] we rotate all remaining, unclicked and unnamed, features and check for those with a positive $z-$component if there is a close feature from image A.

This process of identifying common features, finding the rotation matrix and copying names is accelerated if some features are already known to be shared. Consequently, only a few are actually done by the user. Once the features with their positions and names are known, one proceeds with the technique described earlier.

[12] Actually one doesn't have to find all, about 6 features are fully sufficient

B.6 Fitting an ellipsoid

As stated by Eq. (7.3) the equation of the 3D accelerometer at rest defines an ellipsoid which is shifted but not rotated:

$$\frac{(A_x - O_x)^2}{S_x^2} + \frac{(A_y - O_y)^2}{S_y^2} + \frac{(A_z - O_z)^2}{S_z^2} = \boldsymbol{g}^2 \tag{B.20}$$

For simplicity, we set $|\boldsymbol{g}| \equiv 1$. Expanding Eq. (7.3) yields:

$$\begin{aligned} 1 &= \frac{1}{S_x^2}A_x^2 + \frac{1}{S_y^2}A_y^2 + \frac{1}{S_z^2}A_z^2 - 2\frac{O_x}{S_x^2}A_x - 2\frac{O_y}{S_y^2}A_y - 2\frac{O_z}{S_z^2}A_z + \frac{O_x^2}{S_x^2} + \frac{O_y^2}{S_y^2} + \frac{O_z^2}{S_z^2} \\ &= \frac{1}{1 - \frac{O_x^2}{S_x^2} - \frac{O_y^2}{S_y^2} - \frac{O_z^2}{S_z^2}} \cdot \left[\frac{1}{S_x^2}A_x^2 + \frac{1}{S_y^2}A_y^2 + \frac{1}{S_z^2}A_z^2 - 2\frac{O_x}{S_x^2}A_x - 2\frac{O_y}{S_y^2}A_y - 2\frac{O_z}{S_z^2}A_z\right] \\ &= \xi_1\, A_x^2 + \xi_2\, A_y^2 + \xi_3\, A_z^2 - 2\xi_4\, A_x - 2\xi_5\, A_y - 2\xi_6\, A_z \end{aligned} \tag{B.21}$$

Hence, the offset is

$$O_i = \frac{\xi_{3+i}}{\xi_i} \tag{B.22}$$

Combining Eq. (B.22) and Eq. (B.21):

$$\begin{aligned} \frac{1}{C} \equiv 1 - \frac{O_x^2}{S_x^2} - \frac{O_y^2}{S_y^2} - \frac{O_z^2}{S_z^2} &= 1 - \frac{\xi_4^2}{\xi_1\, C} - \frac{\xi_5^2}{\xi_2\, C} - \frac{\xi_6^2}{\xi_3\, C} \\ \Leftrightarrow \qquad C &= 1 + \frac{\xi_4^2}{\xi_1} + \frac{\xi_5^2}{\xi_2} + \frac{\xi_6^2}{\xi_3} \end{aligned} \tag{B.23}$$

Consequently, the sensitivity is

$$S_i = \sqrt{\frac{C}{\xi_i}} \tag{B.24}$$

To find a best fit for $\xi_1 \ldots \xi_6$, one searches an optimal solution for an overdetermined set of equations:

$$\underline{\underline{\boldsymbol{\zeta}}} \cdot \boldsymbol{\xi} = \begin{pmatrix} A_{x,1}^2 & A_{y,1}^2 & A_{z,1}^2 & -2A_{x,1} & -2A_{y,1} & -2A_{z,1} \\ A_{x,2}^2 & A_{y,2}^2 & A_{z,2}^2 & -2A_{x,2} & -2A_{y,2} & -2A_{z,2} \\ \vdots & \vdots & \vdots & \vdots & \vdots & \vdots \\ A_{x,N}^2 & A_{y,N}^2 & A_{z,N}^2 & -2A_{x,N} & -2A_{y,N} & -2A_{z,N} \end{pmatrix} \begin{pmatrix} \xi_1 \\ \xi_2 \\ \vdots \\ \xi_6 \end{pmatrix} = \begin{pmatrix} 1 \\ 1 \\ \vdots \\ 1 \end{pmatrix} \tag{B.25}$$

We find its solution with the help of the pseudo-inverse:

$$\boldsymbol{\xi} = \left(\underline{\underline{\boldsymbol{\zeta}}}\right)^{+} \begin{pmatrix} 1 \\ \vdots \\ 1 \end{pmatrix} = \left(\underline{\underline{\boldsymbol{\zeta}}}^T \underline{\underline{\boldsymbol{\zeta}}}\right)^{+} \underline{\underline{\boldsymbol{\zeta}}}^T \begin{pmatrix} 1 \\ \vdots \\ 1 \end{pmatrix} \tag{B.26}$$

where $\underline{\underline{\boldsymbol{\zeta}}}^{+}$ is the pseudo-inverse of $\underline{\underline{\boldsymbol{\zeta}}}$, which can be calculated from a singular value decomposition of $\underline{\underline{\boldsymbol{\zeta}}}$.

Bibliography

[1] http://www.electroiq.com/articles/sst/2008/05/two-different-approaches-to-integrated-mems.html.

[2] http://www.infoneedle.com/print/24763.

[3] Atkins, P., Höpfner, A., Schleitzer, A., and Bär, M. *Physikalische Chemie*, vol. 2. VCH Weinheim, Germany, 1990.

[4] Aumaître, S., Fauve, S., McNamara, S., and Poggi, P. Power injected in dissipative systems and the fluctuation theorem. *The European Physical Journal B-Condensed Matter and Complex Systems 19*, 3 (2001), 449–460.

[5] Auton, T. R. The lift force on a spherical rotational flow. *Journal of Fluid Mechanics 183* (1987), 199–218.

[6] Auton, T. R., Hunt, J., and Prud'homme, M. The force exerted on a body in inviscid unsteady non-uniform rotational flow. *Journal of Fluid Mechanics 197* (1988), 241–257.

[7] Bachelor, G. *an introduction to fluid dynamics*. Cambridge University Press, 2000.

[8] Bergveld, P. Thirty years of ISFETOLOGY What happened in the past 30 years and what may happen in the next 30 years. *Sensors and Actuators B 88*, 1 (2003), 1–20.

[9] Blum, D. B., Bewley, G. P., Bodenschatz, E., Gibert, M., Gylfason, Á., Mydlarski, L., Voth, G. A., Xu, H., and Yeung, P. K. Signatures of non-universal large scales in conditional structure functions from various turbulent flows. *New Journal of Physics 13*, 11 (Nov. 2011), 113020.

[10] Brainard, D. H. The Psychophysics toolbox. *Spatial vision 10*, 4 (1997), 433–436.

[11] Brown, R., Warhaft, Z., and Voth, G. A. Acceleration statistics of neutrally buoyant spherical particles in intense turbulence. *Physical Review Letters 103* (2009), 194501.

[12] Ciliberto, S., Garnier, N., Hernandez, S., Lacpatia, C., Pinton, J.-F., and Ruiz Chavarria, G. Experimental test of the Gallavotti-Cohen fluctuation theorem in turbulent flows. *Physica A: Statistical Mechanics and its Applications 340*, 1-3 (2004), 240–250.

[13] Eberly, D., and Schneider, P. *Geometric Tools for Computer Graphics*. Elsevier Science (USA), 2003.

[14] Elghobashi, S., and Truesdell, G. C. Direct simulation of particle dispersion in a decaying isotropic turbulence. *Journal of Fluid Mechanics 242* (1992), 655–700.

[15] Fiabane, L., Volk, R., Pinton, J.-F., Monchaux, R., Cartellier, A., and Bourgoin, M. Do finite size neutrally buoyant particles cluster? *arXiv.org physics.flu-dyn* (Jan. 2012).

[16] Fiabane, L., Zimmermann, R., Volk, R., Pinton, J.-F., and Bourgoin, M. Spatial structuration of finite size particles seeded in a turbulent water flow. *submitted to PRL physics.flu-dyn* (2012).

[17] Frisch, U. *Turbulence: The Legacy of A. N. Kolmogorov*. Cambridge University Press, 1995.

[18] Frish, M. B., and Webb, W. W. Direct measurement of vorticity by optical probe. *Journal of Fluid Mechanics 107* (1981), 173–200.

[19] Gallavotti, G., and Cohen, E. G. D. Dynamical ensembles in nonequilibrium statistical mechanics. *Physical Review Letters* (1995).

[20] Gasteuil, Y. *Instrumentation Lagrangienne en Turbulence: Mise en œuvre et Analyse*. PhD thesis, École Normale Supérieure de Lyon, November 2009.

[21] Gasteuil, Y., Shew, W. L., Gibert, M., Chillà, F., Castaing, B., and Pinton, J.-F. Lagrangian temperature, velocity, and local heat flux measurement in Rayleigh-Bénard convection. *Physical Review Letters 99*, 23 (2007), 234302.

[22] Gatignol, R. The Faxén formulae for a rigid particle in an unsteady non-uniform Stokes flow. *Journal de Mecanique Theorique et Appliquée 2*, 2 (Jan 1983), 143–160.

[23] Goldstein, H. *Classical Mechanics*. Pearson, 2002.

[24] Hill, R. Methods for measuring energy dissipation rate in anisotropic turbulence. *Arxiv preprint arXiv:0802.3937* (2008).

[25] Horowitz, P., and Winfield, H. *The Art of Electronics*, second edition ed. Cambridge University Press, 1989.

[26] Ito, Y. Long-term drift mechanism of Ta2O5 gate pH-ISFETs. *Sensors and Actuators B 64*, 1-3 (2000), 152–155.

[27] Janata, J. *Principles of Chemical Sensors*, 2nd ed. Springer-Verlag Berlin-Heidelberg, Mar. 2010.

[28] Joubaud, S. *Fluctuations dans les systèmes hors d'équilibre*. PhD thesis, École Normale Supérieure de Lyon, June 2008.

[29] Joubaud, S. private communication. 2012.

[30] Kabsch, W. A discussion of the solution for the best rotation to relate two sets of vectors. *Acta Cryst. Sec. A 32*, 5 (1976), 827–828.

[31] Kabsch, W. A solution for the best rotation to relate two vector sets. *Acta Cryst. Sec. A 32* (1976), 922–923.

[32] Klein, S., Gibert, M., Bérut, A., and Bodenschatz, E. Simultaneous 3D measurement of the translation and rotation of finite size particles and the flow field in a fully developed turbulent water flow. *arXiv.org physics.flu-dyn* (May 2012).

[33] Kovesi, P. D. MATLAB and Octave functions for computer vision and image processing http://www.csse.uwa.edu.au/~pk/research/matlabfns/. Centre for Exploration Targeting, School of Earth and Environment, The University of Western Australia.

[34] Kühnel, W. *Differentialgeometrie: Kurven – Flächen – Mannigfaltigkeiten*, 5th ed. Vieweg+Teubner Verlag, Apr. 2010.

[35] Landau, L., and Lifschitz, E. M. *Lehrbuch der theoretischen Physik – Hydrodynamik*, 5 ed., vol. 4. Akademie Verlag, 1991.

[36] Landau, L., and Lifschitz, E. M. *Lehrbuch der theoretischen Physik – Mechanik*, 5 ed., vol. 1. Akademie Verlag, 1991.

[37] Lattman, E. E. Optimal sampling of the rotation function. *Acta Cryst. Sec. B 28*, 4 (1972), 1065–1068.

[38] Loth, E., and Dorgan, A. J. An equation of motion for particles of finite reynolds number and size. *Environ Fluid Mech 9*, 2 (Apr 2009), 187–206.

[39] Magnus, G. Über die Abweichung der Geschosse, und: Über eine auffallende Erscheinung bei rotierenden Körpern. *Annalen der Physik und Chemie 88*, 1 (1853), 1–29.

[40] Maxey, M. The motion of small spherical particles in a cellular flow field. *Physics of Fluids 30* (1987), 1915.

[41] Maxey, M., and Riley, J. Equation of motion for a small rigid sphere in a nonuniform flow. *Physics of Fluids 26* (1983), 883.

[42] Monchaux, R., Cortet, P.-P., Chavanis, P.-H., Chiffaudel, A., Daviaud, F., Diribarne, P., and Dubrulle, B. Fluctuation-Dissipation Relations and Statistical Temperatures in a Turbulent von Kármán Flow. *Physical Review Letters 101* (Oct 2008), 174502.

[43] Monchaux, R., Ravelet, F., Dubrulle, B., Chiffaudel, A., and Daviaud, F. Properties of steady states in turbulent axisymmetric flows. *Physical Review Letters 96*, 12 (Mar 2006), 124502.

[44] Mordant, N. *Mesure lagrangienne en turbulence : mise en œuvre et analyse*. PhD thesis, École Normale Supérieure de Lyon, 2001.

[45] Mordant, N., Crawford, A., and Bodenschatz, E. Three-Dimensional Structure of the Lagrangian Acceleration in Turbulent Flows. *Physical Review Letters 93*, 21 (Nov. 2004), 214501.

[46] Mordant, N., Crawford, A. M., and Bodenschatz, E. B. Experimental Lagrangian acceleration probability density function measurement. *Physica D 193*, 1-4 (2004), 245 – 251.

[47] Morgenshtein, A. Design and methodology of ISFET (Ion sensitive field effect transistor) microsystems for bio-telemetry. Master's thesis, Israel Institute of Technology, 2003.

[48] Naso, A., and Prosperetti, A. The interaction between a solid particle and a turbulent flow. *New Journal of Physics 12* (2010), 033040.

[49] Otsu, N. A threshold selection method from gray-level histograms. *IEEE Transactions on Systems, Man and Cybernetics 9* (1979), 62–66.

[50] Ouellette, N. T., Xu, H., Bourgoin, M., and Bodenschatz, E. Small-scale anisotropy in Lagrangian turbulence. *New Journal of Physics 8* (2006), 102.

[51] Pelli, D. G. The VideoToolbox software for visual psychophysics: transforming numbers into movies. *Spatial vision 10*, 4 (1997), 437–442.

[52] Pope, S. B. *Turbulent Flows*. Cambridge University Press, 2000.

[53] Qureshi, N. *Experimental Investigation of Finite–Sized Inertial Particles Dynamics in Wind Tunnel Grid Generated Turbulence*. PhD thesis, Université Joseph Fourier - Grenoble 1, May 2009.

[54] Qureshi, N., Arrieta, U., Baudet, C., Cartellier, A., Gagne, Y., and Bourgoin, M. Acceleration statistics of inertial particles in turbulent flow. *The European Physical Journal B 66*, 4 (2008), 531–536.

[55] Qureshi, N., Bourgoin, M., Baudet, C., Cartellier, A., and Gagne, Y. Turbulent transport of material particles: An experimental study of finite size effects. *Physical Review Letters 99*, 18 (2007), 184502.

[56] Rastello, M., Marié, J., Grosjean, N., and Lance, M. Drag and lift forces on interface-contaminated bubbles spinning in a rotating flow. *Journal of Fluid Mechanics 624* (Apr 2009), 159.

[57] Ravelet, F. *Bifurcations globales hydrodynamiques et magnétohydrodynamiques dans un écoulement de von Kármán turbulent*. PhD thesis, École doctorale de l'École Polytechnique, October 2005.

[58] Ravelet, F., Chiffaudel, A., and Daviaud, F. Supercritical transition to turbulence in an inertially driven von Kármán closed flow. *Journal of Fluid Mechanics Digital Archive 601* (2008), 339–364.

[59] Shew, W. L., Gasteuil, Y., Gibert, M., Metz, P., and Pinton, J.-F. Instrumented tracer for Lagrangian measurements in Rayleigh-Bénard convection. *Review of Scientific Instruments 78*, 6 (2007), 065105.

[60] Simand, C. *étude de la turbulence inhomogène au voisinage d'un vortex intense*. PhD thesis, École Normale Supérieure de Lyon, November 2002.

[61] Soille, P. *Morphological image analysis: principles and applications*. Springer-Verlag New York, Inc., 2003.

[62] Stevens, B. L., and Lewis, F. L. *Aircraft Control and Simulation*. Wiley, 2003.

[63] Tennekes, H., and Lumley, J. L. *A First Course in Turbulence*. MIT Press, 1972.

[64] The MathWorks, Inc. http://www.mathworks.com/matlabcentral/.

[65] Toschi, F., and Bodenschatz, E. Lagrangian properties of particles in turbulence. *Annual Review of Fluid Mechanics 41*, 1 (2009), 375–404.

[66] Touchette, H. The large deviation approach to statistical mechanics. *Physics Reports 478*, 1-3 (July 2009), 1–69.

[67] Tropea, C., Yarin, A., and Foss, J. F., Eds. *Springer Handbook of Experimental Fluid Dynamics*. Springer-Verlag Berlin-Heidelberg, 2007.

[68] Tsai, R. A versatile camera calibration technique for high-accuracy 3D machine vision metrology using off-the-shelf TV cameras and lenses. *IEEE Journal of Robotics and Automation 3*, 4 (1987), 323–344.

[69] Van Dyke, M. *An album of fluid motion*, vol. 46. Parabolic Press Stanford, CA, 1982.

[70] van Nierop, E., Luther, S., Bluemink, J. J., Magnaudet, J., Prosperetti, A., and Lohse, D. Drag and lift forces on bubbles in a rotating flow. *Journal of Fluid Mechanics 571* (Jan 2007), 439.

[71] Volk, R. private communication. 2012.

[72] Volk, R., Calzavarini, E., Leveque, E., and Pinton, J.-F. Dynamics of inertial particles in a turbulent von Kármán flow. *Journal of Fluid Mechanics 668*, 1 (2011), 223–235.

[73] Volk, R., Odier, P., and Pinton, J.-F. Fluctuation of magnetic induction in von Kármán swirling flows. *Physics of Fluids 18*, 8 (2006), 085105.

[74] Voth, G. A., Porta, A. L., Crawford, A., Alexander, J., and Bodenschatz, E. Measurement of particle accelerations in fully developed turbulence. *Journal of Fluid Mechanics 469* (2002), 121–160.

[75] Weisstein, E. W. http://mathworld.wolfram.com/.

[76] Wilkinson, M., and Pumir, A. Spherical Ornstein-Uhlenbeck processes. *Journal of Statistical Physics 145* (2011), 113–142. 10.1007/s10955-011-0332-6.

[77] Xu, H. Tracking Lagrangian trajectories in position–velocity space. *Measurement Science and Technology 19*, 7 (June 2008), 075105.

[78] Xu, H., and Bodenschatz, E. Motion of inertial particles with size larger than Kolmogorov scale in turbulent flows. *Physica D 237*, 14-17 (2008), 2095–2100.

[79] Ye, J., and Roco, M. Particle rotation in a couette flow. *Physics of Fluids A 4* (1992), 220.

[80] Zimmermann, R. The Lagrangian Exploration Module. Diploma Thesis, University of Göttingen, 2008.

[81] Zimmermann, R., Fiabane, L., Gasteuil, Y., Volk, R., and Pinton, J.-F. Measuring Lagrangian accelerations using an instrumented particle. *Arxiv preprint arXiv:1206.1617* (2012).

[82] Zimmermann, R., Gasteuil, Y., Bourgoin, M., Volk, R., Pumir, A., and Pinton, J.-F. Rotational Intermittency and Turbulence Induced Lift Experienced by Large Particles in a Turbulent Flow. *Physical Review Letters 106*, 15 (Apr. 2011), 154501.

[83] Zimmermann, R., Gasteuil, Y., Bourgoin, M., Volk, R., Pumir, A., and Pinton, J.-F. Tracking the dynamics of translation and absolute orientation of a sphere in a turbulent flow. *Review of Scientific Instruments 82* (2011), 033906.

[84] Zimmermann, R., Gasteuil, Y., Volk, R., Bourgoin, M., Pumir, A., and Pinton, J.-F. Turbulence induced lift experienced by large particles in a turbulent flow. *Journal of Physics: Conference Series 318*, 5 (Dec. 2011), 052027.

[85] Zimmermann, R., Xu, H., Gasteuil, Y., Bourgoin, M., Volk, R., Pinton, J.-F., and Bodenschatz, E. The Lagrangian Exploration Module: An Apparatus for the Study of Statistically Homogeneous and Isotropic Turbulence. *Review of Scientific Instruments 81* (2010), 055112.

Abstract: The aim of this dissertation is to gain a better understanding of the Lagrangian dynamics of solid large spheres in a complex turbulent environment. Therefore, a novel measurement technique to optically track the 6–dimensional dynamics – position and absolute orientation – of large spheres advected by a complex flow is developed. Although the sphere's diameter is comparable to the integral length of the underlying flow, we find intermittency for both the translation and the rotation. Moreover, rotation and translation couple in agreement with a lift force. Apart from the fact that the acceleration statistics are not gaussian, and the exchange of energy between the particle and the carrier flow falls into the mathematical theory of large deviations. Additionally, we find that the particle diameter has a surprisingly strong influence on how a particle samples the flow.

The 6D–tracking technique is then applied to an instrumented particle, which embarks a 3D–accelerometer and a radio-transmission system to constantly emit the felt Lagrangian acceleration as it is advected in the flow. Measuring the particle's absolute orientation is a crucial step here to project the acceleration measured by the particle into the laboratory reference frame and enables us to compare the forces obtained by the two independent measurements. Based thereon methods for interpreting the acceleration signals of the instrumented particle are developed and tested.

Keywords: turbulence, instrumented particle, Lagrangian dynamics, finite-size effects, fluctuation theorem, image and signal processing

Résumé : Le but de ce travail de thèse est l'étude de la dynamique de sphères de grande taille dans un écoulement fortement turbulent. Pour ce faire, nous avons développé une nouvelle technique optique permettant de suivre la dynamique à 6 dimensions – position et orientation absolues – de plusieurs particules dans un écoulement complexe. Bien que la taille des particules soit comparable à l'échelle intégrale de l'écoulement, nous trouvons que sa dynamique de rotation et de translation est intermittente. De plus, nous observons que la translation et la rotation sont reliées par la force de Magnus. La répartition statistique de l'accélération n'est pas gaussienne et l'échange d'énergie avec le fluide est gouverné par la théorie mathématique des grandes déviations. Nous trouvons que le diamètre influence fortement la manière dont la particule explore l'écoulement.

Nous avons ensuite appliqué le suivi de position et d'orientation à une particule instrumentée. Ce système mesure en permanence l'accélération lagrangienne qu'il subit via un accéléromètre embarqué et émet l'information à travers une électronique radio fréquence. L'orientation absolue est nécessaire pour exprimer les signaux de l'accéléromètre et ceux du suivi optique dans un repère commun; cela nous permet de comparer rigoureusement les mesures issues de ces deux techniques indépendantes. À partir de ces résultats nous avons développé des méthodes pour inférer des propriétés de l'écoulement à partir des signaux d'accélération de la particule instrumentée.

Mots-clefs : turbulence, dynamique lagrangienne, effets de taille, particule instrumentée, théorème de fluctuations, traitement d'image et du signal